Textural and petrological studies of anatexis and melt transfer in the Himalayan Orogen



Brendan Dyck

University College

University of Oxford

Thesis submitted in support of an application for leave to supplicate for the degree of

Doctor of Philosophy

Trinity 2016

Abstract

Mineral textures, preserved in the metamorphosed sedimentary sequences that are exposed in orogenic hinterlands, are crucial to understanding the architecture and evolution of collisional mountain belts. In this thesis the textural record of anatexis and melt transfer in the Himalayan metamorphic core is decoded and the controls that these processes exert on the tectonic evolution of the Himalaya are explored. The problem is divided into two parts, corresponding to variations in protolith lithostratigraphy: *melt source* – the pelitic region where melt was first generated, and *melt sink* – the psammitic region where melt accumulated and crystallised. Dehydration melting of muscovite has long been recognized as a critical reaction for the generation of anatectic melt in the Himalaya, but a textural understanding of how this reaction progresses is limited by the inherent difficulties in identifying specific reaction products. Using samples collected from the Langtang area in central Nepal, a mechanistic model for muscovite dehydration melting was constructed, and a set of textural criteria were developed, which were used to distinguish peritectic K-feldspar from K-feldspar grains formed during melt crystallisation. Melt is transferred from the source to the sink in two stages: firstly along a pervasive network of mineral grain boundaries, and secondly via a channelised network of sills and dykes in the melt sink where it solidified as leucogranite. Variation in the primary mineral assemblage and appearance of leucogranite bodies reflect the degree of interaction that occurred between the melt and metasedimentary country rock, rather than a change in primary melt composition. The modal proportion of K-feldspar in the melt source requires vapour-absent conditions during muscovite dehydration melting and leucogranite formation, indicating that the generation of large volumes of granitic melts in orogenic belts is not necessarily contingent on an external source of fluids. The crystallisation of hydrous minerals in leucogranite consumes <15.5 % of water released by the breakdown of muscovite. These results indicate that anatexis efficiently dehydrates the middle crust and suggests that the continents have limited potential to store water over geological time.

Extended abstract

Anatectic melts are a product of high-temperature metamorphism. As such, the spatial and temporal distribution of crystallised anatectic melt provides a record of the thermal evolution of the crust. In the Himalaya, the relationship between crustal thickening, metamorphism, anatexis, and the exhumation of the middle and lower crust has been subject to intense multidisciplinary study; one of the main aims of which has been to understand how metamorphism affects crustal strength. Outstanding questions remain, regarding the role of crustal fluids in Himalayan anatexis, the source of melt for the voluminous leucogranites, and the control that anatexis exerts on the thermomechanical evolution of collisional mountain belts. In this thesis these questions are addressed by separating the problem into two parts, corresponding to variations in protolith lithostratigraphy: *melt source* – the pelitic region where melt was first generated, and *melt sink* – the psammitic region where melt accumulated and crystallised. The tectonic implication of anatexis and melt transfer, and the protolith lithostratigraphy of the Himalayan metamorphic core, were elucidated by integrating field and petrographic observations with chemical, geochronological, and thermodynamic analyses. Furthermore, analyses of rock textures and mineral microstructure were used as a basis for inferring grain-scale petrological processes.

Chapter 2 focuses on the textures, reaction mechanisms, and regional implications of muscovite dehydration melting in the pelitic melt source. Dehydration melting of muscovite in metasedimentary sequences is the initially dominant mechanism of granitic melt generation in orogenic hinterlands. In dry (vapour-absent) crust, muscovite dehydrates to produce K-feldspar, sillimanite, and monzogranitic melt. When water vapour is present,

sillimanite and melt are the sole products of muscovite dehydration melting, and any K-feldspar produced is as a result of melt crystallisation. In this thesis, I document the reaction mechanisms that control nucleation and growth of K-feldspar, sillimanite and silicate melt in the metamorphic core of the Himalayas, and outline the textural criteria used to distinguish peritectic K-feldspar from K-feldspar grains formed during melt crystallisation. I have characterised four stages of textural evolution in selected psammitic and pelitic samples from the Langtang and Everest regions: 1) K-feldspar nucleated epitaxially on plagioclase while intergrowths of fibrolitic sillimanite and the remaining hydrous melt components replaced muscovite. 2) In quartzofeldspathic domains K-feldspar replaced plagioclase by K^+ – Na^+ cation exchange, while melt and intergrowths of sillimanite + quartz formed in the aluminous domains. 3) At 7-8 % melt generation, the system transitioned from a closed to open system and all phases coarsened by up to two orders of magnitude, resulting in large K-feldspar porphyroblasts. 4) Preferential crystallisation of residual melt on K-feldspar porphyroblasts and coarsened quartz resulted in an augen gneiss texture with a monzogranitic-tonalitic matrix that contains intergrowths of sillimanite + tourmaline + muscovite + apatite. Initial poikiloblasts of peritectic K-feldspar trapped fine-grained inclusions of quartz and biotite by replacement growth of matrix plagioclase. During subsequent coarsening, peritectic K-feldspar grains overgrew and trapped fabric-aligned biotite, resulting in a core to rim coarsening of inclusion size. These textural criteria enable a mass-balance of peritectic K-feldspar and sillimanite to constrain the amount of free water present during muscovite dehydration. The resulting modal proportion of K-feldspar in the Himalayan metamorphic core require vapour-absent conditions during muscovite dehydration melting and leucogranite formation, indicating that the generation of large volumes of granitic melts in orogenic belts is not necessarily contingent on an external source of fluids.

Melt transfer from the source to the sink resulted in the formation of the leucogranite sills and dykes, which are ubiquitous amongst the upper levels of the Himalayan metamorphic core. In chapter 3 I review the variety of leucogranite types found in the Langtang region of northern Nepal, and propose a process for the formation of the most enigmatic type, termed the 'nebulitic tourmaline leucogranite'.

The nebulitic tourmaline leucogranite presents an interesting petrological problem because it exhibits rhythmic, compositional layering that is continuous with the transposed bedding of its psammitic country rock. Closely associated with intrusive muscovite-biotite leucogranite sills and dykes of a demonstrably anatectic origin, the formation of nebulitic tourmaline leucogranite in the Himalaya is an indirect product of the high-temperature metamorphism and anatexis. A comparison of microstructures in the nebulitic tourmaline leucogranite, muscovite-biotite leucogranite, and psammitic country rock indicate the nebulitic tourmaline leucogranite formed by the pervasive infiltration of a volatile-rich melt. The *in-situ* alteration and textural modification of the compositionally layered psammite resulted in the growth of the volatile-bearing minerals: tourmaline and apatite (reaction 1).

(1) $\text{melt}_{(r)}$ + biotite + plagioclase = $\text{melt}_{(p)}$ + tourmaline + K-feldspar + apatite + quartz

Where $melt_{(r)}$ represents the initial (reactant) melt composition and $melt_{(p)}$ is the evolved final (product) melt composition. Propagation of the reaction front was governed by the chemical permeability of the psammite and the availability of boron as the limiting reagent, and was driven by the energy released by the exothermic tourmaline-forming reaction. The distribution and orientation of product phases were ordered by interface-controlled processes, operating on the domain-scale, which ultimately resulted in the inheritance of the psammitic compositional fabric. The removal of biotite and the presence of melt along

protolith grain boundaries encouraged grain boundary mobility, resulting in a bulk grain-size coarsening. Highly irregular grain boundaries preserve a record of the late-stage crystallisation of interstitial melt along mineral grain boundaries. These findings suggest that the transient passage of melt through a rock leaves a textural record, which may be preserved during cooling and exhumation from mid-crustal levels. Field estimates, based on the proportion of medium- and coarse-grained leucocratic rock, considerably overestimate the volume of melt in the Himalaya (by up to 60 %), because they do not account for the volume of sub-solidus psammite that was involved in forming the nebulitic tourmaline leucogranites. Accounting for the processed presented in chapter 3, the volume of crystallised anatectic melt in the Himalaya could have been sourced from a 2.5 to 3.5 km thick layer of pelite, which generated ~20 modal % of segregated melt.

The transport of anatectic melt through the Greater Himalayan Series occurred in two main stages: 1) The first stage originated in the pelitic source, where melt migration was initially pervasive, operating along a network of grain boundaries. With increasing distance from the melt source, melt became channelised and migrated along a meter-scale network of sills and dykes. 2) The second stage of anatectic melt migration operated during melt solidification and the emplacement of leucogranite. Fractionated melt migrated pervasively through the psammitic country-rock, driving mineral reactions in the psammite, and ultimately, the formation of nebulitic tourmaline leucogranite. Beyond this stage, the fate of remaining fractionated melt and exsolved volatile components is uncertain; however it is expected that the fluid flow became increasingly channelised with further transport, reducing the degree of fluid-rock interaction, and consequently the degree of textural modification in the host rock.

In chapter 4, results from the textural studies of anatexis and melt transfer are integrated into a study of protolith lithostratigraphy in the Greater Himalayan Series. Reconstruction of the protolith lithostratigraphy of amphibolite-facies metasedimentary rocks of the Greater Himalayan Series in Nepal documents a single, long-lived passive margin sequence deposited on the northern margin of the Indian craton. In the Langtang area, Paleoproterozoic cratonic gneiss is unconformably overlain by a prograding sequence of fluvio-deltaic quartzite and basinal pelite. The maximum flooding surface of the paleo-basin is demarked by accumulation of psammitic turbidite strata that grade up-section into micaceous semipelite and fluvial pelite. U-Th-Pb zircon and monazite geochronology constrain the timing of deposition of the Greater Himalayan Series in Langtang between ca. 815 and 460 Ma. Regional variation in the first-order composition and thickness of the Greater Himalayan Series along the length of the Himalaya is attributed to the occurrence of siliciclastic depocenters centered on Zanskar in northern India, and Langtang and Everest in central to western Nepal, which contrast with coeval marine carbonate shelf strata in Annapurna. The protolith lithostratigraphy documented for Langtang and Everest provides a coherent framework for interpreting subsequent Cenozoic Himalayan deformation, specifically the homogeneously-distributed layer-parallel shortening that characterizes the Greater Himalayan Series. Within the context of a single protracted northern Indian marginal sedimentary sequence, the distinction between the Lower, Greater and Tethyan Himalaya appears to be more tectonostructural than lithostratigraphic in origin.

In chapter 5, the results of the textural and lithostratigraphic studies are integrated into a petrographically informed mass-balance calculation, which traces the efficiency of water release during Himalayan anatexis. Following muscovite dehydration melting at ~700°C, liberated water is expected to have moved through the crust in two stages. Firstly, as a

component of hydrous silicate melt (i.e. leucogranitic melt), and secondly as a free aqueous fluid. The results of the calculation indicate that >84.5 % of the initial amount of water released by muscovite dehydration migrated away from the metamorphic middle crust in the Langtang region of the Greater Himalayan Series. Similarly low values are expected in other middle and lower crustal environments, since the efficiency of water release is primarily a function of the volume of hydrous minerals formed during melt crystallisation, and is independent of the leucogranite host lithology. Equilibrium phase models indicate that rock composition and the pre-existing mineral assemblage exert a primary control on the amount of water that can be retained in the upper crust. As well as interpreting the textural record of past anatectic events, this study may provide insight into the anatectic processes that are inferred to be active beneath the Tibetan Plateau today.

To Claire

Table of contents

1 Introduction 1

1.1 A statement of the problem 1

1.2 Aims and objectives 3

1.3 Thesis structure 4

1.4 Geological setting of the Himalaya 5

1.4.1 Himalayan tectonic domains 7

1.5 Metamorphic evolution of the Greater Himalayan Series 9

1.5.1 Models of Himalayan anatexis 11

2 Muscovite dehydration melting; reaction mechanisms, textures, and implications for anatexis 15

2.1 Introduction 15

2.2 Geological context 20

2.3 Sample selection 23

2.4 Analytical methods 27

2.5 Reaction textures 29

2.5.1 Nature of protoliths 29

2.5.2 K-feldspar microstructures 31

2.5.3 Interpretation of K-feldspar microstructures 40

2.5.4 Sillimanite microstructures 43

2.5.5 Interpretation of sillimanite and melt growth 48

2.5.6 Further discussion on melting textures 50

2.6 Model for muscovite dehydration melting 55

2.7 Insights into the governing reaction mechanisms 58

2.7.1 Epitaxial nucleation 58

2.7.2 Sillimanite and quartz intergrowths 58

2.7.3 Chemically driven mineral growth 60

2.7.4 Grain-size coarsening processes 61

2.7.5 Textural modification during melt crystallisation 62

2.8 Implications for crustal anatexis 63

2.9 Conclusions 67

3 Melt-rock interaction and the formation of the Himalayan nebulitic tourmaline leucogranites 69

3.1 Introduction 69
3.2 Geological setting and samples 72
3.3 Analytical methods 74
3.4 Field relations and macrofeatures 75
3.4.1 Psammitic country-rock 75
3.4.2 Leucogranitic bodies 77
3.5 Microstructures 81
3.5.1 Psammitic country-rock: sample BD1413 81
3.5.2 Muscovite-biotite-(sillimanite) leucogranite: sample BD1213 83
3.5.3 Nebulitic tourmaline leucogranite: sample BD1414 86
3.5.4 Contact between psammite and nebulitic tourmaline leucogranite: sample BD1415 90
3.6 Interpretation of microstructures 93
3.6.1 Psammitic country-rock 93
3.6.2 Muscovite-biotite-(sillimanite) leucogranite 94
3.6.3 Nebulitic tourmaline leucogranite 95
3.6.4 Contact features 97
3.7 Microstructural analysis 99
3.7.1 Grain-size analysis 99
3.7.2 Grain shape 102
3.7.3 EBSD analysis 105
3.8 Nature of the transforming agent 106
3.9 Synthesis of reaction process 108
3.10 Chemical evolution of the reacting melt 113
3.11 Formation of irregular grain boundaries 115
3.12 Thermodynamic considerations 118
3.13 Implications for crustal anatexis 122
3.14 Summary and conclusions 126

4 Protolith lithostratigraphy of the Greater Himalayan Series in the Langtang and Everest regions of Nepal: implications for the architecture of the northern Indian margin 127

4.1 Introduction 127
4.2 Regional lithostratigraphic context 130
4.3 Geological background and samples 133

4.4 Langtang lithostratigraphy 136
4.5 Timing of Greater Himalayan Series deposition 140
4.5.1 Analytical methods 140
4.5.2 Results 143
4.6 Protolith identification 155
4.7 Greater Himalayan Series protolith lithostratigraphy 156
4.8 Implications for Himalayan structure 159

5 Synthesis and conclusions 163
5.1 Fate of water released by muscovite dehydration melting 163
5.1.1 Motivation for calculation 164
5.1.2 Muscovite dehydration melting in the Himalaya 168
5.1.3 Methods and model assumptions 169
5.1.4 Initial contribution of water 171
5.1.5 Two stages of water retention 172
5.1.6 Mechanism of fluid escape 174
5.1.7 Retrograde reactions in the upper crust 175
5.1.8 Control on upper crustal strength 177
5.1.9 Upward flux of water beneath the Tibetan Plateau 177
5.1.10 Contribution to global water cycle 178
5.2 Thermal evolution of the Greater Himalayan Series 179
5.3 High-grade reaction textures 180
5.4 Future directions 183

Bibliography 185

Appendices 222
A1 Description of external contributions 223
A2 Protolith map of Langtang area 224
A3 Zircon and monazite BSE & CL images 225
A4 Sample GPS coordinates 226

List of figures

Figure 1.1 Digital elevation map (DEM) of the Himalaya and Tibetan Plateau 6
Figure 1.2 Generalised geological map of the Himalaya..... 9
Figure 2.1 (a) Equilibrium phase diagram 17
Figure 2.2 Simplified Himalayan tectonostratigraphic map and cross-section of the Greater Himalayan Series 22
Figure 2.3 Geological map and cross-section of the Langtang field area..... 25
Figure 2.4 Cross-section of the Everest field area 26
Figure 2.5 Protolith textures 30
Figure 2.6 K-feldspar nucleation textures..... 32
Figure 2.7 Back scattered image and feldspar pole figures 33
Figure 2.8 K-feldspar poikiloblasts 34
Figure 2.9 Photomicrographs showing K-feldspar porphyroblasts 36
Figure 2.10 Photomicrographs of sample E203 and E204 39
Figure 2.11 Sillimanite microstructures and the textures 44
Figure 2.12 Cathodoluminesence images of quartzofeldspathic and aluminous micro-domains..... 46
Figure 2.13 Sillimanite microstructures..... 47
Figure 2.14 Accessory mineral textures..... 54
Figure 2.15 Schematic diagram of the vapour-absent muscovite dehydration reaction mechanisms..... 57
Figure 2.16 Outcrop photographs of the representative textures..... 64
Figure 3.1 Geological map and cross-section of the Langtang field area..... 72
Figure 3.2 Field relations and macro-features of the psammitic country-rock..... 76
Figure 3.3 Muscovite-biotite leucogranite field relations..... 78
Figure 3.4 Field relations and macro-features of the nebulitic tourmaline leucogranite . 80
Figure 3.5 Microstructures in the psammitic country-rock 83
Figure 3.6 Microstructures in the muscovite-biotite-(sillimanite) leucogranite 85
Figure 3.7 Cathodoluminesence textures in the muscovite-biotite-(sillimanite) leucogranite..... 86
Figure 3.8 Microstructures in the nebulitic tourmaline leucogranite..... 89

Figure 3.9 Cathodoluminesence textures in the nebulitic tourmaline leucogranite 90
Figure 3.10 Microstructural features across the contact between psammite and nebulitic tourmaline leucogranite 92
Figure 3.11 Histogram 100
Figure 3.12 Bivariate scatter plots 104
Figure 3.13 EBSD analyses of mosaic plagioclase 106
Figure 3.14 (a) Schematic model for the formation of irregular grain boundaries 117
Figure 3.15 Schematic illustrating the two thermodynamic scenarios 121
Figure 3.16 Schematic illustrating the consequence of melt-rock interaction 125
Figure 4.1 Simplified geological map of the Himalaya 128
Figure 4.2 Geological map of Langtang 134
Figure 4.3 Cross-section through the Greater Himalayan Series in Langtang 135
Figure 4.4 Outcrop photographs of the major lithostratigraphic units 139
Figure 4.5 Concordia plots 141
Figure 4.6 U-Pb Zircon and monazite geochronology results 142
Figure 4.7 Schematic along-strike section 159
Figure 5.1 Schematic of the global water cycle 165
Figure 5.2 Equilibrium phase diagram 167
Figure 5.3 Schematic cross-section through the Himalaya and Tibetan Plateau 169
Figure 5.4 Schematic of the water fluxes 174
Figure 5.5 Phase equilibrium models 176

List of tables

Table 2.1 Theriak output 18
Table 2.2 Sample metadata. 27
Table 3.1 Sample metadata 74
Table 3.2 Bivariate Linear Regression Statistics 103
Table 3.3 Modal % change in mineral phases for the proposed reactions 112
Table 3.4 Melt compositions 114
Table 3.5 Standard enthalpies of formation 120
Table 3.6 Enthalpy calculation – input parameters 121
Table 5.1 Calculation input parameters. Note the structural thickness of pelite only include the layers that have reached solidus temperatures. 172

1 Introduction

1.1 A STATEMENT OF THE PROBLEM

The formation and migration of partial melts in Earth's crust (i.e. anatexis) are among the most important processes in the tectonic evolution of mountain belts. This is because incomplete melting, followed by separation of the melt from the residual solid, causes chemical differentiation; the ultimate result is the concentration of the more evolved rock types in the upper continental crust. The processes that operate at the intersection between solid crust and partial melt characterise a critical stage in a range of geological feedback cycles, from shear-zone development (e.g. Rosenberg & Handy, 2005) to the thermal and chemical ordering of continents (e.g. Brown, 2007a). Anatectic melts are a product of high-temperature metamorphism. As such, the spatial and temporal distribution of crystallised anatectic melt provides a record of the thermal evolution of the crust. Furthermore, based on our understanding of how the crust melts and the mechanisms that allow a melt phase to segregate and migrate, we can infer the composition and thermal conditions of deep and inaccessible portions of the crust (Brown & Rushmer, 2006).

In continent-continent collision zones (e.g. the Himalaya), the relationship between crustal thickening, metamorphism, anatexis, and exhumation of the middle and lower crust has been subject to intense multidisciplinary study in an attempt to understand how metamorphism affects crustal strength (e.g. Brown, 1994, Harrison *et al.*, 1998, Beaumont *et al.*, 2001). This has led to a division of opinion and opposing theories about the role that anatexis plays on the mechanisms of mid- and lower crustal exhumation (c.f. Godin *et al.*, 2006b, Kohn, 2008 and references therein). In the Himalaya, where much of this discussion is focused, several fundamental aspects of anatexis in continent-continent collisions remain disputed, including: what were the boundary conditions at the onset of

anatexis, was melting caused by the influx of externally sourced water (i.e. dry or wet melting), was all of the melt (crystallised as leucogranite) locally derived or was there mass and heat input from the mantle? Consequently, multiple models exist to describe Himalayan anatexis and the formation of leucogranites (which are explored in detail in section 1.5). Answers to these questions are critical to understanding crustal processes ongoing today beneath the Tibetan Plateau, where high-grade metamorphism and anatexis are inferred from the results of deep (~20–40 km) seismic and magnetotelluric surveys (e.g. Brown *et al.*, 1996, Nelson *et al.*, 1996).

To address these questions, methods are required that can be used to examine the record of anatexis and melt transfer from the grain scale to the regional scale. Due in part to the large timescales (Ka–Ma) and spatial extent (μm–km) over which anatexis operates, it cannot be studied directly, or fully replicated in a laboratory environment. However, it is possible to study the record of anatexis in natural samples (e.g. leucogranite and metamorphic restite) and make inferences about key processes. This record can be decoded using field and petrographic observations, and quantified by integrating chemical, geochronological, and thermodynamic constraints. Studies of anatexis and melt transfer in the Himalaya have focused on the chemistry, timing, and ambient conditions of partial melting (e.g. Le Fort *et al.*, 1987, Visonà & Lombardo, 2002, Searle *et al.*, 2010). As a consequence of this focus, the ambient conditions and timing of crustal melting along the length of the Himalaya are reasonably well constrained (e.g. Wang *et al.*, 2016 and references therein). However, despite recent advances, many of the original questions pertaining to the generation and emplacement of anatectic melts in the Himalaya remain unanswered.

1.2 AIMS AND OBJECTIVES

The aim of this thesis is to decipher the mechanisms of partial melt generation and melt transfer in the Himalaya using the textural and microstructural information contained within natural samples. This is achieved by integrating field and microscopic observations with thermochemical analyses to produce process-oriented petrological models. In doing so, grain-scale mechanisms are elucidated and the broader implications for crustal anatexis are explored.

The problem is divided into two parts, corresponding to two crustal regions: *melt source* – the region where melt is first generated, and *melt sink* – the region where melt accumulates and crystallises. Both regions and the relationship between them were studied in Langtang, which is an area in central Nepal containing two large valleys that transect the Himalayan metamorphic core. Three topics were targeted for multidisciplinary study: the generation of anatectic melt by muscovite dehydration melting (chapter 2), the mechanisms of melt transfer and melt–rock interaction (chapter 3), and the protolith stratigraphy of the high-grade Himalayan metamorphic core (chapter 4). These topics were first identified in the field, and once a suitable range of samples were collected, each study was designed to address the following objectives:

- Construct a set of natural samples that preserve a record of the targeted anatectic process (i.e. muscovite dehydration melting, melt–rock interaction).
- Determine the most appropriate method of analysing and interpreting the textural record contained in each sample.
- Identify the key textures and microstructures formed during anatexis and melt transfer, and develop a textural framework from which reaction mechanisms can be inferred.
- Incorporate the results of each study into a self-consistent regional tectonic model.

This thesis presents the results of the three studies listed above in the form of three research papers (chapters 2-4). In chapter 5, the results from each study are integrated into a discussion on the fate of water released by anatexis in the Himalaya. Contributions to these studies made by collaborators are listed in Appendix A1; all other work is my own.

1.3 THESIS STRUCTURE

Chapter 2–3 - These chapters comprise the bulk of the thesis and document two detailed textural and petrological studies of melt generation and transfer, and melt–rock interaction. Regional introductions, motivation for sample selection, data analysis, interpretations, and conclusions are presented in both chapters.

Chapter 4 - The results from the preceding textural studies are integrated into a study of protolith stratigraphy in the Himalayan metamorphic core. This chapter discusses the architecture and age of the north Indian margin prior to the formation of the Himalaya and the constraints that protolith stratigraphy place on the structure and evolution of the Himalaya.

Chapter 5 - In this chapter, the main results are integrated into a mass-balance of the water that is released and sequestered during Himalayan anatexis. This chapter also presents a summary of the general reaction processes discussed in this thesis and gives suggestions for future research.

Appendices – Supplementary data relevant to each chapter can be found in this section, together with as summary of samples collected and a statement of external contribution.

1.4 GEOLOGICAL SETTING OF THE HIMALAYA

The collision between India and Eurasia ca. 50 Myr (Garzanti *et al.*, 1987, Zhu *et al.*, 2005, Green *et al.*, 2008) ago resulted in the uplift of the Himalaya-Karakoram ranges and the Tibetan Plateau, forming the youngest and largest continent-continent collisional belt on Earth. Convergence between the two continents resulted in crustal thickening along the north Indian margin (forming the Himalaya) and along the southern margin of Eurasia (forming the Karakoram, Hindu Kush, and much of the Tibetan Plateau; figure 1.1). The Himalayan Range (or 'Himalaya'), which forms one section of the much larger Himalaya-Alpine orogenic system, stretches for ~2400 km from the Afghanistan-Pakistan border in the west to the Burma-south China border in the east (figure 1.1). Due to their pre-eminence, the Himalaya and Tibetan Plateau have been subject to numerous seismic, magnetotelluric, and GPS investigations, which have unambiguously shown that these regions are still undergoing active deformation today (Molnar, 1988).

Across the central Himalaya, the current rate of convergence between India and Eurasia is estimated to be around 18 ± 2 mm/yr (Larson *et al.*, 1999, Bettinelli *et al.*, 2006). However, estimates of the rate of convergence prior to terminal collision are on the order of 150 mm/yr (Molnar & Stock, 2009), and so the current rate does not reflect the full degree of crustal shortening. Crustal thickening of Indian margin sediments and the occurrence of high-pressure metamorphic rocks in the Himalayan metamorphic core indicate that a significant degree of shortening was accommodated in the upper and middle crust of the Indian plate. Additional shortening was accommodated by homogeneous thickening (Dewey *et al.*, 1988) and lateral extrusion (Royden *et al.*, 1997) of material within the Eurasian Plate. Estimates of total shortening across the Himalaya based on mass balanced cross-sections range between 650–1500 km (e.g. Argand, 1924, Dewey *et al.*, 1989, DeCelles *et al.*, 2002). In contrast, estimates based on the available paleomagnetic

plate reconstructions suggest up to 3200 km of shortening has occurred (e.g. Molnar & Tapponnier, 1975, Van Hinsbergen *et al.*, 2012). The deformational response of the rigid Indian lower crust differs significantly from the dominantly sedimentary upper and middle crust (ibid). The Indian lower crust underthrusts the Tibetan Plateau, resulting in a lithosphere that is approximately twice as thick as the unaffected portions of the Indian and Eurasian plates (Dewey *et al.*, 1988). As background to the studies presented in this thesis, a brief overview of the principal tectonic domains of the Himalaya is given below (after Le Fort, 1986, Hodges *et al.*, 1996, Hodges, 2000, Searle *et al.*, 2008 unless otherwise stated).

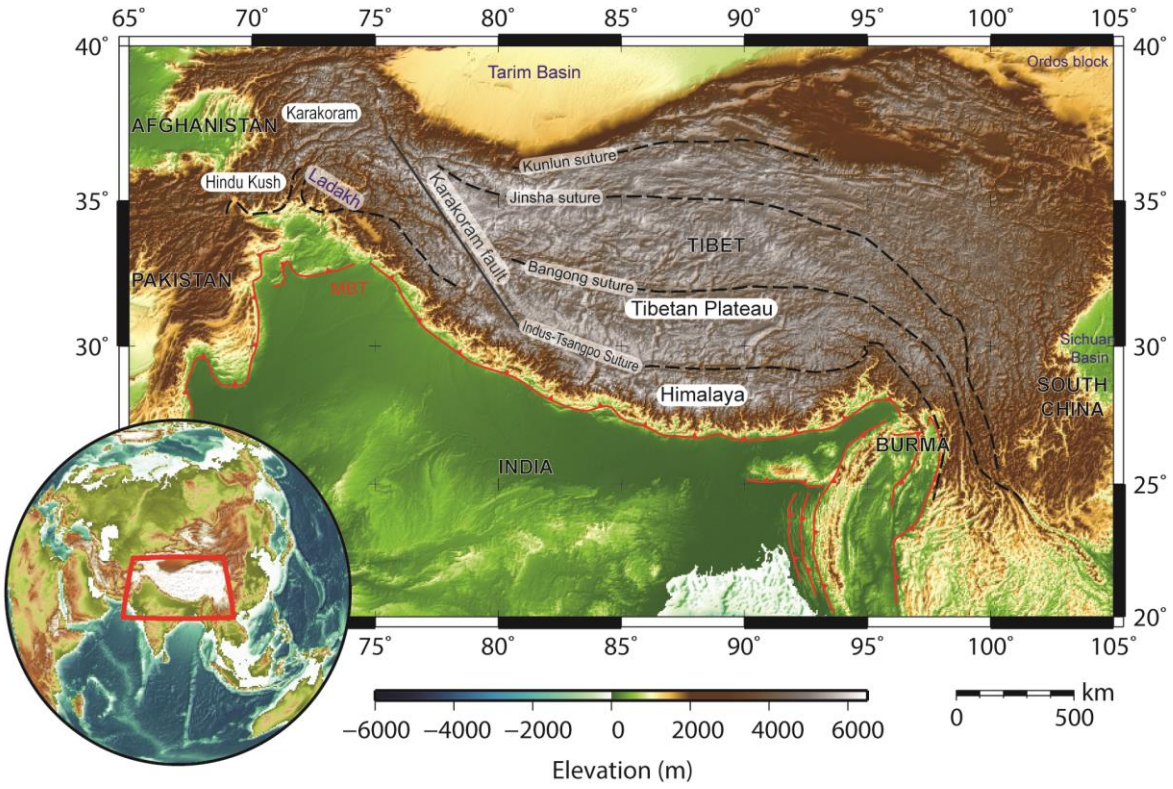


Figure 1.1 Digital elevation map (DEM) of the Himalaya and Tibetan Plateau, showing the bounding structures and major lithotectonic domains after (Taylor & Yin, 2009). DEM data and source: 90 m resolution topography from the Shuttle Radar Topography Mission (SRTM; Farr *et al.*, 2007).

1.4.1 Himalayan tectonic domains

The India-Eurasia collision zone can be divided into six lithotectonic domains running parallel to the length of the range: the Transhimalayan batholith, the Kohistan-Ladakh arc, the Indus Tsangpo Suture Zone, the Tethyan Himalayan Series, the Greater Himalayan Series, and the Lesser Himalayan Series (figure 1.2). The Transhimalayan batholith is a continental arc, formed along the southern margin of Eurasia prior to its collision with India. It consists of volcanic and plutonic rocks hosted in variably metamorphosed Precambrian–Mesozoic country rock (Searle, 1991). The region around the Transhimalayan batholith is poorly documented due to geopolitical limitations and as such there have been few studies that explore the pre-Himalayan geology on the southern margin of Eurasia.

The Kohistan-Ladakh arc is an island arc complex whose accretion to Eurasia in the late Cretaceous to Paleocene marks the final pre-Himalayan accretionary event (Rolfo *et al.*, 1997). The Kohistan-Ladakh arc consists of Lower Cretaceous to Paleocene volcanic and sedimentary units overlying a lower crust comprised of gabbro, garnet-bearing granulite, and ultramafic rocks that are intruded by granite (Jan & Howie, 1981).

The Indus Tsangpo Suture Zone marks the zone of collision between India and Eurasia, and consists of remnant Neo-Tethyan components (dismembered ophiolites, ophiolitic melange, and basinal sedimentary rocks); Transhimalayan components (forearc volcanoclastic strata); as well as exotic components removed from Tethyan seamounts (Permian–Triassic limestone). The Indus Tsangpo Suture Zone is separated from the southern Tethyan Himalayan Series by the aptly named Great Counter Thrust, a steep southward-dipping backthrust fault (figure 1.2).

The Tethyan Himalayan Series forms the broad region of the southern Tibetan Plateau, between the Greater Himalayan Series and the Indus Tsangpo Suture Zone. It

comprises a near complete Cambrian–Eocene stratigraphic record of the northern Indian margin, beginning with Lower Cambrian shallow-marine dolomites and siliciclastic strata and passing upwards into Upper Cambrian deep-marine strata. Along the length of the Himalaya, these strata are unconformably overlain by passive/rifted margin sequences that record the opening of the Paleo–Neotethys (Stampfli *et al.*, 1991). The Tethyan Himalayan Series is bound at its base by an array of low-angle northwards dipping normal faults, the South Tibetan Detachment System. The South Tibetan Detachment System comprises a series of sub-parallel detachments that were active in the Miocene, until ca. 11 Ma (Cottle *et al.*, 2015). The timing of movement along the South Tibetan Detachment System has important implications for the exhumation of the underlying Greater Himalayan Series, which are discussed further below (section 1.5).

The Greater Himalayan Series makes up the kyanite-sillimanite-grade metamorphic core of the Himalaya. It crops out as a continuous package along the main Himalayan range, and in isolated structural domes north of the Himalaya. The Greater Himalayan Series consists of a package of biotite/garnet- to sillimanite-K-feldspar-grade metamorphosed siliciclastic and carbonaceous rocks with panels of granodioritic augen gneiss and K-feldspar augen gneiss, which experienced peak metamorphic conditions in the Eocene–Miocene. In the upper portion of the Greater Himalayan Series, widespread sillimanite-grade metamorphism and associated anatexis resulted in the emplacement of muscovite-biotite and tourmaline leucogranite sills and dykes. The thickness of the Greater Himalayan Series varies along strike from ~5–25 km, corresponding to variations in the protolith stratigraphic architecture of the northern Indian margin. A more detailed description of the metamorphic and tectonic evolution of the Greater Himalayan Series is provided below (in section 1.5). At its base, the Greater Himalayan Series is bounded by the Main Central Thrust zone, an imbricated zone of northwards-dipping thrusts that

juxtapose the high-grade Greater Himalayan Series over the low-grade or unmetamorphosed Lesser Himalayan Series.

The Lesser Himalayan Series is characterised by a sequence of predominately Neoproterozoic clastic and carbonate units, Paleozoic limestones and shales, and late Cambrian to early Ordovician granites. The low-grade Lesser Himalayan Series strata are bound along their base by the Main Boundary Thrust.

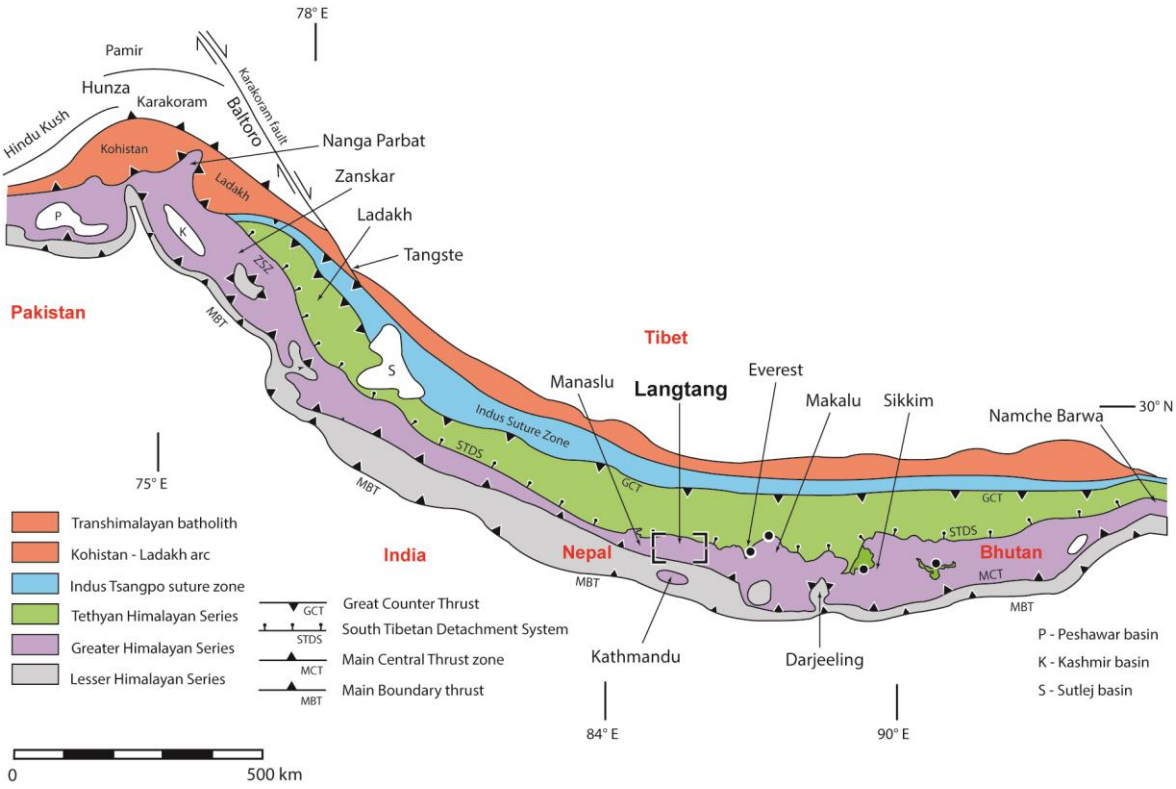


Figure 1.2 Generalised geological map of the Himalaya, modified after Searle *et al.* (2008).

1.5 METAMORPHIC EVOLUTION OF THE GREATER HIMALAYAN SERIES

The tectonic evolution of the Greater Himalayan Series presents a unique problem because, while it is the high-grade metamorphic core of the orogeny, it is both overlain and underlain by low-grade to unmetamorphosed tectonic domains. As such it has received much attention from metamorphic petrologists and structural geologists alike. Nearly four

decades of metamorphic and geochronology studies conducted along valley transects of the Greater Himalayan Series and the related northern structural domes, have produced a two-stage metamorphic model that is largely consistent along the strike of the Himalaya.

Following initial collision, the northern Indian margin experienced crustal thickening and Barrovian-style metamorphism, which culminated in a regional kyanite-grade metamorphism (e.g. Godin *et al.*, 2001). U–Pb dating of metamorphic monazite (e.g. Godin *et al.*, 2001, Stephenson *et al.*, 2001, Walker *et al.*, 2001), and Sm–Nd dating of garnet cores (e.g. Vance & Harris, 1999) indicate this first stage of metamorphism peaked between ca. 37–30 Ma. During this stage, the Greater Himalayan Series was subject to pressures (*P*) between 0.9–1.2 GPa, and temperatures (*T*) of 550–660 °C (e.g. Vannay & Hodges, 1996, Macfarlane, 1999).

Subsequent decompression and heating along an open clockwise *P–T* loop resulted in a regional sillimanite-K-feldspar-grade metamorphism (Searle *et al.*, 2010). This second stage of metamorphism resulted in widespread anatexis and the associated formation of leucogranite (ibid). U–Pb ages of monazites from sillimanite-K-feldspar-grade pelitic and psammitic samples span between ca. 26–15 Ma (e.g. Simpson *et al.*, 2000, Godin *et al.*, 2001, Kohn *et al.*, 2005, Groppo *et al.*, 2010, Searle *et al.*, 2010, Wang *et al.*, 2016 and references therein). Similar U–Pb ages are reported from studies on the oscillatory zoned zircon present in Himalayan leucogranites (ca. 24–18 Ma; Le Fort *et al.*, 1987, Simpson *et al.*, 2000, Kellett *et al.*, 2010, Searle *et al.*, 2010, Streule *et al.*, 2010b, Wang *et al.*, 2016), indicating peak-metamorphism and associated anatexis spanned a 2–6 Myr range. Available *P–T* data indicate that the peak metamorphic conditions reached temperatures of approximately 700–790°C, at pressures between 0.4–0.7 GPa (e.g. Inger & Harris, 1992, Macfarlane, 1999, Kohn, 2008, Streule *et al.*, 2010b, Groppo *et al.*, 2013). While the high-temperature limit of the second metamorphic stage has proven difficult to constrain by

conventional thermobarometric methods, owing to the increased rate of intracrystalline diffusion at the high temperatures and retrograde resorption of garnet rims upon cooling, temperatures in the Greater Himalayan Series remained below the conditions required for biotite dehydration melting. In general, metamorphic temperatures increased structurally upwards through the Greater Himalayan Series, resulting in the Himalaya's iconic inverted metamorphic isograds (e.g. Bird, 1978).

There are two notable exceptions to the along-strike continuity of metamorphism in the Greater Himalayan Series, the Himalayan syntaxes; Nanga Parbat in the west and Namche Barwa in the east (figure 1.2). While Nanga Parbat experienced similar peak metamorphic conditions to the rest of the Greater Himalayan Series, ≥ 700°C at 0.5 GPa during the Miocene (Whittington *et al.*, 2000), it also experienced a widespread younger sillimanite-grade anatectic event during the Pliocene–Pleistocene (ca. 1.7 Ma; Zeitler *et al.*, 2001, Crowley *et al.*, 2009). In contrast, rocks from the core of the Namche Barwa massif display unusually high metamorphic grade and young leucogranite ages (e.g. Burg *et al.*, 1997, Booth *et al.*, 2009). Based on the available *P–T* data, Namche Barwa is inferred to have experienced peak temperatures ≥ 800°C at 1.1–1.5 GPa, which were high enough for biotite dehydration melting (e.g. Ding & Zhong, 1999, Guilmette *et al.*, 2011). Peak conditions were followed by isothermal decompression to mid-crustal pressures ~ 0.6 GPa (ibid). U–Pb zircon and monazite ages from the Namche Barwa gneisses and leucogranites yield a complete range of ages from 40–3 Ma (e.g. Booth *et al.*, 2004, Booth *et al.*, 2009, Zhang *et al.*, 2012), indicating a protracted period of heating and anatexis.

1.5.1 Models of Himalayan anatexis

The relationship between inverted metamorphism, anatexis, and Greater Himalayan Series exhumation has spawned several thermo-mechanical models. The classic 'hot-iron' model

(Le Fort, 1975) argued for post-thrust conductive heating and dehydration of the Lesser Himalayan Series. In this model, fluids released from the Lesser Himalayan Series infiltrate the Greater Himalayan Series, resulting in vapour-present (wet) melting. In contrast, Harris and Massey (1994) suggested exhumation and associated decompression triggered vapour-absent (dry) muscovite dehydration melting based on isotopic geochemistry, negating the need for an external fluid source. The other commonly considered models all assume that anatexis resulted from progressive accretion of metasedimentary rocks and the heat source is radiogenic, frictional, mantle-derived, or a combination of these sources. These models can be sorted into three categories. In the first, metamorphism and anatexis predate exhumation (e.g. Searle & Rex, 1989, Hubbard, 1996). In the second, decompression melting occurs during the ductile extrusion of the Greater Himalayan Series (e.g. Grujic *et al.*, 1996). In this model, vapour-present melting is thought to precede vapour-absent melting (Harrison *et al.*, 1997). A modified version of the ductile extrusion model, termed channel flow (Beaumont *et al.*, 2001), invokes significant mechanical weakening during anatexis, resulting in significantly further displacement of the Greater Himalayan Series relative to its peak metamorphic position. Both ductile extrusion and channel flow require coeval motion along the South Tibetan Detachment System and the Main Central Thrust zone. The third category interprets the Greater Himalayan Series as a 'critical-taper', where material is continually added by frontal accretion, or underplating. The geometry of the critical taper is maintained during frontal accretion and surface erosion, by backthrusts (e.g. Elliott, 1976, Dahlen, 1990). In the critical-taper model, the source of heat for anatexis is internal, and the metamorphosed material is not transported great distances from its protolith position. In contrast with the models of ductile extrusion and channel flow, coeval motion along the bounding South Tibetan Detachment System and Main Central Thrust zone is not a requirement for critical-

taper. Critical-taper models have been satisfactorily invoked to explain the large scale structure of the Himalaya, but do not offer any unique predictions for the timing or style of anatexis.

This brief summary illustrates the most significant differences in the various thermo-mechanical models; namely, the presence or absence of a free vapour phase during anatexis, and the contribution (if any) of heat and mass from the mantle. Accordingly, these questions are the motivation for the study of muscovite dehydration melting presented in chapter 2.

2 Muscovite dehydration melting; reaction mechanisms, textures, and implications for anatexis

2.1 INTRODUCTION

Dehydration melting of muscovite has long been recognized as a critical reaction for the generation of anatectic melt in pelitic rocks (e.g. Thompson & Algor, 1977, Le Breton & Thompson, 1988, Vielzeuf & Holloway, 1988, Brearley & Rubie, 1990), but a textural understanding of how this reaction progresses is limited by the inherent difficulties in identifying specific reaction products. Muscovite dehydration melting progresses under vapour-present and vapour-absent conditions resulting in two incongruent anatectic reactions with distinct peritectic products. When water is present as a vapour phase, the first melt-producing reaction encountered under the pressure and temperature conditions of orogenesis and crustal thickening (Barrovian metamorphism) is K-feldspar-absent muscovite dehydration melting (2.1), which produces sillimanite (or kyanite) as a peritectic phase (e.g. Petö, 1976, Thompson, 1982, St-Onge, 1984, Pattison & Tracy, 1991, Patiño-Douce & Harris, 1998). If water vapour is not present then the first voluminous melt producing reaction encountered is the vapour-absent muscovite dehydration melting reaction (2.2) (e.g. Evans & Guidotti, 1966, Thompson & Algor, 1977, Gardien *et al.*, 1995, Patiño-Douce & Harris, 1998). This reaction yields both sillimanite (or kyanite) and K-feldspar as peritectic products.

(2.1) $Ms + H_2O + Qz + Pl = Sil\ (Ky) + Melt$

(2.2) $Ms + Qz + Pl = Kfs + Sil\ (Ky) + Melt$

Developing a textural understanding of the muscovite dehydration melting reactions requires not only the ability to differentiate the reaction products from the pre-existing

solid phases (i.e. quartz, plagioclase, biotite, sillimanite), and an appreciation of how components diffuse on the grain-scale, but also an understanding of how melt solidification and sub-solidus recrystallisation may modify grain microstructure. In theory, both K-feldspar absent and vapour-absent muscovite dehydration melting reactions can be distinguished from (sillimanite-absent) wet-granite melting if sillimanite and silicate melt are identified. The difficulty in practice lies in distinguishing the products of K-feldspar-absent from vapour-absent muscovite dehydration melting (the latter yielding K-feldspar as a peritectic phase in contrast to the former), since silicate melt crystallises K-feldspar together with quartz and plagioclase upon cooling. This is in contrast to similar studies of biotite dehydration melting which forms peritectic garnet, cordierite, or orthopyroxene that are easily identified (Waters, 1988, Harley, 1998).

The development of a thermodynamic model for haplogranitic melt in Na_2O-CaO-K_2O-FeO-MgO-Al_2O_3-SiO_2-H_2O (White *et al.*, 2001) makes it possible to calculate the melt-bearing equilibria for pelitic compositions, and emphasizes the importance of vapour-absent muscovite-dehydration as an 'effective solidus' with reduced water activity (solid bold line on figure 2.1a). Figure 2.1b shows the predicted change in the volume % of stable phases along a 0.7 GPa isobaric transect of the pelitic composition presented in figure 2.1a. The figure shows that vapour-absent muscovite dehydration melting operates across a narrow 10 to 20 °C temperature window, which can be crossed by either heating or decompression. In theory, the stoichiometry of the vapour-absent reaction (2.2) will vary slightly between rocks with different bulk compositions, as well as within an isochemical system where melt evolves towards a lower water activity across the reaction band. However, in practice, the volume ratio of the product phases: K-feldspar, sillimanite, and melt remains close to 8:5:10 across the reaction band (table 2.1). In the absence of unambiguous evidence for melt having at one point been present in a now cooled rock, the

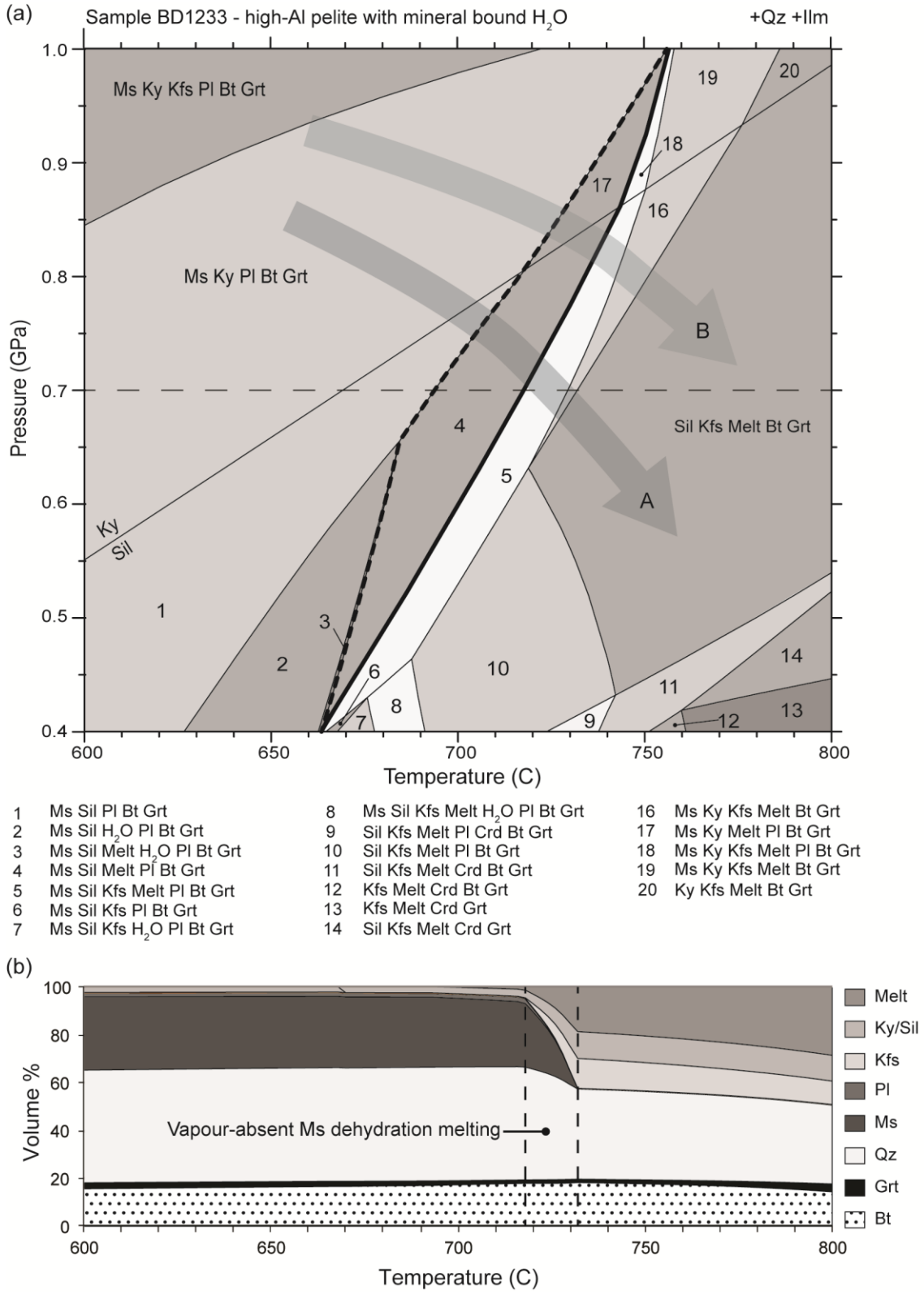


Figure 2.1 (a) Equilibrium phase diagram depicting the stable assemblages of sample BD1233 in pressure (P) and temperature (T) space. Assemblage fields are shaded according to the number of degrees of freedom, with higher-variance assemblages represented by darker shading. Mineral abbreviations presented in the model are: biotite (Bt), cordierite (Crd), garnet (Grt), water vapour (H_2O), ilmenite (Ilm), K-feldspar (Kfs), kyanite (Ky), silicate melt (Melt), muscovite (Ms), plagioclase (Pl), quartz (Qz), sillimanite (Sil). The bold dashed line marks the onset of K-feldspar absent muscovite dehydration melting (reaction 2.1). The solid

bold line denotes the onset of vapour-absent muscovite dehydration melting (reaction 2.2). Path A and B represent P-T conditions of sillimanite-K-feldspar-grade metamorphism reported by previous thermobarometry studies of the Langtang Greater Himalayan Series field area (Inger and Harris, 1993; Kohn 2008). The isobaric transect presented in frame b is marked by the horizontal dashed line. (b) Isobaric (0.7 GPa) cross-section showing the modal % change in minerals with respect to temperature across the vapour-absent muscovite dehydration melting reaction.

Temperature	716°C	720°C	724°C	728°C	732°C	736°C
biotite	17.9	17.9	17.9	18.0	18.3	18.1
garnet	1.4	1.4	1.5	1.5	1.4	1.4
quartz	47.4	46.3	44.4	41.5	37.7	37.6
muscovite	27.2	24.0	18.5	10.6	0.0	0.0
plagioclase	1.9	1.4	0.7	0.2	0.0	0.0
K-feldspar	0.0	1.7	4.5	8.1	12.5	12.4
sillimanite	3.0	4.0	5.7	8.1	11.2	11.2
melt	0.9	2.9	6.5	11.7	18.6	19.0
Normalised volume % of vapour-absent muscovite dehydration melting products						
K-feldspar	0.0	36.4	35.2	33.8	32.6	32.0
sillimanite	0.0	20.7	20.9	21.0	21.3	21.1
melt	0.0	42.9	44.0	45.1	46.1	46.9

Table 2.1 Theriak output calculated at 0.7 GPa: volume % of stable phases across the temperature interval of vapour-absent muscovite dehydration.

proportions of the solid (peritectic) phases (i.e. K-feldspar and sillimanite) can be used to estimate the extent of melting, by applying the stoichiometric volume ratio of the reaction products (c.f. Harris *et al.*, 1995).

At the pressure and temperature conditions where muscovite dehydration and partial melting reactions overlap, any free water (vapour) would promote vapour-present melting (reaction 2.1) until the limited reactant is exhausted (i.e. muscovite or water). In the absence of free water (vapour), any water released by the breakdown of muscovite will go directly into the water-undersaturated melt without the generation of a free vapour phase (Thompson, 1982). Kerrick (1972) demonstrated this with muscovite melting experiments that were performed in the presence of a free fluid phase with reduced water activity, and

concluded that vapour-absent muscovite dehydration melting does not alter the composition of a free fluid phase with low water activity that is in equilibrium with the product assemblage. Changing the water activity does nevertheless affect the composition of the product melt; higher water activities generate a trondhjemitic melt (Patiño-Douce & Harris, 1998).

One consideration to make before using a volume ratio to calculate the extent of melting is whether the solid (peritectic) phases were all produced by incongruent melting of muscovite. While the first occurrence of K-feldspar in a Barrovian sequence is as a peritectic product of vapour-absent muscovite dehydration melting, as the rock is exhumed to the surface and cooled additional K-feldspar will crystallise from the melt phase. In the case of open-system melt behaviour, peritectic sillimanite may be entrained during melt loss effectively removing it from the source pelite. Moreover, in appropriate compositions, the first sillimanite isograd (i.e. from the kyanite–sillimanite transition or the breakdown of staurolite) precedes vapour-absent muscovite dehydration melting, and so an amount of sillimanite may already be present in the samples before muscovite reacts (e.g. 2–3 % modal in Figure 1b).

Experiments by Patiño-Douce and Harris (1998) on vapour-absent muscovite dehydration melting in Himalayan samples reveal two important considerations for selecting natural samples. First, this reaction consumes a mass of muscovite approximately three times more than that of quartz or plagioclase, which means muscovite is likely to be the limiting reactant. The second consideration pertains to the effect of plagioclase and muscovite solid-solution on the thermal stability of the assemblage muscovite + plagioclase + quartz. The presence of Fe, Mg, Ti and F in muscovite and variable Ca-Na in plagioclase can increase the onset temperature for this reaction by 50–80 °C when compared to a system with pure end-member compositions (c.f. Petö, 1976, Patiño-Douce

& Harris, 1998). In practice, I expect preservation of intermediate stages of the vapour-absent muscovite dehydration melting reaction to be rare, as the reaction band is narrow and can be crossed by both heating and decompression. As a result, all of the samples described in this study have passed through the reaction band without quenching.

Despite the known importance of vapour-absent muscovite-dehydration as the first voluminous melt-producing reaction in most mid-crustal scenarios (e.g. Patiño-Douce & Johnston, 1991, Gardien *et al.*, 1995, Zhang *et al.*, 2004, Raith *et al.*, 2010), limited progress has been made in our ability to recognise associated micro-textures, and in identifying the rheological implications of the reaction in natural examples. In this contribution I demonstrate how vapour-absent muscovite dehydration melting progresses on the grain-scale, at sillimanite-grade conditions, and propose the reaction mechanisms involved in the formation of peritectic K-feldspar, peritectic sillimanite and anatectic melt. The framework for this study is based on the textural observations of four distinct K-feldspar generations found in rocks that experienced vapour-absent muscovite dehydration melting. Modal proportions of K-feldspar (in rocks that were initially K-feldspar-absent) are used to estimate the extent of melting, expressed as melt % generated. I discuss the processes operating at each stage of the reaction and propose a reaction model for muscovite dehydration melting.

2.2 GEOLOGICAL CONTEXT

Subduction of the leading edge of the Indian plate immediately preceding the India-Asia collision and closure of the NeoTethys Ocean at ca. 50 Ma (Searle *et al.*, 1987b, Green *et al.*, 2008) resulted in eclogite-facies metamorphism of packets of thinned continental crust (O'Brien *et al.*, 2001, St-Onge *et al.*, 2013). Following the (ultra)-high-pressure metamorphism and rapid exhumation of eclogites to lower-crustal levels (Palin *et al.*,

2014), crustal shortening and thickening led to widespread kyanite-grade metamorphism during the late Eocene-Oligocene (Streule *et al.*, 2010a) followed by a widespread sillimanite-grade metamorphism during the Miocene (Searle *et al.*, 2010). The orogenic belt is divided into four tectonic domains (figure 2.2): The Indus Tsangpo suture zone demarks the northern extent of the orogen, and is separated from the metamorphic core by the low-grade or unmetamorphosed sedimentary Tethyan Himalayan Series (THS). The Greater Himalayan Series (GHS) forms the kyanite-sillimanite-grade metamorphic core, and is structurally bound by two major north-dipping structures; to the north by the South Tibetan Detachment System, which juxtaposes the mainly unmetamorphosed Tethyan Himalayan Series above the Greater Himalayan Series (Searle *et al.*, 1997a, Streule *et al.*, 2010a), and to the south by the Main Central Thrust zone (MCT), which separates the Greater Himalayan Series and the biotite-garnet-grade Lesser Himalayan Series (LHS). The LHS structurally overlies the Sub-Himalayan Siwalik molasse along the north-dipping Main Boundary

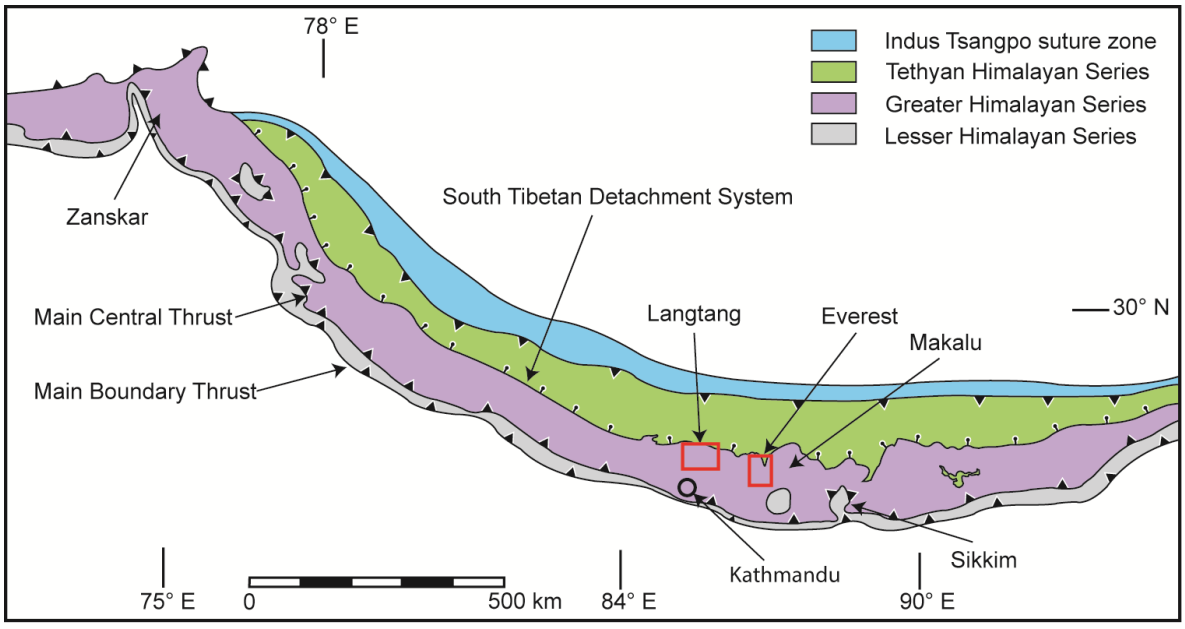


Figure 2.2 Simplified Himalayan tectonostratigraphic map and cross-section of the Greater Himalayan Series. Red boxes mark the location of the Langtang and Everest transects where samples were collected. Modified after Searle *et al.* (2008).

Thrust. The Main Frontal Thrust is the presently active thrust fault that marks the southern boundary of the Himalaya. As a result of the crustal thickening and foreland propagating deformation, subsequent heating and decompression triggered vapour-absent muscovite dehydration melting and widespread late Oligocene-early Miocene sillimanite-grade metamorphism across the Greater Himalayan Series (e.g. Goscombe *et al.*, 2006, Searle *et al.*, 2008, Streule *et al.*, 2010a). In the late Miocene, exhumation of the Greater Himalayan Series was accommodated by a series of in-sequence thrusts and post-metamorphic south-vergent recumbent folding, resulting in a structurally inverted sequence of Barrovian metamorphic isograds (Le Fort, 1986, Searle & Rex, 1989).

The present exposure of the Greater Himalayan Series reveals a tectonic package of biotite/garnet- to sillimanite-K-feldspar-grade metamorphosed siliciclastic and carbonaceous rocks. Along-strike variations in Greater Himalayan Series stratigraphy and unit thickness from 5-10 km thick carbonate-dominated sections (e.g. Annapurna transect; Colchen *et al.*, 1986, Hodges *et al.*, 1996) to 15–25 km thick siliciclastic sections (e.g. Langtang and Everest transects; Reddy *et al.*, 1993, Searle *et al.*, 2003, Searle *et al.*, 2006a), are interpreted to represent inherent variations in the stratigraphic architecture of the protolith margin (see chapter 4). Structurally upwards from the imbricated zone of the Main Central Thrust, the Greater Himalayan Series comprises (figure 2.3 & figure 2.4): kyanite-grade quartzite and pelite, sillimanite-K-feldspar-grade pelitic migmatite, and sillimanite-K-feldspar- to cordierite-grade psammite and pelitic migmatite, interlayered on the sub-meter scale. A framework of leucogranite sills and dykes containing biotite ± muscovite ± tourmaline ± garnet ± cordierite intrude the psammite and overlying pelite unit. Towards the top of the Greater Himalayan Series the leucogranite bodies become

more widespread and form the large foliation-parallel sheets that make up many of the highest peaks in the Himalaya (e.g. Manaslu, Makalu, Shisha Pangma, Kangchenjunga, and much of the Everest-Nuptse-Lhotse massif; Searle, 1999, Searle *et al.*, 2003, Searle *et al.*, 2006a, Streule *et al.*, 2010a). In this chapter, I concentrate on the development of anatectic melt in mica-rich metamorphosed siliciclastic rocks (psammite, semipelite, pelite) sampled from the Langtang and Everest regions, which share a common structural and metamorphic history (e.g. Reddy *et al.*, 1993, Macfarlane, 1995, Patiño-Douce & Harris, 1998, Searle *et al.*, 2003).

Phase equilibria models generated for samples of sillimanite-K-feldspar-grade pelitic migmatite from Everest (Searle *et al.*, 2003, Searle *et al.*, 2006a) and nearby Makalu (Streule *et al.*, 2010a) suggest the mid-upper Greater Himalayan Series experienced vapour-absent muscovite dehydration melting near 6.5 kbar and 700 °C during decompression. Similarly, results from geothermobarometry of sillimanite-K-feldspar grade pelitic migmatite samples from Langtang (Inger & Harris, 1992, Kohn, 2008), imply the pressure-temperature evolution of the mid-upper Greater Himalayan Series incurred vapour-absent muscovite dehydration melting around 8 kbar and 720 °C (path A and B on figure 2.1).

2.3 SAMPLE SELECTION

To isolate the micro-textural evolution across the vapour-absent muscovite dehydration melting reaction, samples were selected that represent both a range of compositions with varying modal amounts of K-feldspar and sillimanite, and an array of peak-metamorphic conditions from ~680 to 740 °C. Samples were used from complementary traverses across the Main Central Thrust zone and Greater Himalayan Series in the Langtang and Everest regions to ensure a complete range of micro-textures was considered, and to safeguard the

study from isolated conditions that may not be representative of more generally developed/applicable reaction textures. Table 2.2 presents the rock type, estimates of total melt % generated (based on observed proportions of peritectic K-feldspar and sillimanite), sample coordinates, and denotes how each sample was used in this contribution. The position of the Langtang and Everest samples with respect to the major structures and Greater Himalayan Series tectonostratigraphy are presented in figure 2.3 and figure 2.4. The Langtang samples were collected during two field seasons, in 2012 and 2014, and the Everest samples were borrowed from the Himalayan collection housed at the Oxford University Museum of Natural History. Within the context of the tectonostratigraphy of the Langtang region, samples E203 and E204 would be from the central Greater Himalayan Series pelitic augen gneiss unit, and E184 from the overlying sillimanite-grade psammite/semipelite (Simpson, 2002, Searle *et al.*, 2003).

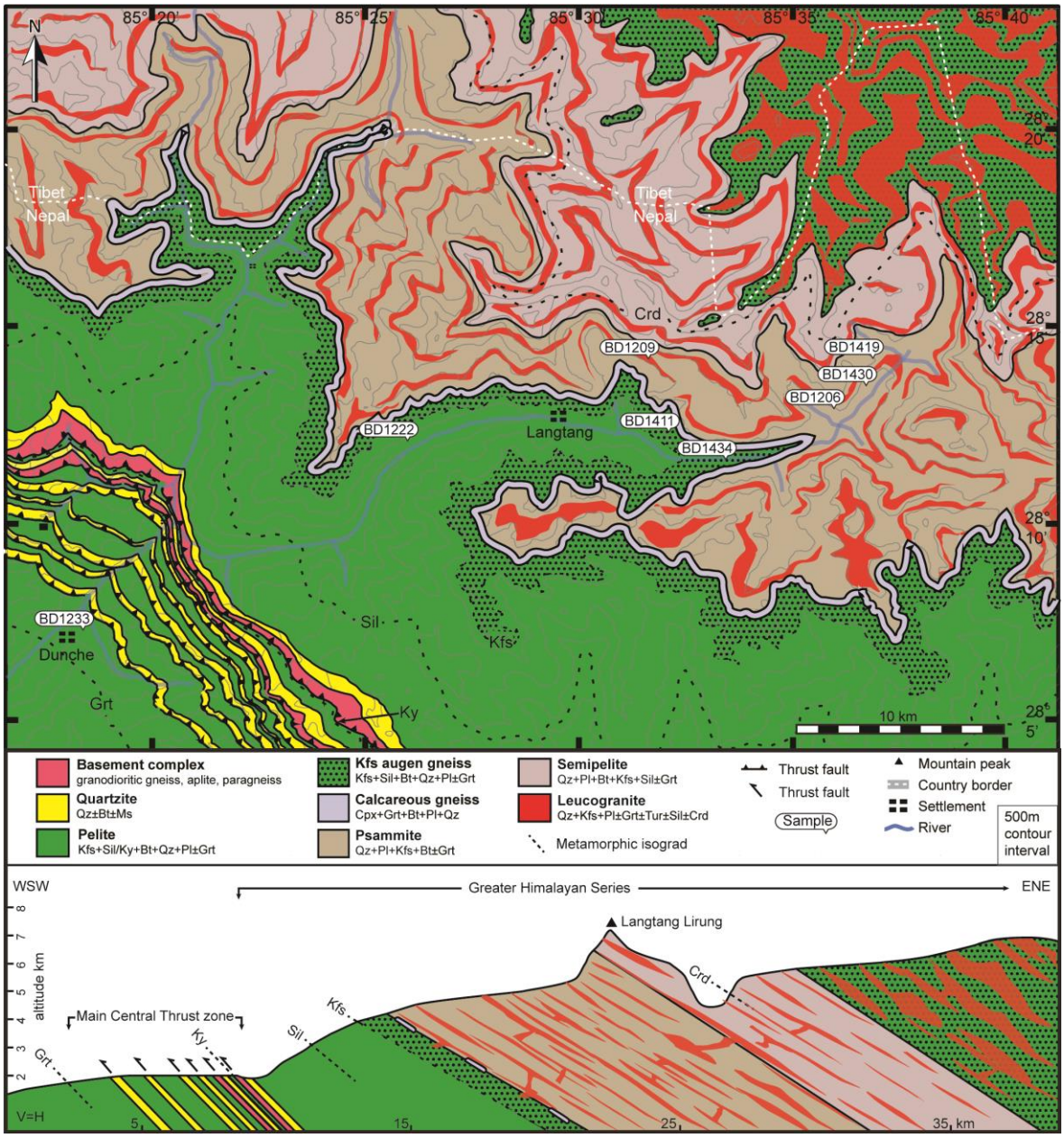


Figure 2.3 Geological map and cross-section of the Langtang field area, showing the lithology, structure, and position of metamorphic isograds across the Main Central Thrust zone and Greater Himalayan Series. Labels denote the locations of samples used in this study, for sample coordinates and rock type see table 2.1.

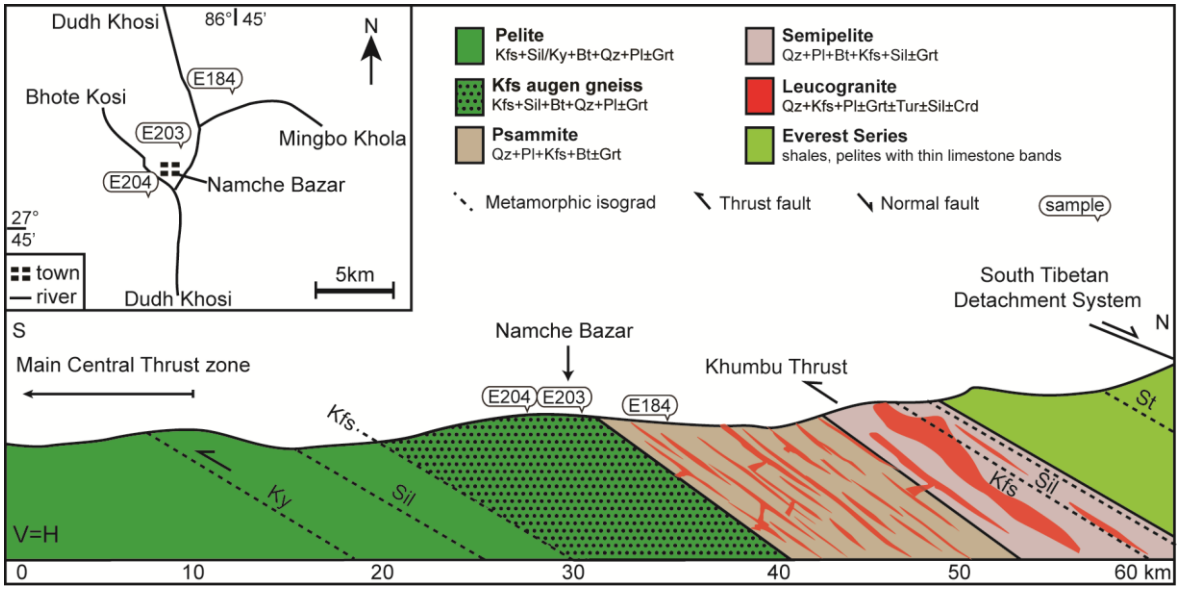


Figure 2.4 Cross-section of the Everest field area, showing the lithology, structure, and position of metamorphic isograds across the Main Central Thrust zone and Greater Himalayan Series. The inset map shows the location of samples used in this study, modified after Searle et al, (2003).

In order to view the evolution of mineral textures at different stages of melting, samples with varying compositions expressed as different modal amounts of K-feldspar, sillimanite and melt were selected, from which the modal amount of protolith muscovite is inferred. The resulting sample set comprises a range of compositions with varying modal amounts of sub-solidus muscovite; from arkosic psammite (muscovite-absent; quartz + biotite + plagioclase + ilmenite), through semipelite (0-5 % muscovite; quartz + biotite + plagioclase + muscovite + ilmenite), to pelite (5-15 % muscovite; quartz + biotite + muscovite + plagioclase + garnet + ilmenite) and high-Al pelite (15-30 % muscovite; quartz + muscovite + biotite + plagioclase + garnet + ilmenite).

Sample ID	Rock type	Estimate melt %	Longitude	Latitude	Comments
		Langtang Samples			
BD1233	Grt-Ms-Bt schist	0 % (sub-solidus)	85.33006	28.16015	Fig. 1; Fig. 5c
BD1430	Bt-Pl arkosic psammite	0%	85.55879	28.21247	Fig. 5b
BD1206	Bt-Sil-Kfs semipelite	2-3 %	85.66725	28.21582	Fig. 16a
BD1419	Bt-Sil-Kfs pelite	5-6 %	85.68480	28.22850	Fig. 14a,c,d; Fig. 16b
BD1411	Sil-Kfs-Grt pelitic augen gneiss	8-10 %	85.58324	28.20261	Fig. 13a; Fig. 16c
BD1222	Sil-Kfs-Grt pelitic augen gneiss	15-20 %	85.45514	28.20044	Fig. 13b,d
BD1434	Sil-Kfs pelitic augen gneiss	25-30 %	85.55852	28.23224	Fig. 14e,f; Fig. 16d
BD1209	Sil-Bt-Ms leucogranite dyke	100%	85.68827	28.23714	Fig. 13c
		Everest Samples			
E184	Bt-Sil-Kfs semipelite	2-3 %	27.83040	86.73822	Fig. 6; Fig. 7; Fig. 8; Fig. 11; Fig. 12; Fig.14b
E203	Sil-Kfs pelitic augen gneiss	25-30 %	27.80728	86.71958	Fig. 9a-f; Fig. 10b,e,f
E204	Sil-Kfs-Grt pelitic augen gneiss	25-30 %	27.79752	86.71136	Fig. 9g; Fig. 10a,c,d;

Table 2.2 Sample metadata.

2.4 ANALYTICAL METHODS

Backscattered electron (BSE) and cathodoluminescence (CL) images along with energy-dispersive X-ray spectroscopy (EDS) and electron backscatter diffraction (EBSD) data were collected using a FEI Quanta 650 field emission gun scanning electron microscope (SEM) at the Department of Earth Sciences, University of Oxford. CL images were produced by a Centaurus FEI monochromatic CL detector operating at 20 kV with a 25–30 mm working distance. The grayscale images produced are a sum of mineral luminescence over the complete visible spectrum. EDS analyses of polished thin sections were produced using a X-Max^N Silicon Drift Detector operating at 20 kV at a working distance of 10 mm. Processing of EDS element maps was done using Aztec 2.1 software from Oxford Instruments.

For EBSD measurements, the thin section was finely polished with colloidal silica (0.04 μm) and mounted on a stage tilted 70° to the primary beam. The thin section was uncoated and data were acquired in a low-vacuum operating mode at 50 Pa chamber

pressure. The accelerating voltage was 30 kV at a working distance of 15 mm. EBSD patterns were imaged using an Oxford Instruments Nordlys S EBSD camera and electron backscatter patterns were indexed for plagioclase and orthoclase using Aztec 2.1 acquisition software by Oxford Instruments. Subsets were selected using Channel 5 software from Oxford Instruments and the EBSD pole-plots presented in this chapter were created using the Matlab toolbox MTEX (Bachmann *et al.*, 2010).

The phase equilibria calculations presented in figure 2.1 were modelled in the chemical system MnNCKFMASHTO ($MnO–Na_2O–CaO–K_2O–FeO–MgO–Al_2O_3–SiO_2–H_2O–TiO_2–O$). The phase diagrams were calculated using *Theriak–Domino* version *03.01.2012* (de Capitani & Brown, 1987, de Capitani & Petrakakis, 2010) using the Holland and Powell (1998) thermodynamic database (dataset 5.5). Activity models used were: melt, biotite and ilmenite (White *et al.*, 2007), feldspar (Baldwin *et al.*, 2005), white mica (Coggon & Holland, 2002), and garnet (Kelsey *et al.*, 2004). The accuracy of the melt model was verified by reproducing the experimental melt compositions presented by Patiño-Douce and Harris (1998), using their muscovite schist and muscovite-biotite schist starting compositions. In both cases, the calculated evolution of melt composition as a function of temperature closely matched the experimental melt compositions. The input composition presented in this study was a modified whole-rock XRF analyses of sample BD1233 (figure 2.3; table 2.2), a high-Al pelite from the Main Central Thrust zone with ~30% muscovite at conditions immediately below the solidus. Accessory apatite and monazite in equal proportions was corrected for by removing P_2O_5 from the bulk with a proportional adjustment to CaO (Palin *et al.*, 2015). Sufficient H_2O was added to saturate the assemblage in the immediate sub-solidus at a pressure of 0.6 GPa, equivalent to 6.75 mol. %. The effective bulk composition in oxide mol. % was: H_2O – 6.75; SiO_2 – 71.03; Al_2O_3 – 10.52; CaO – 0.21; MgO – 2.86; FeO – 4.47; K_2O – 3.30; Na_2O – 0.27; TiO_2 –

0.45; MnO – 0.13; O – 0.02. Unless stated otherwise, mineral abbreviations follow Whitney and Evans (2010).

2.5 REACTION TEXTURES

2.5.1 Nature of protoliths

The majority of samples described in this study contain K-feldspar and sillimanite without any primary muscovite. In order to assess the textural evolution of muscovite dehydration melting, it is necessary to first consider the textures of unmelted samples with varying proportions of muscovite. A range of compositions are considered, which predominantly vary in primary muscovite content.

Samples of sub-solidus muscovite-biotite-garnet schist (BD1233) and arkosic psammite (BD1430) provide two end-member reference points for the micro-textural evolution detailed in this study. The distribution of muscovite in sample BD1233 reflects primary compositional layering, alternating between aluminous (muscovite + biotite) and quartzofeldspathic (quartz + plagioclase + biotite) micro-domains on the millimetre-scale (figure 2.5a). In contrast, samples that do not contain sub-solidus muscovite (e.g. BD1430) comprise quartz, plagioclase, and biotite that are equally distributed in a quartzofeldspathic domain (figure 2.5b). Aluminous domains comprise muscovite, biotite, garnet, and minor amounts of quartz, and contain most of the mineral-bound water in the rock (figure 2.5c). Quartzofeldspathic domains contain quartz, plagioclase, and interstitial biotite, with an average grain-size of 75–150 μm (figure 2.5b). Semipelitic compositions (e.g. BD1206, BD1419, E184) exhibit weak primary compositional layering, with discontinuous and foliation parallel aluminous micro-domains separated by quartzofeldspathic matrix. The spacing of aluminous micro-domains in pelitic samples is on the order of 2–3 millimetres (figure 2.5c). The alignment of fine-grained rectangular biotite defines the foliation. Biotite

Zener pinning structures, where quartz and plagioclase grain growth is restricted by the distribution of biotite (Evans *et al.*, 2001), are ubiquitous within the quartzofeldspathic matrix. Stubby rectangular plagioclase grains are aligned with the biotite foliation and evenly distributed throughout the granoblastic matrix, commonly forming plagioclase-plagioclase grain boundaries. Apart from the 3–5 mm long intergrowths of muscovite and biotite, and small (2–3 mm diameter) garnet grains, there are no other porphyroblastic phases in the protolith compositions studied that could affect the kinetics of vapour-absent muscovite dehydration melting.

The primary compositional layering of the muscovite-bearing protoliths plays an important role in the micro-textural evolution of vapour-absent muscovite dehydration melting by imparting chemical anisotropy on the pelitic and semipelitic rocks. Variations in protolith muscovite content govern the melt % generated in rocks that have experienced muscovite dehydration melting. In order to see the textures at the different stages of melting (melt % generated), it is necessary to use samples with a range in compositions. In the following sections, the melt % generated by vapour-absent muscovite dehydration melting in any given sample is inferred by the amount of K-feldspar present. This inferred value of melt % is itself taken as a proxy for the amount of protolith muscovite.

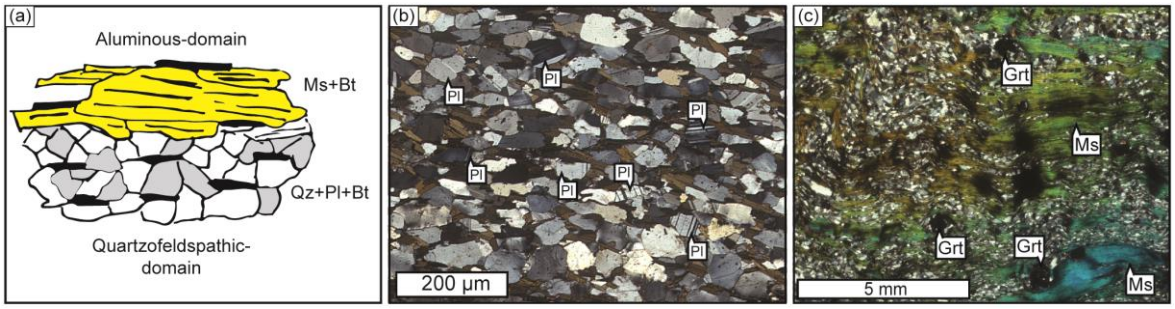


Figure 2.5 Protolith textures. (a) Schematic sketch of the aluminous and quartzofeldspathic protolith domains in compositionally graded pelites. (b) Photograph of sample BD1430 viewed under crossed polars. Fine-grained arkosic quartzofeldspathic matrix with fabric-aligned biotite. Note the stubby form and distribution of plagioclase grains. (c) Thin section scan of sample BD1233 viewed under crossed polars, showing the distribution of muscovite + biotite + garnet aluminous domains in a high-Al pelite.

2.5.2 K-feldspar microstructures

1) First appearance of K-feldspar

Sample E184 has minor modal abundances of K-feldspar and sillimanite, and an estimated melt % generated of 2–3 %. The majority of the sample is made up of quartzofeldspathic domains with granoblastic plagioclase, quartz, and biotite. The smallest (10–50 μm) K-feldspar grains occur at plagioclase-plagioclase and plagioclase-quartz grain boundaries in the quartzofeldspathic domain (figure 2.6a, b). K-feldspar-plagioclase grain boundaries are typically irregular and appear ragged, in contrast to the well-defined and straight grain boundaries between K-feldspar-quartz and amongst quartz, plagioclase, and biotite (figure 2.6a, b). Automated EBSD maps of K-feldspar grains within a quartz + plagioclase + biotite matrix are shown in figure 2.7. The highlighted areas shown in the back-scattered electron images on the left side of figure 2.7 correspond to binned sub-grain analyses presented in the corresponding pole figure. The pole figure for all analysed plagioclase grains (figure 2.7a) shows that the plagioclase grains in the quartzofeldspathic domain are randomly oriented. The subset of plagioclase grains that share irregular and ragged grain boundaries with K-feldspar (e.g. figure 2.6b) are presented in figure 2.7b, which shows one cluster of similarly orientated analyses with a small angular spread (<10 °) amongst a background of randomly orientated analyses. Within the area analysed, K-feldspar appears poikiloblastic. K-feldspar shares both well-defined and irregular grain boundaries with plagioclase, and well-defined grain boundaries with quartz and biotite. The pole figure with all K-feldspar analyses of the (001) plane shown in figure 2.7c, reveals two clusters of orientations. The dominant cluster has a small angular spread and forms one continuous population of analyses. Likewise, the orientations of the smaller cluster of analyses form one continuous population. The orientation of the dominant cluster of plagioclase grains, which have irregular K-feldspar-plagioclase grain boundaries, overlaps with the dominant

orientation of K-feldspar analyses, indicating that the crystallographic axes of these grains are aligned.

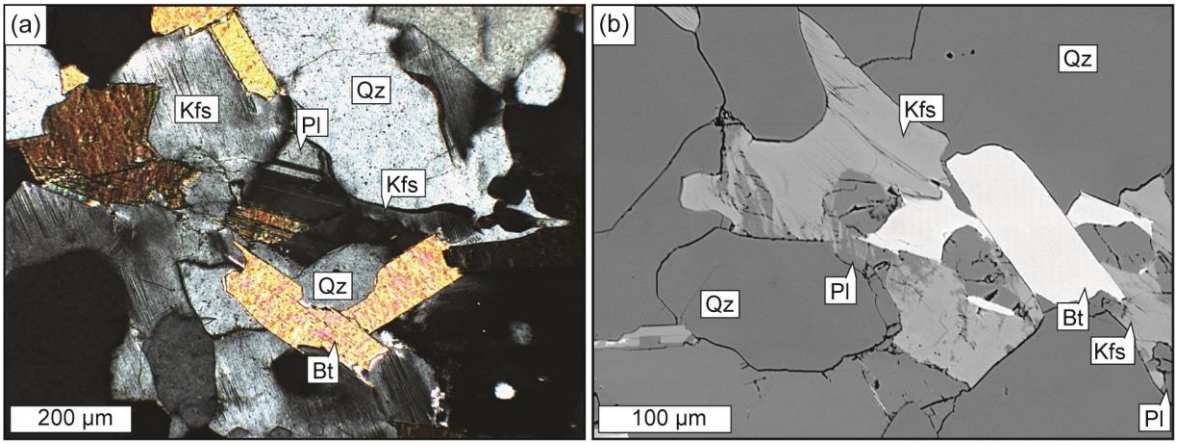


Figure 2.6 K-feldspar nucleation textures (sample E184). (a) Photomicrograph under crossed polars. K-feldspar nucleation on plagioclase grains in the biotite bearing quartzofeldspathic domain. Note the irregular K-feldspar-plagioclase grain boundary. (b) Back-scattered electron image of K-feldspar-plagioclase reaction textures. Note that the growth of K-feldspar is constrained to the original plagioclase grain shape.

2) K-feldspar poikiloblasts

Samples E184, BD1206 and BD1419 are estimated to have generated a low melt % (≤ 6 %) and preserve a record of the initial growth of K-feldspar within the quartzofeldspathic domains. K-feldspar in sample E184 forms anhedral, skeletal poikiloblasts that are ~1–3 mm in diameter (figure 2.8a-d). The poikilitic texture is a result of abundant quartz and biotite inclusions, which are similar in size (250–500 µm) to surrounding matrix grains and preserve the matrix fabric. Poikiloblasts of K-feldspar comprise regularly distributed lobes that are 200–350 µm wide, which are interconnected by thin (100–200 µm) limbs formed along grain boundaries of quartz and biotite. The stubby and rectangular shape, orientation, and distribution of the K-feldspar lobes mirror that of plagioclase in the unreacted quartzofeldspathic matrix and in equivalent protolith compositions. In samples that contain ~5–6 melt %, the distribution of K-feldspar poikiloblasts within certain quartzofeldspathic domain is dense enough for poikiloblasts to share grain boundaries with each other (e.g. figure 2.8d).

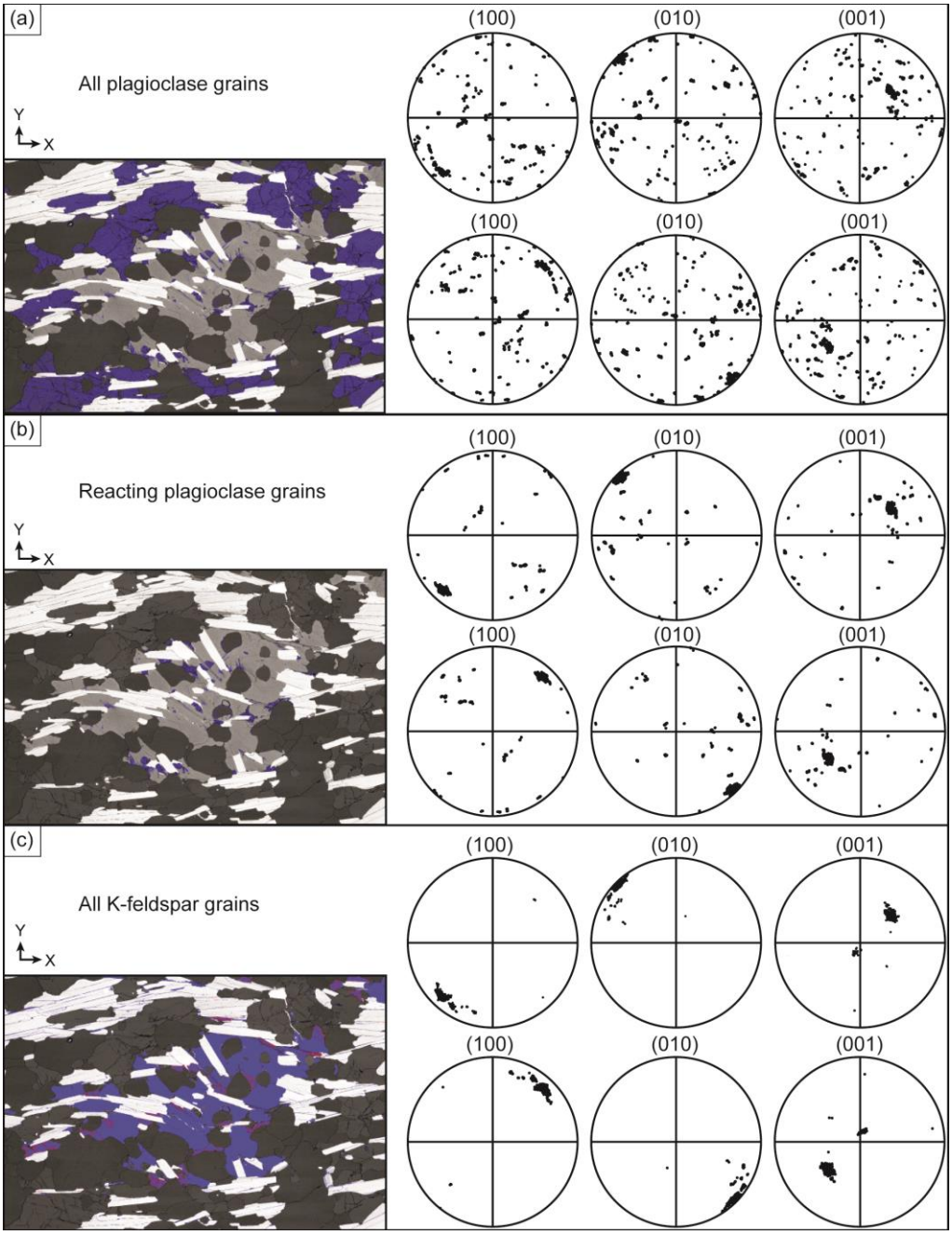


Figure 2.7 Back scattered image and feldspar pole figures, showing the orientation of plagioclase and K-feldspar in the quartzofeldspathic matrix of sample E184. Pole figures are upper and lower hemisphere equal-area stereonets; see orientation key above back scattered image. The coloured grains in the 3 x 2 mm field of view denote the grain subsets plotted in the corresponding pole figures. (a) All plagioclase analyses, showing a random distribution of plagioclase orientations in the quartzofeldspathic domain. (b) Subset of partially replaced plagioclase grains, which share an irregular K-feldspar-plagioclase grain boundary, showing one cluster of similarly orientated analyses amongst a background of randomly orientated analyses. (c) All analyses of K-feldspar poikiloblasts, showing two orientation clusters. Note the dominant cluster of K-feldspar analyses overlaps with the orientation of the main cluster of partially replaced plagioclase grains, indicating that the crystallographic axes of these grains are aligned.

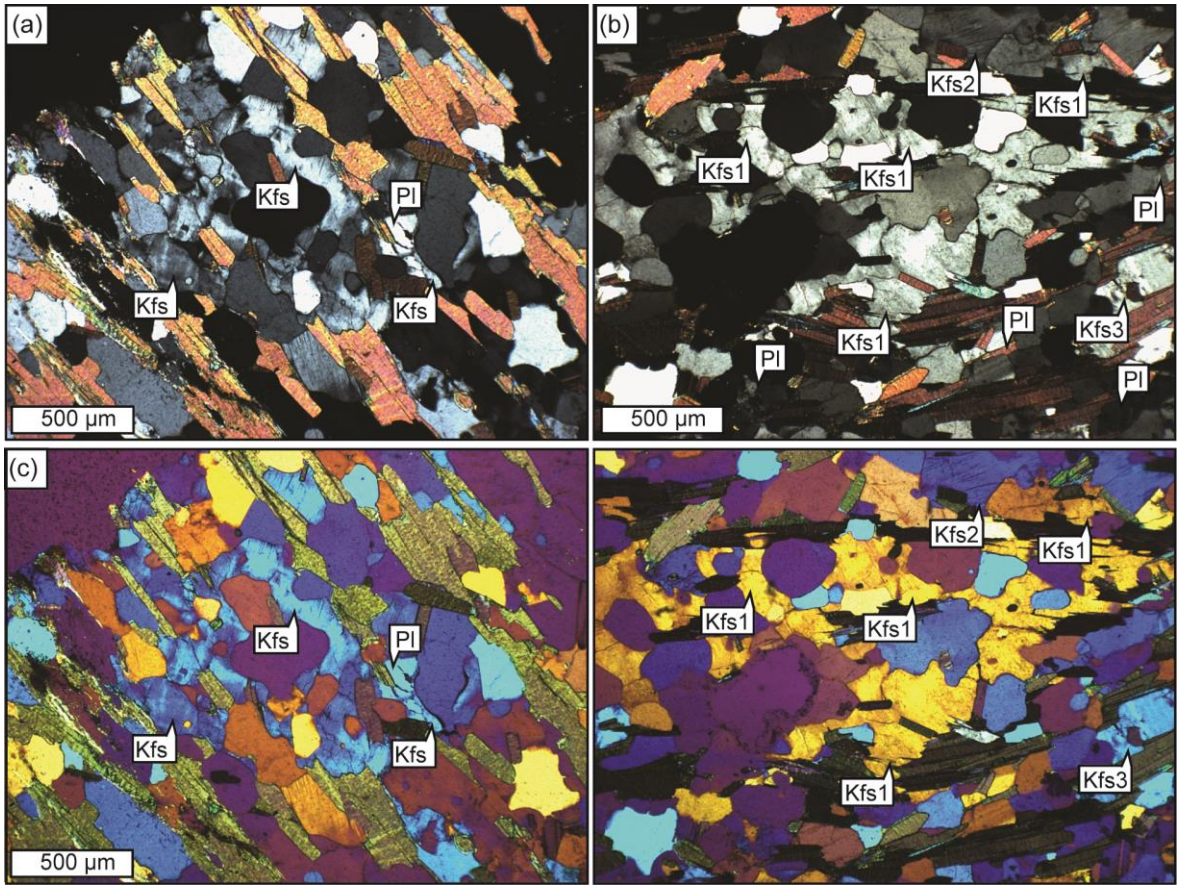


Figure 2.8 K-feldspar poikiloblasts (sample E184). (a) Photomicrograph taken under crossed polars. Anhedral K-feldspar poikiloblasts replacing multiple plagioclase grains in quartzofeldspathic micro-domain. Note the sub-rounded inclusions of quartz and fabric-aligned biotite, and the rectangular nodes of K-feldspar. (b) Photomicrograph viewed under crossed polars. Anhedral K-feldspar poikiloblasts replacing plagioclase in the quartzofeldspathic domain. The density of poikiloblasts is such that they share grain boundaries with other K-feldspar grains (Kfs1, Kfs2, Kfs3). (c,d) Photomicrograph taken under crossed polars with the sensitive tint plate, showing crystallographic continuity of K-feldspar poikiloblasts in contrast with the multiple individual plagioclase and quartz grains.

3) K-feldspar porphyroblasts

There is a marked increase in grain-size and notable change in K-feldspar microstructure within samples that have experienced more than ~ 8 melt %, in comparison with the fine-grained matrix and K-feldspar poikiloblasts that are found in low melt % samples. However, amongst samples that have generated ~ 8 melt % or more, there are no discernible differences in either the microstructure of K-feldspar or the texture of quartzofeldspathic domains, apart from a marked increase in modal proportion of K-feldspar. Samples of pelitic augen gneiss with high-Al pelitic compositions (E203, E204, BD1222, BD1434) were used to document the effect of moderate to high melt % generated. In these samples, K-feldspar commonly forms porphyroblasts that are 2–20 mm in diameter (figure 2.9). Where K-feldspar and quartz share grain boundaries with biotite grains, they form 180° dihedral angles along biotite's [001] crystal face and produce a grain boundary texture that implies overgrowth of Zener pinning structures (e.g. figure 2.9a). The shape of individual porphyroblasts may vary, and it is common to find anhedral appendaged grains with multiple adjoined segments (e.g. central K-feldspar grain seen at extinction; Fig. 2.9b), rounded porphyroblasts (figure 2.9c), and elongate sub-tabular grains (figure 2.9g) all within one sample. The outer grain boundaries of K-feldspar porphyroblasts are irregular, forming cuspate and embayed boundaries with quartz and biotite (e.g. figure 2.9g). The majority of porphyroblasts observed are untwinned; however, Carlsbad twinning has been observed in sample E204 (figure 2.9g). Porphyroblasts typically contain inclusions of fine-grained biotite with a matrix aligned fabric and quartz inclusions, which increase in grain-size from the porphyroblast core to rim (figure 2.9c-f). Biotite grains that are not enshrined by quartz and K-feldspar form millimetre-scale intergrowths that define the matrix foliation (figure 2.9c, g). Within these samples, there is

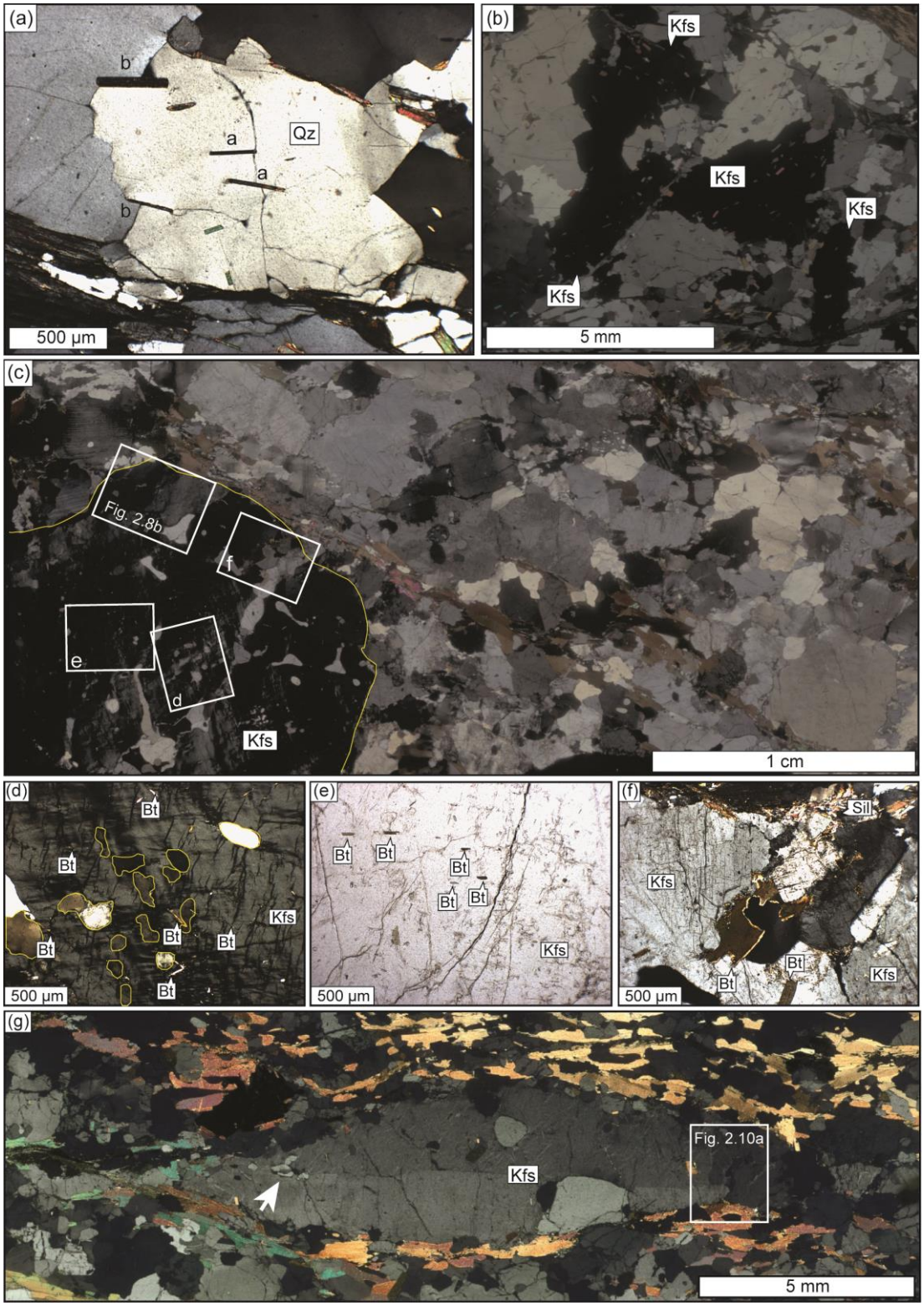


Figure 2.9 Photomicrographs showing K-feldspar porphyroblasts in the quartzofeldspathic domains of medium-grained pelitic augen gneiss (25–30 melt % generated). All photographs except image (e) were taken under crossed polars. Sample E203: (a) Coarsened quartz microstructure, showing fine-grained inclusions of fabric-aligned biotite (example marked 'a') and biotite pinning microstructures (example marked 'b'). (b) The centre grain in extinction is an anhedral 'appendaged' K-feldspar porphyroblast. Note the fabric-aligned fine-grained biotite inclusions. (c) K-feldspar porphyroblast surrounded by a matrix of quartz + plagioclase + K-feldspar + biotite + sillimanite. The size, orientation and distribution of quartz and biotite inclusions vary

from core to rim. (d) Fine-grained inclusions of quartz (200–350 μm) and aligned biotite (100–200 μm) creating a poikilitic texture in the core of the K-feldspar porphyroblast. (e) Fine-grained (100–200 μm) paleo-fabric aligned biotite inclusions surrounding the porphyroblast core. (f) Rim of porphyroblast containing coarsened inclusions of biotite and quartz (500–1000 μm). Sample E204: (g) K-feldspar porphyroblast exhibiting Carlsbad twinning. The arrow points to a poikilitic domain with quartz and biotite inclusions.

a bimodal grain-size distribution of biotite and quartz, as inclusions in K-feldspar (250–500 μm), and as matrix quartz and biotite (1–5 mm). The grain-size of K-feldspar, quartz, and plagioclase in the coarsened quartzofeldspathic matrix that surrounds the K-feldspar porphyroblasts ranges from 2–10 mm (Fig. 9c, g). On the macroscale, these coarsened matrix domains may be termed leucosome since the quartzofeldspathic assemblage and coarse grain-size gives them a lighter colour. In sample E203, which is representative of samples that have generated > 8 melt%, the average composition of the leucosome is: ~70 % quartz, ~15 % K-feldpsar, and ~15 % plagioclase.

4) Appendages and interstitial films

A fourth type of K-feldspar microstructure, found in samples that have experienced vapour-absent muscovite dehydration melting, forms thin (< 200 μm wide) interstitial films and medium-grained appendages (1–4 mm wide) on existing quartzofeldspathic grains. Figure 2.10a, b shows two examples of anhedral grains of K-feldspar that are 1–4 mm in diameter occurring as appendages to large K-feldspar porphyroblasts, located along the porphyroblast grain boundaries. The appended grains are not in crystallographic continuity with the porphyroblasts, and are typically un-twinned, which is a feature that has been used elsewhere to differentiate K-feldspar of igneous rather than metasomatic origin (e.g. Vernon, 1986, Vernon, 1990). In both examples, the porphyroblasts and appended K-feldspar grains are separated by a thin (10–50 μm) sodic-plagioclase film (figure 2.10a, b). Elsewhere within the quartzofeldspathic domain, thin monomineralic films (i.e. plagioclase, quartz, or K-feldspar) commonly form irregular shaped and highly cuspate

grain boundaries (figure 2.10c-f). Figure 2.10c shows small (100–200 μm) beads of quartz, and thin (10–50 μm) films of quartz along a K-feldspar-biotite and plagioclase-biotite grain boundary. Figure 2.10d shows a K-feldspar-plagioclase grain boundary that is decorated by 100 μm beads of quartz and a thin (50–150 μm) plagioclase film, which forms a 'string of pearl' texture. Along decorated and irregular grain boundaries that lack intergranular films, it is common to find highly cuspate features and beads that are in crystallographic continuity with neighbouring megacrysts or porphyroblasts (figure 2.10e). Grain boundaries that are decorated by films or irregular shaped overgrowths generally form low dihedral angles (< 25°) giving the appearance of sharp terminations at triple junctions. Figure 2.10f is an example where an aggregate of medium-sized (500–1500 μm) quartz grains separate three large plagioclase grains. However, quartz still forms sharp terminations at quartz-plagioclase-plagioclase grain boundaries. These features are most commonly observed in samples which have generated moderate to high melt %. Nonetheless, rare examples are found within the quartzofeldspathic matrix of low melt % samples, particularly in the regions that surround aluminous domains.

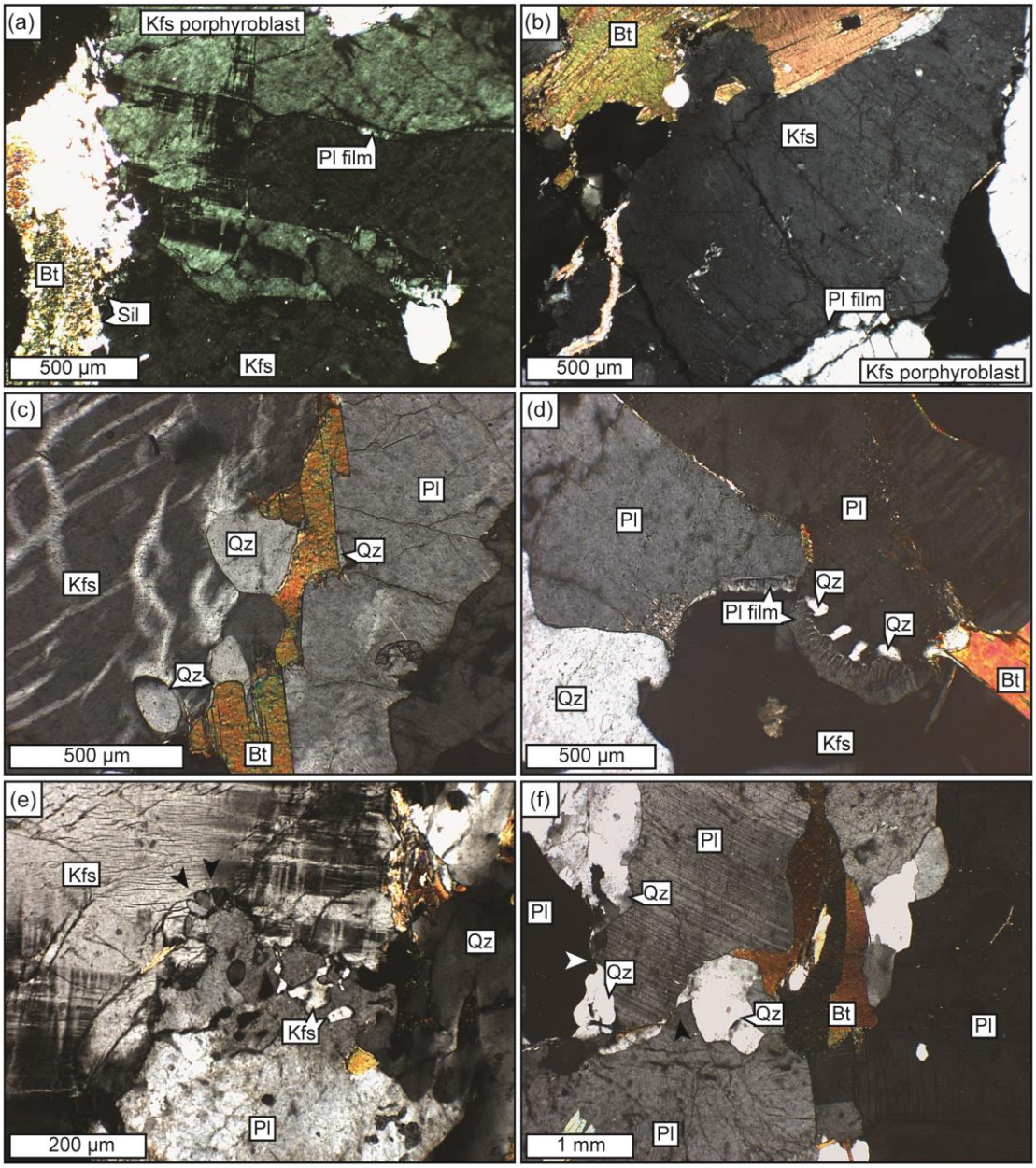


Figure 2.10 Photomicrographs of sample E203 and E204 taken under crossed polars, showing a range of grain boundary microstructures found in the quartzofeldspathic domains of pelitic augen gneiss samples (25–30 melt % generated). (a) K-feldspar grain formed at the lateral tip of a twinned K-feldspar porphyroblast (figure 2.9g). A thin (10–50 µm) film of plagioclase marks the contact between the K-feldspar grains. The smaller appended grain is untwinned and inclusion-free. (b) K-feldspar grain formed along the perimeter of the K-feldspar porphyroblast presented in Figure 2.9c. A thin (10–50 µm) film of plagioclase lines the contact between the two K-feldspar grains. Note the medium grain-size of the matrix biotite, in contrast to the fine-grained inclusions trapped in the peritectic K-feldspar grains presented in figure 2.9d,e. (c) Matrix K-feldspar grain with small (100–200 µm) quartz inclusions. A thin (10–50 µm) film of quartz with sharp grain boundary terminations separates K-feldspar from biotite and plagioclase from biotite. (d) K-feldspar-plagioclase grain boundary decorated by 100 µm beads of quartz and a thin (50–150 µm) plagioclase film. (e) Irregular K-feldspar-plagioclase grain boundary showing inclusions of rounded k-feldspar appendages within plagioclase, and highly cuspate grain boundary features (denoted by arrows). (f) Aggregate of medium-sized (500–1500 µm) quartz grains formed along plagioclase grain boundaries. Note the sharp terminations of quartz at plagioclase-plagioclase grain boundaries (denoted by arrows).

Interpretation of K-feldspar microstructures

1) Nucleation preference

Observations of small K-feldspar grains along plagioclase-plagioclase and plagioclase-quartz grain boundaries are interpreted to show a nucleation preference for K-feldspar on the interface of plagioclase grains. Plagioclase does not exhibit a crystallographic preferred orientation, as is demonstrated by the random distribution of EBSD analyses in figure 2.7a. The two distinct populations of K-feldspar analyses presented in figure 2.7c suggest the scanned area contains two poikiloblasts, one larger grain in the centre of the scanned area, and a second smaller grain in the upper right hand corner. The overlapping orientation of the centre poikiloblasts and the dominant cluster of ragged plagioclase grains are interpreted to show a topotactic replacement of plagioclase by K-feldspar. This topotactic relationship suggests that the initial nucleation of K-feldspar is epitaxial to the isomorphic plagioclase.

2) Selective replacement of plagioclase

The growth of K-feldspar by replacing matrix plagioclase is indicated by: the containment of K-feldspar poikiloblasts to the quartzofeldspathic domain, the absence of plagioclase within the K-feldspar inclusion assemblage, the topotactic K-feldspar-plagioclase relationship exhibited by select grains (e.g. figure 2.6b), and the observations of patchy and irregular K-feldspar-plagioclase grain boundaries. A close similarity in size, shape, and distribution of the K-feldspar poikiloblasts nodes and the initial granoblastic plagioclase grains suggests that K-feldspar growth is a non-displacive interface-controlled process. There is no crystallographic preferred orientation amongst K-feldspar poikiloblasts. However, the orientation data presented in figure 2.7 are interpreted to suggest that once

K-feldspar has nucleated epitaxially on plagioclase, the advancing K-feldspar interface may preferentially replace plagioclase grains with similarly aligned crystal axes.

3) Grain-size coarsening

The significant increase in the size of K-feldspar grains, from the ~1–3 mm poikiloblasts characteristic of samples that are inferred to have generated less than ~8 % melt, to the 2–20 mm porphyroblasts in samples that are estimated to have generated at least 8 % melt implies that melt % and mass transfer have a non-linear relationship. The textural transition that occurs when the rock generates ~8 % melt is interpreted to represent a percolation threshold, where melt is connected throughout the rock along grain boundaries. Above this threshold, there is greater mobility of grain boundaries and mass transfer, represented by the increase of grain-size by up to two orders of magnitude. The observation that there are considerably fewer individual K-feldspar porphyroblasts in samples that have generated more than ~8 melt % in contrast to the number of poikiloblasts in samples with a low melt % indicates poikiloblasts merged during coarsening. Quartz and biotite embayments along the margin of K-feldspar porphyroblasts, and inclusions of quartz and biotite within the porphyroblasts suggest the coarsening process is interface controlled and conserves volume on the domain-scale. The apparent increase in mass transfer and the interpretation that the mobility of grain boundaries is greater in samples that have generated more than ~8 melt % is seen to affect: K-feldspar, quartz, biotite, sillimanite ± plagioclase (i.e. the solid phases that comprise > 10% of the rock after vapour-absent muscovite dehydration melting).

4) Melt crystallisation

Above the percolation threshold melt may migrate throughout the rock. However, as the rock cools, grain growth reduces permeability and melt can become trapped in pores and

interstitial space. At the slow cooling rates of regional metamorphism, all residual melt will crystallise to form: quartz, K-feldspar, and plagioclase together with lesser amounts of biotite and other accessory phases (Holness & Sawyer, 2008). Since there is no kinetic barrier to nucleation when a component of melt can crystallise on an existing grain interface (i.e. SiO_2 from a melt crystallising on existing quartz grains), the melt composition in isolated pores can fractionate to form interstitial grains and films that are monomineralic (Holness & Sawyer, 2008). The geometry of these interstitial growths, termed 'melt pseudomorph structures', are discussed at length in Holness and Sawyer (2008), but can be summarised as interstitial grains with: 1) irregular or cuspate boundaries, 2) low dihedral angles (10–35°; Holness, 2006), 3) fine- or coarse- grained granophyric intergrowths, 4) 'string of pearl' texture. Holness and Sawyer (2008) noted a critical pore width of ~250 μm, above which intergrowths and grain aggregates form; the observations presented in this study (figure 2.10) support their conclusion. The peritectic K-feldspar porphyroblasts record a final stage of K-feldspar growth as the melt crystallises, and a component of the melt crystallises on existing K-feldspar porphyroblasts. The small grains of K-feldspar that form appendages to larger porphyroblasts in samples E203 and E204 are interpreted to have formed by melt crystallisation rather than continued peritectic K-feldspar growth, because they are separated by thin films that are interpreted as melt pseudomorphs. Crystallisation of K-feldspar from residual melt directly onto K-feldspar porphyroblasts does not significantly contribute to the size of coarsened K-feldspar grains (e.g. figure 2.9c, g), although this final stage of growth must be accounted for in cases where distinguishing initial peritectic and late-stage growth is important.

2.5.4 Sillimanite microstructures

1) Growth in aluminous domains

In fine-grained semipelitic samples with poorly developed compositional layering, and low melt % (≤ 6 %), fibrolitic sillimanite commonly forms foliation parallel mats, and intergrowths with quartz in the aluminous domains. The sillimanite-bearing aluminous domains and the K-feldspar-bearing quartzofeldspathic domains are clearly defined in sample E184 (figure 2.11a, b). Figure 2.11c shows an aluminous domain that contains fibrolitic sillimanite, aligned with the [001] plane of biotite, as well as foliation parallel grains of sillimanite forming intergrowths with quartz. Relict muscovite is rarely observed; however, the few grains that have been found are closely association with quartz + sillimanite intergrowths within aluminous domains (figure 2.11d).

2) Lenticular sillimanite and quartz intergrowths

In outcrop and thin section, semipelite and pelite with low melt % (≤ 6 %), which have undergone vapour-absent muscovite dehydration melting, exhibit a common texture characterised by lenticular intergrowths of sillimanite and quartz formed in aluminous domains. The sillimanite and quartz intergrowths have an aspect ratio of approximately 5:1 and generally define a mineral lineation fabric (figure 2.11e). With increasing melt % generated, the size and distribution density of the intergrowths increases. In the sillimanite-K-feldspar-grade semipelitic sample E184, the internal texture of the aluminous domains comprise: sillimanite + quartz intergrowths, anastomosing mats of fibrolitic sillimanite, biotite + sillimanite intergrowths, and rare relict muscovite (figure 2.11d, g). The grain-size of quartz is similar in both the aluminous and quartzofeldspathic domains, ranging from 200–500 μm (e.g. figure 2.11a, b). At the lateral tips of the intergrowths, fibrolitic

sillimanite grains occur along quartz-quartz and quartz-biotite grain boundaries and along some [001] biotite planes (figure 2.11f).

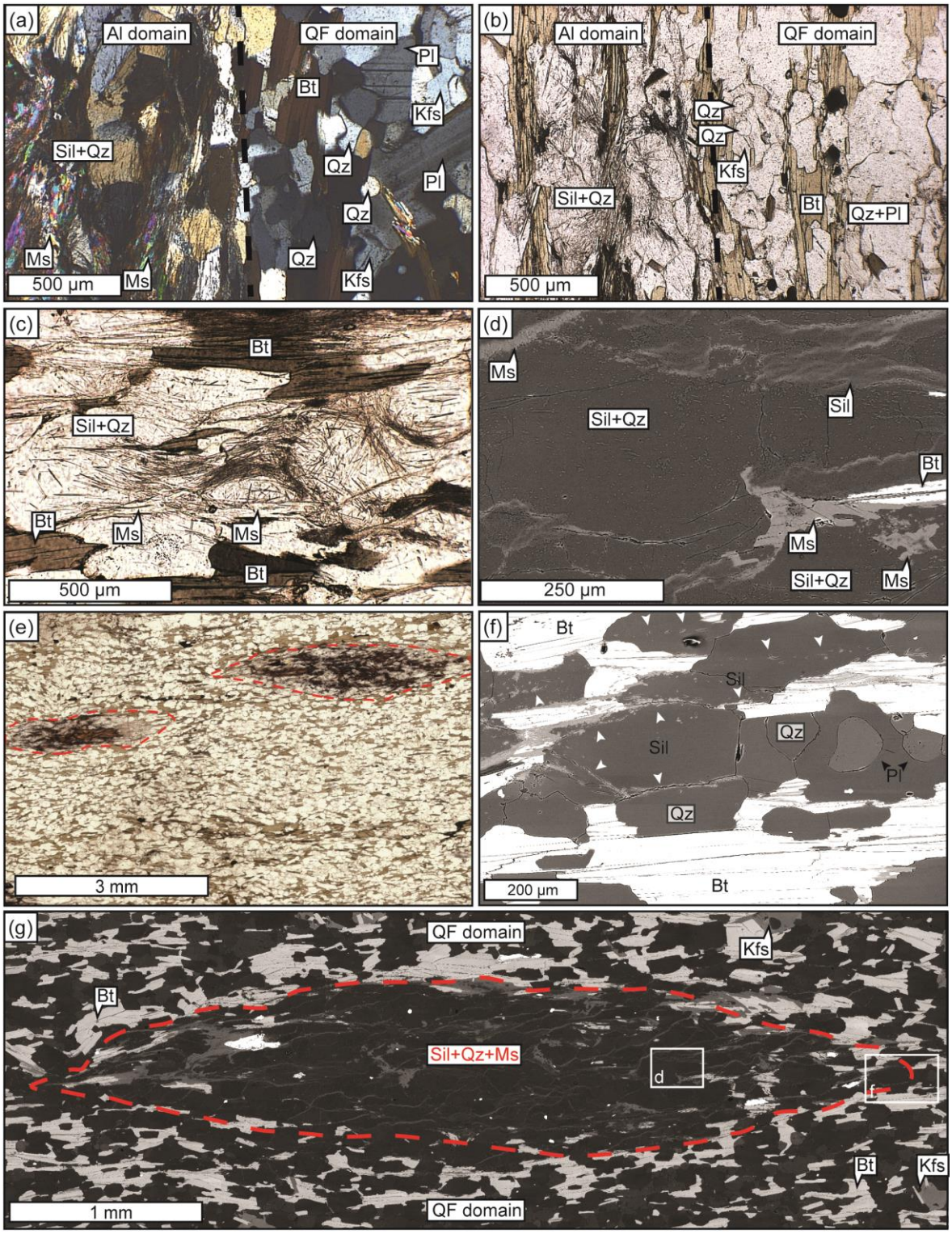


Figure 2.11 Sillimanite microstructures and the textures of aluminous domains in a sample that has generated ≤ 6 % melt (E184). (a) Photomicrograph viewed under crossed polars, showing the boundary between the aluminous and quartzofeldspathic domain (dashed line). In the aluminous domain, sillimanite forms

intergrowths with quartz and biotite. The quartzofeldspathic domain comprises: quartz – plagioclase – K-feldspar – biotite. (b) The contact between the domains is marked by the extent of the intergrowths of sillimanite and quartz. (c) Photomicrograph showing the alignment of sillimanite grains in sillimanite + quartz intergrowths, and along the [001] plane of biotite and relict muscovite. (d) Backscattered electron image of sillimanite + quartz intergrowths that surround a relict muscovite grain. (e) Thin-section scan, showing the distribution of lenticular sillimanite and quartz intergrowths (marked by dashed line). (f) Backscattered electron image, showing the lateral tip of a sillimanite + quartz intergrowth and the quartzofeldspathic matrix. Grains of fibrolitic sillimanite (marked by arrows) decorate the grain boundaries of matrix quartz and biotite, and form linear inclusion arrays in quartz. (g) Backscattered electron image of a lenticular sillimanite and quartz intergrowth surrounded by the quartzofeldspathic domain.

Under CL, the quartz formed within the aluminous domain exhibits a different texture to the quartz and plagioclase grains that comprise the quartzofeldspathic domain. In the fine-grained quartzofeldspathic matrix of sample E184, quartz and plagioclase exhibit a characteristic ‘bulls-eye’ CL texture, with dark cores and light rims (figure 2.12a). The ‘bulls-eye’ zoning is best defined in micro-domains that contain equigranular quartz and plagioclase that are 200–350 μm in diameter (figure 2.12b). Quartz grains that form intergrowths with sillimanite in the aluminous domains exhibit homogeneous luminescence, with a similar intensity to the rims of the ‘bulls-eye’ zoned matrix grains (figure 2.12c-f). Figure 2.12c focuses on the lateral tip of a sillimanite + quartz intergrowth, where intergrowths of CL homogeneous quartz and sillimanite are found along grain boundaries of zoned matrix quartz. Matrix quartz grains that share a grain boundary with the intergrowths of homogenous quartz and sillimanite are coarser (350–500 μm) than the nearby ‘bulls-eye’ zoned grains (200–350 μm). The occurrence of sillimanite inclusions correspond with the boundaries of quartz zoning, and are exclusively hosted in domains of CL bright quartz (figure 2.12d-f). The mottled texture shown in figure 2.12f is characteristic of quartz grains that border the aluminous domains.

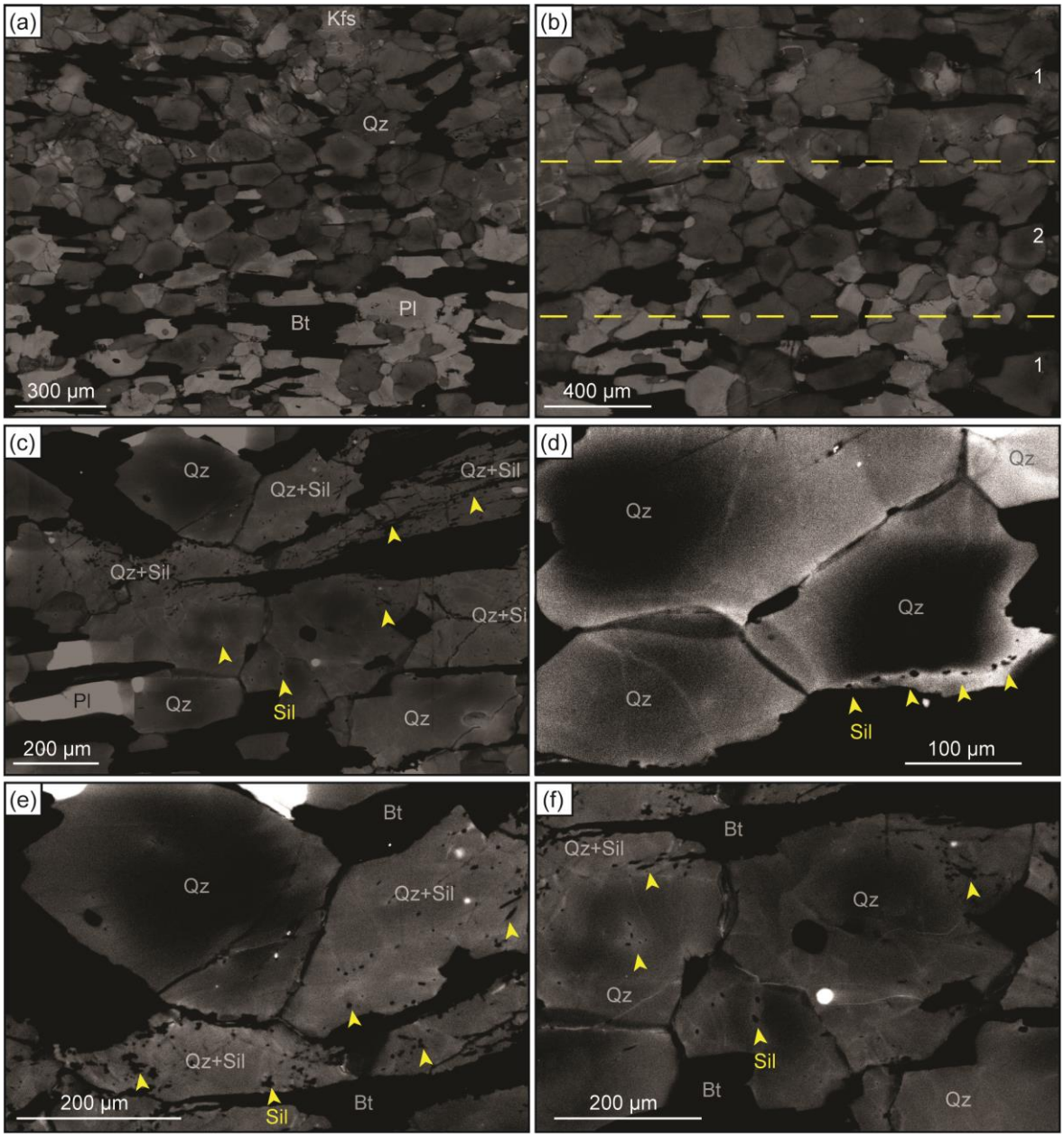


Figure 2.12 Cathodoluminesence images of quartzofeldspathic and aluminous micro-domains in sample E184, which has experienced a low degree of melting (2–3 melt %). Note biotite and sillimanite do not luminesce. (a) Solid-state textures of a quartzofeldspathic domain, showing core to rim 'bulls-eye' zoning in quartz and plagioclase. (b) Solid-state textures of a quartzofeldspathic domain, demonstrating the effect of biotite Zener pinning. The dashed line denotes the subdomain boundaries between: 1) sparsely-distributed medium-grained biotite and un-zoned quartz, and 2) closely-distributed fine-grained biotite with fine-grained zoned quartz. Quartz has coarsened to the confines of biotite. In subdomains 1, the quartz grains have increased by 2–3x compared with grains in domain 2, resulting in textural overprinting of the darker core domains. (c) Left margin of a lenticular sillimanite + quartz intergrowth, showing the relationship between the bulls-eye zoned solid-state quartz textures and the intergrowth between sillimanite and brighter, un-zoned quartz. Arrows indicate the location of sillimanite inclusions, which are always contained within micro-domains of CL brighter quartz. (d) Contact between the quartzofeldspathic matrix and an intergrowths of sillimanite and quartz (bottom right). A linear array of sillimanite inclusions demarcates the solid-state quartz grain-boundary, which has been overgrown by CL brighter quartz. (e) Contact between a bulls-eye zoned and inclusion-free matrix quartz, and Cl brighter quartz with sillimanite inclusions. (f) Modification of bulls-eye zoned matrix grains by micro-fractures and grain boundaries filled with CL brighter quartz + sillimanite. The

textural modification of matrix grains is most pronounced in grains nearest to the sillimanite + quartz bearing aluminous micro-domain.

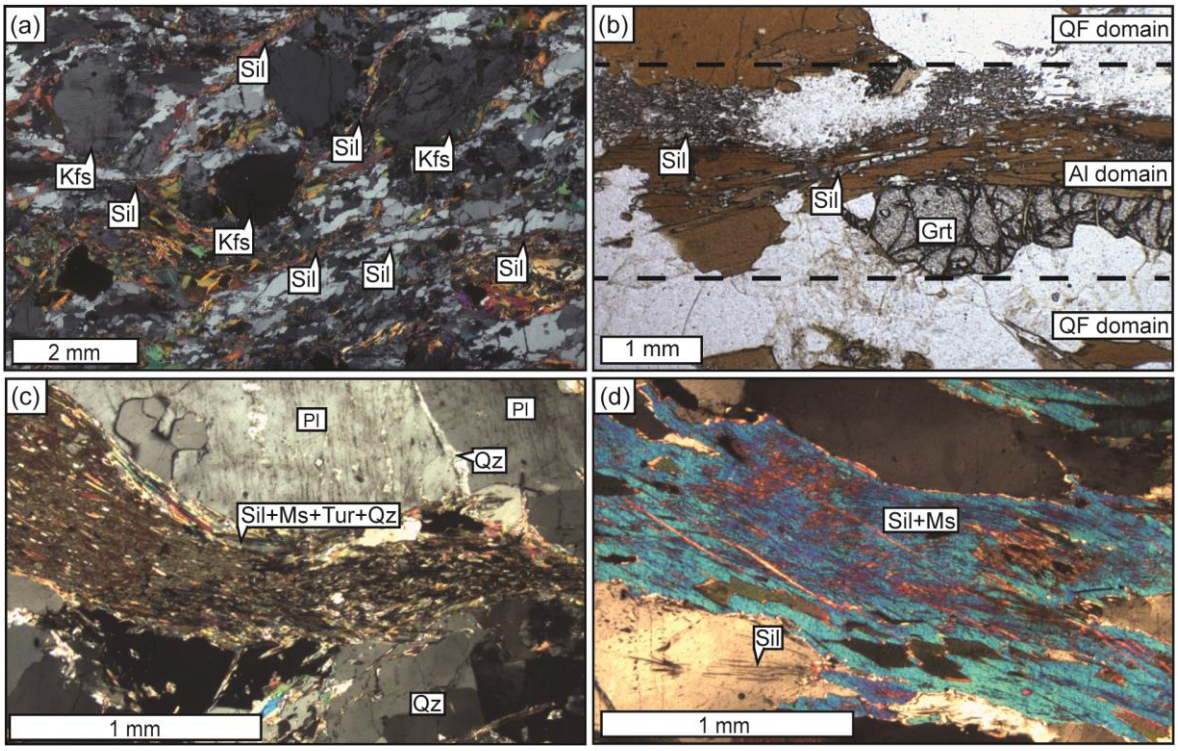


Figure 2.13 Sillimanite microstructures in rocks that have generated >8 melt %. (a) Photomicrograph of sample BD1411 taken under crossed polars, showing a network of thin (200–500 μm) schlieren of sillimanite that wrap around K-feldspar porphyroblasts and quartzofeldspathic microlithons. (b) Photomicrograph of sample BD1222 showing an aluminous domain with garnet, biotite, quartz and, sillimanite (fibrolitic and prismatic). (c) Photomicrograph of sample BD1209 taken under crossed polars, showing an intergrowth of sillimanite, muscovite, tourmaline and, quartz. Note the thin (200 μm) film of quartz along the grain boundary of plagioclase (top right), which is interpreted as a melt pseudomorph. (d) Photomicrograph of sample BD1222 viewed under crossed polars. Millimetre-sized sheets of secondary muscovite overgrowing fibrolitic sillimanite. Note that the sillimanite is preserved when isolated as inclusions in quartz.

3) Coarsening, grain growth, and recrystallisation

In samples that have generated more than ~8 melt %, sillimanite forms: schlierens, prismatic grains, and intergrowths with tourmaline, quartz, and secondary (retrograde) muscovite. Pelitic augen gneiss samples (e.g. BD1222 and BD1411) contain foliation defining sillimanite schlieren, which are intergrown with fine-grained quartz (figure 2.13a). The sillimanite schlieren exhibit both a mineral alignment lineation and a foliation, with a very high aspect ratio of >20:1 in thin-section. The growth of prismatic sillimanite

grains is restricted to the fibrolite-rich aluminous domains. Figure 2.13b shows a prismatic grain of sillimanite that is intergrown with biotite, and surrounded by garnet and fibrolitic sillimanite. Intergrowths of sillimanite with the volatile-rich phases: tourmaline, muscovite, and apatite are commonly observed in the matrix of coarse-grained samples (e.g. figure 2.13c,d). Large plates (1–4 mm) of secondary (retrograde) muscovite overgrow patches and schlieren of fibrolitic sillimanite in some samples (figure 2.13d). However, the replacement of sillimanite with secondary muscovite is often incomplete and typically occurs in close proximity to penetrative folia of biotite and sillimanite where fluids may migrate.

2.5.5 Interpretation of sillimanite and melt growth

1) Nucleation of sillimanite on mica template

The growth of fibrolitic sillimanite in low melt % samples is restricted to the plagioclase- and K-feldspar- absent aluminous domain. In the absence of primary muscovite (except for the rare relict grain), the sillimanite + quartz intergrowths are interpreted to replace former muscovite sites. Considering the relative immobility of Al, the intimate association of sillimanite and quartz would be expected with an interface-controlled reaction that locally conserved volume (Carmichael, 1969). The tendency for sillimanite to form intergrowths with biotite, along the [001] plane, suggests nucleation on the mica template is preferred. This nucleation preference may also extend to the dehydrating muscovite, although for the reasons outlined above and because sillimanite is the product and muscovite the reactant, microstructural evidence of this association is unlikely to be preserved. Based on the observation of fibrolite in all samples, the initial growth of sillimanite is interpreted to be fibrolitic. However, subsequent coarsening of grains and growth of prismatic sillimanite may occur in rocks that have generated a melt % exceeding the percolation threshold.

2) Initial melt localisation and migration

An inherent difficulty in studying melting reactions in natural samples is determining where the melt phase first forms and distinguishing modified solid-state grains from those that crystallised from the melt. The modal abundance of peritectic minerals can provide a constraint on the amount of melt generated in a given rock, on the condition that the peritectic grains are not liable to melt entrainment or retrogression. Films of quartz and plagioclase along quartzofeldspathic grain boundaries, irregular shaped appendages with low quartz and feldspar dihedral angles, and granophyric intergrowths all record the former presence of melt (Holness & Sawyer, 2008). However, many of the diagnostic melt micro-textures form during the final stages of crystallisation and so do not directly inform the discussion on where melt nucleation and growth occurs within a crystallised rock.

Since experimental studies of vapour-absent muscovite dehydration melting are quenched before melt can crystallise, they provide an opportunity to study the site of initial melt growth in analogue conditions. Brearley and Rubie (1990) ran muscovite melting experiments on quartz-muscovite schist in vapour-absent and -present conditions, and found in both cases that initial melt pockets formed at the interface of dehydrating muscovite (c.f. figure 2a, figure 7c in Brearley & Rubie, 1990). Furthermore, Brearley and Rubie (1990) noted an affinity between melt and sillimanite, which formed intergrowths oriented parallel to precursor muscovite [001] planes. A recent study by Almqvist *et al.* (2015), which explored the effect of muscovite dehydration melting on seismic velocity using muscovite and quartz grain aggregates, likewise found that melt growth initiated along dehydrating-muscovite grain boundaries (c.f. figure 2c, figure 5 in Almqvist *et al.*, 2015). The natural affinity between sillimanite and melt is documented in a number of experimental studies on muscovite dehydration melting (e.g. Patiño-Douce & Harris, 1998,

Buick *et al.*, 2004, Almqvist *et al.*, 2015). Moreover, natural examples of quenched anatectic metapelitic enclaves in dacites from the Spanish volcano El Hoyazo preserve porphyroblasts of nodular pseudomorphs of fibrolitic sillimanite intergrown with glass/melt (Cesare, 2000, Acosta-Vigil *et al.*, 2010).

Based on the experimental textures, and the presence of the hydrous reactant (muscovite), I would expect melt to initiate in the aluminous domains. However, the formation of sillimanite + quartz intergrowths within the aluminous domain is not taken to directly represent a crystallised melt but rather it is interpreted to be the site of initial melt growth.

2.5.6 Further discussion on melting textures

1) Cathodoluminescence textures

Cathodoluminescence (CL) of quartz and plagioclase is associated with lattice defects and inclusion of trace elements (Smith & Stenstrom, 1965, Seyedolali *et al.*, 1997, Müller *et al.*, 2000, Götze *et al.*, 2001, Brokus *et al.*, 2015). Although CL peak intensities can vary between mineral grains of the same phase within a single rock, differences in the relative intensity within a grain impart a texture that can be used to differentiate the origin of a grain. While the mechanisms that control quartz luminescence are highly variable, lattice defects generally suppress CL (Götze *et al.*, 2001).

The occurrence of ‘bulls-eye’ zoning in quartzofeldspathic domains of sample E184 is attributed to solid-state *grain-recycling* by grain boundary migration, a process that involves sweeping of grain boundaries within single-phase aggregates (Pearce & Wheeler, 2010). The matrix grain size appears to correlate with the size and distribution of biotite (figure 2.12b), suggesting biotite grains pin quartz and plagioclase grain-growth and the ‘bulls-eye’ zoning is best preserved in domains with limited grain boundary mobility.

Apart from the topotactic growth of K-feldspar on plagioclase, there are no evident changes in CL textures within the quartzofeldspathic matrix that are attributed to vapour-absent muscovite dehydration melting.

At the margins of the aluminous domains, the association of sillimanite inclusions in domains of CL bright quartz suggest that the crystallisation of sillimanite and *grain-recycling* lattice-diffusion processes are linked. Observations of sillimanite grains along the boundaries of matrix minerals and as linear arrays within matrix quartz suggest that sillimanite may have been transported by a fluid phase (melt) along grain boundaries and fractures.

As melt % increases, the distribution of sillimanite grains along quartz and plagioclase grain boundaries is more pervasive, and the distances that sillimanite grains are observed, relative to the lenticular intergrowths of sillimanite and quartz, increases. Once the melt percolation threshold is reached, melt forms a pervasive intergranular network that connects the primary compositional aluminous domains with the quartzofeldspathic domains. As melt migrates away from the aluminous domain, bundles of fibrolitic sillimanite with minor interstitial quartz are all that remain from the primary aluminous domains. Discerning the effect of solid-state diffusional coarsening from melt crystallisation in quartz remains difficult; CL imaging of quartz only provides a textural distinction when *grain-recycling* partially modifies a grain. Once quartz grains have experienced a grain-size increase of 3-5x by solid-state grain boundary migration, they no longer contain the diagnostic CL-dark cores of un-melted matrix.

2) Melt percolation threshold

Previous estimates of the liquid percolation threshold of granitic melt, derived from both the geometric relations of crystal aggregates and rheological experiments, are consistently

between 7–8 % (e.g. Vigneresse *et al.*, 1996, Rosenberg & Handy, 2005). The uniform fine-grained texture observed in all low melt % samples (<6 %), suggests that although a melt phase was generated and peritectic K-feldspar and sillimanite were produced, the melt phase was constrained to isolated interstitial pores. It is only after a total of ~8 % melt is generated that the interstitial melt forms a connected network. Importantly, the melt percolation threshold marks the transition from closed to open system behaviour, where melt forms a transient phase. Beyond this threshold, the melt phase is able to migrate away from the source, and may segregate and coalesce to form veins, dykes, and large granitic bodies.

Aligned bundles of fibrolitic sillimanite may act as an efficient pathway for melt migration and escape, by forming an anisotropic and permeable grain-boundary network. The initial association of sillimanite in the melt-producing aluminous domains, and following grain-size coarsening, the formation of foliation-defining sillimanite schlieren that bound quartzofeldspathic domains, suggest that melt and sillimanite may remain closely associated throughout the melting process. Moreover, migration of melt along sillimanite schlieren may also explain the absence of sillimanite in the regions of the rock that represent in-situ melt crystallisation (i.e. melt pseudomorphs). Intergrowths of fibrolitic sillimanite with tourmaline, apatite, and muscovite may form during a late stage of melt fractionation once the melt is enriched in volatile components (i.e. B, OH, F). An alternative interpretation of these intergrowths is that they formed during a late event of fluid infiltration as the rock cooled. In either scenario, the schlieren of fibrolitic sillimanite may act as an efficient pathway for melt or brine.

3) Accessory mineral textures

There is a notable difference in the grain-size and distribution of ilmenite, monazite, apatite, and tourmaline amongst samples that experienced varied degrees of vapour-absent muscovite dehydration melting. Figure 2.14a shows the distribution of ilmenite and monazite in a section of sample BD1419 cut perpendicular to lineation. Ilmenite is found along the perimeter of the aluminous domain, surrounded by coarsened quartz grains with fine-grained inclusions of sillimanite (figure 2.14a-c). Biotite grains within the aluminous domain are ragged in appearance, suggesting they may have participated in the reaction either actively as a consumed reactant or passively through dissolution – reprecipitation (figure 2.14b). Ilmenite grains range in size from 50–500 μm; the largest grains are commonly found along the contact between aluminous and quartzofeldspathic micro-domains (figure 2.14a,d). Monazite is equally distributed across the quartzofeldspathic domains, and commonly forms small (20–40 μm) round grains with dark cores and cuspate lobes and patches (figure 2.14d). Small (30–70 μm) monazite grains that are sub-rounded and un-zoned in back scattered images dot the perimeter of the aluminous domain. By contrast, monazite grains in sample BD1434, which has generated up to 30 modal % melt, are notably larger (300–500 μm) and generally form oscillatory zoned prismatic grains (figure 2.14e,f).

The lobe and patch zoning observed in monazites from the quartzofeldspathic domains of samples with low melt % (≤ 6 %) closely matches the description of textures produced by fluid-mediated dissolution – reprecipitation (Putnis & Putnis, 2007, Harlov *et al.*, 2011), which forms when a fluid-assisted reaction front migrates inwards from a grain boundary. The fluid-mediated dissolution – reprecipitation reaction mechanism can operate in conditions where the rate of diffusion is low and the reaction has a very small equilibration volume. Conversely, samples with moderate to high melt percent (8–30 %),

which have crossed the melt percolation threshold, contain fewer and larger monazite grains than samples with low melt percent, indicating higher diffusion rates and larger equilibration volumes.

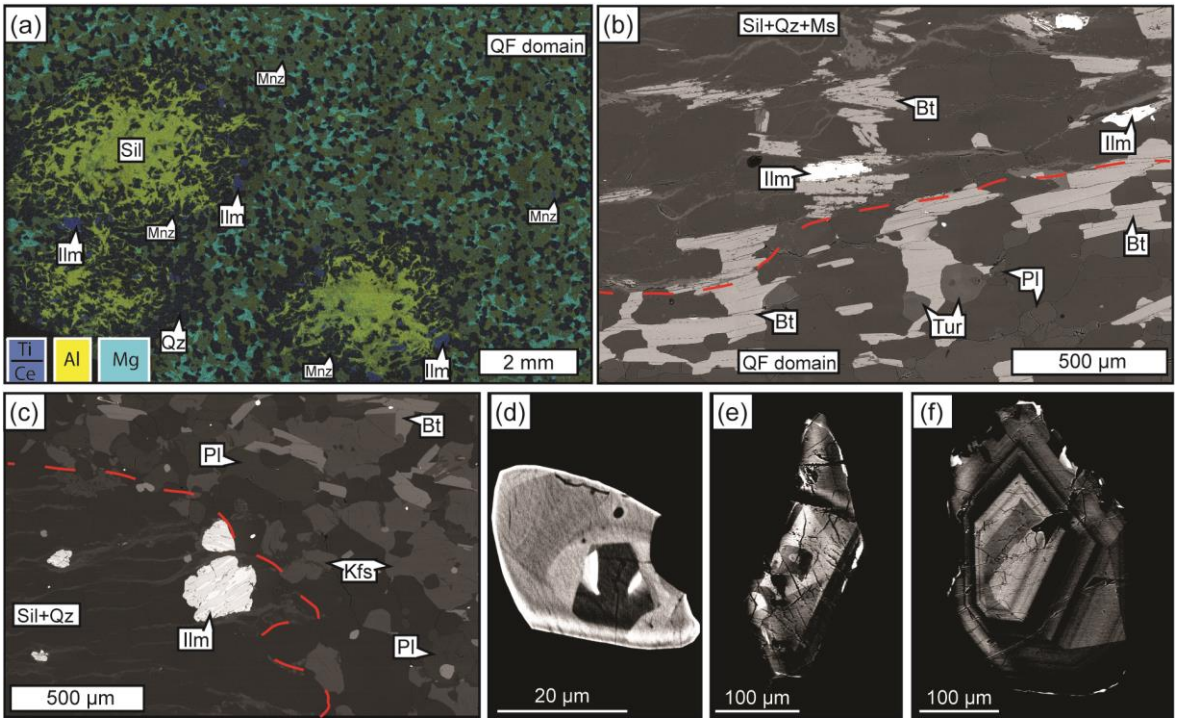


Figure 2.14 Accessory mineral textures formed during melting. (a) EDS element map of sillimanite + quartz intergrowths in sample BD1419, which has experienced 5–6 melt %. The aluminous micro-domains are differentiated with sillimanite-rich cores and coarsened quartz rims. Monazite (Mnz) is evenly distributed throughout the quartzofeldspathic matrix, and concentrated along the rims of sillimanite + quartz intergrowths. Ilmenite (Ilm) is only found along the rims of the sillimanite + quartz intergrowths. (b) Back-scattered electron image of sample E184. Dashed red line marks the contact between the intergrowths of sillimanite + quartz + relict muscovite, and the quartzofeldspathic matrix. Biotite grains appear ragged within the intergrowths, compared to the well-formed matrix grains. (c) Back-scattered electron image of sample BD1419, showing ilmenite grains along the contact of a sillimanite + quartz intergrowths and the quartzofeldspathic matrix. (d) Back-scattered image of a small (30 µm) monazite grain from sample BD1419 showing the cuspate lobe and patch zoned texture that is characteristic of monazite grains found in the quartzofeldspathic matrix. (e,f) Back-scattered images of monazite grains from sample BD1434, a pelitic augen gneiss that has generated 25–30 melt %. The grains exhibit oscillatory zoning and range size from 300–500 µm.

2.6 MODEL FOR MUSCOVITE DEHYDRATION MELTING

Domain-scale chemical ordering in muscovite-bearing protolith compositions imparts the basic framework for the textural evolution of muscovite dehydration melting. Within this framework, muscovite dehydration melting is self-organising with coupled behaviour in the aluminous and quartzofeldspathic domains (figure 2.15a). The distances between the domains are on the order of several millimetres, large enough for aluminium to remain relatively immobile (i.e. the aluminous domain is maintained), but small enough that other cations may diffuse between domains. Nucleation preferences, driven by the reduction of free energy, exert control over the distribution of product phases. Sillimanite nucleation is restricted to the aluminous domain where intergrowths of fibrolitic sillimanite and quartz replace muscovite. However, during vapour-absent muscovite dehydration melting, the processes in both textural domains are directly coupled by the preferred nucleation of K-feldspar on plagioclase grains in the quartzofeldspathic domain.

Melt is generated in the aluminous domains, at the interface of the hydrous reactant (muscovite). The generation of melt in the aluminous domain is in proportion to K-feldspar growth in the quartzofeldspathic domains. Exchange of cations between muscovite and melt in the aluminous domain (figure 2.15b), and plagioclase in the quartzofeldspathic domain drives the initial microstructural evolution of K-feldspar. For the reaction to progress as observed, both domains must remain in near equilibrium with respect to the exchanged cations (i.e. K^+ and Na^+). At the stage of initial K-feldspar growth (i.e. poikiloblasts), volume is conserved within the quartzofeldspathic domain by the topotactic replacement of plagioclase by K-feldspar. Correspondingly, the melt generated in the aluminous domain migrates away from the muscovite reaction interface, towards the quartzofeldspathic domain. The movement of melt, along grain boundaries and micro-fractures, is driven by a relatively small overpressure (i.e. increased volume of the reaction

products) as well as the capillary effect of melt-free grain boundaries in the neighbouring quartzofeldspathic domain. As the reaction progresses, melt is driven further from the aluminous domains, filling triple junctions in the quartzofeldspathic domain. Coarsening of all major phases reflects the communication of melt throughout the entire network of grain boundaries (figure 2.15c). Moreover, reaching the melt percolation threshold (~8 %) marks the transition from a closed (isochemical) system to one where melt can freely migrate. It then follows that once a rock exceeds the melt percolation threshold it becomes susceptible to melt loss. The collapse of aluminous domains to form networks of sillimanite mats or schlieren, may conduct melt away from the melting pelite. As the melt phase migrates away from the initial source domain, it may coalesce to form segregated veins and dykes that conduct melt towards larger granitic bodies. Upon cooling, the relatively small amount of melt remaining in the source pelitic rock can further modify minerals to form the ‘melt pseudomorph’ textures that are observed in the final exhumed rock.

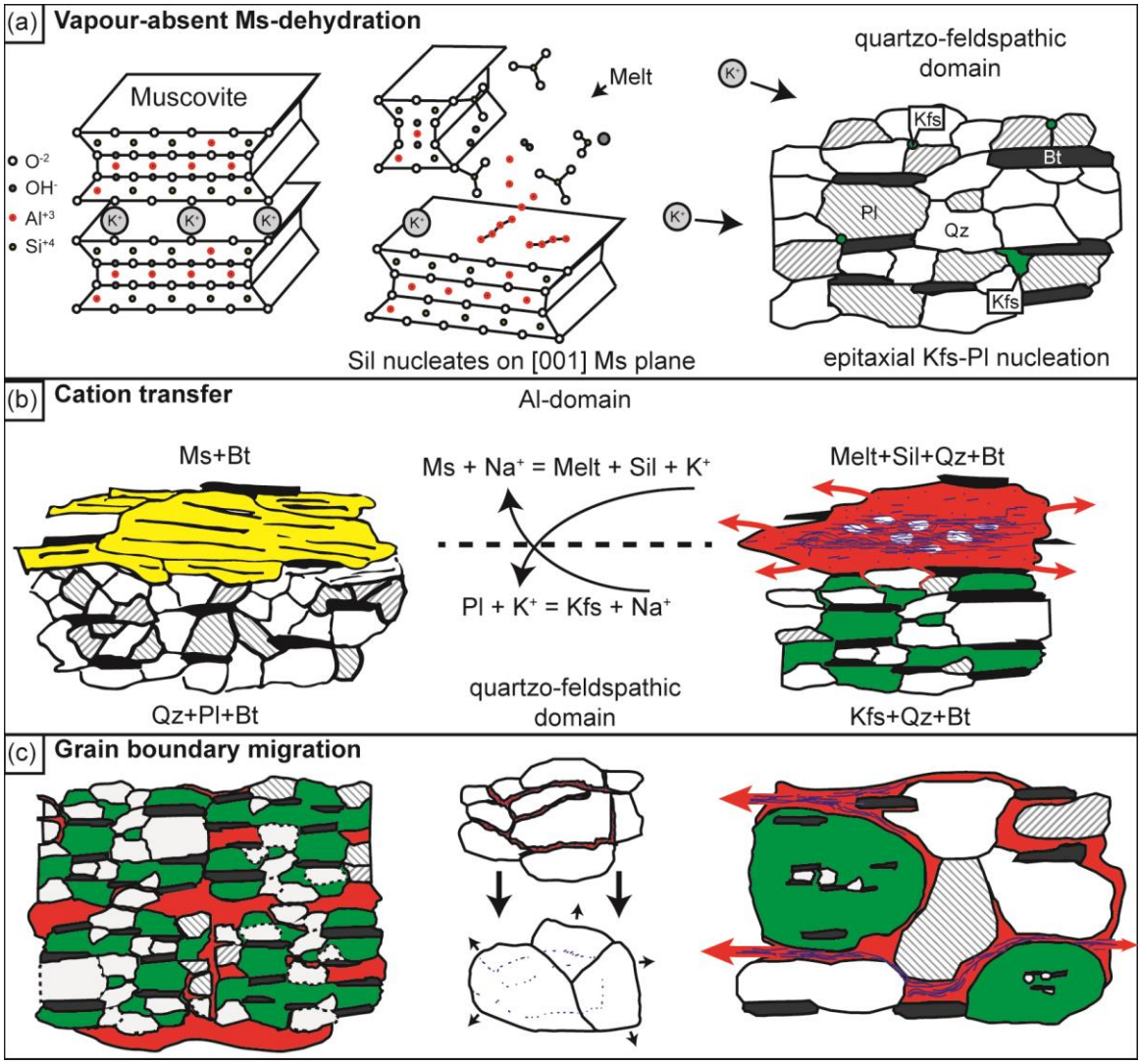


Figure 2.15 Schematic diagram of the vapour-absent muscovite dehydration reaction mechanisms. (a) During the dehydration of muscovite, sillimanite nucleates on the remaining [001] muscovite cleavage planes leading to a high nucleation-rate within the aluminous domains. The breakdown of muscovite produces a chemical gradient of K+ ions between the aluminous and quartzofeldspathic domains. Peritectic K-feldspar nucleates epitaxially on plagioclase grain boundaries. (b) The high K+ chemical gradient between domains drives a K+–Na+ cation exchange that replaces plagioclase with K-feldspar, while Na+ is dissolved into the silicate melt. Silicate melt forms at the interface of dehydrating muscovite, and then migrates from the aluminous- to quartzofeldspathic- domains along grain boundaries and micro-fractures. (c) Once melt forms an interconnected grain-boundary network, the rates of intergranular diffusion increase significantly, enabling grain-size coarsening by grain boundary migration and dissolution – reprecipitation. Networks of fibrolitic sillimanite, which wrap around K-feldspar porphyroblasts and quartzofeldspathic microlithons, provide a pathway for efficient melt escape.

2.7 INSIGHTS INTO THE GOVERNING REACTION MECHANISMS

2.7.1 Epitaxial nucleation

The K-feldspar microstructures formed by muscovite dehydration melting agree with studies that suggest K-feldspar has limited nucleation potential (e.g. Vernon, 1986, Cashman, 1990), such as the observations of: plagioclase grains that lack shared grain boundaries with K-feldspar, simple twinning in peritectic K-feldspar (inferred as difficult nucleation assisted by a twinned nuclei), and the porphyroblastic texture of larger K-feldspar grains (>1 mm). Epitaxial nucleation of K-feldspar on plagioclase grains is energetically favourable for two reasons: (1) K-feldspar and plagioclase are both framework silicates that share a similar crystal structure, (2) plagioclase and quartz are consumed by muscovite dehydration melting as K-feldspar is produced, creating space for nucleation and growth of K-feldspar at the reacting grain boundaries (i.e. volume is conserved in the quartzofeldspathic domains). Once a nucleus of K-feldspar has formed, it grows by replacing the structure of the parent plagioclase grain (topotaxy). The poikiloblastic texture of initial K-feldspar growth demonstrates the relative ease with which the advancing K-feldspar interface replaces neighbouring plagioclase grains in contrast to grains of quartz or biotite.

2.7.2 Sillimanite and quartz intergrowths

In general, lenticular intergrowths of fibrolitic sillimanite and quartz, commonly referred to as faserkiesel (e.g. Dyck & St-Onge, 2013), are associated with muscovite dehydration. However, the texture may not be unique to vapour-absent muscovite dehydration melting. St-Onge (1981) documents a similar porphyroblastic sillimanite texture in samples from the low pressure (<0.4 GPa) sub-solidus sillimanite + K-feldspar metamorphic zone in the Wopmay Orogen. Waters (2001) noted an intergrowth affinity between sillimanite and

quartz in both sub- and supra-solidus conditions in samples from Namaqualand Metamorphic Complex, that is attributed to the low diffusion mobility of silica and aluminium in siliceous melts and the relative immobility of aluminium in lattice and grain-boundary diffusion (Cashman, 1990). The close association of sillimanite and quartz as a product in multiple reactions may reflect a common process that operates over a range of conditions. Two reaction mechanisms are considered. In the first, muscovite dehydration (producing Sil+Kfs+Melt/H_2O) is treated as an interface-controlled process that conserves volume. If the mobility of aluminium is restricted across the reaction interface, one might expect the resulting texture to be a fine-grained intergrowth of the aluminium-rich and aluminium-poor minerals (i.e. sillimanite and quartz). Carmichael (1969) suggests a similar process for the close association of sillimanite with quartz and biotite in reactions that consume staurolite, kyanite, and muscovite. The second mechanism that could contribute to the development of fibrolitic sillimanite and quartz intergrowths is analogous to base-leaching (i.e. removal of large mobile cations by a fluid phase; Vernon, 1979). The growth of K-feldspar in the quartzofeldspathic domain removes potassium from the aluminous domain, effectively enriching the aluminous domain in the aluminium and silica required to form a sillimanite and quartz intergrowth. Correspondingly, at lower pressures where H_2O is a product phase, leaching potassium from the aluminous domain could have the same affect.

The abundance of fibrolitic sillimanite grains in aluminous domains suggests sillimanite experiences a high rate of nucleation in the aluminous domains, possibly nucleating on the reacting muscovite crystal structure itself (figure 2.15a). The importance of sillimanite nucleation on decomposing muscovite becomes apparent when looking for a textural clue to how melt migrates, because protolith muscovite was (per definition) in the aluminous domain, and so the presence of fibrolitic sillimanite in regions outside the

aluminous domain implies sillimanite was transported by a migrating fluid (melt). Melts first forms at the site of the hydrous reactant, in this case muscovite, since melt nucleation is not necessary limited by the same energetic constraints as solid phases. The co-nucleation of melt and sillimanite provides a record of early melt distribution in cases where retrograde crystallisation and melt pseudomorphing obscure the supra-solidus history.

2.7.3 Chemically driven mineral growth

The irregular K-feldspar-plagioclase grain boundaries and anhedral shape of K-feldspar advocates a growth step that precludes textural equilibrium. These textures suggest the growth mechanism for peritectic K-feldspar is an interface-controlled replacement of matrix plagioclase by K^+ – Na^+ cation exchange, with an intergranular diffusion step transferring potassium from domains of reacting muscovite (i.e. the sillimanite + quartz intergrowths) to the domains of concentrated K-feldspar growth (figure 2.15b). The cation exchange reaction is driven by a chemical potential gradient between the aluminous and quartzofeldspathic domains that is established when muscovite destabilises, releasing potassium. The preservation of protolith fabric suggests K-feldspar replacement growth was accommodated within plagioclase microdomains by the concurrent consumption of albitic plagioclase during partial melting. In addition to the low nucleation potential of K-feldspar, the poikiloblastic texture could indicate a plagioclase-K-feldspar reaction rate similar to the rates of intergranular diffusion, involving a fluid-present interface-coupled dissolution – reprecipitation reaction mechanism (Putnis & Putnis, 2007). The composition of melt within the aluminous domain would become increasingly alkalic as sodium is added, resulting in an increased volatile solubility (Rapp & Watson, 1986, Webster *et al.*, 2014). Equilibrium calculations of the volume change during vapour-absent muscovite

dehydration melting predict an increase of around 4 % for a high-aluminium pelite with 30 modal % muscovite. If the topotactic replacement of plagioclase by K-feldspar does indeed conserve volume, as the poikiloblastic texture suggests, then the relatively small volume increase should be concentrated in the aluminous domains. The distribution of fine sillimanite grains, in the quartzofeldspathic matrix that surrounds the aluminous domains, suggests melt moves primarily along grain boundaries and micro-fractures.

2.7.4 Grain-size coarsening processes

The transition from melt generation in isolated aluminous micro-domains to connectivity of melt through a grain boundary network marks the shift from a closed to an open system where melt is a transient phase. The high diffusion rates of species in silicate melt encourage grain boundary migration (Cabane *et al.*, 2001) and the reduction of grain boundary energy by grain-size coarsening (Fig. 15c). Grain boundaries *wetted* by melt experience increased grain boundary migration at rates proportional to the diffusion rate and solubility of components in the melt (Dell'Angelo & Tullis, 1988, Evans *et al.*, 2001). Grain boundary migration is also related to the melt-solid interaction volume, which increases with melt mobility. Hence, grain boundary migration is most rapid when melt forms a pervasive network with thoroughgoing advective migration.

As grain boundaries sweep across K-feldspar-K-feldspar boundaries, multiple poikiloblasts of K-feldspar merge to form single porphyroblasts, which can grow up to 10 centimetres in diameter in extreme cases. For each large porphyroblast, the process of merging by grain boundary migration preserves the crystallographic orientation and fine-grained quartz and biotite inclusion pattern of a parent poikiloblast. In cases where the preserved poikiloblast was twinned, a twinned porphyroblast is formed (e.g. figure 2.9g). A record of grain boundary migration-induced coarsening is preserved in both K-feldspar

and quartz grains, where inclusions of fabric-aligned fine-grained biotite record a passive overgrowth of the protolith *Zener pinning* microstructures. As coarsening progresses in all phases, the size of quartz and biotite grains increase, preserving a record of inclusion coarsening from the initial poikiloblastic grain to the merged overgrowth domains (figure 2.9c-f). The process of grain-size coarsening of the peritectic K-feldspar grains, aided by dissolution – reprecipitation of quartzofeldspathic phases in the melt, effectively segregates K-feldspar, quartz and plagioclase. The recognition of fine-grained quartz inclusions surrounded by an array of fabric-aligned fine-grained biotite can be used to distinguish peritectic K-feldspar from anatectic K-feldspar, which crystallises from the residual melt. Coarsening of fibrolitic silllimanite needles to prismatic grains is rare and may be limited by the ease of grain boundary sliding within fibrolitic sillimanite intergrowths, which could act to reduce the internal grain energy by accommodating strain energy that could otherwise accumulate in sillimanite grains (Vernon, 1987). As the system establishes chemical equilibrium, the communication of components operates on a centimetre – decimetre length-scale abating the inherited compositional layering. Monazite growth by the redistribution of small grains suggests the rate-limiting dissolution of phosphorus (Harrison & Watson, 1984) occurs at a higher rate when melt operates under open system behaviour than when melt remains isolated. As in samples that have experienced moderate to high melt %, the coarsened grains are interpreted as the parts of the rock that were texturally modified in the presence of melt.

2.7.5 Textural modification during melt crystallisation

As the system cools or the melt fractionates to a composition with lower volatile concentrations, K-feldspar, quartz and plagioclase will crystallise. In a pelitic composition, where K-feldspar, plagioclase and quartz are all present as solid phases when muscovite

has fully dehydrated, there is no kinetic barrier to form overgrowths of the haplogranitic melt phases (Holness & Sawyer, 2008). Nucleation and growth of anatectic K-feldspar is observed both as new grains in the matrix and as a concentration of grains around K-feldspar porphyroblasts. K-feldspar grains that have crystallised from residual melt make up a small portion (<10 %) of the final porphyroblast size, but serve to remove a portion of the K-feldspar component from residual melt domains, yielding a residual melt composition in the quartzofeldspathic *leucosome* that trends towards a quartz-rich tonalite rather than monzogranitic in composition. As grain-size increases, the permeability of the solid assemblage is reduced, resulting in lowered melt-solid interaction, and isolation of melt in pockets at triple-grain junctions (Holness & Sawyer, 2008). The residual melt pockets are enriched in volatile-rich phases, often forming intergrowths of tourmaline + muscovite + sillimanite. The coarsened grain-size and resulting isolation of chemical components together with the loss of volatiles by melt fractionation during open-system migration prevents complete retrogression of sillimanite + K-feldspar + melt to secondary muscovite.

2.8 IMPLICATIONS FOR CRUSTAL ANATEXIS

Two conditions must be met to form granitic bodies by crustal anatexis. First, there must be a source rock with a suitable composition to generate the melt. The capacity of a source rock to generate granitic melt is termed ‘fertility’ (Thompson, 1996, Clemens, 2006). At the conditions of vapour-absent muscovite dehydration melting, the fertility of a rock is proportional to the amount of muscovite present at the solidus. Second, there must be a mechanism that segregates granitic melt from the source. Melt segregation can be driven by both internal (e.g. buoyancy) and external (e.g. deformation) forces (Brown, 1994). However, for melt segregation to occur, the melt percolation threshold must first be

reached. Grain-size coarsening is the stage of muscovite dehydration melting that links the local domain-scale mineral processes with the transfer and accumulation of melt on a regional-scale.

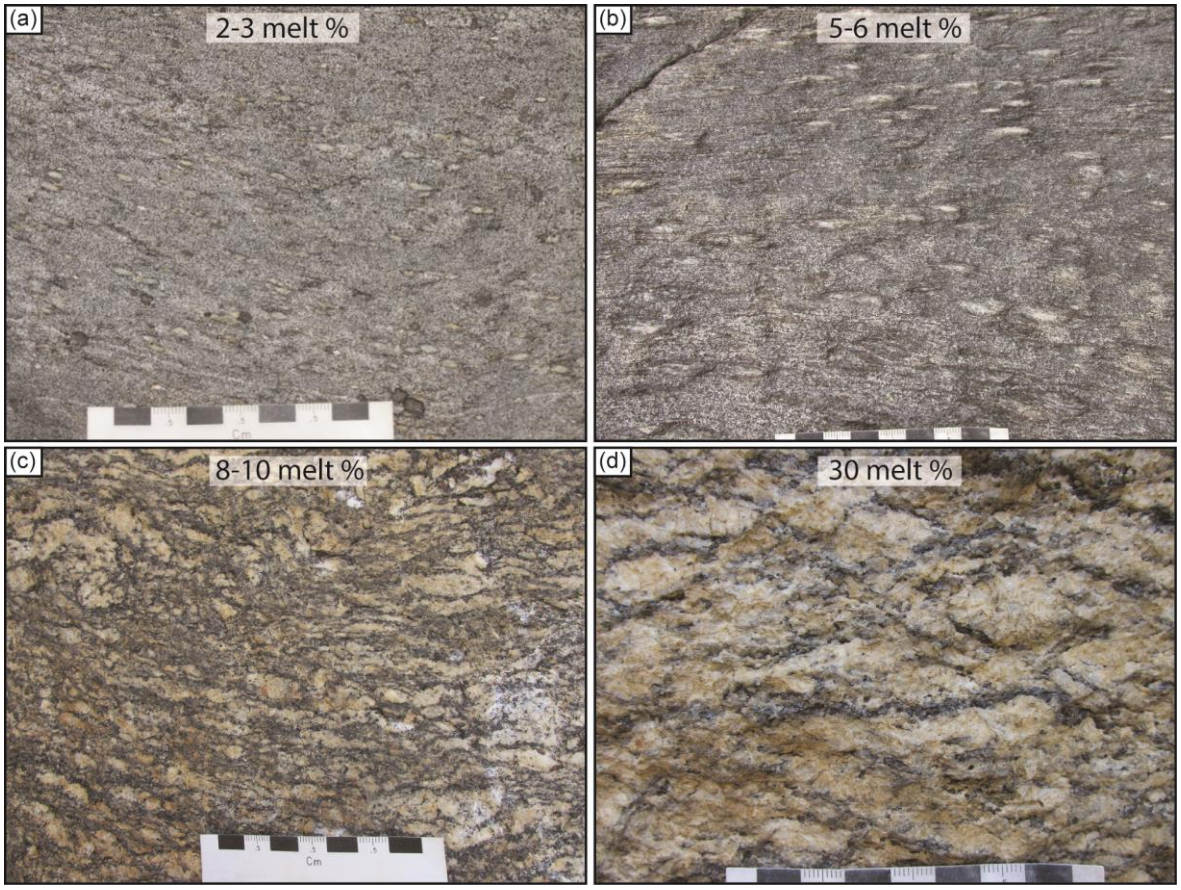


Figure 2.16 Outcrop photographs of the representative textures for a variety of melt %. The major ticks on the scale card are in centimetres. Note that all rocks are from a similar structural level that has experienced similar metamorphic conditions and deformation, and the variation is due to differences in the modal amount of muscovite in the sub-solidus protolith. (a) Sample BD1206, a fine-grained semipelite with an arkosic matrix, which has experienced 2–3 melt %. The characteristic texture is formed by the replacement of muscovite by lenticular intergrowths of sillimanite + quartz. (b) Sample BD1419, a fine-grained pelite, which has experienced 5–6 melt %. The only appreciable difference between the textures in frames (a) and (b) is the size and amount of sillimanite + quartz intergrowths. (c) Coarse-grained pelitic augen gneiss texture of a pelite that has experienced 8–10 melt % (BD1411). (d) Coarse-grained K-feldspar- and sillimanite-rich pelitic augen gneiss texture formed in a high-Al pelite (BD1434), which has experienced 25–30 melt %.

Based on the substantial change in texture that results from melt connectivity and the transition in melt behaviour from a closed to open system, outcrop textures can inform on whether or not a rock acted as a source for segregated melt. Figures 2.16a and 2.16b show rocks that have undergone vapour-absent muscovite dehydration melting generating 2–3

and 5–6 melt % respectively (table 2.2). Both rocks exhibit the characteristic lenticular sillimanite + quartz intergrowth texture indicative of muscovite dehydration, but apart from the modal % of sillimanite + quartz intergrowths, these rocks are indistinguishable on the macro-scale. Figure 2.16c shows a coarsened pelite that has generated 8–10 melt %, exceeding the melt percolation threshold. There is little change in texture amongst rocks that have undergone grain-size coarsening, although the amount of peritectic K-feldspar increases with further quantities of melting (figure 2.16d). The resulting (coarsened) K-feldspar and sillimanite bearing rock is mapped in the field as pelitic augen gneiss (figure 2.3 & figure 2.4). In metamorphic terrains where muscovite dehydration melting is the dominant melt producing reaction, it might be possible to determine the source of segregated granite bodies by mapping out the extent of coarsened sillimanite- and K-feldspar- bearing pelitic augen gneiss (e.g. figure 2.16c,d). The extent of the coarsened rocks marks the region over which melt might have acted as a transient phase, without necessarily accumulating in channelized dykes and sills.

The close association of peritectic sillimanite and melt, originating in the aluminous domains, may not only provide an efficient means for melt migration, but may also encourage entrainment of sillimanite xenocrysts. In regions where exposure is poor or restricted to one structural level, a granitic body formed by muscovite dehydration melting can possibly be recognised by the presence of entrained sillimanite xenocrysts. When H_2O is available during crystallisation or retrograde cooling, plates of secondary muscovite may overgrow the peritectic sillimanite. The growth of secondary muscovite is often incomplete, so grains of sillimanite may be preserved in the core domains (e.g. figure 2.13d).

In view of the proposed mechanisms of growth, the following textural criteria are suggested as diagnostic indicators to distinguish peritectic porphyroblasts from anatectic

grains of K-feldspar: (1) clusters of fine-grained equigranular inclusions of quartz, which may mimic the distribution and retain the orientation of an earlier matrix fabric, (2) textural domains with paleofabric-aligned biotite, which are not arranged in orientations crystallographically controlled by K-feldspar; the biotite inclusions resemble the size and distribution of matrix biotite pinning microstructures, (3) a coarsening of inclusion size away from the nuclei, with a medium- to coarse-grained matrix. In contrast, K-feldspar grains that crystallised from the melt phase are distinguishable by: (1) an absence of fine-grained inclusions, owing to grain-size coarsening precluding the crystallisation of residual melt, (2) monomineralic melt pseudomorphs along K-feldspar–K-feldspar grain boundaries.

The development of reliable criteria to identify peritectic K-feldspar enables a mass-balance of the muscovite dehydration melting products to quantify the amounts of H_2O present during melting. Under vapour-absent conditions, the modal proportions of the muscovite dehydration melting products are: K-feldspar – 35%; Sillimanite – 20%; Melt – 45% (see Table 2.1). The modal % of peritectic K-feldspar and sillimanite in all samples used in this study necessitates vapour-absent conditions at the time of melting and implies that the primary melting reaction in the Langtang and Everest Greater Himalayan Series is vapour-absent muscovite dehydration melting rather than by vapour-fluxed melting. Using this approach in other regional settings may provide valuable insights into the presence and amounts of a hydrous pore-fluid in the middle and lower crust.

As suggested above, the co-generation of sillimanite and melt in the aluminous domain could set up efficient pathways for melt migration, by making a highly anisotropic network of grain boundaries. On the scale of which muscovite dehydration melting occurs, one potential implication of this textural association would be a greater efficiency in the way that melt is extracted from the source pelite. A further implication of this line of

reasoning is that in other crustal settings, where vapour-absent muscovite dehydration melting is not the dominant melt generating reaction, a higher proportion of generated melt may be retained in migmatite complexes.

2.9 CONCLUSIONS

Comparison of grain-scale textures in metamorphosed siliciclastic rocks that have undergone vapour-absent muscovite dehydration melting shows that the reaction follows four stages of mineral growth:

(1) Nucleation – Peritectic K-feldspar nucleates epitaxially on isomorphic plagioclase grains in quartzofeldspathic domains. Peritectic sillimanite nucleates in (muscovite-rich) aluminous domains, initially on [001] mica cleavage planes. Nucleation of silicate melt does not require nucleation energy; rather it is generated at the interface of the hydrous reactant (muscovite).

(2) Chemically driven growth – In quartzofeldspathic domains, peritectic K-feldspar replaces plagioclase by a K^+ – Na^+ cation transfer reaction driven by the chemical gradient established when muscovite dehydrates, freeing K^+. Intergrowths of sillimanite and quartz replace muscovite.

(3) Merge and coarsening – Melt migrates into the quartzofeldspathic domains along grain boundaries and micro-fractures. A melt percolation threshold is reached once the grain-boundary network is *wetted* by melt, increasing the rate of diffusion on a rock scale and significantly increasing the effect of grain boundary migration. This leads to a grain-size increase of up to two orders of magnitude. The melt percolation threshold (7–8 %) denotes the transition from isolated melting in the aluminous domains to an open-system on the lithology scale (1–1000's of meters), where melt is a transient phase.

(4) Residual melt crystallisation – Residual melt crystallises preferentially on existing peritectic grains as anatectic quartz, plagioclase, and K-feldspar. As the system cools and closes, grain growth forces melt into the intersections of grain-boundaries, forming melt pseudomorph microstructures and intergrowths of the volatile-rich phases (i.e. tourmaline + muscovite + apatite). Secondary muscovite forms when free H_2O reacts with sillimanite and K-feldspar during cooling.

The inherent coupling of aluminous and quartzofeldspathic domains, by the nucleation preferences of K-feldspar and sillimanite, sets up a self-organising system that encourages melt extraction and the formation of K-feldspar-rich restite.

3 Melt-rock interaction and the formation of the Himalayan nebulitic tourmaline leucogranites

3.1 INTRODUCTION

The Himalayan leucogranites, which form a network of intrusions in the upper structural portion of the Greater Himalayan Series, are a product of high-temperature metamorphism and regional anatexis. Leucogranite thickness and total volume of accumulated melt varies along the length of the orogen; however there is a relation between the occurrences of large leucogranite bodies, such as the Manaslu leucogranite, with the thick domains of the underlying Greater Himalayan Series (Le Fort *et al.*, 1987). The larger leucogranite bodies are notably heterogeneous, in terms of their constituent mineral assemblages, and poly-phase comprising numerous individual sills and dykes that exhibit complex cross-cutting relations (e.g. Reddy *et al.*, 1993, Searle *et al.*, 1997b, Streule *et al.*, 2010a).

The leucogranites exhibit a wide range of compositions, which previous studies have partitioned into two end-member lithologies: the muscovite-biotite leucogranite (also referred to as two-mica leucogranite) with tourmaline ≤2.6 % and biotite >1.5 % modal, and tourmaline leucogranite with tourmaline >2.2 % and biotite <1.5 % modal (e.g. Reddy *et al.*, 1993, Visonà & Lombardo, 2002). Previous descriptions of the Himalayan muscovite-biotite leucogranites note a lack of internal compositional structure, while a portion of the tourmaline leucogranites in contrast display compositional layering and are nebulitic in appearance (e.g. Reddy *et al.*, 1993, Searle *et al.*, 1997b). Both types display heterogeneous isotopic values for strontium, with initial $^{87}Sr/^{86}Sr$ ratios of 0.738–0.750 in the two-phase Shisha Pangma leucogranite (Searle *et al.*, 1997b) and 0.765–0.785 for the two-phase Gangotri leucogranite (Scaillet *et al.*, 1990), suggesting that mixing did not occur between individual pulses of melt. Major element trends are notably homogenous,

varying only in concentration of Na and K, while trace element trends are highly variable (Le Fort *et al.*, 1987, Inger & Harris, 1993). The ratios of radiogenic isotopes (Pb, Sr, Nd) indicate melt was sourced from Greater Himalayan Series pelites (Le Fort *et al.*, 1987), and the small variation in reported ^{18}O values (13.04% ± 0.25), is consistent with a single melt source with homogeneous ^{18}O values (Scaillet *et al.*, 1990).

The age of Himalayan leucogranites are unambiguously Miocene; however, most leucogranite bodies contain monazite, xenotime, and zircon that display a 1–6 Ma range in U-Pb ages, reflecting a protracted history of melting with variations in the timing of accessory mineral growth (Searle *et al.*, 1997b, Harrison *et al.*, 1999, Catlos *et al.*, 2001, Godin *et al.*, 2001, Cottle *et al.*, 2009, Kellett *et al.*, 2009, Searle *et al.*, 2010, Streule *et al.*, 2010a, Leloup *et al.*, 2015). A study by Parrish and Hodges (1996) on monazite and xenotime growth in the Langtang leucogranites and the underlying migmatitic pelite constrain the timing of anatexis in Langtang to ca. 21 Ma.

Questions regarding the petrogenesis of the Himalayan leucogranites and in particular, the origin of the two end-member lithologies, have long been the focus of petrological, geochemical, and geochronological studies (Vidal *et al.*, 1982, Inger & Harris, 1993, Guillot & Le Fort, 1995, Harris *et al.*, 1995, Ayres & Harris, 1997, Searle, 1999, Visonà & Lombardo, 2002). Based on differences in Ti content (normalised to Li), Visonà and Lombardo (2002) suggest that the tourmaline leucogranite in the Cho Oyu region was generated by muscovite dehydration melting, whereas the muscovite-biotite leucogranite, with higher Ti values, was generated by biotite dehydration melting. However, both field cross-cutting relationships between the two types of leucogranite (Reddy *et al.*, 1993, Searle *et al.*, 1997b), and Rb/Ba ratios (Harris & Inger, 1992) indicate that the leucogranites formed during one continuous vapour-absent muscovite dehydration melting event (see chapter 2). There are two views on the origins of the muscovite-biotite

leucogranite and tourmaline leucogranite that invoke muscovite dehydration melting as the sole melting reaction. In the first view, the two melt compositions arise from different melt fractions (e.g. Ayres & Harris, 1997). The alternative view, suggests that the two melt compositions stem from different lithological sources (e.g. Vidal *et al.*, 1982, Le Fort *et al.*, 1987, Guillot & Le Fort, 1995). Depleted-mantle Nd model ages for both the tourmaline leucogranite and muscovite-biotite leucogranite, range between ca. 1500 and 2200 Ma with an assumed crustal $^{147}Sm/^{144}Nd$ of 0.10 ± 0.02, indicating a Himalayan source composition with Mesoproterozoic to Paleoproterozoic detritus (Searle *et al.*, 1997b). In a study of H-isotopic values in the Manaslu leucogranite, Le Fort *et al.* (1987) conclude that the late stage or post-magmatic alteration of the muscovite-biotite leucogranite is extremely localised, and that magmatic compositions are preserved. At present, there is a gap in our understanding of Himalayan anatexis, where the field, microtextural, and isotopic evidence suggest a single melting reaction (vapour-absent muscovite dehydration) but nevertheless two distinct leucogranite compositions are preserved.

In this chapter I describe and interpret the macroscopic features and microstructures of the rocks in the leucogranite-rich 'melt sink' region of the Greater Himalayan Series, specifically, the formation of the nebulitic tourmaline leucogranite and the microstructural evolution of the psammitic country-rock. I present the results of a thorough microstructural analysis and discuss the grain-scale mechanism of a proposed melt-rock reaction. Furthermore, I consider the thermodynamic conditions of reactive melt flow in the middle crust, and discuss its implications for crustal anatexis.

3.2 GEOLOGICAL SETTING AND SAMPLES

The Greater Himalayan Series is a ~20 km thick package of metamorphosed sedimentary rocks, orthogneiss, and anatectic leucogranite that extends along the length of the orogen (see chapter 1). Bounded by the Main Central Thrust zone at its base (to the south), and the South Tibetan Detachment System at its top (to the north), the Greater Himalayan Series represents an exhumed package of mid-crustal rocks (e.g. Le Fort, 1986, Searle *et al.*, 1987a, Macfarlane, 1993, Searle *et al.*, 2006b, Webb *et al.*, 2007).

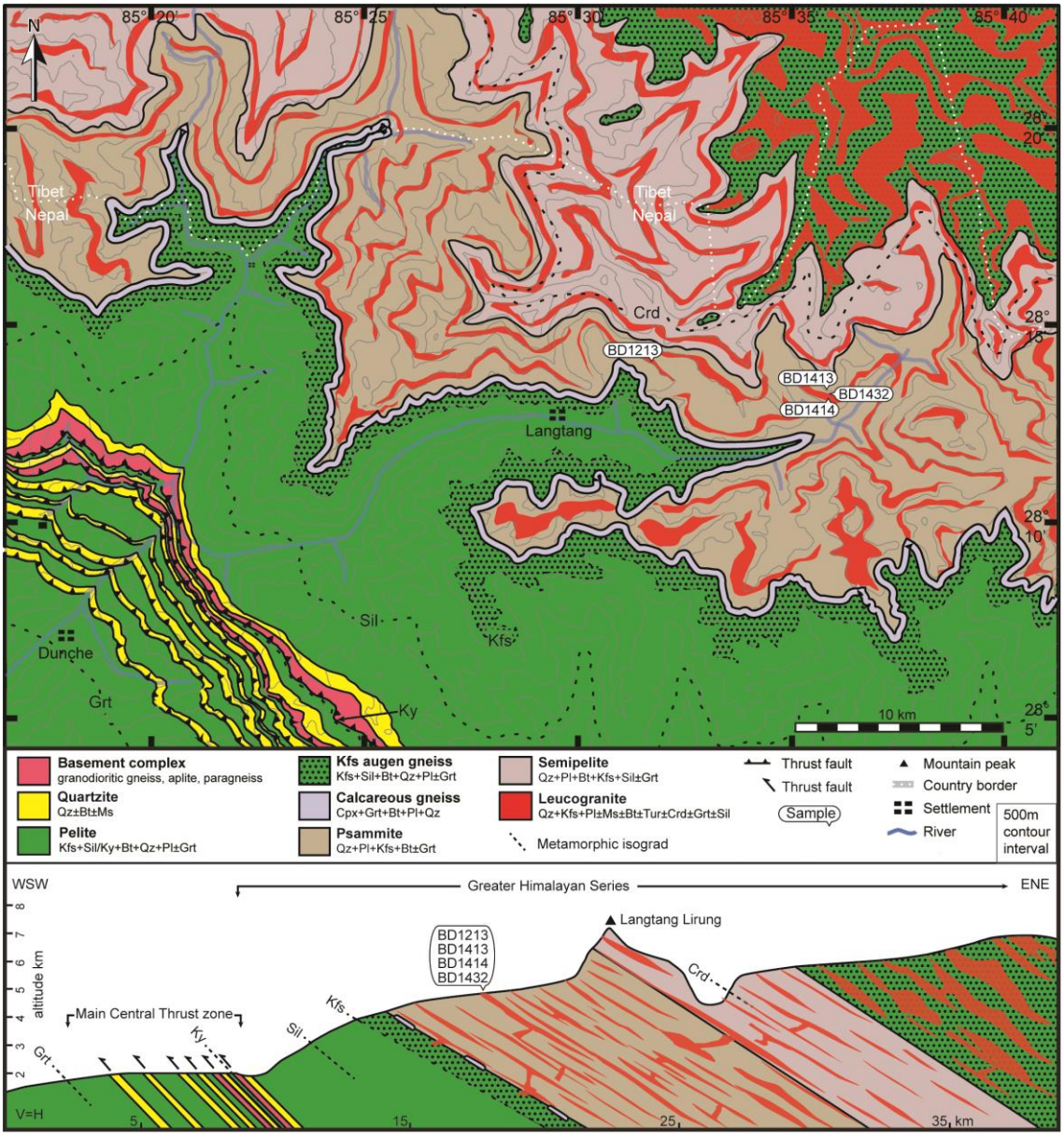


Figure 3.1 Geological map and cross-section of the Langtang field area, showing the lithology, structure, and position of metamorphic isograds across the MCT and GHS. Labels denote the locations of samples used in this chapter, for sample coordinates and rock type see table 3.1.

Two major valleys in Langtang transect the Greater Himalayan Series, exposing a superb record of anatexis and related mid-crustal processes. Traversing up structural-section from its base at the Main Central Thrust zone, the stratigraphy of the Langtang Greater Himalayan Series comprises: polymetamorphic orthogneiss and paragneiss, thickly bedded quartzite, fine-grained pelite topped by pelitic augen gneiss, calcareous gneiss, and a thick package of arkosic psammite that grades upwards into semipelite and pelite (figure 3.1). A network of leucogranite sills and dykes, which are the focus of this chapter, intrude the top structural two-thirds of the Greater Himalayan Series. The leucogranite bodies are hosted in a sequence of psammite, pelite, and K-feldspar augen gneiss country-rock (figure 3.1). The structurally lowermost leucogranite sills intrude along the base of the psammitic unit and comprise ~10 % of the rock volume. The size of leucogranite bodies and the ratio of leucogranite to country-rock increase structurally upwards to ~50 % of the total rock volume in the uppermost valleys of the Langtang region. The leucogranite-bearing domain within the Greater Himalayan Series, is termed the 'melt sink', because it represents the tectonostratigraphic level where anatectic melt accumulated and crystallised. Consequently it offers an ideal natural laboratory to study the effects of melt-rock interaction in a continental setting.

The metasedimentary country-rocks that host leucogranite experienced a history of pervasive ductile deformation and high-temperature metamorphism prior to leucogranite emplacement (Reddy *et al.*, 1993, Macfarlane, 1995). Thin pelitic layers within the psammite record a sillimanite–K-feldspar metamorphic grade and evidence for local vapour-absent muscovite dehydration melting (see chapter 2). The presence of sillimanite and K-feldspar suggests the psammite experienced similar metamorphic conditions to the underlying K-feldspar- and sillimanite-bearing pelitic augen gneiss and that there is no

significant tectonic or thermal break between these units (Reddy *et al.*, 1993). Transposed bedding in the metasedimentary country-rock dips shallowly to the north. Meter- to kilometer-scale, south-verging folds with shallowly north dipping axial planes reorientate the country-rock foliation and foliation-parallel leucogranite sills within the entire 'melt sink' region (Reddy *et al.*, 1993). In the northeastern portion of Langtang, the country-rock foliation and foliation-parallel leucogranite bodies are locally reoriented by kilometer-scale late open folds with near-vertical north–south trending axial planes.

Samples used in this study were all collected along the same structural level of the Greater Himalayan Series, where leucogranite intrudes psammitic country-rock (figure 3.1). Type samples of the intrusive leucogranite and the psammite that exhibit all of the characteristic microstructures were selected from a larger collection of seventy-nine samples. Table 3.1 is a summary of samples used in this chapter including the rock type, sample coordinates, and analytical purpose of each sample. All samples were collected during two field seasons, in 2012 and 2014, with the logistics of the second season focussed on mapping the 'melt sink' region.

Sample ID	Rock type	Longitude[‡]	Latitude[‡]	Comments
BD1213	Ms-Bt-(Sil)-leucogranite	85.56957	28.22942	Fig. 3.3; Fig. 3.6; Fig. 3.7; Fig. 3.11-12
BD1413	Arkosic psammite	85.66917	28.21287	Fig. 3.2; Fig. 3.5; Fig. 3.11-12
BD1414	Nebulitic Tur-leucogranite	85.66917	28.21287	Fig. 3.4; Fig. 3.8; Fig. 3.9; Fig. 3.11-13
BD1415	Contact: psammite - Tur-leucogranite	85.66917	28.21287	Fig. 3.10
[‡] WGS84 grid reference system				

Table 3.1 Sample metadata.

3.3 ANALYTICAL METHODS

A Quanta FEI scanning electron microscope (SEM) at the Department of Earth Sciences, University of Oxford was used to generate backscattered electron (BSE) and cathodoluminescence (CL) images along with energy-dispersive X-ray spectroscopy (EDS) and electron backscatter diffraction (EBSD) data. EDS analyses were produced using a X-

Max^N Silicon Drift Detector operating at 20 kV with a working distance of 10mm. EDS and montaged CL and BSE maps were processed using Oxford Instruments software, Aztec 2.1. CL images were generated with a Centaurus FEI monochromatic CL detector operating at 20 kV with a long working distance of 27 mm. Acquisition deadtime was set to 70% to avoid detector saturation, and the brightness and contrast were set so quartz, plagioclase, and K-feldspar could be imaged simultaneously.

EBSD analyses were collected using a finely polished thin section that was mounted on a stage tilted 70° to the primary beam. The thin section was uncoated and data were acquired in a low vacuum operating mode. The accelerating voltage was 30 kV at a working distance of 15 mm. The angular resolution of individual absolute crystal orientation measurements under these operating conditions is expected to be 0.1–0.5° (Ruggles *et al.*, 2016). EBSD patterns were imaged using an Oxford Instruments Nordlys S EBSD camera. Electron backscatter patterns were indexed for plagioclase using Aztec 2.1 acquisition software by Oxford Instruments. Results were plotted using Channel 5 software from Oxford Instruments.

3.4 FIELD RELATIONS AND MACROFEATURES

3.4.1 Psammitic country-rock

A two kilometer thick package of fine-grained arkosic psammite forms the dominant lithology into which the leucogranitic sills and dykes are emplaced. The psammite is rhythmically layered on the centimeter scale, alternating between layers of varying biotite and quartzofeldspathic content (figure 3.2a). The largely homogeneous unit is well-deformed, exhibiting a foliation that is defined by biotite, and a mineral lineation that is defined by elongate minor phases, such as sillimanite and tourmaline. Primary bedding (S_0) is transposed by layer parallel shear, resulting in attenuated, foliation (S_1) parallel bedding,

in lineation-parallel view (e.g. figure 3.2a, b). Perpendicular to the mineral lineation, isoclinal and ptygmatic folding of primary layering record a history of shear-strain and crustal thickening (figure 3.2a). Foliation and bedding are crosscut by leucogranitic veins, sills, and dykes (figure 3.2a, c, d), which are in turn sheared, folded, and boudinaged (e.g. figure 3.2b, c). The primary assemblage of the psammite is biotite – plagioclase – quartz – K-feldspar, with varying minor proportions of sillimanite, tourmaline, and magnetite. K-feldspar content varies between compositional layers, comprising only a minor phase in plagioclase- and quartz-rich layers. In low strain domains, the individual beds are compositional gradated, increasing in biotite, K-feldspar, and sillimanite content towards the top of each layer.

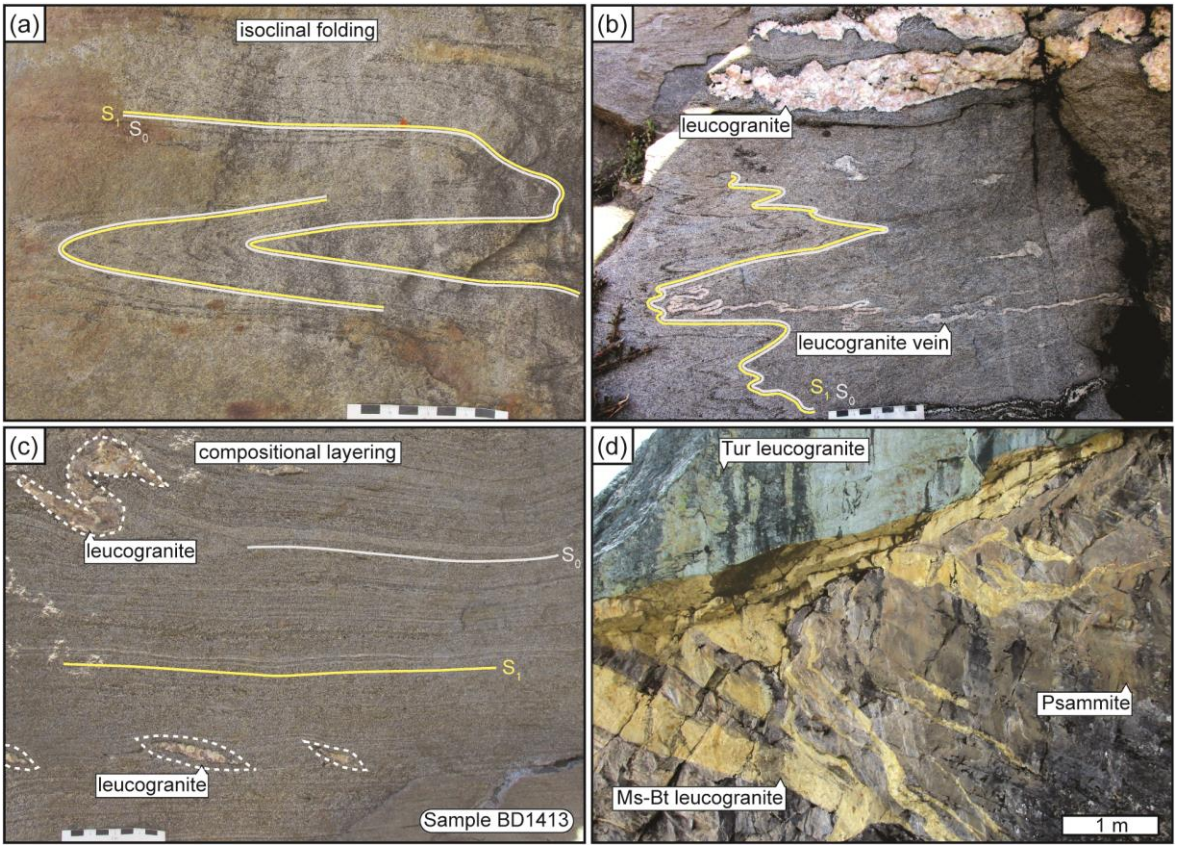


Figure 3.2 Field relations and macro-features of the psammitic country-rock. (a) Field photograph showing isoclinal folding of the transposed bedding. (b) Field photograph showing the psammitic country-rock crosscut by veins of syenogranite. Ptygmatic folding of the psammite is outlined by dark biotite-rich folia. (c) Field photograph showing the rhythmically layered arkosic psammite crosscut by an en echelon array of syenogranite veins. The photograph displays horizontal transposed bedding with primary bedding (S0)

parallel with a foliation (S1) defined by biotite. (d) Field photograph of leucogranite sills and dykes (highlighted) intruded into the psammitic country-rock.

3.4.2 Leucogranitic bodies

Leucogranitic veins, sills, and dykes with a range of compositions and mineralogy form a complex intrusion network, hosted in the psammitic country-rock (figure 3.3). The leucogranite compositions represent a continuum between two common end-members, muscovite-biotite monzogranite and muscovite-sillimanite syenogranite, which are collectively referred to as muscovite-biotite leucogranite. A third leucocratic unit, termed the nebulitic tourmaline leucogranite, which is spatially associated with the other leucogranite end-members and comprises a major portion of the intrusion network (~ 60–80% of leucocratic bodies), is described in more detail below. Both the muscovite-biotite monzogranite and muscovite-sillimanite syenogranite end-members occur as variably deformed dykes and sills, which exhibit complex cross-cutting relationships formed by multiple generations of leucogranite intrusion (figure 3.3a, b, c). Bodies of muscovite-biotite monzogranite are commonly cross-cut by the more syenograntitic compositions (e.g. figure 3.3c); however, there are examples of composite intrusions that show no clear cross-cutting relationship between the monzogranitic and syenogranitic components (figure 3.3d). The margins of both end-member compositions are notably biotite-rich, commonly forming discrete (1–5 mm thick) dark contacts with the host psammite. Medium- to coarse-grained muscovite-biotite monzogranite generally forms large (1–10 m thick) sills and dykes. The primary assemblage of the monzogranite is muscovite – biotite – quartz – plagioclase – K-feldspar, with varying minor amounts of sillimanite, tourmaline, garnet, and cordierite. Whereas, the muscovite-sillimanite syenogranite is generally coarse-grained or pegmatitic, occurring as smaller veins, sills, and dykes (1–100 cm thick). The primary

syenogranite assemblage is muscovite – sillimanite – K-feldspar – quartz – plagioclase, with varying minor amounts of tourmaline, and biotite.

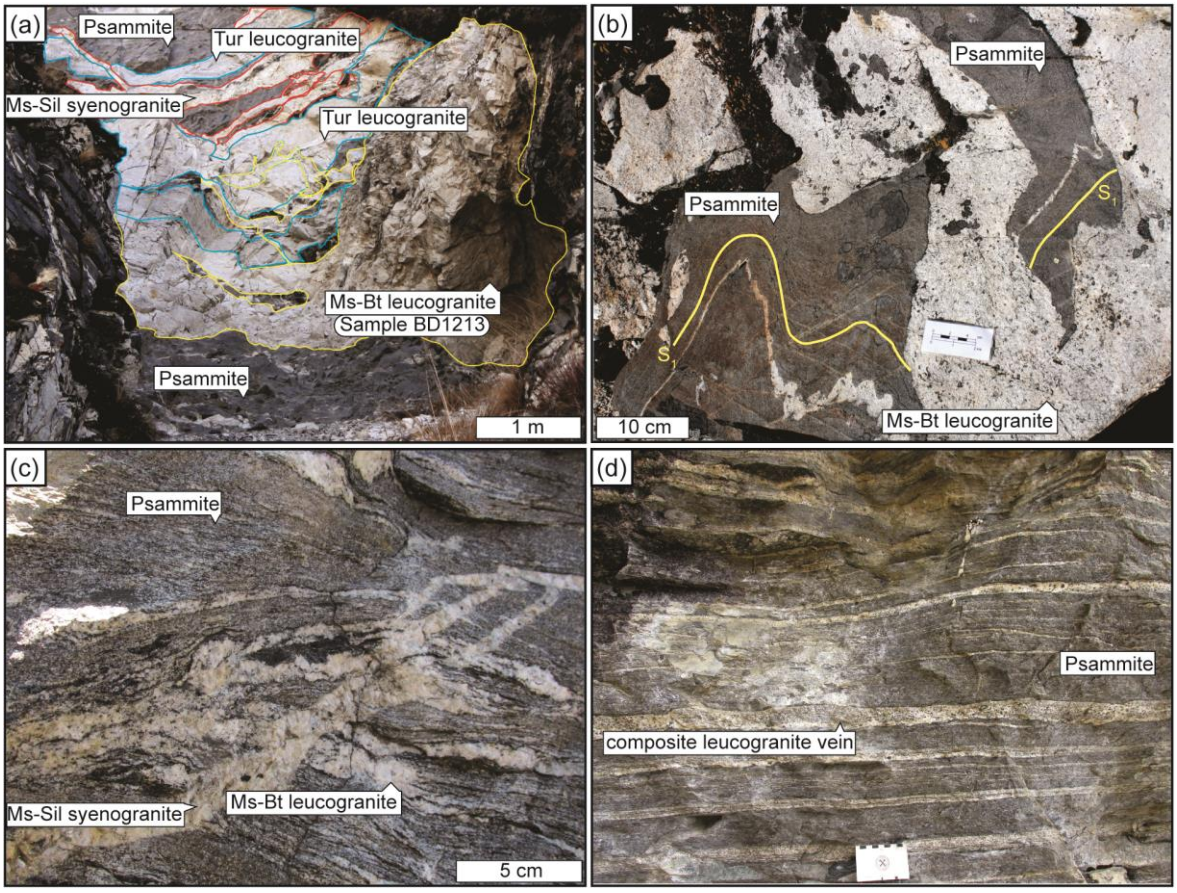


Figure 3.3 Muscovite-biotite leucogranite field relations. (a) Highlighted field photograph showing relationship between the different types of leucogranite. (b) Field photograph showing a composite leucogranite body that crosscuts psammite, forming both cross-cutting (dyke) and layer-parallel (sill) features. (c) Field photograph showing multiple leucogranite phases that crosscut and intruded psammite. (d) Field photograph showing composite veins of muscovite-biotite leucogranite and tourmaline leucogranite oriented parallel with the psammite layering.

Nebulitic tourmaline leucogranite

The nebulitic tourmaline leucogranite is a heterogeneous leucocratic unit that occurs in close association with intrusions of muscovite-biotite monzogranite and muscovite-sillimanite syenogranite. The term ‘nebulitic’ is used to describe the heterogeneous compositional layering that is characteristic of this unit. Field estimates suggest that the nebulitic tourmaline leucogranite accounts for 60–80 % of the leucocratic material that is

hosted by psammite. Localised examples of the unit are found along the upper contacts of muscovite-sillimanite syenogranitic sills (figure 3.4a, b), and within domains of local dilation (i.e. fold hinge) in the host psammite (figure 3.4c). The margins of the nebulitic tourmaline leucogranite bodies are typically parallel with the transposed beds of the host psammite, forming contacts that lie along biotite-rich folia. In detail, contacts between nebulitic tourmaline leucogranite and psammite are tourmaline-rich and irregularly shaped, exhibiting a centimetre-scale lobe and cuspate interface (figure 3.4b). Figure 3.4c provides an example of nebulitic tourmaline leucogranite that is localised within an asymmetric fold of the psammite foliation; the tourmaline-rich layers are continuous with the biotite folia in the host psammite. Figure 3.4d shows the orientation of tourmaline crystals along the tourmaline selvage that separates the host psammite from the nebulitic tourmaline leucogranite. The leucogranite is typically medium-grained and displays a sugary or granular texture. Rhythmic centimeter-scale compositional layering between tourmaline and layers rich in tourmaline and K-feldspar, and more quartzofeldspathic layers gives the unit a banded or gneissic appearance (figure 3.4e). The compositional layers within the nebulitic tourmaline leucogranite have an orientation similar to that of the transposed bedding in the host psammite. Ptygmatic (figure 3.4e) and isoclinal (figure 3.4f) folds of the compositional layers are similar in form and appearance to those exhibited in the host psammite (e.g. figure 3.2b, c). The quartz and feldspar grains in the nebulitic tourmaline leucogranite generally do not define either a foliation or lineation, while tourmaline grains are commonly orientated parallel to the compositional layering and display a lineation parallel to the mineral lineation in the host psammmite.

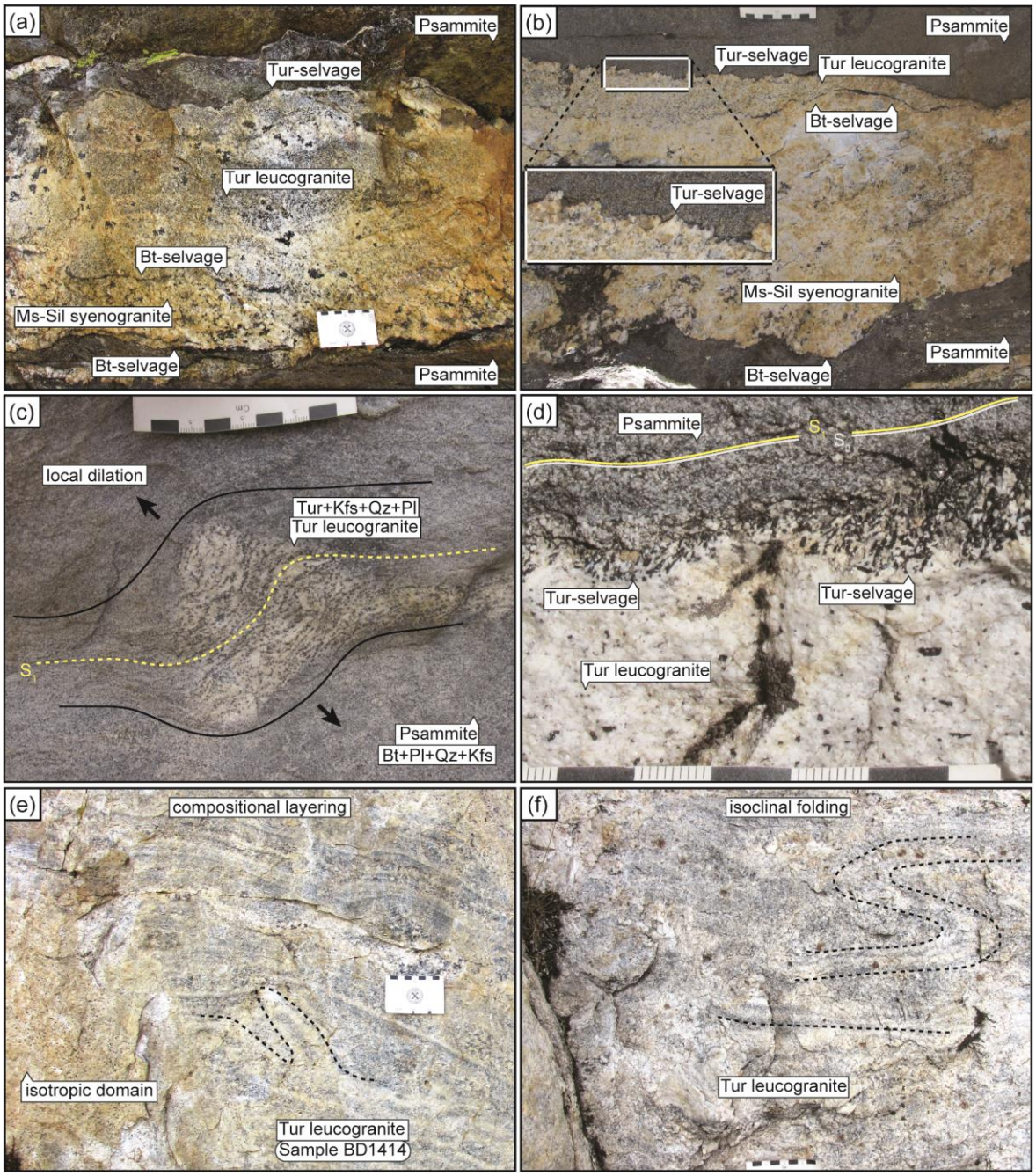


Figure 3.4 Field relations and macro-features of the nebulitic tourmaline leucogranite. (a) Field photograph showing a composite leucogranite sill intruded into psammite. The lower 5–10 cm of the sill is syenogranite with biotite-rich margins (selvage). Nebulitic tourmaline leucogranite forms the upper portion of the sill, exhibiting both the characteristic compositional layering and a tourmaline-rich selvage along the contact with psammite. (b) Field photograph showing a composite leucogranite sill. A biotite-rich selvage marks the contact between lower syenogranite and upper tourmaline leucogranite. Inset shows the irregular cuspate contact between the tourmaline leucogranite and psammite. (c) Field photograph showing a small buckle fold in the psammite foliation. Tourmaline leucogranite forms the centre of the fold structure. Note that the layers of tourmaline are continuous with the biotite-rich folia in the host psammite. (d) Field photograph of the contact between psammite and a sill of nebulitic tourmaline leucogranite. The photograph is of an uneven surface, where the psammite is set back relative to the sill, exposing the plane of contact. Note the alignment of tourmaline along the selvage plane and as layers within the nebulitic tourmaline leucogranite. (e) Field photograph of the nebulitic tourmaline leucogranite showing the compositional layering and internal folding that is characteristic of the unit. (f) Field photograph showing an isoclinal fold feature preserved in the compositional layering of the nebulitic tourmaline leucogranite.

3.5 MICROSTRUCTURES

3.5.1 Psammitic country-rock: sample BD1413

Sample BD1413 was chosen as a representative sample for the psammitic country-rock, because it displays the range of compositions and textures that are characteristic of the unit within the scale of a standard 3.5 x 2 cm thin section. The sample was collected from a clean outcrop that is cross-cut by small veins of leucogranite (e.g. figure 3.2c) and is host to both muscovite-biotite leucogranite and nebulitic tourmaline leucogranite. The primary assemblage is quartz – plagioclase – biotite – K-feldspar with minor amounts of tourmaline and ilmenite.

On the microscale, the sample displays compositional layering, alternating between domains rich in quartz – plagioclase, and K-feldspar – biotite (figure 3.5a). Biotite displays a preferred alignment parallel to the compositional layering, and a general grain-size coarsening (0.1–0.5 mm) towards the K-feldspar- and biotite-rich domains (figure 3.5a). Grains of quartz, plagioclase and K-feldspar all display a uniform range in size from 0.1 to 0.3 mm in diameter. Quartz grains are notably rounded, forming smooth and convex quartz-plagioclase and quartz-K-feldspar grain boundaries (figure 3.5b). In contrast, plagioclase and K-feldspar are more rectangular in appearance, forming aggregates with well-defined triple junctions and straight plagioclase-plagioclase, K-feldspar-K-feldspar, and plagioclase-K-feldspar grain boundaries (figure 3.5a, c).

Under CL, quartz displays a characteristic ‘bulls-eye’ texture with dark cores and light rims (figure 3.5d). The ‘bulls-eye’ texture is best developed in the smaller and more rounded quartz grains, while larger irregular shaped grains exhibit weak core to rim zoning (figure 3.5d, e). Plagioclase exhibits a core to rim ‘bulls-eye’ CL texture similar to quartz, which is best developed in smaller equant grains (figure 3.5e). The CL response of K-

feldspar is not as regular as it is for quartz or plagioclase. Figure 3.5f shows a range of K-feldspar grains, which exhibit domains with CL bright lines and patches as well as homogenous CL darker domains. In general, the CL response of K-feldspar mirrors the microcline twinning and does not exhibit any discernable core to rim pattern (figure 3.5f).

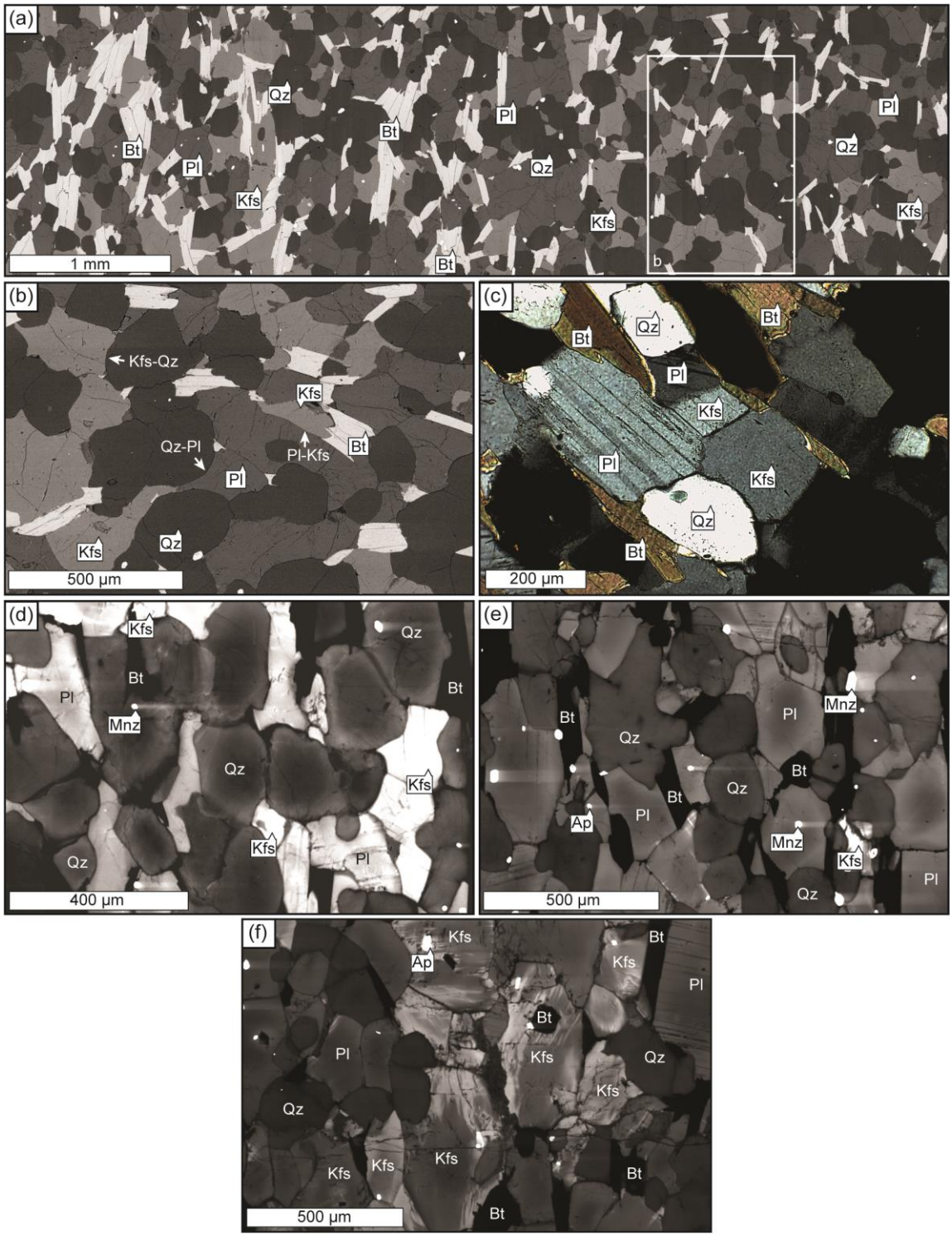


Figure 3.5 Microstructures in the psammitic country-rock, sample BD1413. (a) Overview backscattered electron image, showing compositional layering between domains rich in quartz – plagioclase, and K-feldspar – biotite. (b) Backscattered electron image, showing rounded grains of quartz within a matrix of K-feldspar, plagioclase, and biotite. Note the smooth and convex quartz-feldspar grain boundaries. (c) Photomicrograph viewed under crossed polars, showing ~120° feldspar three grain junctions and straight feldspar-feldspar grain boundaries. (d) Cathodoluminesence image, showing 'bulls-eye' texture in quartz, with dark cores and light rims. Note that biotite does not exhibit any cathodoluminescence (e) Cathodoluminesence image, showing 'bulls-eye' texture in plagioclase and quartz. (f) Cathodoluminesence image of a K-feldspar grain aggregate. The patchy and irregular zoning pattern in K-feldspar mirrors the microcline twinning.

3.5.2 Muscovite-biotite-(sillimanite) leucogranite: sample BD1213

Sample BD1213 is a medium-grained muscovite-biotite leucogranite with near equal proportions of quartz and K-feldspar, and sparsely distributed schlieren of sillimanite. It was chosen as a representative sample for the intrusive leucogranite unit because it has an intermediate granitic composition and displays a range of textures that are common to both the monzogranitic and syenogranitic end-members. The sample was collected from a metre-wide sill that intrudes the psammitic country-rock (e.g. figure 3.3a). The primary assemblage is quartz – K-feldspar – plagioclase – muscovite – biotite – sillimanite with minor amounts of tourmaline and ilmenite. Grain-size varies from 0.5 to 3.0 mm diameter (figure 3.6a), and the sample does not display a preferred grain alignment or foliation. Quartz displays a range of grain-shape from rectangular with straight grain boundaries to anhedral with curved grain boundaries and irregular appendages (figure 3.6a, b). Plagioclase forms tabular, euhedral grains, which typically display well-defined crystal facets (figure 3.6a, b). Most plagioclase grains display thin (100 μm) rims of albite (figure 3.6c). K-feldspar forms the largest grains, ranging from 1.5 to 3.0 mm wide. Grains of K-feldspar are typically tabular and subhedral, with inclusions of fine-grained plagioclase, quartz, and biotite (figure 3.6b). K-feldspar exhibits both microcline twinning (figure 3.6d) and string perthite texture (figure 3.6c). Vermicular intergrowths of quartz and plagioclase

(i.e. myrmekites) form bulbous structures along K-feldspar grain boundaries (figure 3.6d). Muscovite and biotite form randomly distributed blocky aggregates that do not display any preferred orientation or alignment (figure 3.6a, b, e). Figure 3.6e shows a coarse blocky muscovite grain that forms a spongy intergrowth with plagioclase. Along some of the triple junctions of coarse euhedral quartz and feldspars, there are anhedral intergrowths of net-veined muscovite and K-feldspar, and quartz and K-feldspar (figure 3.6f). Intergrowths of fibrolitic sillimanite and muscovite form anastomosing schlieren that lie along quartz and feldspar grain boundaries (figure 3.6g). Most quartz-feldspar grain boundaries are straight and smooth, although isolated examples of cuspate boundaries or appendages with low dihedral angles (< 60°) are observed along some interstitial domains (eg. figure 3.6f).

Under CL, quartz exhibits a mottled texture that is formed by a webbed array of CL dark lines amongst a CL brighter background (figure 3.7a, b). Plagioclase displays albite twinning and a CL darker albitic rim, however, apart from these textures; the plagioclase grains are featureless with no discernable internal domains (figure 3.7c). K-feldspar exhibits a variable CL response, which commonly mirrors twinning textures. In non-twinned K-feldspar grains, CL images reveal a complex internal texture with faceted core domains surrounded by oscillatory zoned rims (figure 3.7d).

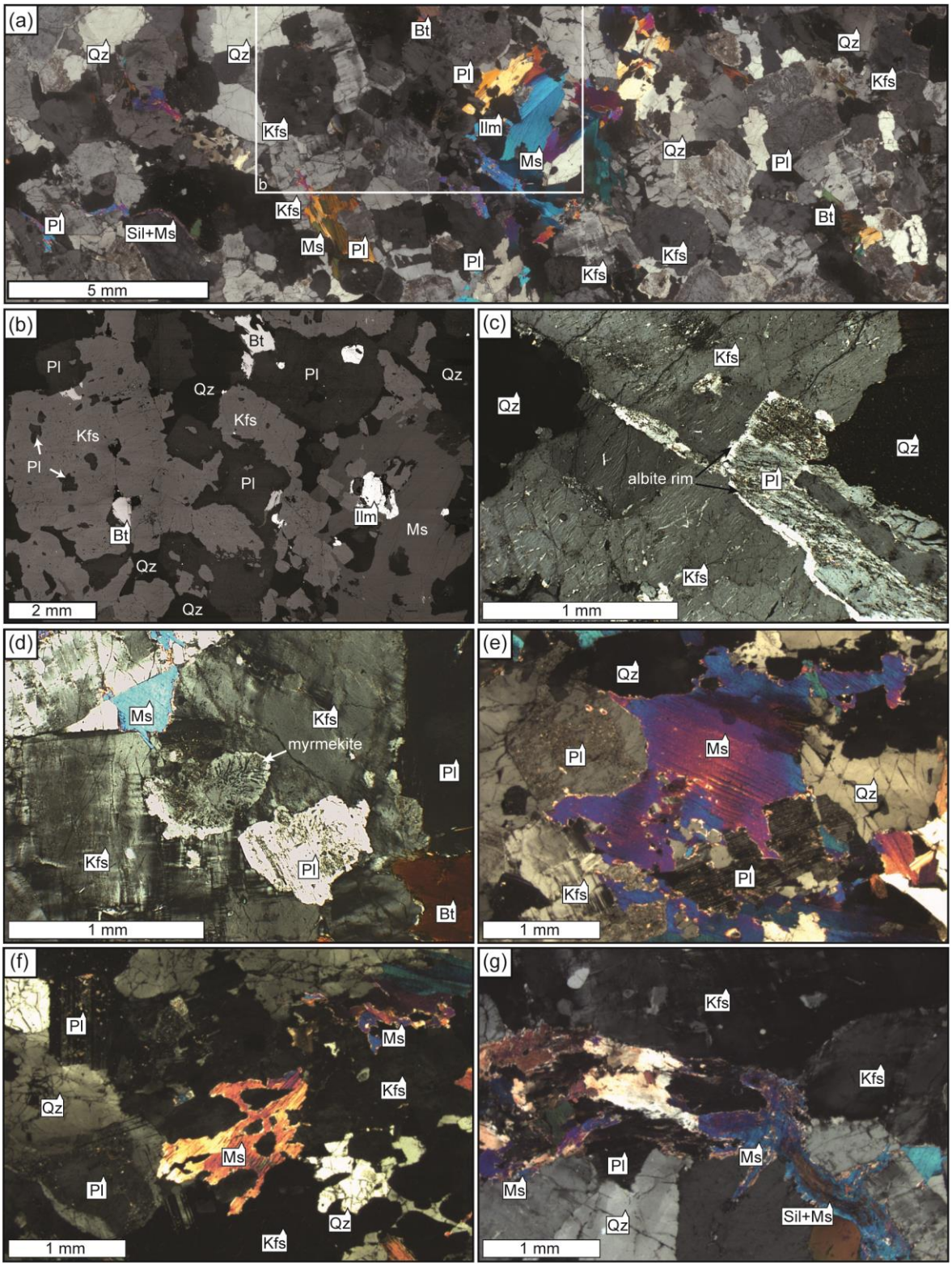


Figure 3.6 Microstructures in the muscovite-biotite-(sillimanite) leucogranite, sample BD1213. (a) Overview photomicrograph viewed under crossed polars, showing the shape, size, and distribution of mineral phases. (b) Backscattered electron image, showing large blocky poikilitic grains of K-feldspar with fine-grained inclusions of plagioclase, quartz, and biotite. (c) Photomicrograph viewed under crossed polars, showing string perthite K-feldspar texture and a tabular plagioclase grain with a thin albitic rim. (d) Photomicrograph viewed under crossed polars, showing variably microcline twinned K-feldspar and a myrmekitic intergrowth of quartz and plagioclase. (e) Photomicrograph viewed under crossed polars, showing a coarse muscovite

grain that exhibits both blocky euhedral and spongy anhedral textures where muscovite is intergrown with plagioclase. (f) Photomicrograph viewed under crossed polars, showing net veining of K-feldspar by muscovite and quartz. (g) Photomicrograph viewed under crossed polars, showing a xenocrystic schlieren consisting mainly of muscovite enclosing sheaves of fibrolitic sillimanite.

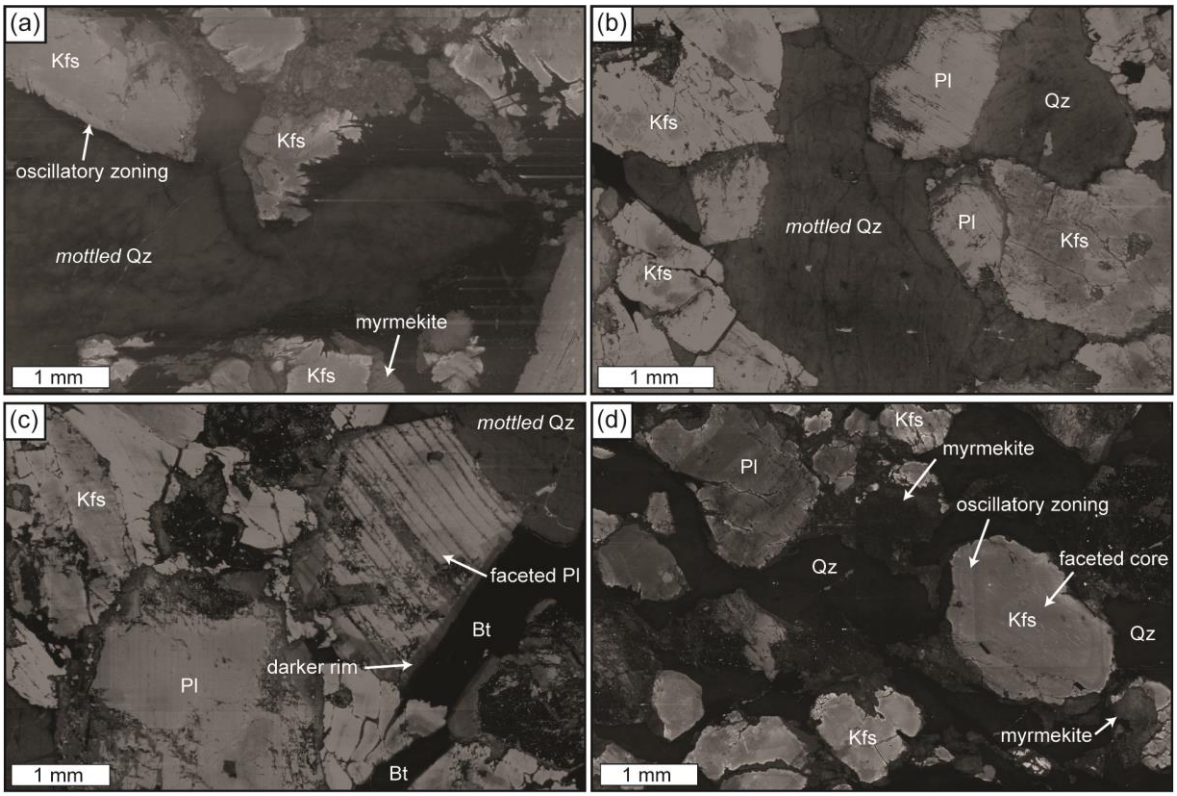


Figure 3.7 Cathodoluminesence textures in the muscovite-biotite-(sillimanite) leucogranite, sample BD1213. (a) Cathodoluminesence image, showing: quartz with a mottled texture of dark lines amongst a brighter background, an oscillatory zoned K-feldspar grain, and rim myrmekite textures along K-feldspar grain boundaries. (b) Cathodoluminesence image, showing: mottled quartz texture, featureless plagioclase, and irregular or patchy K-feldspar textures. (c) Cathodoluminesence image, showing: faceted plagioclase with albite twinning and a thin dark albitic rim. (d) Cathodoluminesence image, showing: a K-feldspar grain that exhibits string perthite texture and internal zoning. The CL zoning outlines a faceted core domain and an oscillatory zoned rim.

3.5.3 Nebulitic tourmaline leucogranite: sample BD1414

Sample BD1414 was collected from an outcrop of medium-grained nebulitic tourmaline leucogranite, which exhibits the rhythmic centimetre-scale compositional layering that is characteristic of the unit (e.g. figure 3.4e). The sampled leucogranite body forms a 5 x 20 m sill hosted in psammitic country-rock (i.e. sample BD1413). The primary assemblage is

K-feldspar – quartz – plagioclase – tourmaline with minor amounts of sillimanite and muscovite. Compositional layering is defined by alternating K-feldspar – tourmaline – plagioclase and quartz – plagioclase layers. Grain-size varies notably amongst the major phases; quartz and plagioclase grains range from 0.1 to 2.0 mm in diameter with abundant small (<0.5 mm) grains, whereas, K-feldspar forms larger grains that range from 0.7 to 2.5 mm in diameter. The sample does not exhibit a foliation or lineation (figure 3.8a); however, tourmaline displays a moderate preferred orientation, with c-axes aligned parallel to the planes of compositional layering (figure 3.8b). Quartz exhibits a range of shapes from small (<0.5 mm) round grains with smooth grain boundaries (figure 3.8b) to larger (1.0–2.0 mm) ovoid grains with irregular and cuspate grain boundaries (figure 3.8c). Quartz also forms thin (100 μm) films along feldspar-feldspar grain boundaries, and thin polycrystalline appendages (figure 3.8c). The irregularly shaped quartz-feldspar grain boundaries are a textural feature that is ubiquitous amongst samples of nebulitic tourmaline leucogranite. The shape of individual quartz-feldspar grain boundaries varies from a cuspate or 'saw-tooth' appearance (figure 3.8c) to a 'string of pearl' texture with small (50–100 μm) beads of quartz, which form inclusions or embayments within the neighboring feldspar grains (figure 3.8d, e). There is a notable polarity to the cuspate structures, with the low dihedral angle formed at feldspar-quartz-quartz interfaces rather than quartz-feldspar-feldspar (i.e. the 'saw-teeth' point towards quartz). Figure 3.8f depicts an irregular quartz-plagioclase grain boundary with cuspate features and an array of fine-grained tourmaline. Plagioclase forms stubby tabular grains with well-developed crystal facets and straight plagioclase-plagioclase and plagioclase-K-feldspar grain boundaries (figure 3.8g). K-feldspar grains are subhedral, often containing abundant inclusions of small (<0.5 mm) plagioclase, quartz, and tourmaline grains (figure 3.8h). Most K-feldspar grains exhibit microcline twinning. The string perthite texture that is typical in the

muscovite-biotite-(sillimanite) leucogranite is seldom observed in the nebulitic tourmaline leucogranite. Intergrowths of fibrolitic sillimanite and muscovite form long (1–10 mm) anastomosing schlieren, which lie along quartz and feldspar grain boundaries (e.g. figure 3.8a). Tourmaline forms euhedral grains that range in size from 20 µm to > 1cm. They occur as linear arrays that follow the compositional layering, and as fine-grained inclusions within quartz and feldspar (e.g figure 8h).

Under CL, most quartz grains display a homogenous and featureless texture (e.g. figure 3.9a); however, as depicted in figure 3.9b, some quartz grains exhibit a faintly darker core domain. In grains where a CL darker core domain is observed, it is outlined by fine-grained inclusions of tourmaline (denoted by white arrows in figure 3.9b). The size of tourmaline inclusions generally increase outwards from the CL darker cores (e.g. figure 3.9b). In contrast with the featureless CL images of plagioclase from the muscovite-biotite-(sillimanite) leucogranite, plagioclase grains in the nebulitic tourmaline leucogranite exhibit a variety of internal CL textures. One common feature is CL bright equant 'core' domains, which are 200 to 300 µm in diameter (figure 3.9c). Figure 3.9d shows a plagioclase grain with a mosaic CL texture that highlights an aggregate of domains with varying brightness. Domain contacts are sharp, and the shape of individual domains varies from small (200–300 µm) equant domains to larger rectangular or elongate domains (e.g. figure 3.9c, d). The CL response for K-feldspar is variable and typically mirrors the microcline twinning pattern (e.g. figure 3.9c, d). Most K-feldspar grains do not exhibit any discernable internal CL domains; in grains that contain CL darker domains, the contacts are diffuse and obscured by the twinning pattern (e.g. Figure 3.9a).

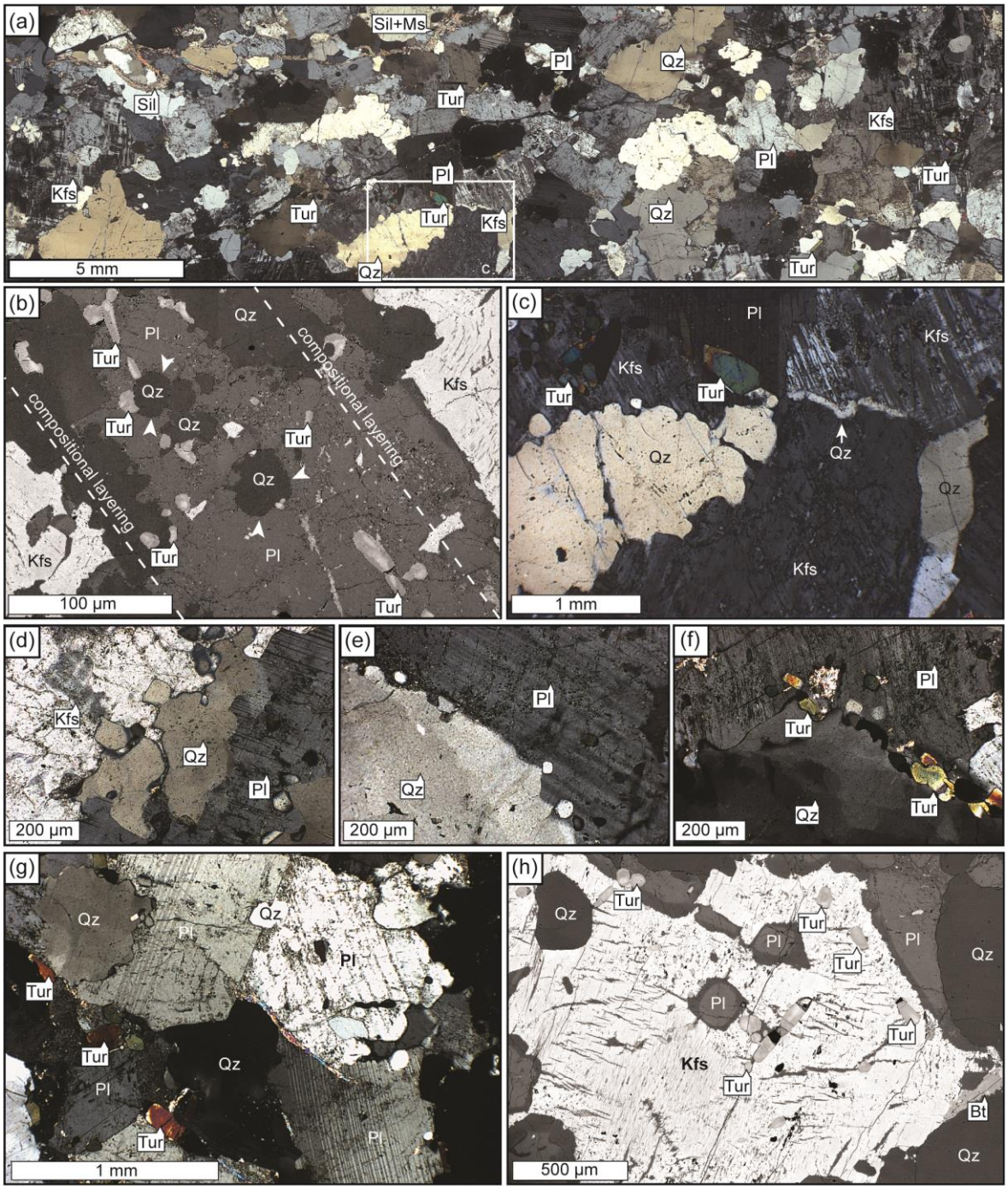


Figure 3.8 Microstructures in the nebulitic tourmaline leucogranite, sample BD1414. (a) Overview photomicrograph viewed under crossed polars, showing the shape, size, and distribution of mineral phases. Note the irregularity of grain boundaries. (b) Backscattered electron image, showing an array of fine-grained tourmaline inclusions within plagioclase. Tourmaline c-axes are orientated parallel with the compositional layering (outlined by dashed line). Inclusions of quartz in plagioclase are equant and typically display smooth grain boundaries (arrows). (c) Photomicrograph viewed under crossed polars, showing an ovoid-shaped quartz grain with highly irregular quartz-K-feldspar grain boundaries. This image shows a variety of grain boundary features including cuspate 'saw-tooth' structures and quartz micro-beads or 'string of pearl' texture. Note the thin quartz film (arrow) that separates two grains of K-feldspar (d) Photomicrograph viewed under crossed polars, showing highly irregular quartz-feldspar grain boundaries. The quartz-plagioclase boundary displays a 'saw-tooth' lobe-cuspate structure and the quartz-K-feldspar boundary exhibits an incomplete 'string of pearl' texture with small (50–100 µm) quartz embayments and inclusions. (e)

Photomicrograph viewed under crossed polars, showing a developed 'string of pearl' texture. (f) Photomicrograph viewed under crossed polars, showing a cuspate quartz-plagioclase grain boundary that is marked by an array of fine-grained tourmaline. (g) Photomicrograph viewed under crossed polars, showing straight plagioclase-plagioclase grain boundaries and irregular quartz-plagioclase boundaries. (h) Backscattered electron image, showing a K-feldspar grain with inclusions of small (200 μm) equant plagioclase and quartz, and fine-grained arrays of tourmaline.

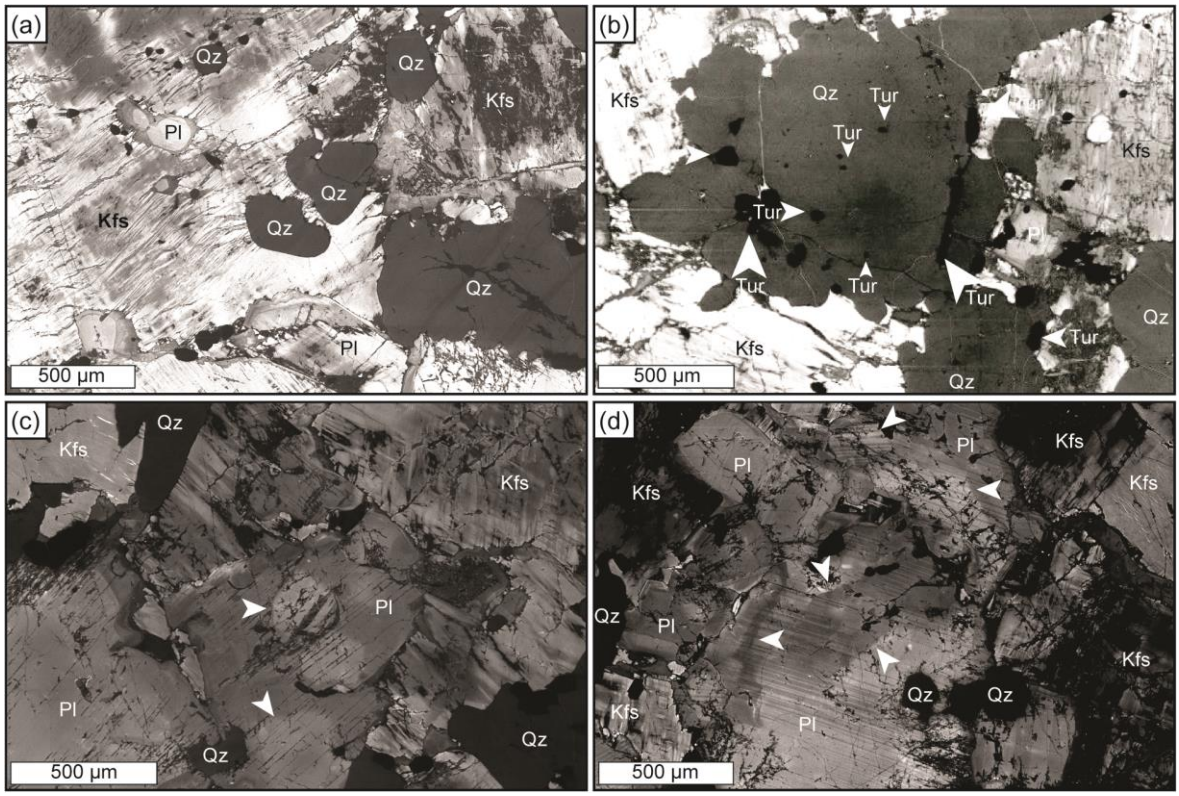


Figure 3.9 Cathodoluminesence textures in the nebulitic tourmaline leucogranite, sample BD1414. (a) Cathodoluminesence image, showing K-feldspar with a patchy texture that mirrors microcline twinning, and featureless quartz. (b) Cathodoluminesence image, showing a medium-sized (1 mm) quartz grain with a small (200 μm) faintly darker core. The size of tourmaline inclusions that surround the core increase outwards from the core domain. Note that tourmaline does not luminesce. (c) Cathodoluminesence image, showing a plagioclase grain (centre) with a mosaic texture comprised of small (200 μm) bright 'core' domains (arrows) surrounded by a darker rim. (d) Cathodoluminesence image, showing a plagioclase grain with mosaic texture. Note the sharp contacts between internal textural domains (arrows).

3.5.4 Contact between psammite and nebulitic tourmaline leucogranite: sample BD1415

Sample BD1415 was taken along the contact between the above described nebulitic tourmaline leucogranite (BD1414) and psammitic country-rock (BD1413). The contact is sharp and oriented parallel with both the transposed beds in the psammite and the

compositional layers in the nebulitic tourmaline leucogranite (figure 3.10a). The psammite is fine-grained and contains: quartz – plagioclase – biotite, with minor K-feldspar. The nebulitic tourmaline leucogranite is medium-grained is composed of K-feldspar – quartz – plagioclase – tourmaline, with minor biotite and apatite. Figure 3.10a shows a tourmaline- and K-feldspar-rich layer within the nebulitic tourmaline leucogranite that contains large (1–10 mm) tourmaline grains with their c-axes oriented parallel with the contact.

On the microscale, the contact is demarcated by a biotite-rich folium with intergrowths of biotite and tourmaline (figure 3.10a). The biotite-rich folia exhibits a patchy aggregate texture formed by the intergrowth of variably orientated rectangular grains. Figure 3.10b shows an intergrowth of tourmaline and ragged biotite formed along the contact. The central tourmaline grain displays a complex zoning pattern, which mimics the patchy grain aggregate texture of the surrounding biotite (figure 3.10b). Element mapping reveals that the zoning in tourmaline is primarily caused by variations in magnesium content (figure 3.10c). The surrounding patchy biotite grains show a similar variation in magnesium content, which runs along the [001] cleavage plane (figure 3.10c). Fine-grained rutile, K-feldspar, apatite, and quartz form inclusions within the tourmaline, and along the tourmaline-biotite grain boundaries. The inclusions are oriented parallel with the [001] biotite planes and the tourmaline zoning pattern (figure 3.10c). The tourmaline intergrowth texture indicates that the growth of tourmaline followed the growth of the biotite-rich folium that marks that sharp contact between the psammite and nebulitic tourmaline leucogranite.

There is a marked change in the appearance of mineral grain boundaries near the contact between the psammite and nebulitic tourmaline leucogranite. In the psammite, quartz-feldspar grain boundaries are smooth and regular at distances greater than 3 to 4 mm from the contact (figure 3.10d). Nearer to the contact (within 3–4 mm), the quartz-

feldspar grain boundaries are more irregular shaped; displaying cuspate ‘saw-tooth’ patterns and fine-grained embayments (figure 3.10e). On the other side of the contact, in the nebulitic tourmaline leucogranite, quartz-feldspar grain boundaries display the irregular ‘saw-tooth’ and ‘string of pearl’ texture that is characteristic of the unit (figure 3.10f).

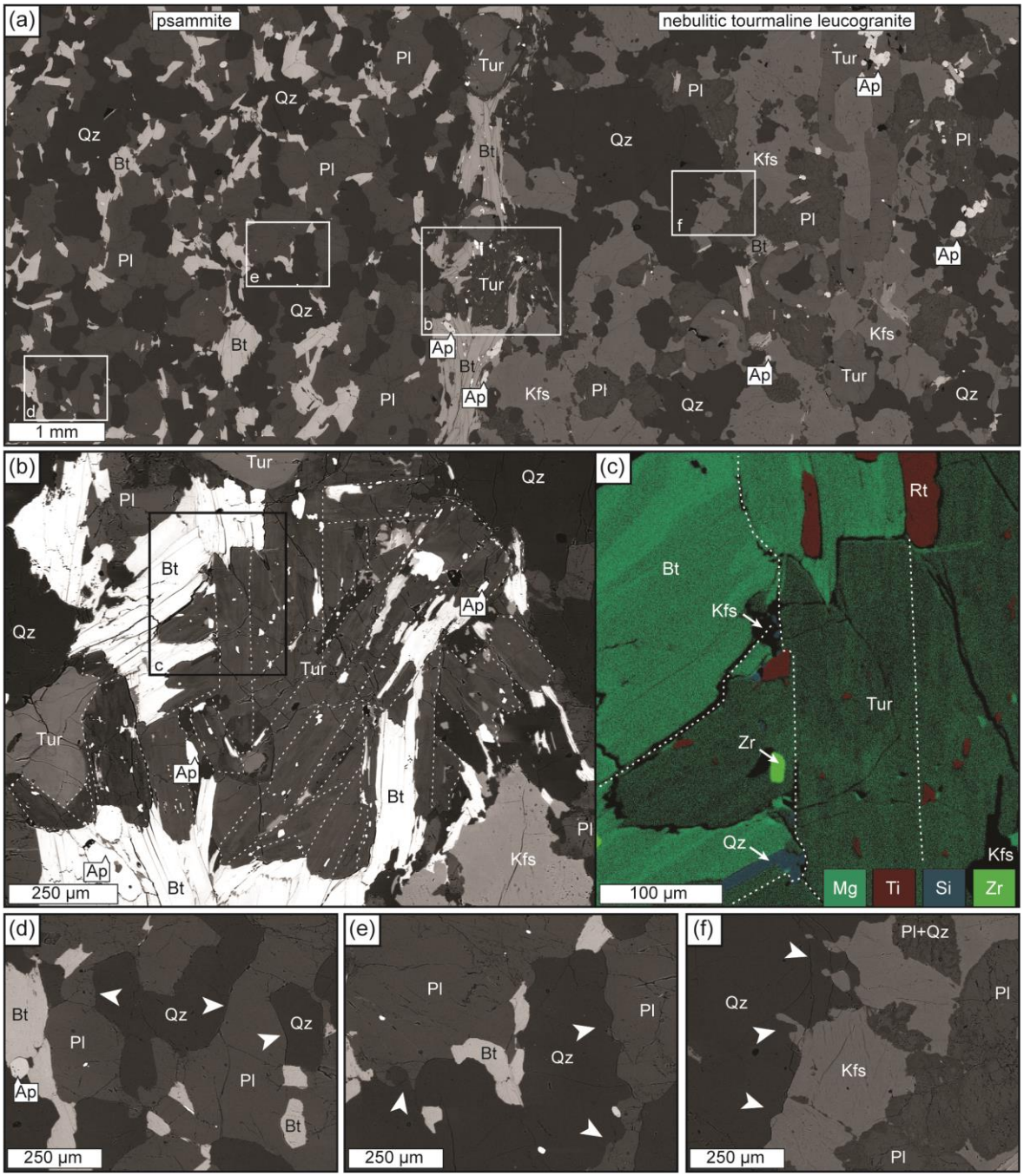


Figure 3.10 Microstructural features across the contact between psammite and nebulitic tourmaline leucogranite, sample BD1415. (a) Overview backscattered electron image of the contact, showing the distribution of phases and location of magnified frames. (b) Backscattered electron image, showing a reaction

texture between tourmaline and biotite. The biotite exhibits a patchy aggregate texture that appears ragged where it is in contact with tourmaline. Internal zoning in tourmaline (outlined by dashed line) displays a patchy texture that is continuous with the surrounding biotite. (c) EDS element map, showing magnesium zoning in tourmaline and biotite, and fine-grained inclusions of rutile, K-feldspar, quartz, and zircon, all aligned with the zoning orientation. (d) Backscattered electron image, showing the smooth quartz-plagioclase grain boundaries (arrows) that are common in the psammite. (e) Backscattered electron image taken near the contact, showing highly irregular quartz-plagioclase grain boundaries with lobate quartz embayments, and cuspate features that point inwards towards the quartz. (f) Backscattered electron image, showing the irregular quartz-K-feldspar grain boundary features that are characteristic of the nebulitic tourmaline leucogranite.

3.6 INTERPRETATION OF MICROSTRUCTURES

3.6.1 Psammitic country-rock

In contrast with the neighboring pelitic units (see Chapter 2), the psammite remains largely unaffected by the high-temperature metamorphism and partial melting that is prevalent in the Greater Himalayan Series. Despite a protracted history of metamorphism and deformation and a well-developed textural equilibrium, the psammite preserves microstructural evidence of its sedimentary origin. The uniform sizing of the rounded quartz grains, with smooth and convex quartz-feldspar grain boundaries indicates a well-sorted sedimentary protolith (e.g. figure 3.5a, b). Textural equilibrium is demonstrated by the smooth grain boundaries, the uniform grain-size of all major phases, and the abundant triple junctions that display dihedral angles near 120° (e.g. figure 3.5c). The absence of melting reaction textures and peritectic phases suggests the psammite was not affected by incongruent melting (i.e. muscovite dehydration melting). Moreover the lack of grain-scale melt pseudomorph features, such as cuspate boundaries, low dihedral angles, granophyric intergrowths, and ‘string of pearl’ texture (Holness, 2006, Holness & Sawyer, 2008), are taken to indicate the psammite had a notionally solid-state history.

Grain boundary migration is interpreted to have had a limited role in the textural development of the psammite because the primary sedimentary grain shapes are preserved (i.e. rounded quartz). The equal distribution of the constituent phases throughout the

psammite, and the ubiquitous fine-grained biotite may have constrained grain boundary growth in the way that *Zener pinning* restricts coarsening in multi-phase aggregates (Hillert, 1988). This notion is further supported by the observation of 'bulls-eye' CL textures in quartz and plagioclase, where grain boundaries are interpreted to have swept back and forth between grains on a scale less than 100 μm (e.g. figure 3.5e), clearing the rims of CL-inhibiting dislocations (Pearce & Wheeler, 2010). Upon cooling, the inversion from orthoclase to microcline reorders the K-feldspar crystal lattice (Eggleton & Buseck, 1980), overprinting any prior core-rim pattern that may have contained information about high-temperature grain boundary processes.

3.6.2 Muscovite-biotite-(sillimanite) leucogranite

The microstructures observed in the muscovite-biotite-(sillimanite) leucogranite sample BD1213 are taken as a representative or 'control' of the standard crystallisation features of an anatectic melt under orogenic metamorphic conditions. Both the faceted euhedral grain shape and oscillatory zoning of the feldspars suggest that initial nucleation and growth occurred in the presence of silicate melt (Cox, 2013). The range in grain microstructure from euhedral feldspars to anhedral net-veined intergrowths of muscovite, K-feldspar, and quartz is interpreted to represent a system that evolved through three stages of crystallisation: 1) suspension and isolated crystal growth, 2) the formation of an interconnecting crystal framework, 3) crystallisation in interstitial and pore space (Bryon *et al.*, 1994, Bryon *et al.*, 1995). A change in melt chemistry, throughout the successive stages of crystallisation, towards a more volatile-rich composition is evidenced by the net-veined and spongy muscovite intergrowths that occupy voids and junctions between euhedral quartz and feldspar grains (e.g. figure 3.6e, f). Schlieren of fibrolitic sillimanite, which are commonly intergrown with muscovite (e.g. figure 3.6g), are interpreted as being

restitic (i.e. xenocryst), since sillimanite is not expected as a primary igneous phase nor is there textural evidence for a sillimanite-producing reaction. The presence of sillimanite xenocrysts link the leucogranite melt to a pelitic source that underwent muscovite dehydration melting, and the production of peritectic sillimanite (see Chapter 2).

A uniform range in grain-size may indicate that crystal nucleation and growth occurred continuously throughout the crystallisation of the leucogranite (Zieg & Marsh, 2002), while the tendency for K-feldspar to form the largest grains may indicate a lower nucleation potential (Cashman, 1990). Limited K-feldspar nucleation is suggested by: the oikocrystic K-feldspar texture, with plagioclase, quartz, and biotite inclusions; the absence of K-feldspar inclusions in quartz and plagioclase; and the observation that K-feldspar forms consistently larger grains.

The different grain boundary textures observed in sample BD1213, ranging from smooth and straight quartz-feldspar boundaries to boundaries with cuspate or net-veined features, are interpreted to represent the evolution of melt connectivity along the network of grain boundaries, and the effect that interstitial melt has on grain boundary modification (Holness *et al.*, 2011). Cuspate features and grain appendages are interpreted to form during late-stage melt crystallisation in interstitial pores (Holness & Sawyer, 2008), while smooth and straight grain boundaries are thought to have formed while melt was still mobile and grain boundary migration was rapid.

3.6.3 Nebulitic tourmaline leucogranite

On the microscale, the nebulitic tourmaline leucogranite shares many similarities with the muscovite-biotite-(sillimanite) leucogranite, with the exception of the characteristic compositional layering. The medium-grained quartz and feldspar crystals are generally euhedral and well-formed, indicating that grain boundary mobility was not limited during

growth of the main mineral phases. Some of the features present in the nebulitic tourmaline leucogranite are distinctly igneous, for example, the presence of sillimanite xenocrysts, and the abundant pseudomorphed melt pores (i.e. monomineralic films, cuspate and 'string of pearl' grain boundaries, and granophyric intergrowths; Holness & Sawyer, 2008). In contrast, the presence of compositional layering that is continuous with the transposed bedding of the host psammite indicates the nebulitic tourmaline leucogranite contains inherited metasedimentary features.

The primary textural differences between the nebulitic tourmaline leucogranite and the muscovite-biotite-(sillimanite) leucogranite are in the form and appearance of grain boundaries and the internal plagioclase and quartz microstructures. The ubiquity of cuspate and irregular grain boundary textures suggests that the process responsible for forming these microstructures operated pervasively along the grain boundary network. The polarity of 'saw-tooth' features (i.e. 'saw-teeth' point towards quartz; figure 3.8c-f) suggests that the grain boundary process is phase-dependent (i.e. the direction of boundary mobility is governed by the neighboring minerals). The observation that fine-grained tourmaline forms inclusions both within the medium-grained feldspars (e.g. figure 3.8b, h), as well as along grain boundaries (e.g. figure 3.8f) is interpreted to suggest that tourmaline grew throughout the development of the final microtexture. Moreover, the outwards coarsening of tourmaline inclusions from the CL dark quartz core domains (e.g. figure 3.9b) may indicate that tourmaline nucleation and growth was coeval with grain boundary migration and coarsening of quartz from 200 μm to 1 mm. The observation of small (200–300 μm) CL bright core domains in plagioclase as well as the mosaic CL texture are interpreted to suggest that the millimetre-sized plagioclase grains grew by the amalgamation of multiple smaller grains. The size and rounded or equant shape of the CL bright core domains suggests that the protolith plagioclase texture would have been a fine-grained mineral

aggregate without a strong preferred shape orientation. Elsewhere in the sample, plagioclase and quartz form equant fine-grained (< 500 μm) features, often as inclusions in larger feldspars (e.g. figure 3.8b, h). K-feldspar is oikocrystic with abundant plagioclase, quartz, and tourmaline inclusions, indicating that when K-feldspar grew there was already a matrix of fine-grained quartz, plagioclase, and tourmaline.

3.6.4 Contact features

The contact between the nebulitic tourmaline leucogranite and the psammite contains the most information about the origin of the compositional layering in the nebulitic tourmaline leucogranite. Tourmaline overgrowth features along the penetrative folium of patchy biotite that demarcates the contact illustrate how tourmaline grows by replacing biotite. For the patchy biotite texture to be preserved in the internal tourmaline compositional zoning (magnesium content), tourmaline must overgrow a layer of patchy biotite by an interface reaction; a reaction process that involved a diffusion step would not preserve the compositional zoning of the parent biotite grains. If this is an interface-controlled process, it is possible that tourmaline nucleation preference is ordered by the structural anisotropy of the biotite crystal lattice, which may ultimately result in the c-axes of tourmaline grains aligned parallel with the primary biotite foliation. This texture is similar to previously reported cases of tourmaline c-axis growth aligned with biotite [001] cleavage planes, which occur in the metasomatic zones of metasedimentary wall-rock along the margins of S-type granites (Wolf & London, 1997, London, 1999). London and Manning (1995) observed that tourmaline-rich, metasomatised wall-rock often preserve the compositional layering of the protolith, and concluded that the metasomatic reaction was driven by a boron-rich fluid released during late-stage granite crystallisation.

As a local reaction, the replacement of biotite with tourmaline produces excess Ti and K. If the chemical mobility of Ti is limited in high-temperature metamorphic conditions, as previous studies suggest (e.g. Carmichael, 1969), then the growth of a Ti bearing phase near the biotite-tourmaline reaction domain would be expected. This may explain the occurrence of fine-grained rutile intergrown with tourmaline (e.g. figure 3.10c). The fine-grained inclusions of K-feldspar observed in the tourmaline reaction texture would not consume enough K for this reaction to be isochemical on the local domain-scale; however, growth of K-feldspar elsewhere within the nebulitic tourmaline leucogranite may balance the reaction. The compositional layering between K-feldspar – tourmaline – plagioclase and quartz – plagioclase layers could form as a result of tourmaline and K-feldspar replacing biotite in a rock that has primary biotite layering, such as the psammitic country-rock. This reaction would not only produce a compositionally layered rock, but one with preferred alignment of tourmaline grains that have c-axes oriented parallel to compositional layering (i.e. transposed bedding in the protolith).

Differences in the quartz-plagioclase grain boundary texture of the host psammite, which vary with proximity to the contact, are interpreted to indicate that processes involved in formation of the nebulitic tourmaline leucogranite also affected the grain boundary network of the host psammite. The modification of straight and smooth quartz-plagioclase grain boundaries to form the irregular cuspate textures affected all grains within a zone that is 2 to 3 mm from the contact (e.g. figure 10d, e), indicating that it was a pervasive grain boundary process. The formation and preservation of the irregular grain boundary features indicates that the mobility of grain boundaries varied throughout the metamorphic history of the rock. Moreover, the preservation of irregular textures and limited subsequent textural modification suggest that there may have been a period of more

rapid grain boundary mobility followed by a reduction of grain boundary mobility during exhumation and cooling.

3.7 MICROSTRUCTURAL ANALYSIS

A two dimensional analysis of the shape and size of individual mineral grains and their internal microstructures was completed with the aim of quantifying the observed textures and to constrain the mechanisms of textural modification. Three samples were analysed, representing the principal lithologies: psammitic country-rock (sample BD1413), muscovite-biotite-(sillimanite) leucogranite (sample BD1213), nebulitic tourmaline leucogranite (sample BD1414). Individual quartz, plagioclase, and K-feldspar grains as well as internal microstructural domains (i.e. CL bright cores) were traced out on whole thin section CL and BSE maps, then digitised and processed with JMicroVision version 1.2.7. (Roduit, 2008). An equal area (34 x 19 mm) of thin section was analysed for both the muscovite-biotite-(sillimanite) leucogranite and the nebulitic tourmaline leucogranite, however, due to the fine-grained nature of the psammite, a smaller area was analysed (5.3 x 3.8 mm) and the results were normalised to the area of the leucogranite samples for plotting (figure 3.11).

3.7.1 Grain-size analysis

Figure 3.11 presents the results of the grain-size analyses of quartz, plagioclase, and K-feldspar in all three samples. The results are depicted as a frequency distribution histogram with a linear scale (square root of grain area) that ranges from 0.0 to 3.0 mm, using 0.05 mm bins.

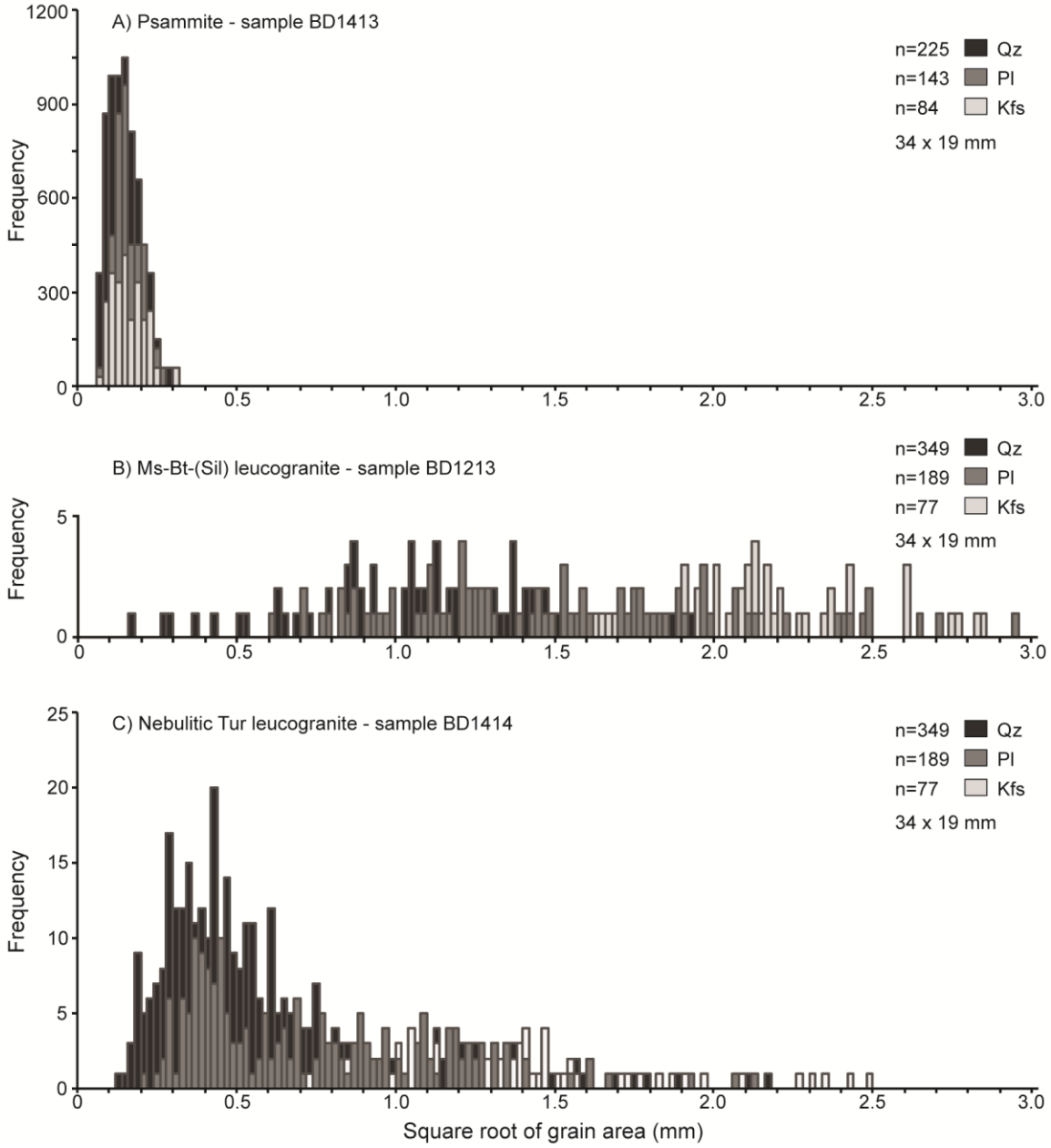


Figure 3.11 Histogram showing the distribution frequency of quartz, plagioclase, and K-feldspar grain-size in the psammite (a), muscovite-biotite leucogranite (b), and nebulitic tourmaline leucogranite (c). Grain-size (square root of grain area) is presented on a linear scale with a constant range from 0.0 to 3.0 mm, and 0.05 mm bins. The number of grains (n) and the area analysed are listed in the legend.

Psammite

The psammite displays a unimodal population of grain-size analyses for all phases, which range from 0.07 to 0.32 mm (figure 3.11a). The arithmetic mean of the psammite grain-size analyses is 0.14 mm.

Muscovite-biotite-(sillimanite) leucogranite

Analyses of the quartzofeldspathic grains in the muscovite-biotite (sillimanite)-leucogranite display a broad range in grain-size, from 0.15 to 2.95 mm (figure 3.11b). The distribution of grain-size varies amongst the quartzofeldspathic phases; K-feldspar forms larger grains (1.7–2.8 mm), quartz generally forms smaller grains (0.15–1.95 mm), whereas, plagioclase grain-size ranges between 0.6 and 2.95 mm.

Nebulitic tourmaline leucogranite

The distribution of nebulitic tourmaline leucogranite grain-size analyses varies markedly between K-feldspar, and quartz and plagioclase (figure 3.11c). Both quartz and plagioclase display a bimodal distribution of grain-sizes, with a large population of fine-grained analyses (<0.5 mm) and a skewed pattern of analyses up to 2.2 mm, whereas the size of K-feldspar grains is normally distributed between 0.7 and 2.5 mm.

Interpretation

The distribution of grain-sizes in the psammite and muscovite-biotite-(sillimanite) leucogranite are interpreted as representative grain-size populations for a 'control' metasedimentary and igneous protolith. The bimodal grain-size distribution in the nebulitic tourmaline leucogranite shows that there is a large population of small (<0.5 mm) grains, with a similar size to that in the psammite, and a frequency distribution that trends towards that of the medium-grained muscovite-biotite-(sillimanite) leucogranite. The skewed distribution of quartz and plagioclase grain-size follows a natural logarithmic growth trend, which is interpreted as a record of grain-size coarsening in the nebulitic tourmaline leucogranite (Higgins, 2000). Moreover, these results suggest that there may be remnant

fine-grained sedimentary microstructures preserved in the nebulitic tourmaline leucogranite.

3.7.2 Grain shape

The shape of individual quartz, plagioclase, and K-feldspar grains were analysed to explore the mechanisms of grain growth during coarsening of the nebulitic tourmaline leucogranite. The two variables calculated are a measure of grain-size, *Equivalent Circular Diameter*: the diameter of a circle with the same area of the grain (equation 3.1); and grain shape, *Compactness*: a ratio of the grain area to the area of a circle with the same perimeter (equation 3.2).

$$EquivalentCircularDiameter = \sqrt{\frac{4 * Area}{\pi}} \tag{3.1}$$

$$Compactness = \frac{4\pi * Area}{(Perimeter)^2} \tag{3.2}$$

The results of bivariate linear regression models run for the quartzofeldspathic phases in each sample are presented in table 3.2, corresponding to the bivariate plots in figure 3.12. There is only a weak correlation between the grain *Compactness* and *Equivalent Circular Diameter* of grains in either the psammite (sample BD1413) or the muscovite-biotite-(sillimanite) leucogranite, suggesting that either grain-size coarsening has not occurred or grains have coarsened symmetrically, with grain boundaries advancing equally in all directions. In the nebulitic tourmaline leucogranite however, both quartz and plagioclase display a strong correlation between grain *Compactness* and *Equivalent Circular*

Diameter, with a Multiple R and R^2 value of 0.79 and 0.62, and 0.74 and 0.55, respectively. Grains with larger *Equivalent Circular Diameters* are less compact than the smaller grains (figure 3.12c). If the larger grains are formed by coarsening, as the grain-size analyses indicates, then this correlation implies that the growth of quartz and plagioclase was asymmetric, with grain boundaries advancing further in some directions rather than equally in all directions. K-feldspar conversely, only displays a weak correlation between grain *Compactness* and *Equivalent Circular Diameter*, suggesting that the process involved in the coarsening of quartz and plagioclase did not affect K-feldspar. These observations support the idea that grain coarsening in the nebulitic tourmaline leucogranite was an interface controlled process (c.f. grain boundary sweeping; Pearce & Wheeler, 2010) rather than a diffusion controlled process like *Ostwald ripening* (Voorhees, 1985).

	Psammite (BD1413)			Ms-Bt-(Sil) leuco. (BD1213)			Nebulitic Tur leuco. (BD1414)		
	Qz	Pl	Kfs	Qz	Pl	Kfs	Qz	Pl	Kfs
Multiple R	0.174	0.043	0.283	0.301	0.419	0.514	**0.787**	**0.738**	0.257
R Square	0.030	0.002	0.080	0.091	0.175	0.264	**0.620**	**0.545**	0.066
Adjusted R Square	0.026	-0.005	0.069	0.080	0.162	0.255	0.619	0.543	0.054
Standard Error	0.089	0.117	0.121	0.128	0.078	0.096	0.104	0.106	0.145
Observations (n)	225	143	84	87	63	83	349	189	77
Intercept	0.904	0.767	0.801	0.834	0.968	0.938	1.072	1.031	0.759
Std. error	0.017	0.033	0.039	0.038	0.035	0.032	0.010	0.016	0.049
P-value	0.000	0.000	0.000	0.000	0.000	0.000	0.000	0.000	0.000
X variable	-0.285	-0.105	-0.616	-0.081	-0.094	-0.094	-0.317	-0.267	-0.074
Std. error	0.108	0.208	0.231	0.028	0.026	0.018	0.013	0.018	0.032
P-value	0.009	0.613	0.009	0.005	0.001	0.000	0.000	0.000	0.024

*Bolded values indicate models with strong correlation (R>0.7)

Table 3.2 Bivariate Linear Regression Statistics - Compactness vs Equivalent Circular Diameter.

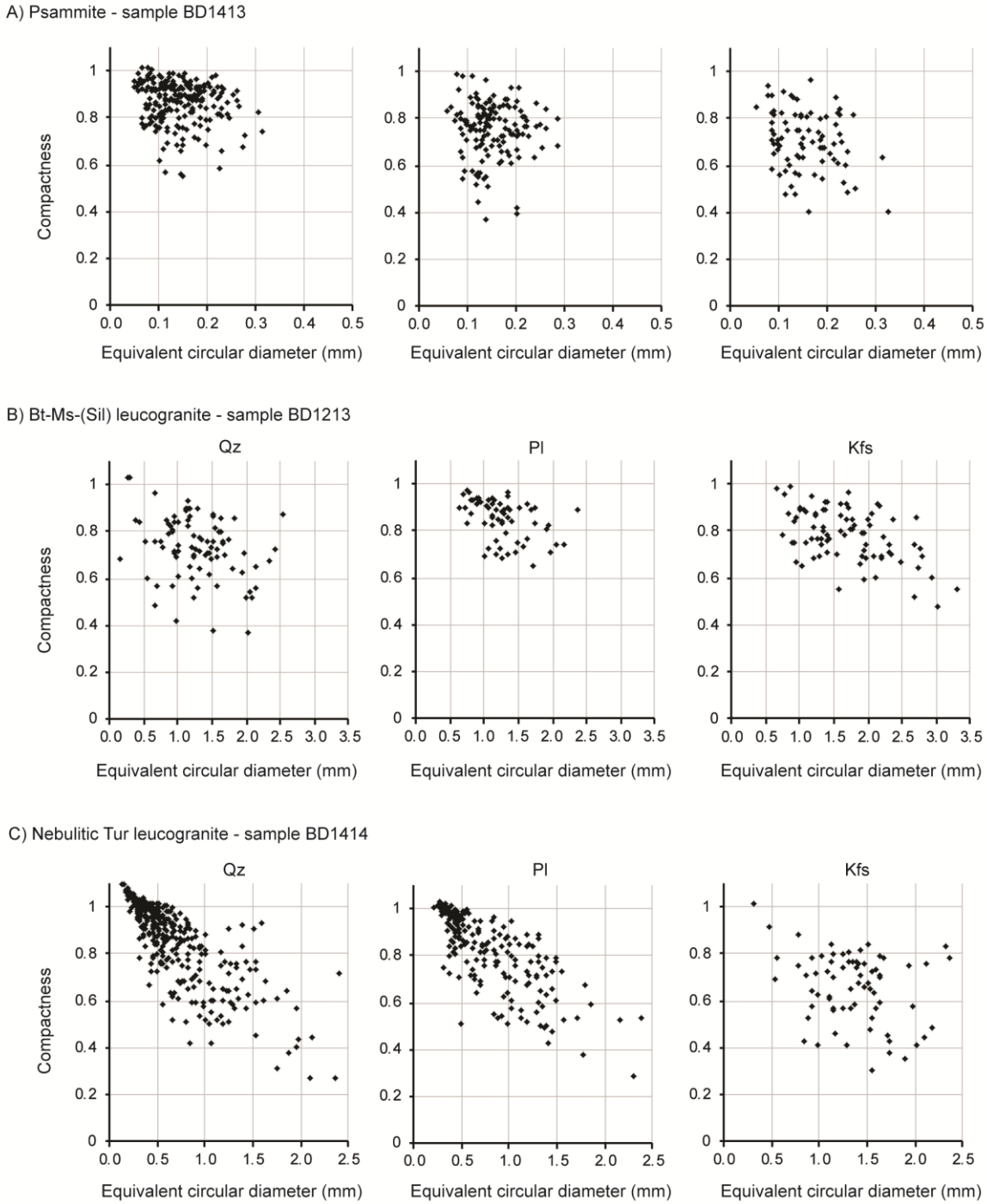


Figure 3.12 Bivariate scatter plots showing grain compactness versus equivalent circular diameter for analysed grains of quartz, plagioclase, and K-feldspar in the psammite (a), muscovite-biotite leucogranite (b), and nebulitic tourmaline leucogranite (c). Note the covariance in quartz and plagioclase grains from the nebulitic tourmaline leucogranite, corresponding to the regression statistics presented in table 3.2.

3.7.3 EBSD analysis

EBSD was used to measure the variations in intracrystalline lattice orientation within a medium sized (1 mm diameter) plagioclase grain from the nebulitic tourmaline leucogranite (sample BD141). The grain chosen for analyses exhibits the characteristic mosaic CL texture, with a well-defined small (200 μm) CL bright core that is surrounded by a rim with variable luminescence (figure 3.13a). As shown in the local misorientation map (figure 3.13b), the lattice of the core exhibits greater local misorientation than the rim. It is important to note that while the measured difference in angular distortion across the core and rim (~1.5°) is near the angular resolution of the technique (0.1–0.5°); there is a consistent pattern of greater misorientation in the core. Furthermore, the orientations of the misorientation axes are different for the core and rim domains (figure 3.13c). The spread of misorientation axes in the misorientation pole figures is likely to result from poor precision of the misorientation axes associated with small misorientation angles (Prior, 1999), rather than a true spread. However, the large number of repeat measurements increases confidence in the results.

Greater lattice misorientation in the core than in the rim indicates that the core and rim domains not only preserve unique records of intracrystalline deformation, but the core domain may have experienced a longer history of deformation (and greater accumulative deformation) than the rim. If the CL bright core is representative of the fine-grained population of microstructural features observed in the nebulitic tourmaline leucogranite, these results imply that the fine-grained features are remnant protolith grains with crystal lattices that remained unmodified by the coarsening process.

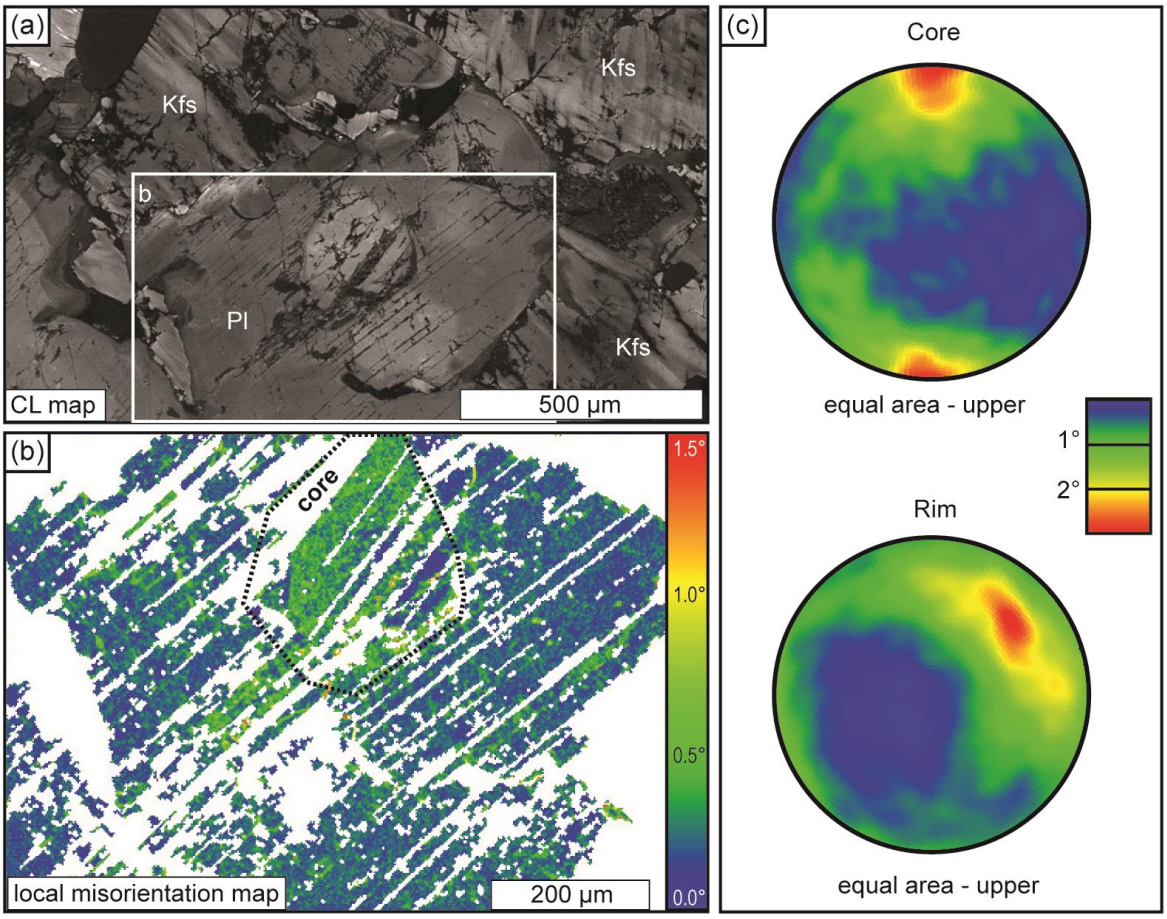


Figure 3.13 EBSD analyses of mosaic plagioclase in the nebulitic tourmaline leucogranite. (a) Cathodoluminesence image of the analysed area (white line), showing a bright core domain surrounded by a rim with mosaic texture. (b) Local misorientation map, showing variations in the angular distortion of the plagioclase lattice. Data were collected over a 453 x 311 pixel grid with a pixel size of 2 µm. (c) Equal area upper-hemisphere pole figures, showing the rotation axes in crystal coordinates for the analyses in the core and rim domains.

3.8 NATURE OF THE TRANSFORMING AGENT

The nebulitic tourmaline leucogranite is an enigmatic lithology that upon close inspection reveals both igneous and metasedimentary features. Closely associated with intrusive leucogranite sills and dykes of a demonstrably anatectic origin, the formation of nebulitic tourmaline leucogranite in the Himalaya is a consequence of the high-temperature metamorphism and partial melting that affected the Greater Himalayan Series. Preservation of metasedimentary compositional layering in a uniformly medium-grained nebulitic tourmaline leucogranite indicates that while the process was pervasive, it did not

completely reorder the solid mineral framework of the affected mass. The microstructural evidence and grain analyses indicate that the nebulitic tourmaline leucogranite is a product of *in-situ* alteration and textural modification of compositionally layered psammite. The transformation of psammite to nebulitic tourmaline leucogranite and growth of the volatile-bearing minerals tourmaline and apatite is inferred to be an open-system process that requires an external source of B and P. The localised occurrence of nebulitic tourmaline leucogranite in psammite fold hinges (e.g. figure 3.4c) and along the contact of muscovite-biotite-leucogranite sills (e.g. figure 3.4a, b) point to a transformation that involves a mobile fluid/melt agent.

The actual nature and composition of the transforming agent is difficult to constrain, and it may have evolved throughout the reaction and crystallisation process. However, based on (1) the close association of the nebulitic tourmaline leucogranite with anatectic melt (i.e. muscovite-biotite leucogranite), and (2) documentation that the tourmaline-forming reaction influenced the mobility of mineral grain boundaries, the initial reaction agent is expected to be a silicate melt rather than an aqueous solution. Studies by London and Manning (1995), London (1999) and others, demonstrate the importance of late-stage melt fractionation in the production of a volatile-rich melt that has the potential to drive tourmaline-producing reactions. Separation of a volatile-rich melt phase during melt fractionation is analogous to the formation of pegmatitic melt during granite crystallisation.

Experimental studies on the stability of fluid components in granite-pegmatite systems have broadened the understanding of melt-fluid evolution, showing a complete miscibility between water and silicate melt at temperatures above 712–735°C, over a pressure range of 0.1–2.0 GPa (Bureau & Keppler, 1999, Thomas *et al.*, 2000). Above this critical point, a melt that is rich in B, P, and F may dissolve unlimited water (Thomas *et*

al., 2000). When the melt cools below the critical point it separates into two silicate melts, one of which is volatile-rich (not exceeding 45 wt% H_2O) and can dissolve large amounts of Si and Al, and a second volatile-poor melt (Thomas *et al.*, 2003). The composite leucogranite sills presented in this study (e.g. figure 3d; figure 4a, b) may be direct evidence of two-phase melt immiscibility. Upon cooling and crystallisation of muscovite-biotite leucogranite, a volatile-rich melt may have separated from the parent anatectic melt. This volatile-rich phase would have a considerably lower density and viscosity to its parent melt, resulting in high ionic diffusivity and melt mobility (Thomas *et al.*, 2000). These characteristics, together with an anomalously low liquidus temperature ($\geq$ 340°C at 0.3 GPa; Sirbescu & Nabelek, 2003), allow the volatile-rich melt to readily migrate along mineral grain boundaries (Thomas *et al.*, 2003). Infiltration of a reactive volatile-rich melt would significantly modify the psammite texture by increasing grain boundary mobility among the solid phases, which enables grain growth and ultimately, the amalgamation of fine-grained aggregates. Evidence of the fine-grained protolith texture is preserved in domains where primary grains of quartz and plagioclase are enveloped by coarser grains. The preservation of relict fine-grained microstructures with evidence for greater lattice distortion could have happened early in the textural modification process, when grain boundary migration and coarsening could overgrow and encapsulate protolith grains.

3.9 SYNTHESIS OF REACTION PROCESS

In the following section, sample BD1415 (the contact between psammite and nebulitic tourmaline leucogranite) is viewed as a ‘frozen’ reaction-front and the changes in mineral assemblage and texture on either side of the reaction boundary are considered in terms of elementary processes operating on the domain-scale. The reactions discussed below are notionally balanced using idealized mineral end-member compositions. The choice of

elementary reactions is based on interpretation of the following three textures. (1) Tourmaline replaces biotite, and this process preserves the original Fe–Mg zoning present in the parent biotite (e.g. figure 3.10b, c). (2) Quartz grows at the expense of plagioclase, resulting in irregular quartz-plagioclase grain boundaries (e.g. figure 3.10e). (3) K-feldspar, rutile, and apatite form intergrowths with tourmaline (e.g. figure 3.10b), and are generally found in the nebulitic tourmaline leucogranite and not in the psammite (e.g. figure 3.10a).

Starting with the assumption that this reaction is between solid mineral phases and externally sourced H_2O and B (B_2O_3), a reaction can be balanced that consumes biotite and produces tourmaline and K-feldspar. Expressed as a balanced chemical equation in the Na_2O–FeO–K_2O–Al_2O_3–SiO_2–H_2O–B_2O_3 (NFKASHB) model system, the notional reaction consumes biotite, plagioclase, quartz, and sillimanite, while producing tourmaline and K-feldspar (reaction 3.1).

3.1
$$\underset{\mathrm{KFe3AlSi3O10(OH)}}{\text{annite}} + \underset{\mathrm{NaAlSi3O8}}{\text{albite}} + 2.5\,\underset{\mathrm{Al2SiO5}}{\text{sillimanite}} + 0.5\,\underset{\mathrm{SiO2}}{\text{quartz}} + 1.5\,\underset{\mathrm{B2O3(aq)}}{\text{boride}} + 1.5\,\underset{\mathrm{H2O}}{\text{water}} = \underset{\mathrm{NaFe3Al6(BO3)3Si6O18(OH)4}}{\text{schorl}} + \underset{\mathrm{KAlSi3O8}}{\text{Kfeldspar}}$$

It is important to note that there is no sillimanite in the psammitic portion of sample BD1415. Accordingly, the reaction responsible for producing the observed textures requires an alternative source of Al. If we isolate the reaction texture in figure 10b, where tourmaline replaces a biotite folium, and treat it as a local domain (i.e. biotite-tourmaline domain), then an elementary reaction can be balanced that consumes biotite and plagioclase while producing tourmaline and K-feldspar (reaction 3.2). As written, reaction 3.2 requires a source of aqueous Al that is external to the biotite-tourmaline domain. If we consider a second local domain where plagioclase is replaced by quartz, and cations are

allowed to enter or leave the domain, there is a potential source of the required aqueous Al (reaction 3.3). This elementary reaction can be balanced to conserve volume if n is equal to ~1.4. The reaction textures produced in this second domain (i.e. quartz-plagioclase domain) would reflect the replacement of plagioclase by quartz, and the mobility of quartz-plagioclase grain boundaries (e.g. figure 3.10e). Observations of irregular quartz-plagioclase grain boundaries in the portion of the psammite that is nearest to tourmaline-biotite reaction texture (e.g. figure 3.10a), support the notion of a coupled reaction between two domains.

3.2 $$\underset{KFe3AlSi3O10(OH)}{\text{annite}} + \underset{NaAlSi3O8}{\text{albite}} + 5\,\underset{Al(OH)3(aq)}{\text{aluminic acid}} + 3\,\underset{H3BO3(aq)}{\text{boric acid}} + 3\,\underset{SiO2}{\text{quartz}} = \underset{NaFe3Al6(BO3)3Si6O18(OH)4}{\text{schorl}} + \underset{KAlSi3O8}{\text{Kfeldspar}} + 10.5\,\underset{H2O}{\text{water}}$$

3.3 $$\underset{NaAlSi3O8}{\text{albite}} + n\,\underset{SiO2(aq)}{\text{quartz}} + \underset{H2O}{\text{water}} + H^{+} = (3+n)\underset{SiO2}{\text{quartz}} + \underset{Al(OH)3(aq)}{\text{aluminic acid}} + Na^{+}$$

If reaction 3.2 and 3.3, were both in progress simultaneously, and cations were mobile between the two domains, the net reaction would consume biotite and plagioclase while producing tourmaline, K-feldspar, and quartz (reaction 3.4). Alternatively, a combined reaction might be favoured that conserves Al between the two domains so that a greater volume of plagioclase is consumed and more quartz is produced (reaction 3.5). This balanced combined reaction (3.5) resembles a base-leaching process (Vernon, 1979) where a reactive fluid phase delivers B in the form of the neutral B_2O_3 or as boric acid (i.e. $B(OH)_3$), and removes alkali ions.

3.4 $$\underset{KFe3AlSi3O10(OH)}{\text{annite}} + \underset{NaAlSi3O8}{\text{albite}} + 5\,\underset{Al(OH)3(aq)}{\text{aluminic acid}} + 3\,\underset{H3BO3(aq)}{\text{boric acid}} + 3\,\underset{SiO2(aq)}{\text{quartz}} = \underset{NaFe3Al6(BO3)3Si6O18(OH)4}{\text{schorl}} + \underset{KAlSi3O8}{\text{Kfeldspar}} + 10.5\,\underset{H2O}{\text{water}}$$

3.5 $$\underset{KFe3AlSi3O10(OH)}{\text{annite}} + 6\,\underset{NaAlSi3O8}{\text{albite}} + 3\,\underset{H3BO3(aq)}{\text{boric acid}} + 5\,H^{+} = \underset{NaFe3Al6(BO3)3Si6O18(OH)4}{\text{schorl}} + \underset{KAlSi3O8}{\text{Kfeldspar}} + 12\,\underset{SiO2}{\text{quartz}} + 5\,Na^{+} + 5.5\,\underset{H2O}{\text{water}}$$

It is important to note that the tourmaline growing reaction (3.2) occurs along the biotite-tourmaline interface, and that Fe–Mg zoning is preserved. This implies that both Fe and Mg are locally conserved and that reaction 3.2 can be extended to the Na_2O–K_2O–FeO–MgO–Al_2O_3–SiO_2–H_2O–B_2O_3 (NKFMASHB) model system. Solid solution in plagioclase can be accounted for by further extending the model system to include Ca (CaO) and P (P_2O_5), and balancing a third elementary reaction that consumes anorthite to produce hydroxylapatite and quartz (reaction 3.6).

3.6 $$\underset{CaAl2Si2O8}{\text{anorthite}} + 0.6\,\underset{H3PO4(aq)}{\text{phosphoric acid}} + 2.2\,\underset{H2O}{\text{water}} = 0.2\,\underset{Ca5(PO4)3(OH)}{\text{hydoxylapatite}} + 2\,\underset{Al(OH)3(aq)}{\text{aluminic acid}} + 2\,\underset{SiO2}{\text{quartz}}$$

The sum of all three elementary reactions (3.2, 3.3, and 3.6) in the Na_2O–CaO–K_2O–FeO–MgO–Al_2O_3–SiO_2–H_2O–B_2O_3–P_2O_5 (NCKFMASHBP) model system describes a combined reaction that consumes biotite, and plagioclase to produce tourmaline, K-feldspar, apatite, and quartz (reaction 3.7). In this combined reaction, both Fe and Mg are locally conserved in the biotite-tourmaline domain, while Al is balanced between the two domains.

3.7 $$\underset{K(Fe,\,Mg)3AlSi3O10(OH)}{\text{biotite}} + 4\,\underset{NaAlSi3O8}{\text{albite}} + \underset{CaAl2Si2O8}{\text{anorthite}} + 0.6\,\underset{H3PO4(aq)}{\text{phosphoric acid}} + 3\,\underset{H3BO3(aq)}{\text{boric acid}} + 3\,H^{+}$$

$$= \underset{Na(Fe,\,Mg)3Al6(BO3)3Si6O18(OH)4}{\text{tourmaline}} + \underset{KAlSi3O8}{\text{Kfeldspar}} + 0.2\,\underset{Ca5(PO4)3(OH)}{\text{hydoxylapatite}} + 8\,\underset{SiO2}{\text{quartz}}$$

$$+ 5.3\,\underset{H2O}{\text{water}} + 3\,Na^{+}$$

Phase	Bt	Pl	Sil	Qz	Tur	Kfs	Ap	Melt		
*Molar vol (cm^3/mol)	152.6	101.4	50.3	23.4	‡318.8	108.2	§159.3	[a]156.1	reactants	products
reaction 3.1	*Bt + Pl + 2.5 Sil + 0.5 Qz = Tur + Kfs*									
%	19.0	12.6	15.6	1.5	37.9	13.5	-	-	48.7	51.3
reaction 3.2	*Bt + Pl + 3 Qz = Tur + Kfs*									
%	20.3	13.5	-	9.4	42.4	14.4	-	-	33.8	66.2
reaction 3.3	*Pl = 3 Qz*									
%	-	59.0	-	41.0	-	-	-	-	59.0	41.0
reaction 3.4	*Bt + Pl + 3 Qz = Tur + Kfs*									
%	19.3	25.6	-	3.0	38.5	13.7	-	-	44.9	55.1
reaction 3.5	*Bt + 6 Pl = Tur + Kfs + 12 Qz*									
%	10.4	41.4	-	19.1	21.7	7.4	-	-	51.8	48.2
reaction 3.6	*Pl = 0.2 Ap + 2 Qz*									
%	-	56.3	-	26.0	-	-	17.7	-	56.3	43.7
reaction 3.7	*Bt + 5 Pl = Tur + Kfs + 0.2 Ap + 8 Qz*									
%	11.7	38.8	-	14.4	24.4	8.3	2.4	-	50.5	49.5
reaction 3.8	*20 $Melt_R$ + Bt + 5 Pl = Tur + Kfs + 0.2 Ap + 8 Qz + 19 $Melt_P$*									
	18.0	23.3	-	12.3	19.9	14.2	2.1	10.2	51.5	48.5

*Molar volume of haplogranitic phases extracted from the thermodynamic data set ds55 (Holland & Powell, 1998) using the theriak software (Capitani & Petrakakis, 2010), at a pressure of 8 kbar and temperature of 710°C.

‡Tourmaline (schorl) molar volume taken from Anovitz & Hemingway (1996)

§Hydroxlapatite molar volume taken from Smyth and McCormick (1995)

[a]Melt molar volume based on 8 oxygen p.f.u. (c.p. Holland & Powell, 2001)

Table 3.3 Modal % change in mineral phases for the proposed reactions.

Table 3.3 presents the relative change in mineral proportions (i.e. modal %) for the proposed reactions. Of the seven reactions proposed above, reaction 3.7 best satisfies the textural observations in Sample BD1415 (e.g. figure 3.10), although the predicted modes of plagioclase consumption and tourmaline production are higher than the proportions of phases observed in figure 3.10a. Biotite and plagioclase are both consumed in the biotite-tourmaline domain (e.g. figure 3.10b), while tourmaline, apatite, and K-feldspar are

produced. Within the nearby quartz-plagioclase domain, plagioclase is consumed by the growth of quartz (e.g. figure 3.10e). There is a small negative change in volume across reaction 3.7 (table 3.3), due to the large volume change predicted in the local plagioclase-quartz and plagioclase-apatite reactions (3.3 and 3.6). Alternatively, if there was an external source of Al, reaction 3.7 could be balanced to conserve volume by minimising the contribution of reactions 3.3 and 3.6.

3.10 CHEMICAL EVOLUTION OF THE REACTING MELT

Reaction 3.7 describes the modification of psammite in terms of end-member phases and components in an aqueous solution. This is still a simplification because it does not involve melt as the reacting agent. To consider how the composition of the infiltrating melt evolved as the reaction progressed; the mineral components of reaction 3.7 were subsumed into a reaction with melt present on both sides, (reaction 3.8). The composition of melt is different on either side of reaction 3.8, reflecting the subtraction and addition of components required to balance the proportions of solid phases. The initial melt composition ($Melt_{reactant}$) in reaction 3.8 is taken from a study of melt inclusions by Thomas *et al.* (2000), and represents the composition of an immiscible volatile-rich melt phase formed directly below the critical point at ~ 700°C and 0.1 GPa. The only major difference between $Melt_{reactant}$ and the primary melt compositions formed during muscovite melting experiments (e.g. Douce & Harris, 1998), is $Melt_{reactant}$ contains ~5 times more H_2O. Melt is treated as a theoretical eight component phase that is normalised to eight oxygens per formula unit. The initial melt composition ($Melt_{reactant}$) and evolved composition ($Melt_{product}$) recalculated to oxide weight percent are given in Table 3.4. The aluminum saturation index (ASI) provided for both $Melt_{reactant}$ and $Melt_{product}$ in Table 3.4 is calculated as $Al_2O_3/(Na_2O + K_2O + CaO)$. Reaction 3.8 was balanced to conserve volume

and reflect the observed changes in mineral proportions without exhausting the volatile components. The reaction depletes $Melt_{reactant}$ in Al, Si, B, P, and H_2O, and enriches the $Melt_{reactant}$ in Na and Fe. It is important to note that reaction 3.8 lowers the aluminum saturation index of the melt, and as the reaction progresses, the relative contribution of reactions 3.3 and 3.6 may increase to accommodate tourmaline growth.

3.8 $20\ melt_{reactant} + 1.8\ Bt + 3.5\ Pl = 19\ melt_{product} + Tur + 2\ Kfs + 0.2\ Ap + 8\ Qz$

$$20\ Melt_{reactant}\ [K_{0.39}Na_{0.30}Fe_{0.14}Al_{0.65}Si_{2.98}O_8(P_{0.03}B_{0.18}H_{0.50})] + 1.8\ K(Fe,Mg)_3AlSi_3O_{10}(OH)$$
$$+ 2.5\ NaAlSi_3O_8 + CaAl_2Si_2O_8$$
$$=$$
$$19\ Melt_{product}\ [K_{0.43}Na_{0.32}Fe_{0.29}Al_{0.63}Si_{3.07}O_8(P_{0.01}B_{0.03}H_{0.42})] + Na(Fe,Mg)_3Al_6(BO_3)_3Si_6O_{18}(OH)_4$$
$$+ 2\ KAlSi_3O_8 + 0.2\ Ca_5(PO_4)_3(OH) + 8\ SiO_2$$

	Wet		Dry	
	*$Melt_{reactant}$	$Melt_{product}$	*$Melt_{reactant}$	$Melt_{product}$
SiO_2	46.43	50.06	73.79	79.57
Al_2O_3	8.88	9.09	14.11	14.45
B_2O_3	4.19	0.79		
FeO	1.29	2.85	2.05	4.53
MgO	0.00	0.00	0.00	0.00
CaO	0.00	0.00	0.00	0.00
Na_2O	2.90	4.28	4.60	6.81
K_2O	3.42	3.93	5.44	6.25
P_2O_5	0.58	0.09		
H_2O	32.31	28.89		
‡ASI	1.41	1.11	1.41	1.11
Normalised oxide wt%				
*Melt compostions from Thomas et al. (2000)				
‡ASI = $Al_2O_3/(Na_2O + K_2O + CaO)$				

Table 3.4 Melt compositions.

In the case of the Himalayan nebulitic tourmaline leucogranite, propagation of the melt-fluxed reaction takes place pervasively along the compositional layers of the psammitic country-rock, stopping along biotite-rich folia. The relatively abrupt termination of the

reaction front at biotite-rich folia indicates that the reaction propagation is governed by a chemical permeability, whereby the melt flow and associated textural modification is limited by the biotite-consuming tourminisation reaction. Scaillet *et al.* (1995) were the first to observe that tourmaline does not crystallise spontaneously in experiments using leucogranite compositions. In a purely igneous system, competition with biotite for ferromagnesium components appears to be the crucial parameter for controlling the stability of tourmaline (Scaillet *et al.*, 1990, Wolf & London, 1997). However, in a system where melt reacts with existing biotite it is expected that the activity of Al and B would govern tourmaline growth. One of the implications of a reaction front that is governed by chemical permeability is that the textural modification is limited by the availability of chemical reactants. In reactions 3.7 and 3.8, the limiting reagent for tourmaline growth will invariably be B. Consequently, the reaction is expected to stop along biotite-rich layers. The resulting product of the melt-fluxed reaction is a leucocratic quartzofeldspathic rock that has the appearance of an igneous body but has actually experienced a predominantly solid-state metamorphic history.

3.11 FORMATION OF IRREGULAR GRAIN BOUNDARIES

Comparison of quartz-feldspar grain boundaries across the contact between the psammite and nebulitic tourmaline leucogranite shows that the tourmalinisation reaction exerts a crucial control on grain microstructure. While it is rare to find completely equilibrated grain boundary textures in polymineralic rocks, owing to the sluggish rate of diffusion along grain boundaries compared to the relatively rapid rate of grain boundary migration in monomineralic aggregates (Hunter, 1996, Holness & Sawyer, 2008), quartz-feldspar grain boundaries in the unaffected psammite display a very well-equilibrated texture. Figure 3.14 depicts two models for the formation of the highly irregular grain boundaries. In the first,

the plagioclase and K-feldspar components of interstitial melt nucleate and grow on existing mineral interfaces (figure 3.14a). Upon further crystallisation, the ordered nucleation and growth forms a coarse granophyric intergrowth. Holness and Sawyer (2008) first proposed this model to explain the formation of highly irregular grain boundaries in migmatitic rocks, where the presence of a melt is unambiguous. There is additional textural evidence to support the crystallisation of interstitial melt in the nebulitic tourmaline leucograntite (i.e. sillimanite xenocrysts, microstructural features with low dihedral angles, and monomineralic films); however, there is no evidence of melt having been present along the highly irregular quartz-feldspar grain boundaries within the zone of psammite that is immediately adjacent to the nebulitic tourmaline leucogranite contact. An alternative model for the formation of these grain boundary features is depicted in figure 3.14b. In this model, I propose that the presence of a fluid along the quartz-plagioclase boundary may modify the interface by catalysing the replacement of plagioclase by quartz (reaction 3.3). The nebulous geometry of boundary embayments suggests a propagating reaction front akin to the fluid-assisted dissolution – reprecipitation mechanism developed by Putnis (2002) and others (Putnis & Putnis, 2007, Rubatto *et al.*, 2008, Putnis & Austrheim, 2013). The direction in which the reaction progresses (i.e. quartz replacing plagioclase) governs the polarity of the reaction texture (i.e. 'saw-teeth' point towards quartz). Progression of reaction 3.3 along quartz-plagioclase interfaces locally reduces the solid phase volume (see table 3.3), generating porosity in plagioclase, which enables the fluid-mediated reaction front to advance further into plagioclase.

Further microstructural modification towards lower energy grain boundary configurations may occur sub-solidus, in the absence of an interstitial fluid. Development of the 'string of pearl' texture is an example where a highly cuspate boundary may enclose and pinch off an embayment to reduce interfacial energy. Grain boundary irregularity may

preserve a record of pervasive but short-lived fluid flow, since there is a significant increase in diffusion rates when an interstitial fluid is present (Rubie, 1986, Holness & Siklos, 2000). Even at high metamorphic temperatures, the textural equilibration of dry grain boundaries in polymineralic rocks is often too sluggish a process to attain equilibrium (Holness *et al.*, 2005). Mechanisms responsible for the formation of the characteristic 'saw-tooth' and 'string of pearl' textures in the nebulitic tourmaline leucogranite may vary both spatially and temporally through the reaction process. It is likely that the final textures represent a collection of grain boundary processes that operated over a range of temperatures and melt conditions, and that the highly irregular microstructures are caused by both melt crystallisation and fluid-mediated dissolution – reprecipitation.

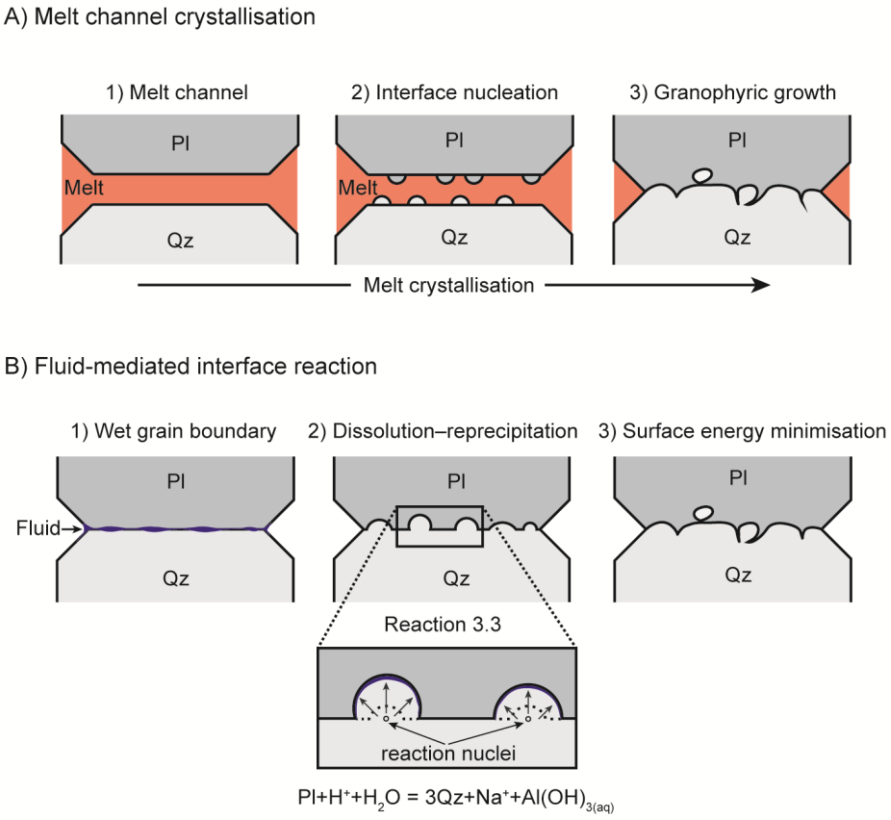


Figure 3.14 (a) Schematic model for the formation of irregular grain boundaries under melt-present conditions. 1) Solid grain boundaries are separated by a channel of silicate melt. 2) As the melt crystallises the plagioclase and quartz components nucleate preferentially on existing mineral interfaces, forming a coarse-grained granophyric intergrowth. 3) The intergrowth is subsequently modified, reducing its surface

energy and forming 'saw-tooth' and 'string of pearl' texture. (b) Schematic model for the formation of irregular grain boundaries under fluid-present conditions. 1) Infiltration of an intergranular fluid wets grain boundaries. 2) The fluid catalyses local dissolution–reprecipitation replacement of plagioclase by quartz (reaction 3.3). The volume-reducing reaction generates porosity in plagioclase, promoting further propagation of the reaction front into plagioclase and producing a bulbous structure. Note the polarity of movement along the grain boundary. 3) As in model (a), subsequent modification of the grain boundary, reduces its surface energy resulting in the 'saw-tooth' and 'string of pearl' texture.

3.12 THERMODYNAMIC CONSIDERATIONS

The formation of tourmaline and apatite in the nebulitic tourmaline leucogranite consumes B, H_2O, and P (see reaction 3.8). Sequestration of these volatile components is expected to be exothermic due to the high negative change in entropy of volitisation reactions (e.g. Haack & Zimmermann, 1996). The change in enthalpy of the tourmaline-forming reaction ($\Delta H_{reaction}$) can be calculated using experimentally constrained standard formation enthalpies ($\Delta H°_f$) and heat capacities (C_p) for the involved phases, where standard conditions are 298K and 1 bar (Table 3.5). To simplify the calculation, the melt composition consumed is assumed to all be the H_2O endmember (h2oL) from the six component CNKASH haplogranitic melt system presented by Holland and Powell (2001). This assumption implies that B, and P have a similar effect as H_2O on the thermodynamic properties of granitic melt. Ideal solution between the reactants and products is assumed, and Fe endmembers annite and schorl are considered for the two ferromagnesium phases (i.e. biotite and tourmaline). The $\Delta H°_f$ and C_p values of annite, albite, anorthite, sanidine, and quartz are taken from the internally consistent database of Holland and Powell (2001), and the thermodynamic data of h2oL is taken from Holland and Powell (2001). Thermodynamic data for schorl and hydroxyapatite are based on values reported by Garofalo *et al.* (2000) and Suda *et al.* (1995), respectively. Since reaction 3.8 is inferred to have occurred at conditions near the granitic solidus (~650°C/923K; White *et al.*, 2001), I have recalculated the enthalpy of formation of all phases at 650°C/923K (ΔH^{923}). This was done by holding pressure constant at 1 bar and integrating the heat capacity equation at

650°C/923K (equation 3.4). Holding pressure constant is a simplifying assumption made based on the relatively low bulk compressibility (i.e. young's modulus) of minerals (Wood, 1976).

$$\Delta H_T = \Delta H°_f \int_{298}^{T} C_p dT \tag{3.3}$$

As shown in equation 3.4, the change in enthalpy at any temperature (T) for reaction 3.8 can be calculated by subtracting the sum of the enthalpies of formation of the reactants from the sum of the enthalpies of the products, where the enthalpy at T is known for all constituent phases. Each phase is multiplied by its respective stoichiometric coefficient (n).

$$\Delta H_{T_{reaction}} = \sum (n\Delta H_T)(products) - \sum (n\Delta H_T)(reactants) \tag{3.4}$$

Substituting in the $\Delta H°_f$ values presented in table 3.5, the change in enthalpy for reaction 3.8 at 650°C/923K is –2852.3 kilojoules per mole of tourmaline (schorl) produced, which implies that reaction 3.8 is strongly exothermic.

Phase	Composition	ΔH°f (kJ/mol)	ΔH_{923} (kJ/mol)	Heat capacity parameters (J/mol·K)					Reaction 3.8 (mols)
				a	b	c	d	(e)	
*Annite	$KFe_3AlSi_3O_{10}(OH)_2$	-5151.67	-5152	815.7	-0.0349	19800	-7.47E+03		1
*Albite	$NaAlSi_3O_8$	-3934.6	-3935	452.0	-0.0134	-1275900	-3.95E+03		4
*Anorthite	$CaAl_2Si_2O_8$	-4233.48	-4233	371.6	0.0126	-4110200	-2.04E+03		1
*Sanidine	$KAlSi_3O_8$	-3964.9	-3965	448.8	-0.0101	-1007300	-3.97E+03		1
*Quartz	SiO_2	-910.88	-911	110.7	-0.0052	0	-1.13E+03		8
[a]Schorl	$NaFe_3Al_6(BO_3)_3Si_6O_{18}(OH)_4$	-14401.37	-14401	2230.1	-0.1155	-25188	8.92E-06	4.88E-05	1
[b]Apatite	$Ca_5(PO_4)_3OH$	-13314	-13314						0.2
[c]h_2oL	H_2O	-295.71	-295.71	80.0					1

*Holland & Powell (1998); [a]Garofalo et al. (2000); [b]Flora et al. (2004); [c]Holland & Powell (2001)

Note: C_p coefficients for Schorl refer to an equation in the form of: $C_p = a + bT + cT^{-0.5} + dT^{-2} + eT^{-2}$

The C_p equation for phases from Holland and Powell (1998) is $C_p = a + bT + cT^{-2} + dT^{-0.5}$

ΔH_{923} of apatite taken from Suda et al. (1995)

Table 3.5 Standard enthalpies of formation. A first order calculation of the relative contribution of reaction 3.8 to the thermal budget of the 'melt sink' can be made by comparing two hypothetical systems. The parameters used in this calculation are summarised in table 3.6 and figure 3.15. In the first scenario (system A; figure 3.15a; equation 3.4); the change in enthalpy is calculated for the crystallisation of a leucogranitic melt that is superheated by 50°C. In the second scenario (system B; figure 3.15b; equation 3.5), the net change in enthalpy of the system represents both the enthalpy of crystallisation for an identical volume and temperature of leucogranite as in the first scenario, as well as the enthalpy contribution of the formation of nebulitic tourmaline-leucogranite by reaction 3.8. The energy released by the crystallisation of melt and formation of the nebulitic tourmaline-leucogranite in system B (3.45×10^9 kJ) is greater than four times the amount released in system A (7.69×10^8 kJ) during crystallisation of melt alone.

$$\Delta H_{\text{systemA}} = L_{\text{granite}} * \rho_{\text{granite}} * V_{\text{granite}} + C_{\text{melt}} * \Delta T * \rho_{\text{melt}} * V_{\text{melt}} \quad (3.4)$$

$$\Delta H_{\text{systemB}} = \Delta H_{\text{systemA}} + \Delta H_{\text{reaction}} * n_{\text{Tur}} \left[\frac{V_{\text{Tur-leuco}} * modal_{\text{Tur}}}{Molar\ volume_{\text{Tur}}}\right] \quad (3.5)$$

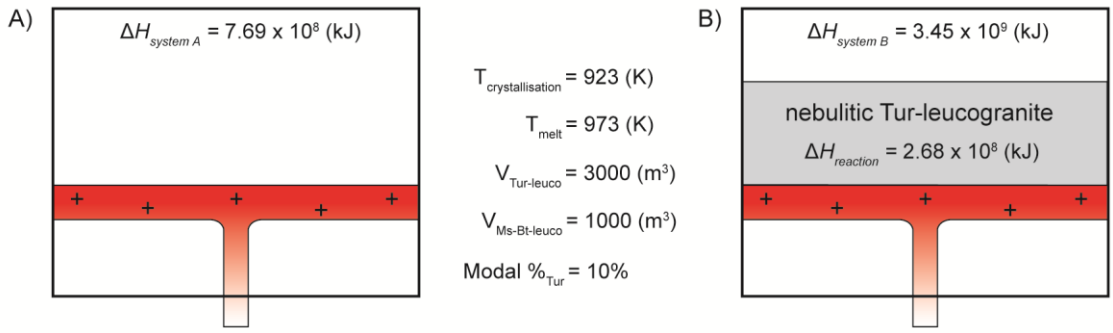


Figure 3.15 Schematic illustrating the two thermodynamic scenarios discussed in text. (a) The change in enthalpy of system A is due to the cooling and crystallisation of 1000 m^3 muscovite-biotite leucogranitic melt that was superheated by 50°C. (b) The change in enthalpy of system B is due to both the cooling and crystallisation of 1000 m^3 muscovite-biotite leucogranitic melt that was superheated by 50°C, and the exothermic formation of tourmaline in 3000 m^3 of the nebulitic tourmaline leucogranite (reaction 3.8).

Ms-Bt-Leucogranite	
Temperature of melt (K)	973
Crystallization temp (K)	923
Density (kg/m^3)	2200
‡Specific heat capacity [melt] (J/kg*K)	1130
‡Latent heat of crystallization (J/kg)	293000
Volume (m^3)	1000
Tur-leucogranite	
Volume (m^3)	3000
Volume fraction of Tourmaline in granite ( )	0.1
*Enthalpy of reaction 3.8 (kJ/mol)	-2852.62
§Molar volume Schorl (cm^3/mol)	318.83
‡ Schon (1983); §Garofalo et al. (2000); *ΔH(reaction 3.8) based on thermodynamic data presented in table 3.5	

Table 3.6 Enthalpy calculation – input parameters.

One of the implications of a strongly exothermic metasomatic reaction is the potential of the reaction to drive fluid advection and maintain pervasive fluid flow (Ague, 1998). Both the field relations and microstructural evidence support a reaction front that propagated pervasively along the network of grain boundaries, rather than along a discrete network of veins and channels. Previous studies on the mechanisms of fluid and melt transport through the crust underscore the importance of fluid accumulation and channelization in the

chemical segregation of the crust, which reduces the degree of fluid-rock interaction with increasing transport distance (e.g. Walther & Orville, 1982, Brown, 1994, Holness, 1997, Brown & Solar, 1998, Scaillet & Searle, 2006). The formation of nebulitic tourmaline leucogranite is a rare example of reactive flow, where fluid flow remains pervasive across the transport network. An analogous process operating in the upper mantle is the formation of dunitic bodies by reactive porous flow (e.g. Kelemen *et al.*, 1997, Spiegelman *et al.*, 2001, Rampone *et al.*, 2004). The importance of peridotite–melt interaction, involving local dissolution – reprecipitation reactions has been proposed to explain the formation of tabular dunites in many exposed ophiolites (Kelemen *et al.*, 1995, Suhr *et al.*, 1998, Suhr, 1999, Xu *et al.*, 2003). In the same way that peridotite–melt interaction influences the spatial and temporal chemical variability in mid-ocean ridge basalts (Spiegelman & Kelemen, 2003), psammite–melt interaction could exert a critical control on the composition of anatectic melt.

3.13 IMPLICATIONS FOR CRUSTAL ANATEXIS

High-temperature fluid-rock interaction, between notionally sub-solidus psammite and silicate melt (leucogranitic) profoundly alters the appearance of the psammite. Mineral textures in the resulting nebulitic tourmaline leucogranite provide some constraints on the melt fraction (φ) required to drive this process. Under isotropic stress, the Einstein-Roscoe relation, which describes viscosity of suspensions of rigid spheres, predicts a connected framework of solid crystals at $\varphi<0.45$ (Roscoe, 1952). While this relation closely describes systems with high melt fractions $1>\varphi>0.5$, experiments on the bulk viscosity of crustal melts suggest crystals form a framework at higher melt fractions $\varphi>0.6$, than predicted by the geometric relation of rigid spheres (Lejeune & Richet, 1995). In experiments on the bulk viscosity of crystallising granite, performed at strain rates of about $10^{-5}s^{-1}$, the

viscosity increases sharply at melt fractions of ~0.25 (Renner *et al.*, 2000). In the case of the nebulitic tourmaline leucogranites, where melt intruded a solid mineral framework, these experimental findings suggest that if the psammite was being actively deformed during melt infiltration the (instantaneous) melt fraction could not have exceeded $\varphi=0.26$ without losing the inherited layering. Texturally constrained estimates on the minimum fraction of melt that is required to form the nebulitic tourmaline-leucogranite are contingent on how the irregular grain boundaries are interpreted. If they are all interpreted as crystallised melt channels, analysis of the area of affected grain boundaries indicates an $\varphi<0.14$. However, this value only describes the proportion of the rock that preserves a textural record of melt. Reaction stoichiometry provides an alternative approach to estimating the total amount of melt involved in the formation of the nebulitic tourmaline-leucogranite. Using the phase volumes presented in table 3.3, if biotite and plagioclase combined comprise half of the initial psammite modal mineralogy then the stoichiometry of reaction 3.8 predicts a melt rock ratio of ~2.5. However, B is the limiting reagent in reaction 3.8 so the melt rock ratio will be highly sensitive to the initial concentration of B in the reacting melt.

The transport of anatectic melt through the Greater Himalayan Series is proposed to have occurred in two main stages. The first stage originated in the pelitic source, where melt migration was initially pervasive, operating along a network of grain boundaries (see chapter 2). By the time melt had separated from its source and intruded the psammite it was migrating along a meter-scale network of sills and dykes (e.g. figure 3.3). This channelized sill and dyke network formed in the psammite suggests hydraulic fracturing aided melt migration by exploiting existing structural anisotropies in the foliated country-rock (Brown, 1994). The second stage of anatectic melt migration operated while the leucogranite bodies were crystallising. Fractionated melt migrated pervasively through the

psammitic country-rock, driving mineral reactions and ultimately the formation of the nebulitic tourmaline leucogranite. Beyond this stage, the fate of remaining fractionated melt and exsolved volatile components is uncertain; however it is likely that the fluid flow became increasingly channelized with further transport, reducing the degree of fluid-rock interaction and consequently the degree of textural modification in the host rock. While a full mass-balance calculation of the volume of fluid released during Himalayan anatexis is beyond the scope of this chapter, it should be noted that the crystallisation of 10–15 modal % hydrates in the Himalayan leucogranites is inadequate to sequester enough water to balance the amount of water released during the breakdown of muscovite dehydration melting in the underlying pelite.

The role of melt-rock interaction in the formation of the nebulitic tourmaline leucogranite presented in this chapter, has major implications for role and extent of anatexis in the Himalayas. Previous estimates of the volume of anatectic melt generated during metamorphism of the Greater Himalayan Series rely on field estimates of the proportion of leucocratic bodies in the melt sink (e.g. Reddy *et al.*, 1993). In the uppermost levels of the Greater Himalayan Series in Langtang, leucocratic bodies comprise up to half of the total rock volume. There is an apparent deficiency in the fertility of the melt source compared to the observed volume of leucocratic material. Previous studies have addressed this apparent source–sink deficiency by extending the source region into structurally lower metamorphic units (e.g. Barbey *et al.*, 1996), or by inferring the lateral extrusion of melt from a larger source below the Tibetan Plateau (e.g. Hodges, 2006). However, field estimates, based on the proportion of medium- and coarse-grained leucocratic rock, considerably overestimate the volume of melt (by up to 60 %), because they do not account for the volume of sub-solidus psammite that is involved in forming the nebulitic tourmaline leucogranite. If the process presented in this chapter is accounted for, the

volume of crystallised anatectic melt in the Greater Himalayan Series can be reasonably accounted for with a pelitic melt source that is 2.5 to 3.5 km thick and has generated ~20 modal % of segregated melt. Figure 3.16 illustrates the proportion of melt estimated based on all leucocratic material (figure 3.16a) versus the sum of muscovite-biotite leucogranite volume and proportion of melt involved in the formation of the nebultitic tourmaline leucogranite (figure 3.16b).

The presence of sillimanite xenocrysts in the muscovite-biotite-(sillimanite) leucogranite and the nebulitic tourmaline leucogranite indicates that muscovite dehydration melting of a pelitic composition is the source of melt for both types of leucogranite. This implies that local variations in the degree of melt-rock interaction, rather than unique melting reactions (Visonà & Lombardo, 2002), reaction conditions (Inger & Harris, 1993), or melt sources (e.g. Vidal *et al.*, 1982, Le Fort *et al.*, 1987, Guillot & Le Fort, 1995) are responsible for the variety of Himalayan leucogranite mineralogy and composition.

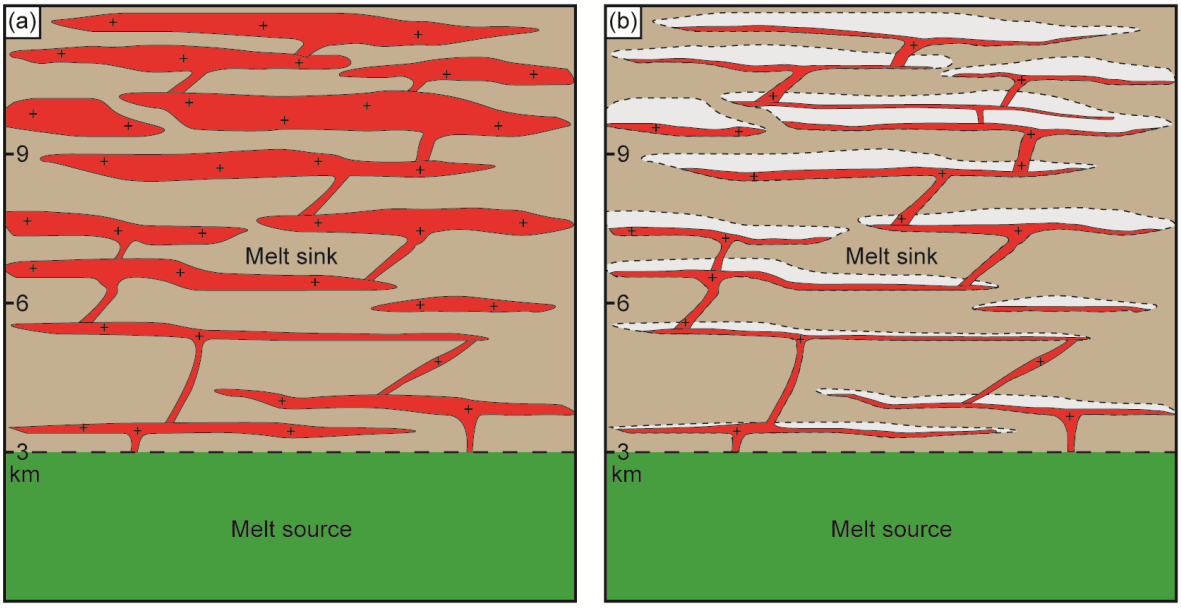


Figure 3.16 Schematic illustrating the consequence of melt-rock interaction on the proportion of leucogranitic melt generated in the Greater Himalayan Series. (a) Previous interpretation of the proportion of melt (red) based on the volume of medium and coarse grained leucocratic bodies. (b) New interpretation of the proportion of melt (red) accounting for the formation of nebulitic tourmaline leucogranite by melt-rock interaction.

3.14 SUMMARY AND CONCLUSIONS

Textural analysis of the Himalayan nebulitic tourmaline leucogranite shows that the infiltration of a small amount of leucogranitic melt (less than $\varphi \approx 0.25$) into notionally sub-solidus psammite results in the formation of a rock that has the appearance of a leucogranite, yet preserves primary metasedimentary layering. The *in-situ* alteration of psammite by a reactive volatile-rich melt produces tourmaline and K-feldspar while consuming biotite and sequestering B, P, and H_2O. Propagation of the reaction front is governed by the chemical permeability of the psammite and the availability of B as the limiting reagent, and driven by the energy released by the exothermic tourmaline-forming reaction. Nucleation of tourmaline may be ordered by the orientation of biotite in the protolith, creating an apparent foliation in a rock which may not have experienced much subsequent deformation.

Both the removal of biotite and the presence of melt along protolith grain boundaries encourage grain boundary mobility, resulting in a bulk grain-size coarsening by an order of magnitude. Analyses of grain-size and shape suggest grain growth was governed by interface processes, locally conserving volume and resulting in preferred growth along monomineralic grain boundaries. Highly irregular grain boundaries preserve a record of the late-stage crystallisation of interstitial melt along mineral grain boundaries. These findings suggest that the transient passage of melt through a rock will leave a textural record, which may be preserved during cooling and exhumation from mid-crustal levels. These textures could be used to identify the migration of melt through an otherwise unreactive lithology, and ultimately provide some real constraints on the volume of melt generated in orogenic belts.

4 Protolith lithostratigraphy of the Greater Himalayan Series in the Langtang and Everest regions of Nepal: implications for the architecture of the northern Indian margin

4.1 INTRODUCTION

The volcano-sedimentary sequence deposited along the northern margin of peninsular India records a long history of rifting and basin formation between the Neoproterozoic and middle Eocene. Tectonic thickening and uplift of the Indian margin, by folding and thrusting, during the collision between India and Eurasia has exposed this sequence across the Himalaya (Searle *et al.*, 1987a). There are four main phases of rifting preserved in the stratigraphy of the Himalaya, with initiation in the 1) Neoproterozoic, 2) Ordovician, 3) late Carboniferous to early Permian, and 4) late Permian to Middle Jurassic (Stampfli *et al.*, 1991, Garzanti, 1999). The strata deposited during the Neoproterozoic to Middle Jurassic unconformably overlie Mesoproterozoic and Paleoproterozoic units (DeCelles *et al.*, 2004). Strictly speaking, the term 'Tethyan Margin' applies only to the sequence of sedimentary rocks deposited during the lower Paleozoic and younger rift phases, which can be separated into the 'Paleotethys' and 'Neotethys' (Stampfli *et al.*, 1991). However, sedimentary rocks deposited on the northern Indian margin during the Neoproterozoic record an early phase of rifting, prior to the opening of the (Paleo)Tethys (Garzanti *et al.*, 1987, Garzanti, 1999, Gehrels *et al.*, 2003, Myrow *et al.*, 2003, Gehrels *et al.*, 2011). Apart from the growing record of detrital zircon ages in the Himalayan metamorphic core (e.g. Parrish & Hodges, 1996, DeCelles *et al.*, 2000, Gehrels *et al.*, 2003, Myrow *et al.*, 2003, Myrow *et al.*, 2009, Gehrels *et al.*, 2011, Spencer *et al.*, 2012), most of what is known about this early rifting phase and the architecture of the Indian margin prior to the breakup

of Gondwana comes from studying the incomplete record of low-grade and unmetamorphosed sedimentary strata that crop out along the Lesser Himalaya Series (LHS; figure 4.1).

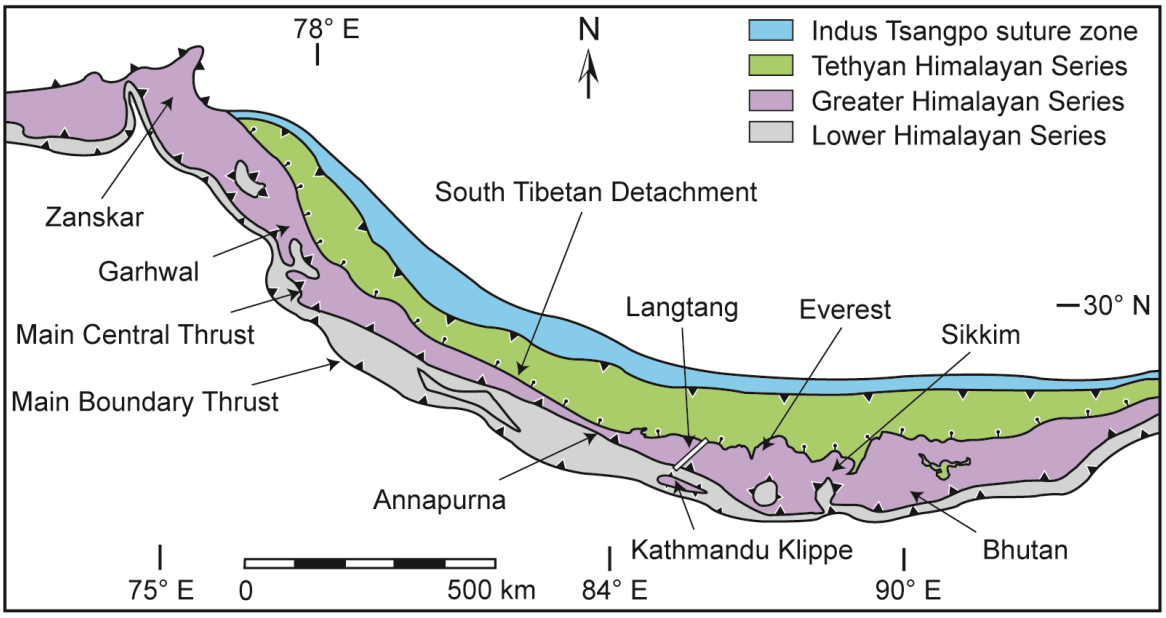


Figure 4.1 Simplified geological map of the Himalaya and location of the Everest, Langtang, Annapurna, and Zanskar regions. Modified after Searle *et al.* (2008).

The early geological history of the northern margin of the Indian craton, prior to terminal collision with Eurasia, is recorded in the low grade stratigraphy of the two lithotectonic domains that flank the Greater Himalayan Series (GHS; figure 4.1). To the south, the Lesser Himalayan Series comprises a predominately Paleoproterozoic to Mesoproterozoic succession that overlies Indian crystalline basement. Within a series of doubly-plunging synclines (Jiang *et al.*, 2002), and paleogeographic lows (Godin & Harris, 2014), these rocks are overlain by Neoproterozoic to Cambrian (McQuarrie *et al.*, 2008), and Ordovician to Mesozoic strata (Brookfield, 1993, Hodges, 2000, Myrow *et al.*, 2010, Martin *et al.*, 2011), which collectively form the 'upper Lesser Himalayan Series'. The origin of the upper Lesser Himalayan Series strata is attributed to the formation of a long-

lived passive margin, with rifting during the Neoproterozoic, Ordovician, Permian, and Cretaceous (Brookfield, 1993, Myrow *et al.*, 2010). The second, low grade lithotectonic unit lies to the north and sits structurally above the Greater Himalayan Series. It comprises the Neoproterozoic to Eocene so-called 'Tethyan' Himalayan Series (THS), which preserves a complete record of the four pulses of Neoproterozoic, Ordovician, late Carboniferous to early Permian, and late Permian to Middle Jurassic rifting (Brookfield, 1993, Garzanti, 1999, Chatterjee *et al.*, 2013). Younger overlapping strata define the influx of foreland basin sedimentation, which resulted from the crustal thickening and uplift of the Himalayas (Myrow *et al.*, 2010).

Previous studies of the Himalayan detrital zircon record have shown that there is considerable overlap in the depositional ages of the upper-Lesser, Greater, and lower Tethyan Himalayan Series strata (DeCelles *et al.*, 2000, Gehrels *et al.*, 2003, Myrow *et al.*, 2003, DeCelles *et al.*, 2004, Richards *et al.*, 2005, Myrow *et al.*, 2009, Myrow *et al.*, 2010). Published detrital age spectrums range between ca. 520–3520 Ma for the upper Lesser Himalayan Series (Myrow *et al.*, 2003), ca. 500–2700 Ma for the Greater Himalayan Series (DeCelles *et al.*, 2000, DeCelles *et al.*, 2004), and ca. 500–3450 Ma for the lowermost strata of the Tethyan Himalayan Series (Myrow *et al.*, 2003, Myrow *et al.*, 2010).

In the simplest scenario, the Lesser, Greater, and Tethyan Himalayan Series constitute the depositional record of a single continental margin that is both spatially and temporally continuous along the length of the Himalaya. The difficulty with this interpretation is that the primary depositional relationship between these first-order lithotectonic domains is obscured by the two major structures that bound the Greater Himalayan Series (figure 4.1). To the south, the Main Central Thrust (MCT) zone carries the Greater Himalayan Series units southward- over the Lesser Himalayan Series (Searle *et*

al., 2008). To the north, the South Tibetan Detachment zone, an array of low-angle north-dipping normal faults, juxtaposes the non-metamorphosed Tethyan Himalayan Series above the Greater Himalayan Series (Searle *et al.*, 2003, Searle *et al.*, 2010).

Reconstructing the architecture of the pre-Himalayan Indian margin is further complicated by the paleotopography of the Precambrian Indian basement. A long history of tectonism, sedimentation, and erosion, through the Archean and Proterozoic (Bhowmik *et al.*, 2012), produced a heterogeneous Indian basement that formed the base on which the sedimentary rocks of the northern Indian margin were deposited. For example, three northeast-trending paleotopographic highs or 'ridges' underlie the Ganga and Brahmaputra alluvial sediments south of the Himalaya range, which are inferred to continue below the Himalaya range (Bollinger *et al.*, 2004, Godin & Harris, 2014).

Unravelling the collisional structure, as well as the original paleogeography of the Himalaya requires knowledge of the protolith lithostratigraphy of the Greater Himalayan Series. In this chapter I combine field mapping, U-Th-Pb monazite and detrital zircon geochronology, and petrographic studies to interpret the regional metamorphic units of the Greater Himalayan Series in terms of their protolith lithostratigraphic significance.

4.2 REGIONAL LITHOSTRATIGRAPHIC CONTEXT

Previous models proposed to explain the pre-Himalaya distribution of the Lesser, Greater, and Tethyan Himalayan Series strata, based on palinspastic restoration of the imbricate stack of thrust sheets, have unique predictions for the Greater Himalayan Series in terms of protolith lithostratigraphy and timing of sediment accumulation. The prevailing model, in which the Lesser, Greater and Tethyan Himalayan Series cumulatively represent the ancient continuous cover margin sequence of the northern Indian craton, implies a rift/passive margin setting for the accumulation of the Greater Himalayan Series during the

late Neoproterozoic to late Cambrian (Searle *et al.*, 1987b, Brookfield, 1993, Gehrels *et al.*, 2003, Myrow *et al.*, 2003, Myrow *et al.*, 2010). Other models, such as the crystalline axis model (Saxena, 1971, Aharon *et al.*, 1987) that interpret the Lesser and Tethyan Himalayan Series as depositional basins respectively south and north of a high-standing crystalline ridge, do not fit with the coeval upper-Lesser, Greater, and lower-Tethyan Himalayan Series detrital zircon record (Myrow *et al.*, 2003). A third model, which incorporates recent work on late Cambrian to early Ordovician granite suites in the western Himalaya, suggests that the Greater and Tethyan Himalayan Series form the basement and cover units of an accreted terrane juxtaposed against India and its Lower Himalayan Series cover (DeCelles *et al.*, 2000). Similar to the crystalline axis model, the accreted terrane model predicts an early depositional and high-grade metamorphic history for the Greater Himalayan Series that predates deposition of the Tethyan Himalaya Series. On the basis of similar detrital zircon and zircon Nd isotopic records in both the Lesser and Greater Himalayan Series rocks, the accreted terrane model is unnecessary (Myrow *et al.*, 2003) and remains unsupported by the absence of intervening suture zone lithologies (Searle *et al.*, 1999, Searle *et al.*, 2003, Searle *et al.*, 2008). Nevertheless, confidence in the continuous margin interpretation would be greatly improved if the protolith lithostratigraphy of the high-grade Greater Himalayan Series was further constrained.

Within the Greater Himalayan Series there are two units of augen gneiss that can be distinguished based on their lithostratigraphic position (at the base versus the upper portions of the Greater Himalayan Series), and their age. The lower augen gneiss unit, termed the Ulleri augen gneiss in Annapurna (Pecher & Le Fort, 1977, Colchen *et al.*, 1986) and Phaplu augen gneiss in Everest (Maruo & Kizaki, 1981), has a granitic to granodioritic composition (Parrish & Hodges, 1996), and yields monazites and zircons with ages between ca. 1400 and 1970 Ma (Catlos *et al.*, 2002, DeCelles *et al.*, 2004). The

upper augen gneiss unit, often referred to as the 'Formation III augen gneiss' after Colchen *et al.* (1986) or 'Pumori K-feldspar augen gneiss' (Searle *et al.*, 2003), is by contrast more varied in both appearance and composition and yields zircons with ages between ca. 470 and 490 Ma (DeCelles *et al.*, 2000, Godin *et al.*, 2001). The origin of the Formation III augen gneiss is widely attributed to deformation of a belt of late Cambrian to early Ordovician granites that extends along strike from Zanskar in the west (Pognante *et al.*, 1990) to Bhutan in the east (Gansser, 1983). Deformed Formation III augen gneiss layers in the Greater Himalayan Series are correlated with undeformed granites exposed in the Kathmandu Klippe (Gehrels *et al.*, 2003), which yield zircons and monazites with an age of ca. 470 Ma (Schärer & Allègre, 1983). The prevalence of late Cambrian detrital zircon grains found within Greater Himalayan Series siliciclastic rocks along the length of the mountain belt (Myrow *et al.*, 2009, Myrow *et al.*, 2010) implies that formation of the late Cambrian to early Ordovician granites was near contemporaneous with the deposition of the Greater Himalayan Series strata. Therefore, the interpretation of whether or not the Formation III augen gneiss represents deformed granite has bearing on how the lithostratigraphic history of the Greater Himalayan Series is interpreted. Pulses of granitic magmatism, tectonic uplift, erosion and sediment deposition all shaped the northern Indian margin in the Ordovician (Garzanti *et al.*, 1986, Funakawa, 2001, Gehrels *et al.*, 2003). However, the record of these events in the Greater Himalayan Series has been overprinted by the Cenozoic Himalayan metamorphism and deformation.

While the change in mineral assemblages as a result of metamorphism for a wide variety of compositions is known (e.g. Bowen, 1940, Spear & Cheney, 1989, Connolly & Trommsdorff, 1991, Frey *et al.*, 1991), and equilibrium phase diagrams can be calculated for most lithologies (cf. Powell *et al.*, 1998, Capitani & Petrakakis, 2010), the change in the penetrative rock texture(s) that accompanies mineral reactions can conceal the features

and structures required to readily identify a rock's protolith. Of relevance to this work is an understanding of the dramatic textural evolution of siliciclastic rocks during vapour-absent muscovite dehydration melting, which is documented in chapter 2. In the context of protolith identification, the most significant finding of the textural study presented in chapter 2 is that the texture of a fine-grained pelite can be modified to form a pelitic K-feldspar augen gneiss. Consequently, if the Formation III augen gneiss was formed by the textural modification of a pelite during muscovite dehydration melting, rather than deformation of granitic bodies, then a modified lithostratigraphic interpretation of the Greater Himalayan Series is certainly required, which does not invoke late Cambrian to early Ordovician granite magmatism along the entire length of the Himalaya (c.f. Gehrels *et al.*, 2003).

In this chapter I identify the first-order protolith lihtostratigraphy of the Greater Himalayan Series exposed in Langtang (central Nepal; figure 4.1), and report new zircon and monazite ages from both the augen gneiss units and the surrounding metasedimentary lithologies. I present an alternative lithostratigraphic interpretation for the Greater Himalayan Series based on my protolith interpretation of the augen gneiss and metasedimentary units, and discuss how this fits into the continuous margin model for the accumulation of the Lesser, Greater, and Tethyan Himalayan Series.

4.3 GEOLOGICAL BACKGROUND AND SAMPLES

Having experienced Cenozoic medium to high temperatures of metamorphism and up to ca. 30 km of tectonic burial, the metasedimentary rocks of the Greater Himalayan Series preserve a record of crustal orogenic evolution. Metamorphic grade is documented to increase structurally upwards from kyanite-muscovite assemblages in the hanging wall of the MCT zone (figure 4.2 & 4.3), through sub-solidus kyanite-sillimanite-muscovite to K-

feldspar-sillimanite at the vapour-absent muscovite dehydration reaction isograd ('Kfs' on figures 4.2 and 4.3; Searle & Rex, 1989, Stephenson *et al.*, 2000, Searle & Godin, 2003). Leucogranite sills and dykes, originating with the muscovite dehydration melting reaction, intrude the upper half of the Greater Himalayan Series, hosted in K-feldspar-sillimanite-bearing metasedimentary rocks (see chapter 3). The uppermost leucogranites of the Greater Himalayan Series record the lowest pressures (and therefore most shallow depth) of peak-temperature metamorphism, preserving cordierite-sillimanite assemblages (Streule *et al.*, 2010a, Groppo *et al.*, 2013).

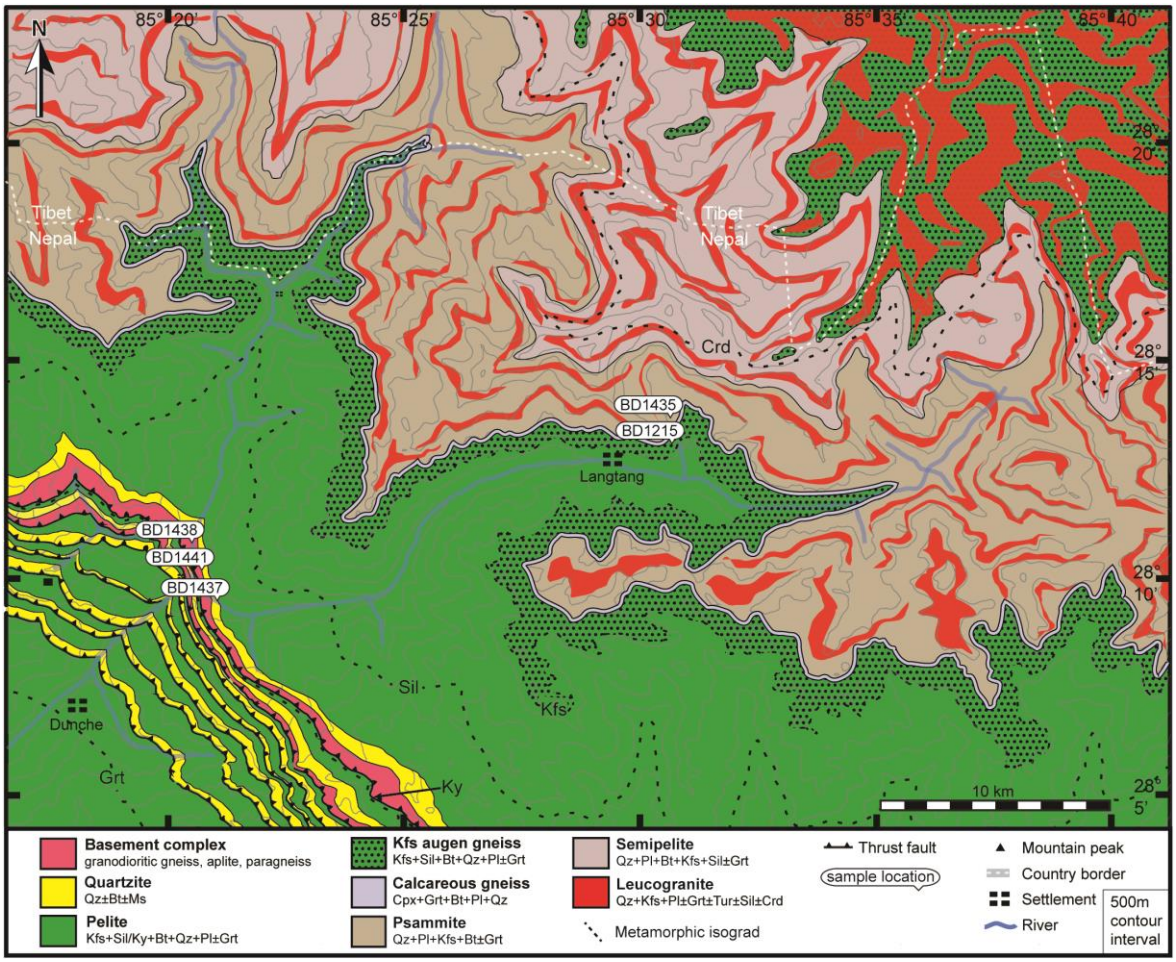


Figure 4.2 Geological map of Langtang, documenting principal lithostratigraphic units, structures, and metamorphic isograds. Labels denote the location of samples used for geochronology.

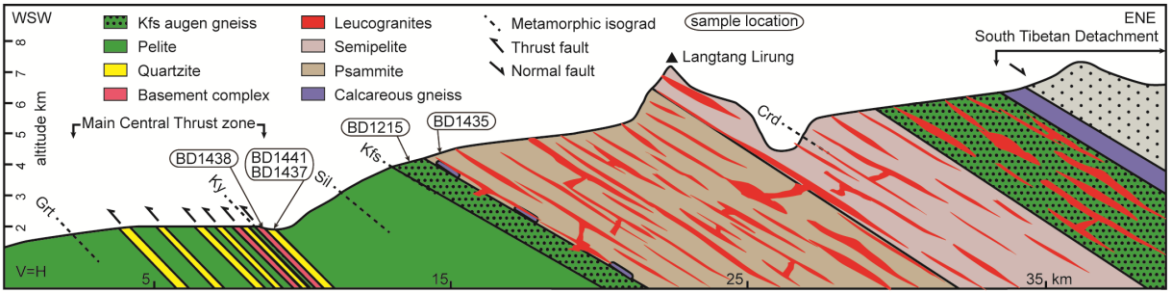


Figure 4.3 Cross-section through the Greater Himalayan Series in Langtang, showing litholostratigraphic units, distribution of metamorphic mineral isograds, and the bounding structures - the Main Central Thrust zone and the South Tibetan Detachment.

Samples used in this study were collected across the Greater Himalayan Series in Langtang (figure 4.1) during field mapping campaigns in 2012 and 2014. Previous work in Langtang (Inger & Harris, 1992, Macfarlane, 1992, Macfarlane, 1993, Reddy *et al.*, 1993, Macfarlane, 1995, Parrish & Hodges, 1996, Fraser *et al.*, 2000, Pearson, 2002, Takagi *et al.*, 2003, Kohn *et al.*, 2004, Kohn *et al.*, 2005, Pearson & DeCelles, 2005, Takagi *et al.*, 2007, Kohn, 2008) has outlined the general structural, chronological, and lithological framework of Langtang, but in general has focused on the lower MCT zone, which can be readily accessed by trekking routes. In this study, we extend the observations to the uppermost levels of the Greater Himalayan Series, beyond the base of the Cenozoic leucoganite bodies (figure 4.2 & 4.3). While not directly accessed in the field, the position of the South Tibetan Detachment zone is constrained in the northern segment of the Langtang transect (figure 4.3) with the use of satellite imagery, and field observations in the neighbouring Shisha Pangma region in south Tibet (Searle *et al.*, 1997b). The degree of deformation is largely consistent along the transect and is characterised by primary lithostratigraphic bedding transposed into a dominant east-west striking metamorphic foliation, defined by the alignment of biotite and the flattening of quartz and feldspars. The exception is the imbricated base of the Greater Himalayan Series, which is punctuated by discrete zones of high strain localized along the base of individual thrust imbricates. Seven

imbricates were identified, which repeat the lowermost Greater Himalayan Series stratigraphic sequence and collectively make up the MCT zone in Langtang (figure 4.2 & 4.3). The thickness of the individual imbricates range from ~50 to 700 m. The upper two imbricates comprise granodioritic augen gneiss overlain by quartzite and pelite, whereas, the lower five thrust sheets involve only quartzite and overlying pelite (figure 4.2 & 4.3). The regional foliation deviates to north-south orientations near the base of the MCT zone, as a result of late cross-folding and/or the presence of a lateral ramp (Macfarlane, 1992), and is accompanied by the development of crenulation-folding with a north-plunging fold axis (Takagi *et al.*, 2003). Structurally upwards from the MCT zone, C-S fabrics and both δ- and σ-type feldspar augen record ductile shear, which transitions from top-to-south thrust motion to top-to-north normal motion in the centre of the Greater Himalayan Series, similar to other transects across the Himalaya (Searle *et al.*, 1997a, Searle *et al.*, 2003). Previous workers have reported thrust faults within the Greater Himalayan Series in the Langtang area based on changes in lithology or the presence of metamorphic index minerals (e.g. Langtang Thrust; Kohn, 2008), but obvious repetitions of lithostratigraphic units, or distinguishable high strain zones that would suggest structures with major displacement, were not observed in the field.

4.4 LANGTANG LITHOSTRATIGRAPHY

The Langtang section exposes a siliciclastic-dominated stratigraphic succession that shares many similarities with parallel sections in the Everest and Zanskar areas (figure 4.1; Searle *et al.*, 1997a, Searle *et al.*, 2003, Searle *et al.*, 2006b). The basal unit of the Greater Himalayan Series is a ~300 m-thick panel of coarse-grained paragneiss and orthogneiss, dominated by biotite augen gneiss of granitic to granodioritic composition (figure 4.4a). The gneiss is strongly deformed and irregularly banded at the centimetre/metre scale and

crosscut by dykes of aplitic monzogranite. The augen gneiss is found across the Nepalese Himalaya, and is correlated with the Ulleri and Phaplu augen gneiss in Annapurna (Pecher & Le Fort, 1977, Colchen *et al.*, 1986) and Everest (Maruo & Kizaki, 1981).

Approximately 400 m of thickly bedded low-grade quartzite directly overlie the gneiss, preserving a relationship interpreted as an unconformable basement-cover contact. In comparison with the underlying granodioritic augen gneiss, the quartzite is relatively nondeformed, and the thickness of the beds decreases systematically upwards from the basal contact, from meter- to decimetre-scale. The quartzite is equigranular with 2–3 mm quartz grains that are recrystallized, displaying a sugary texture. Centimetre-scale trough cross-bedding and heavy mineral laminations denote a stratigraphic right-way-up orientation (figure 4.4b).

The top of the quartzite is interbedded and progressively grades into a ~6 km thick pelitic unit that comprises predominately kyanite-muscovite to sillimanite-K-feldspar grade schist. The lower portion of the unit is characterised by thinly bedded quartzite intervals (figure 4.4c), whereas the top is interbedded with 2–5 cm thick layers of arkosic psammite. The texture and grain size of the pelite changes dramatically across the sillimanite-K-feldspar isograd, where it becomes pelitic K-feldspar augen gneiss with centimetre-sized porphyroblasts of K-feldspar (figure 4.4d). The augen gneiss contains abundant schlieren of fibrolitic sillimanite, which comprise 2–10 modal percent of the mineral assemblage. Rare layers of diopside-rich calcareous marl are distributed throughout the pelite, with the largest forming a ~50 m thick discontinuous interval at the top of the pelitic unit (figure 4.3).

The marl and top of the pelitic unit is overlain by rhythmically bedded sillimanite-K-feldspar-grade arkosic psammite. The beds are characterised by reverse metamorphic grading (figure 4.4e) that shows an increase in biotite, K-feldspar, and sillimanite content

towards the top of each layer, with the contacts between individual beds both discrete and continuous. Bed thickness decreases upwards from ~30–45 to 5–10 cm, with overall biotite, K-feldspar, and sillimanite content increasing towards the top of the ~3.7 km thick unit. There is a gradual transition from rhythmically bedded psammite to micaceous semipelite and irregularly layered, coarse-grained, pelitic K-feldspar augen gneiss, the latter forming the uppermost exposure of the Greater Himalayan Series in Langtang. While not directly observed in Langtang, correlative sequences in Everest and Shisha Pangma expose diopside-grade calc-silicates and marble overlying the uppermost pelitic strata (Searle *et al.*, 1997b, Searle *et al.*, 2003, Searle *et al.*, 2006b).

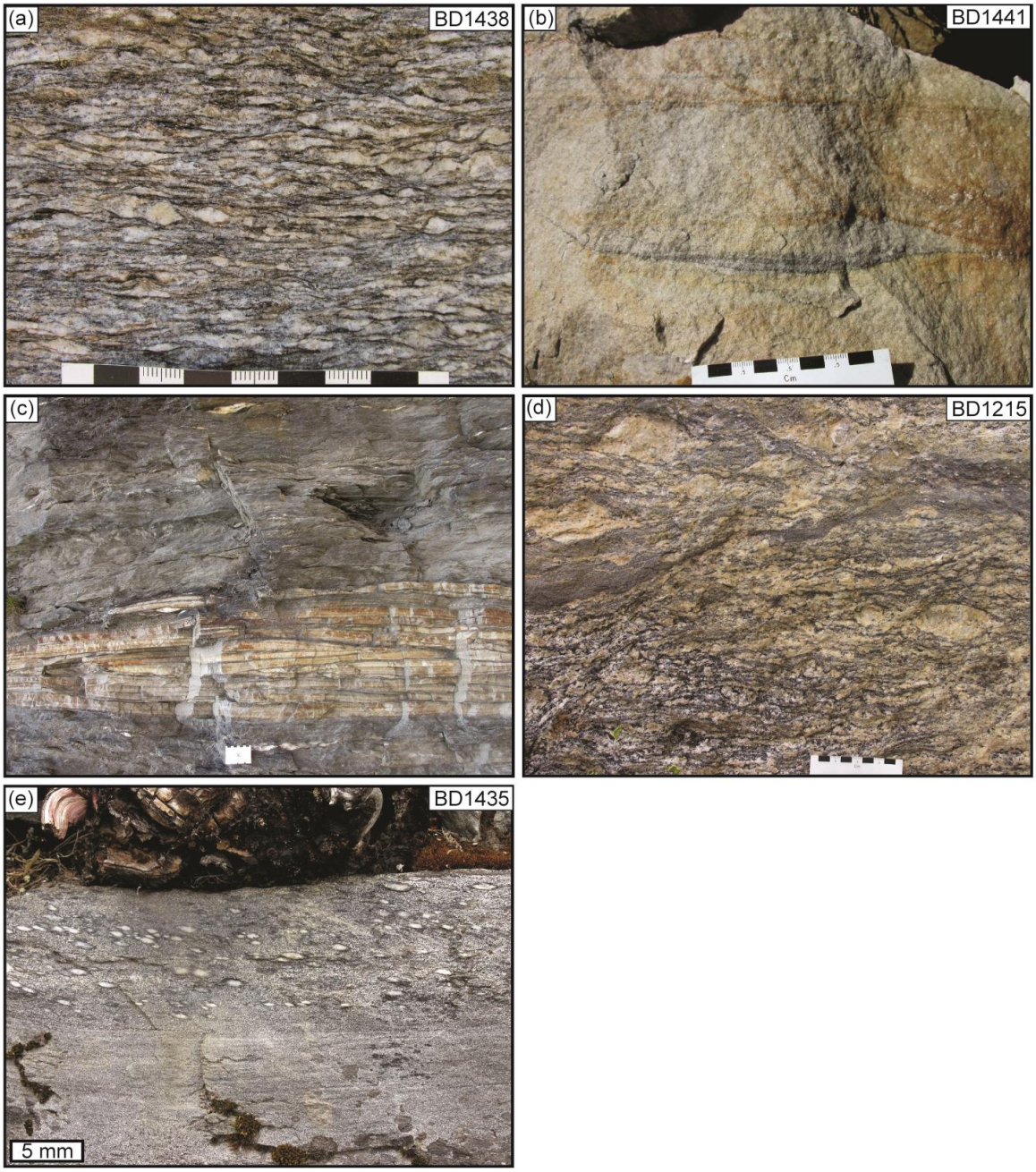


Figure 4.4 Outcrop photographs of the major lithostratigraphic units. Scale card is in centimetres (8cm). (a) Plagioclase and K-feldspar augen orthogneiss, formed by ductile deformation of a coarse-grained granodiorite. The augen orthogneiss together with aplitic dykes and layers of paragneiss comprise the Indian basement, which is unconformably overlain by the Greater Himalayan Sequence metasedimentary units. (b) Medium- to thick-bedded quartzite with heavy mineral banding. The sorting and concentration of heavy minerals into placer-type accumulations suggests reworking by wave action at some point along the transport path. (c) Thin- to medium- bedded low-angle quartzite laminasets interbedded with pelitic garnet-biotite-schist, interpreted as mud drapes. The interbedding of sand and mud deposition with bottom currents suggests a shallow-water, nearshore environment, with alternating deposition and reworking rather than 'event beds', i.e. storm or turbidite deposits. (d) K-feldspar and sillimanite pelitic augen gneiss. The growth of large K-feldspar porphyroblasts is a result of an increase in the rate of grain boundary migration and coarsening as a result of vapour-absent muscovite dehydration melting. (e) Right-way-up psammitic turbidite bed with reverse metamorphic grading formed as a result of the porphyroblastic intergrowth of sillimanite + quartz in more aluminous layers.

4.5 TIMING OF GREATER HIMALAYAN SERIES DEPOSITION

Zircon and monazite were separated from samples of granodioritic augen gneiss (BD1438), quartzite (BD1441 and BD1437), pelitic K-feldspar augen gneiss (BD1215), and arkosic psammite (BD1435) for analysis with the Sensitive High Resolution Ion Microprobe (SHRIMP) at the Geological Survey of Canada (figures 4.5 & 4.6; tables 4.1 & 4.2) in order to constrain the timing of Greater Himalayan Series deposition in Langtang.

4.5.1 Analytical methods

Zircon and monazite separates were cast in two separate epoxy mounts along with fragments of primary and secondary standards. The mounts were polished to expose internal grain features prior to backscattered (BSE) imaging of monazite grains, and cathodoluminescence (CL) and BSE imaging of zircon grains to characterise the internal features of crystals (i.e. zoning, internal microstructure, and alteration). SHRIMP monazite and zircon analyses followed the methods described in Stern and Berman (2001) and Stern (1997), respectively. Analytical details regarding spot size, beam current, data reduction protocol and U-Th-Pb calibration are reported in table 4.1 and table 4.2. Isoplot (version 4.1; Ludwig, 2003) was used to generate Concordia plots and mean ages with related statistics. For analyses younger than 1500 Ma the radiogenic $^{206}Pb/^{238}U$ age was used for the probability density plot (figure 4.6c). The $^{207}Pb/^{206}Pb$ age is used for analyses older than 1500. For these older analyses, those >10% discordant have not been included in the probability density plot, whereas concordance was visually evaluated on Concordia diagrams for the younger analyses (figure 4.5). A summary of results are presented in figure 4.5, figure 4.6, table 4.1, and table 4.2. Uncertainties given for ratios and ages of individual analyses are at the 1σ level. The results from the granodioritic augen gneiss are presented as a weighted $^{207}Pb/^{206}Pb$ ages with errors calculated to the 2σ level.

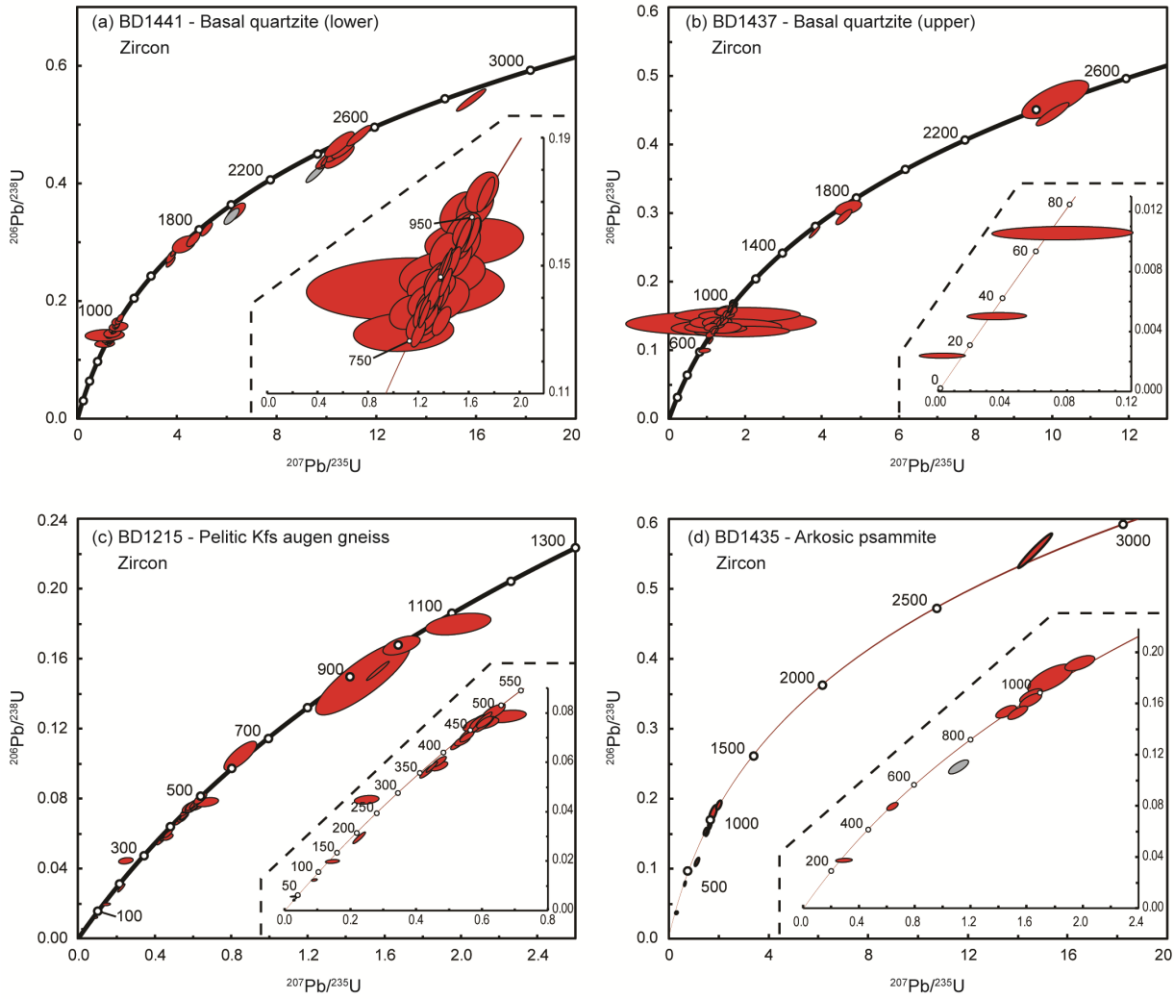


Figure 4.5 Concordia plots showing all detrital zircon analyses for samples: (a) BD1441, (b) BD1437, (c) BD1215, and (d) BD1435. Grey ellipses denote the discordant analyses that were excluded from the probability density diagram (figure 4.6b).

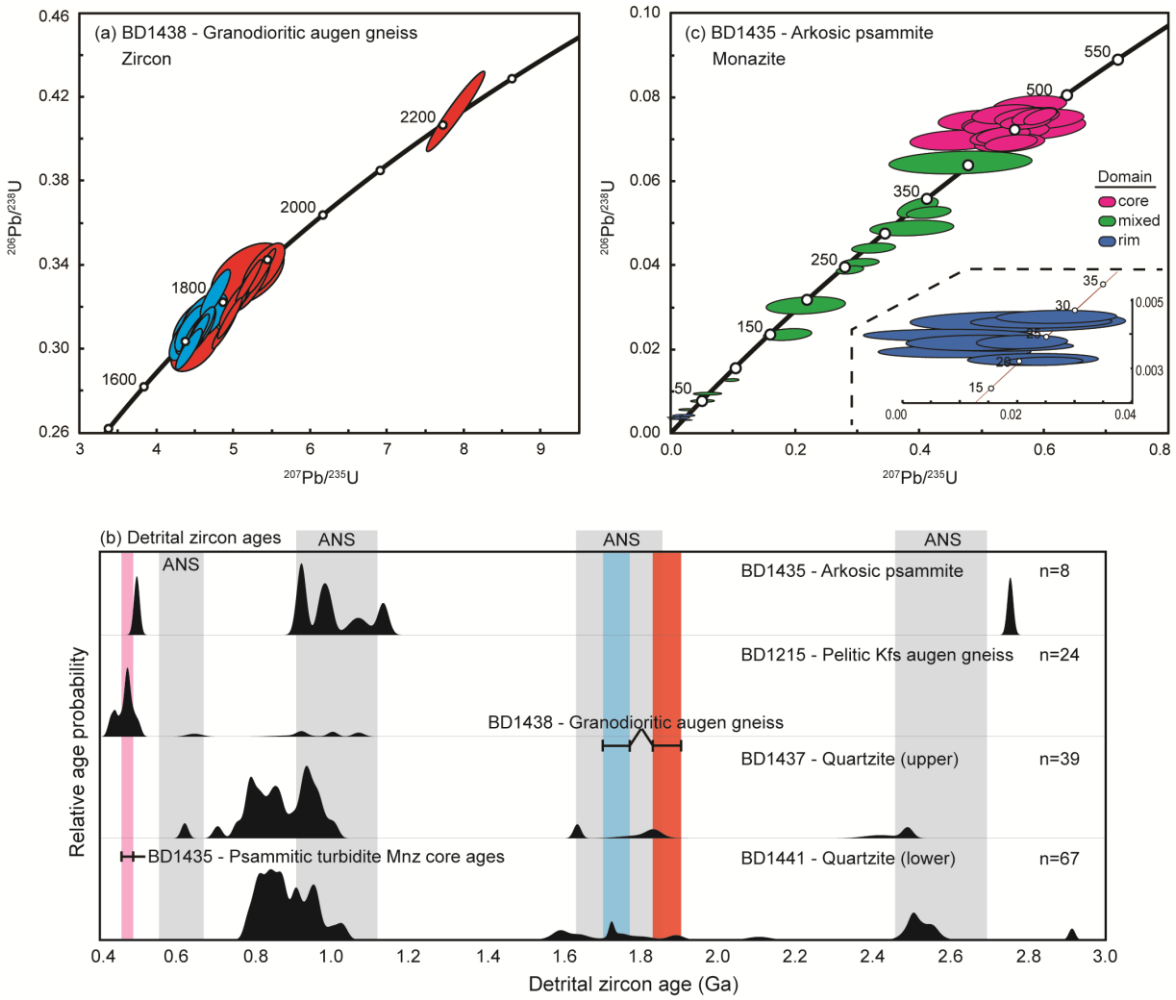


Figure 4.6 U-Pb Zircon and monazite geochronology results. (a) Concordia diagram showing all analyses of zircons from sample BD1438. Ellipses are coloured to show the interpreted crystallisation (blue) and inherited (red) populations. (b) Detrital zircon age spectra from metasedimentary samples (BD1441, BD1437, BD1215, and BD1435) taken across the Greater Himalayan Series in the Langtang region. Each curve represents the sum of the probability distributions of all concordant grains analysed from each sample, with $^{206}Pb/^{238}U$ ages used for <1500 Ma grains and $^{206}Pb/^{207}Pb$ ages used for >1500 Ma grains. Three discordant analyses were excluded from the diagram (11247-68.1, 11247-75.1, and 11245-6.1; table 4.1). Red and blue bands correspond to the granodioritic augen gneiss ages presented in figure 4.6a, and the pink band denotes the range in monazite core ages presented in figure 4.6c. Grey bands denote the subpopulations of detrital ages from the Arabian-Nubian Shield (ANS) reported by Avigad et al. (2003). (c) Concordia diagram showing all monazite analyses for sample BD1435. Ellipses are coloured to show analyses of core (pink), rim (blue), and mixed domains (green).

4.5.2 Results

BD1438 – granodioritic augen gneiss

The granodioritic augen gneiss contains light pink euhedral zircons with sharp crystal facets. Grains range in size from 100 to 200 μm and comprise both smaller equant and larger prismatic morphologies. Under CL, most grains are oscillatory zoned; a few grains display a brighter homogeneous overgrowth. Twenty-four analyses were carried out on twenty-two individual zircon grains which yield ages that fall into two populations (figure 4.6a; table 4.1). The older population consists of dominantly 1890–1830 Ma zircon (weighted mean $^{207}Pb/^{206}Pb$ age of 1864±9 Ma, n=10, MSWD = 1.4), with a single older analysis at 2208 Ma. The younger group of results yields a weighted mean $^{207}Pb/^{206}Pb$ age of 1738±10 Ma (n=13, MSWD = 0.86). Oscillatory zoned zircons are present in both age populations; however, analyses of bright overgrowths only fall in the younger grouping. Oscillatory zoned zircon typically represents magmatic growth and consequently the younger age is interpreted as the crystallization age of the granodiorite. The older ages, which in two instances (grains 11 and 124) occur as cores with ca. 1740 rim, are interpreted to represent inheritance. Field relationships are consistent with an unconformable contact between the augen gneiss and overlying quartzite, thus this unit is inferred to represent the depositional basement to the Greater Himalayan Series.

BD1441 – basal quartzite, lower

A sample of quartzite directly overlying the basement augen gneiss was collected (e.g. figure 4.4b). Colourless to light pink zircons present a range of sizes (75–200 μm) and morphology, from small and round equant grains to long tabular crystals with rounded facets. Sixty grains from the lower quartzite were analysed, yielding ages that range from the 2913±8 Ma to 781±9 Ma (basal quartzite (lower), figure 4.6b; table 4.1). The majority

of analyses cluster between ca. 1000–800 Ma (n=49), with smaller peaks at ca. 1600 Ma (n=3), ca. 1700 Ma (n=3), ca. 2010 Ma (n=2), and ca. 2480 Ma (n=9). The youngest distinct detrital zircon mode occurs at ca. 815 Ma, which is considered the maximum age of deposition of the lower basal quartzite. Notably, there is only a very minor contribution of 1890–1740 Ma zircon as documented in the underlying basement (figure 4.6), suggesting non-local derivation for this quartzite.

BD1437 – basal quartzite, upper

A second quartzite sample was collected from the top of the 400 m-thick unit. The zircons recovered from the quartzite are very similar in terms of morphology and zoning patterns to those from the lower quartzite. Forty-six analyses of thirty-nine grains yield ages that range from 2418±43 Ma to 15.6±0.4 Ma. The majority of analyses cluster between ca. 1000–800 Ma (n=31), with smaller peaks at ca. 1800 Ma (n=2), and ca. 2450 Ma (n=2) (basal quartzite (upper), figure 4.6b; table 4.1). The youngest distinct detrital zircon mode occurs at ca. 790 Ma in the Tonian, which is considered the maximum age of deposition of the upper basal quartzite. Similarly, there is only a very minor contribution of 1890–1740 Ma zircon as documented in the underlying basement, suggesting non-local derivation for this quartzite (figure 4.6). Younger analyses from moderate CL overgrowths display low Th/U ratios (down to 0.002), which increase with progressively older ages. No dates between ca. 750 Ma and ca. 15 Ma were reproduced. Overgrowths were quite complex and often quite thin. I therefore infer that these younger analyses are the result of mixing due to overlap of the analytical spot across older detrital core domains and Miocene metamorphic rims. This interpretation is consistent with the progressive increase in Th/U accompanying the increase in ages. As a single, non-reproducible result, age constraint on Miocene metamorphism is speculative (^{204}Pb corrected ^{206}Pb/^{238}U age =15.6±0.4); however, it

should be noted that it overlaps with a reported age of metamorphic monazite growth in a nearby sample (16±1 Ma; Kohn et al, 2005).

Both quartzite samples show strong similarities in age distribution and range with previously published spectra from quartzite across the Greater Himalayan Series (DeCelles *et al.*, 2000, Myrow *et al.*, 2003, Myrow *et al.*, 2010, Spencer *et al.*, 2012). Based on the prominence of 1100–900 Ma zircons, previous studies suggest the East African Orogen and Arabian-Nubian Shield as plausible sources for Himalayan detritus (DeCelles *et al.*, 2000, Myrow *et al.*, 2010, Spencer *et al.*, 2013). Avigad *et al.* (2003) report detrital zircon ages from a Cambrian sandstone that was deposited on the northern margin of the Arabian-Nubian Shield, which yielded subpopulations with ages of ca. 650–550, 1100–900, 1850–1650, and 2700–2470 Ma (ANS on figure 4.6b). The overlap in the detrital ages presented here and the Arabian-Nubian Shield signature supports the existing source interpretation. Older grains may be attributed to the various Paleoproterozoic orogens and Archean crust interpreted to have been exposed on Gondwana (e.g. Myrow *et al.*, 2010).

BD1215 – pelitic K-feldspar augen gneiss

A sample taken from the top of the pelitic K-feldspar augen gneiss unit contains colourless zircons that range in size, from 50 to 150 μm, and morphology, from small and ovoid grains to large prismatic crystals with rounded facets. Forty-one analyses were carried out on thirty-four individual zircon grains, which yield ages that range from 1069±14 Ma to 26.4±0.4 Ma. Detrital analyses cluster between ca. 500–460 Ma (n=12), with smaller peak at ca. 1100–900 Ma (n=3; Pelitic Kfs augen gneiss; figure 4.6b; table 4.1). The youngest distinct detrital zircon mode occurs at ca. 470 Ma, which is considered the maximum age of deposition of the protolith to the pelitic K-feldspar augen gneiss. In contrast to the underlying quartzite, there is only a very minor contribution of 1100–900 Ma zircon, and

no contribution of 1890–1740 Ma zircon as documented in the basement (figure 4.6). Similar to the upper quartzite, younger analyses from CL dark rims exhibit low Th/U ratios (down to 0.008), which increase progressively with older age. None of the younger ages (ca. 450–26 Ma) were reproducible. As with the upper quartzite, overgrowths were complex and often thin. I therefore interpret these younger analyses as a result of mixing due to overlap of the analytical spot across older detrital core domains and Miocene metamorphic rims.

The prominent late Cambrian to early Ordovician signature matches similar detrital age spectrums from across the Greater Himalayan Series in Garhwal (Spencer *et al.*, 2012), Sikkim (Mottram *et al.*, 2014), and Bhutan (Spencer *et al.*, 2012). These ages overlap with the age of the late Cambrian to early Ordovician magmatic event that is recorded elsewhere along the length of the Himalaya (e.g. Gansser, 1983, Schärer & Allègre, 1983, Pognante *et al.*, 1990, Gehrels *et al.*, 2003). In contrast to Spencer *et al.* (2012), I interpret the late Cambrian to early Ordovician grains as being detrital rather than igneous or inherited. This interpretation is supported by the results of a petrological study in chapter 2, which demonstrates the sedimentary origin of the pelitic K-feldspar augen gneiss in Langtang. The differences in detrital spectrum between the quartzites and the pelitic K-feldspar augen gneiss indicate a change in provenance during the accumulation of strata along the northern Indian margin, potentially attributed to a change in basin subsidence during the early Palaeozoic.

BD1435 – arkosic psammite

The arkosic psammite, was sampled immediately above the contact with the underlying pelitic K-feldspar augen gneiss. Only a small number of small (40–100 μm), ovoid, colourless zircons were recovered. Ten zircon grains were analysed, yielding ages ranging

from 2850±43 Ma to 240±4 Ma (arkosic psammite; figure 4.6b; table 4.1). Given the limited zircon recovery, these results are not adequate to assess the provenance profile of the psammite. However, the zircon age spectrum of the arkosic psammite shares many similarities with the sample of pelitic K-feldspar augen gneiss (figure 4.6). Notably, late Cambrian, Cryogenian and Tonian to Stenian age peaks. This similarity suggests that the provenance of detritus was the same for both units. The maximum age of deposition of the psammite is tentatively interpreted to be ca. 500 Ma based on the analysis of a single, oscillatory zoned zircon.

In order to better constrain the depositional age of the arkosic psammite, monazite grain separates were analysed. The internal textural domains of small (30–60 μm) ovoid shaped monazite grains was separated into core and rim domains. Forty-one monazite domains were analysed, yielding ages ranging from 485±6 Ma to 21±0.3 Ma (figure 4.6c; table 4.2). Eighteen analyses of unambiguous core domains yield a continuous spread in ages from 485±6 Ma to 432±5 Ma. Confidence in the late Cambrian interpretation of the maximum depositional age for arkosic psammite deposition could be improved if the monazite cores are demonstrably detrital as well. However, an alternative interpretation is the monazite cores formed *in-situ* during a late Cambrian to early Ordovician thermal-metamorphic event (i.e. granite emplacement). Based on the available data I am unable to confidently discriminate whether the monazite cores are detrital or *in-situ*, and so the depositional age of the arkosic psammite remains poorly constrained. Ten analyses of rim domains yield a continuous spread of ages from 29±0.5 Ma to 21±0.3 Ma. Younger rim analyses display low Th/U ratios (3–6). I interpret the younger rim analyses as dating monazite recrystallisation during Himalayan metamorphism. This interpretation agrees with previously published Oligocene to Miocene metamorphic monazite ages from the Greater Himalayan Series (e.g. Schärer & Allègre, 1983, Noble & Searle, 1995, Hodges *et*

al., 1996, Godin *et al.*, 2001, Kohn *et al.*, 2005). Thirteen analyses from core domains with complex overgrowths yield ages ranging from 404±7 Ma to 37±0.6 Ma. These analyses display a range of Th/U ratios (7–26), which generally increase with older age. Attempts to reproduce these ages with replicate analyses of the same textural domains resulted in considerably different ages. I therefore interpret these younger analyses as a result of mixing due to overlap of the analytical spot across older core domains and younger rims.

Table 4.1: U–Pb zircon geochronology data

												Ratios										Ages				
												Uncorrected				204 corrected						204 corrected				
Analyses	U (ppm)	Th (ppm)	$^{232}Th/^{238}U$	Yb (ppm)	Hf (ppm)	$^{204}Pb/^{206}Pb$	1σ (%)	f(206)[4] (%)	$^{206}Pb^{*}$ (ppm)	$^{208}Pb^{*}/^{206}Pb^{*}$	1σ (%)	$^{238}U/^{206}Pb$	1σ (%)	$^{207}Pb/^{206}Pb$	1σ (%)	$^{207}Pb^{*}/^{235}U$	1σ (%)	$^{206}Pb^{*}/^{238}U$	1σ (%)	error corr.	$^{207}Pb^{*}/^{206}Pb^{*}$	1σ (%)	$^{206}Pb^{*}/^{238}U$	1σ (Ma)	$^{207}Pb^{*}/^{206}Pb^{*}$	1σ (Ma)	Disc. (%)
Sample BD1438, Granodioritic augen gneiss, Latitude: 28.15120, Longitude: 85.36620																									See footnote A	
11248-053.1	189	47	0.26	81	12134	3.3E-4	24	0.52	49.7	0.072	7.1	3.2	1.6	0.1085	1.0	4.395	2.2	0.3067	1.6	0.719	0.1039	1.5	1724	24	1696	28	-2
11248-008.1	222	29	0.14	57	12236	1.4E-4	32	0.22	59.2	0.036	8.1	3.2	1.5	0.1060	1.2	4.448	2.0	0.3100	1.5	0.731	0.1040	1.4	1741	22	1697	25	-3
11248-006.1	184	32	0.18	67	12020	1.3E-4	35	0.21	48.8	0.058	6.5	3.2	1.5	0.1064	1.0	4.462	1.9	0.3093	1.5	0.779	0.1046	1.2	1737	23	1708	22	-2
11248-046.1	130	67	0.54	132	10551	4.0E-4	22	0.63	34.8	0.153	4.4	3.2	1.6	0.1103	1.7	4.512	2.7	0.3121	1.6	0.590	0.1049	2.2	1751	24	1712	40	-3
11248-056.2	376	211	0.58	325	11144	1.6E-4	23	0.25	105.4	0.167	2.5	3.1	1.4	0.1079	0.7	4.761	1.7	0.3265	1.4	0.857	0.1058	0.9	1821	23	1727	16	-6
11248-110.1	177	69	0.40	120	10373	9.5E-5	41	0.15	48.0	0.123	4.0	3.2	1.5	0.1075	2.1	4.617	2.6	0.3154	1.5	0.569	0.1062	2.2	1767	23	1734	40	-2
11248-071.2	189	61	0.33	98	11788	2.7E-4	27	0.42	50.2	0.092	5.7	3.2	1.5	0.1100	1.0	4.532	2.1	0.3091	1.5	0.738	0.1064	1.4	1736	23	1738	26	+0
11248-089.1	213	71	0.34	58	11506	1.3E-4	32	0.21	56.1	0.112	3.9	3.3	1.4	0.1085	0.8	4.504	1.8	0.3062	1.5	0.819	0.1067	1.0	1722	22	1743	19	+1
11248-344.1	402	56	0.14	139	12748	6.7E-5	33	0.11	103.7	0.040	5.1	3.3	1.3	0.1077	0.7	4.419	1.5	0.3001	1.3	0.871	0.1068	0.8	1692	20	1745	14	+3
11248-075.1	378	73	0.20	139	11978	4.1E-5	41	0.06	99.6	0.062	8.9	3.3	1.3	0.1073	0.6	4.520	1.5	0.3070	1.3	0.898	0.1068	0.7	1726	20	1745	12	+1
11248-011.1	422	58	0.14	148	12734	6.8E-5	38	0.11	110.3	0.046	5.4	3.3	1.4	0.1081	0.8	4.499	1.6	0.3046	1.4	0.852	0.1071	0.9	1714	21	1751	16	+2
11248-124.1	409	64	0.16	150	12427	6.5E-5	38	0.10	108.8	0.048	5.1	3.2	1.4	0.1080	0.8	4.576	1.6	0.3098	1.4	0.853	0.1071	0.9	1740	21	1751	16	+1
11248-024.1	229	101	0.46	54	11536	2.8E-4	26	0.44	59.2	0.142	4.2	3.3	1.5	0.1121	2.1	4.500	2.8	0.3011	1.6	0.547	0.1084	2.4	1697	23	1772	43	+5
11248-014.1	156	65	0.43	75	11113	6.9E-4	21	1.07	45.1	0.107	7.7	2.9	1.8	0.1215	2.5	5.186	3.7	0.3356	1.8	0.486	0.1121	3.3	1865	29	1834	59	-2
11248-066.2	359	118	0.34	43	11159	1.3E-4	26	0.21	99.1	0.093	3.6	3.1	1.4	0.1148	0.7	5.005	1.6	0.3212	1.4	0.864	0.1130	0.8	1795	22	1849	15	+3
11248-088.1	658	128	0.20	77	12389	6.3E-5	25	0.10	176.9	0.057	3.0	3.2	1.3	0.1140	0.5	4.879	1.4	0.3128	1.3	0.932	0.1131	0.5	1755	20	1850	9	+6
11248-052.1	800	356	0.46	85	11030	3.9E-5	29	0.06	228.5	0.137	3.3	3.0	1.3	0.1140	0.4	5.201	1.3	0.3325	1.3	0.945	0.1135	0.4	1850	20	1855	8	+0
11248-054.1	347	118	0.35	65	11207	4.8E-5	41	0.07	98.3	0.103	3.0	3.0	1.4	0.1146	0.6	5.179	1.5	0.3296	1.4	0.893	0.1139	0.7	1837	22	1863	13	+2
11248-011.2	1082	608	0.58	173	8763	5.4E-5	24	0.08	292.5	0.173	1.4	3.2	1.3	0.1147	0.4	4.948	1.3	0.3148	1.3	0.939	0.1140	0.5	1764	19	1864	8	+6
11248-124.2	610	287	0.49	72	11442	2.6E-5	41	0.04	162.5	0.148	1.8	3.2	1.3	0.1146	0.5	4.886	1.4	0.3102	1.3	0.933	0.1143	0.5	1741	20	1868	9	+8
11248-065.1	173	112	0.67	70	9120	6.8E-5	50	0.10	49.2	0.203	6.0	3.0	1.5	0.1158	0.9	5.244	1.9	0.3310	1.5	0.832	0.1149	1.0	1843	25	1879	18	+2
11248-107.1	575	807	1.45	255	8238	2.1E-5	45	0.03	166.8	0.429	1.8	3.0	1.3	0.1157	0.5	5.368	1.4	0.3375	1.3	0.937	0.1154	0.5	1875	21	1886	9	+1
11248-044.1	204	152	0.77	79	9776	8.1E-5	41	0.12	59.5	0.229	2.6	3.0	1.5	0.1166	1.5	5.390	2.1	0.3385	1.5	0.699	0.1155	1.5	1879	24	1888	27	+1
11248-097.1	354	49	0.14	154	12643	4.3E-5	38	0.06	125.7	0.039	4.5	2.4	1.9	0.1390	0.5	7.894	2.0	0.4135	1.9	0.959	0.1385	0.6	2231	35	2208	10	-1
11248-097.1	354	49	0.14	154	12643	4.3E-5	38	0.06	125.7	0.039	4.5	2.4	1.9	0.1390	0.5	7.894	2.0	0.4135	1.9	0.959	0.1385	0.6	2231	35	2208	10	-1
Sample BD1441, Quartzite (lower), Latitude: 28.16116, Longitude: 85.34801																									See footnote B	
11247-090.2	477	326	0.71	89	9364	2.5E-4	21	0.44	52.8	0.252	2.3	7.7	1.3	0.0710	0.9	1.196	2.0	0.1288	1.3	0.649	0.0674	1.5	781	9	849	31	+8
11247-015.1	182	52	0.30	31	11423	1.0E-3	54	1.77	20.2	0.088	29.0	7.6	1.6	0.0752	5.1	1.080	15.0	0.1294	1.9	0.127	0.0605	14.9	784	14	622	322	-28
11247-012.1	240	231	0.99	66	9057	3.9E-4	30	0.67	27.0	0.323	3.7	7.6	1.5	0.0755	2.3	1.265	3.8	0.1310	1.6	0.414	0.0700	3.4	794	12	929	71	+15
11247-057.1	447	439	1.01	78	10451	4.2E-4	24	0.73	50.5	0.308	3.2	7.5	1.5	0.0723	1.9	1.202	3.4	0.1316	1.5	0.434	0.0663	3.1	797	11	814	65	+2
11247-056.1	844	331	0.41	126	11001	1.5E-4	29	0.27	96.3	0.172	3.0	7.5	1.4	0.0775	1.4	1.380	2.2	0.1329	1.4	0.640	0.0753	1.7	804	10	1078	33	+27
11247-051.1	291	136	0.48	72	10707	2.0E-4	38	0.35	33.3	0.171	4.6	7.5	1.5	0.0723	2.1	1.274	3.1	0.1331	1.5	0.488	0.0694	2.7	806	11	911	55	+12
11247-100.1	230	181	0.81	53	10449	6.0E-5	71	0.10	26.5	0.252	3.7	7.5	1.5	0.0689	2.2	1.258	2.8	0.1341	1.5	0.526	0.0681	2.4	811	11	870	50	+7
11247-117.1	576	586	1.05	38	9916	4.3E-5	50	0.07	66.5	0.337	1.9	7.4	1.4	0.0695	2.2	1.274	2.6	0.1342	1.4	0.516	0.0688	2.2	812	10	894	46	+10
11247-058.1	1007	439	0.45	69	11918	1.5E-5	50	0.03	116.8	0.139	1.7	7.4	1.3	0.0671	0.8	1.246	1.5	0.1350	1.3	0.850	0.0669	0.8	816	10	835	17	+2
11247-100.2	135	127	0.97	54	9476	9.4E-4	22	1.64	15.7	0.287	5.0	7.3	1.6	0.0739	1.9	1.125	5.8	0.1356	1.6	0.278	0.0602	5.5	820	12	610	120	-37
11247-103.1	916	915	1.03	48	10009	7.6E-5	30	0.13	106.8	0.324	1.5	7.4	1.5	0.0670	1.9	1.234	2.5	0.1357	1.5	0.608	0.0660	2.0	820	12	805	42	-2

Table 4.1: (continued)

												Ratios										Ages				
												Uncorrected				204 corrected							204 corrected				
Analyses	U (ppm)	Th (ppm)	$^{232}Th/^{238}U$	Yb (ppm)	Hf (ppm)	$^{204}Pb/^{206}Pb$	1σ (%)	$f(206)^4$ (%)	$^{206}Pb^*$ (ppm)	$^{208}Pb^*/^{206}Pb^*$	1σ (%)	$^{238}U/^{206}Pb$	1σ (%)	$^{207}Pb/^{206}Pb$	1σ (%)	$^{207}Pb^*/^{235}U$	1σ (%)	$^{206}Pb^*/^{238}U$	1σ (%)	error corr.	$^{207}Pb^*/^{206}Pb^*$	1σ (%)	$^{206}Pb^*/^{238}U$	1σ Ma	$^{207}Pb^*/^{206}Pb^*$	1σ Ma	Disc. (%)
11247-021.1	581	491	0.87	31	9893	1.7E-4	26	0.30	68.7	0.274	2.2	7.3	1.4	0.0696	1.3	1.273	2.2	0.1375	1.4	0.628	0.0672	1.7	831	11	842	35	+2
11247-029.1	273	179	0.68	78	11080	4.7E-4	24	0.82	32.3	0.200	4.4	7.2	1.5	0.0746	2.0	1.291	3.6	0.1381	1.5	0.423	0.0678	3.2	834	12	863	67	+4
11247-090.1	449	328	0.75	68	9721	1.2E-4	35	0.20	53.5	0.241	2.7	7.2	1.4	0.0710	1.5	1.325	2.3	0.1386	1.4	0.618	0.0693	1.8	837	11	909	37	+9
11247-061.1	269	167	0.64	46	10911	8.4E-4	20	1.45	32.1	0.198	5.4	7.1	1.5	0.0778	2.1	1.259	4.7	0.1390	1.6	0.332	0.0657	4.5	839	12	797	94	-6
11247-116.1	293	261	0.92	35	10828	7.6E-5	41	0.13	35.1	0.286	2.2	7.2	1.4	0.0693	1.4	1.311	2.1	0.1394	1.4	0.653	0.0682	1.6	841	11	874	33	+4
11247-101.1	52	73	1.45	61	8576	4.6E-4	50	0.80	6.3	0.456	5.6	7.1	2.1	0.0778	4.1	1.369	6.9	0.1395	2.1	0.305	0.0712	6.5	842	17	962	134	+13
11247-078.1	559	161	0.30	65	12021	2.5E-4	26	0.43	67.3	0.105	7.7	7.1	1.4	0.0738	1.6	1.358	2.5	0.1402	1.4	0.558	0.0702	2.1	846	11	936	43	+10
11247-038.1	806	423	0.54	100	13287	4.2E-5	45	0.07	97.7	0.170	2.4	7.1	1.3	0.0687	1.2	1.326	1.8	0.1412	1.3	0.734	0.0681	1.2	851	11	872	26	+3
11247-028.1	439	106	0.25	21	10895	3.1E-4	24	0.54	53.6	0.074	6.4	7.0	1.4	0.0733	1.6	1.348	2.7	0.1420	1.4	0.524	0.0688	2.3	856	11	894	47	+5
11247-020.1	432	566	1.35	43	9109	1.9E-4	30	0.33	52.9	0.423	2.2	7.0	1.4	0.0716	1.6	1.355	2.5	0.1426	1.4	0.564	0.0689	2.1	860	11	896	43	+4
11247-006.1	48	28	0.61	29	7818	3.2E-3	23	5.49	5.8	0.195	29.0	6.6	2.5	0.1016	10.9	1.092	29.4	0.1429	2.8	0.095	0.0554	29.3	861	22	429	652	-107
11247-053.1	208	116	0.58	55	9570	6.0E-4	24	1.03	25.7	0.179	12.5	6.9	1.6	0.0742	4.2	1.301	6.0	0.1437	1.6	0.264	0.0656	5.8	866	13	795	121	-10
11247-021.3	335	284	0.88	22	10125	3.3E-4	22	0.56	41.5	0.276	2.7	6.9	1.3	0.0710	1.1	1.319	2.4	0.1444	1.3	0.562	0.0663	2.0	869	11	815	41	-7
11247-005.3	1348	202	0.15	102	15177	6.4E-5	29	0.11	167.8	0.047	4.0	6.9	1.2	0.0717	0.7	1.414	1.5	0.1449	1.2	0.830	0.0708	0.8	872	10	951	17	+9
11247-021.2	596	651	1.13	39	10613	1.7E-4	24	0.30	74.3	0.349	1.9	6.9	1.5	0.0705	0.9	1.359	2.0	0.1450	1.5	0.745	0.0680	1.3	873	12	868	27	-1
11247-033.1	131	50	0.40	36	10979	1.6E-4	45	0.28	16.3	0.145	5.3	6.8	1.5	0.0693	2.3	1.345	3.2	0.1456	1.5	0.478	0.0670	2.8	876	13	837	59	-5
11247-041.1	488	288	0.61	63	10276	2.0E-4	29	0.34	61.3	0.186	3.3	6.8	1.4	0.0707	1.6	1.369	2.5	0.1463	1.4	0.566	0.0679	2.1	880	12	865	43	-2
11247-055.1	91	70	0.79	84	7905	1.8E-3	22	3.06	11.5	0.273	8.3	6.6	2.0	0.0938	3.3	1.388	10.0	0.1473	2.1	0.209	0.0683	9.8	886	17	879	202	-1
11247-090.3	703	536	0.79	101	10157	1.1E-4	25	0.19	90.6	0.243	1.9	6.7	1.3	0.0698	0.8	1.409	1.6	0.1500	1.3	0.786	0.0681	1.0	901	11	873	21	-3
11247-005.1	980	121	0.13	95	14141	1.6E-4	24	0.27	126.9	0.038	6.6	6.6	1.4	0.0723	1.2	1.455	2.0	0.1508	1.4	0.680	0.0700	1.5	905	11	929	30	+3
11247-019.1	4253	285	0.07	323	13434	3.6E-6	58	0.01	551.8	0.022	2.5	6.6	1.3	0.0682	0.4	1.419	1.3	0.1510	1.3	0.945	0.0681	0.4	907	11	872	9	-4
11247-005.2	765	166	0.22	96	13682	1.1E-4	28	0.19	99.4	0.071	4.2	6.6	1.3	0.0723	0.8	1.473	1.7	0.1512	1.3	0.777	0.0707	1.1	908	11	948	22	+4
11247-004.1	590	48	0.08	21	13654	2.1E-4	26	0.36	77.0	0.031	10.0	6.6	1.4	0.0763	1.4	1.536	2.3	0.1521	1.4	0.609	0.0733	1.8	913	12	1022	37	+11
11247-023.1	365	319	0.90	92	9520	1.9E-4	32	0.32	48.1	0.275	2.8	6.5	1.7	0.0735	1.7	1.497	2.7	0.1534	1.7	0.632	0.0708	2.1	920	15	951	43	+4
11247-112.1	228	246	1.12	54	10029	2.9E-4	29	0.49	30.3	0.342	2.9	6.4	1.5	0.0693	1.9	1.389	3.2	0.1548	1.5	0.472	0.0651	2.8	928	13	778	58	-21
11247-048.1	228	164	0.74	76	11470	3.5E-4	30	0.60	30.6	0.236	4.2	6.4	1.6	0.0772	2.1	1.556	3.5	0.1562	1.6	0.452	0.0722	3.1	936	14	993	63	+6
11247-064.1	949	113	0.12	47	13062	1.9E-4	23	0.32	128.4	0.043	6.4	6.3	1.4	0.0751	1.2	1.572	2.0	0.1575	1.4	0.678	0.0724	1.5	943	12	997	30	+6
11247-076.1	122	79	0.67	43	9733	1.1E-3	23	1.88	16.5	0.232	6.9	6.2	1.8	0.0911	6.7	1.641	9.7	0.1576	1.9	0.192	0.0755	9.6	944	16	1082	192	+14
11247-120.1	707	135	0.20	49	12859	3.7E-5	45	0.06	96.1	0.058	3.9	6.3	1.3	0.0717	1.1	1.551	1.7	0.1581	1.3	0.764	0.0711	1.1	946	12	962	23	+2
11247-087.1	1915	219	0.12	40	14124	1.3E-4	18	0.23	262.7	0.034	4.5	6.2	1.3	0.0728	0.8	1.560	1.6	0.1597	1.3	0.815	0.0709	0.9	955	12	953	19	-0
11247-016.1	753	51	0.07	34	13288	3.6E-5	50	0.06	103.4	0.023	7.2	6.3	1.4	0.0739	1.2	1.616	1.8	0.1599	1.4	0.743	0.0733	1.2	956	12	1023	25	+7
11247-080.1	675	271	0.41	44	12370	4.9E-6	100	0.01	93.2	0.131	2.0	6.2	1.3	0.0714	0.9	1.580	1.6	0.1607	1.3	0.830	0.0713	0.9	961	12	966	18	+1
11247-017.1	211	181	0.89	54	8971	4.9E-4	25	0.83	29.2	0.276	7.3	6.2	1.6	0.0771	2.1	1.555	3.8	0.1608	1.6	0.419	0.0701	3.4	961	14	932	70	-3
11247-083.1	907	937	1.07	183	10731	1.7E-4	22	0.29	125.7	0.333	3.4	6.2	1.3	0.0735	2.4	1.581	2.9	0.1613	1.4	0.466	0.0711	2.6	964	12	960	52	-0
11247-034.1	217	152	0.72	33	10523	5.4E-4	24	0.91	31.1	0.227	4.4	5.9	1.6	0.0740	2.4	1.525	4.2	0.1667	1.6	0.380	0.0664	3.9	994	15	817	81	-23
11247-009.1	274	133	0.50	83	11297	5.9E-4	21	1.01	39.7	0.153	5.3	5.9	1.5	0.0794	1.9	1.647	3.6	0.1684	1.5	0.427	0.0709	3.3	1003	14	955	67	-5
11247-009.2	534	166	0.32	132	12260	1.5E-4	24	0.26	79.1	0.100	3.4	5.8	1.3	0.0750	0.8	1.732	1.7	0.1725	1.3	0.762	0.0728	1.1	1026	12	1009	22	-2
11247-009.3	216	106	0.51	77	10455	5.3E-4	22	0.90	32.1	0.155	5.2	5.7	1.5	0.0789	1.4	1.703	3.1	0.1732	1.5	0.469	0.0713	2.8	1029	14	967	57	-7

Table 4.1: (continued)

												Ratios											Ages				
												Uncorrected				204 corrected							204 corrected				
Analyses	U (ppm)	Th (ppm)	$^{232}Th/^{238}U$	Yb (ppm)	Hf (ppm)	$^{204}Pb/^{206}Pb$	1σ (%)	f(206)[4] (%)	$^{206}Pb^*$ (ppm)	$^{208}Pb^*/^{206}Pb^*$	1σ (%)	$^{238}U/^{206}Pb$	1σ (%)	$^{207}Pb/^{206}Pb$	1σ (%)	$^{207}Pb^*/^{235}U$	1σ (%)	$^{206}Pb^*/^{238}U$	1σ (%)	error corr.	$^{207}Pb^*/^{206}Pb^*$	1σ (%)	$^{206}Pb^*/^{238}U$	1σ Ma	$^{207}Pb^*/^{206}Pb^*$	1σ Ma	Disc. (%)
11247-011.1	437	106	0.25	30	12112	1.9E-4	22	0.30	100.8	0.078	4.2	3.7	1.4	0.1033	1.0	3.731	1.8	0.2684	1.4	0.770	0.1008	1.2	1533	19	1639	22	+7
11247-001.1	297	215	0.75	69	9837	1.8E-4	28	0.29	70.8	0.224	2.7	3.6	1.5	0.1004	1.2	3.746	2.1	0.2775	1.5	0.717	0.0979	1.5	1579	21	1584	27	+0
11247-126.1	518	435	0.87	89	8907	5.7E-5	33	0.09	127.8	0.258	1.7	3.5	1.4	0.0990	0.8	3.888	1.6	0.2871	1.4	0.837	0.0982	0.9	1627	20	1591	17	-3
11247-118.1	340	136	0.42	31	9894	1.3E-4	27	0.20	86.1	0.123	3.0	3.4	1.4	0.1083	1.0	4.342	1.8	0.2953	1.4	0.798	0.1066	1.1	1668	21	1743	20	+5
11247-043.1	2057	62	0.03	28	14297	2.6E-5	21	0.04	522.4	0.009	4.5	3.4	1.3	0.1058	0.3	4.300	1.3	0.2957	1.3	0.963	0.1055	0.4	1670	19	1722	7	+3
11247-060.1	108	137	1.31	55	11177	1.3E-3	18	2.10	27.7	0.358	4.5	3.3	2.0	0.1222	2.0	4.282	4.5	0.2984	2.0	0.447	0.1041	4.0	1683	30	1698	74	+1
11247-108.1	141	63	0.46	22	9481	2.5E-4	28	0.40	37.0	0.130	4.5	3.3	1.6	0.1134	1.4	4.637	2.3	0.3059	1.6	0.689	0.1099	1.7	1721	24	1798	31	+5
11247-046.1	404	257	0.66	30	11831	2.7E-4	18	0.41	112.6	0.194	5.8	3.1	1.4	0.1192	0.9	5.172	1.8	0.3245	1.4	0.798	0.1156	1.1	1812	23	1889	20	+5
11247-068.1	248	76	0.32	40	10326	3.5E-4	20	0.54	73.7	0.088	5.1	2.9	1.6	0.1344	1.1	6.191	2.1	0.3461	1.6	0.762	0.1297	1.3	1916	26	2095	23	+10
11247-072.1	206	115	0.57	34	9942	5.6E-4	18	0.86	62.7	0.166	4.3	2.8	1.7	0.1379	1.2	6.355	2.4	0.3534	1.7	0.705	0.1304	1.7	1951	28	2104	30	+8
11247-075.1	430	75	0.18	23	11801	1.6E-4	20	0.24	154.7	0.052	4.4	2.4	1.4	0.1676	0.7	9.562	1.6	0.4189	1.4	0.893	0.1656	0.7	2255	27	2513	12	+12
11247-067.1	254	272	1.11	45	11064	1.4E-4	28	0.20	96.5	0.336	1.9	2.3	1.6	0.1671	0.9	10.085	1.8	0.4424	1.6	0.860	0.1653	0.9	2361	31	2511	16	+7
11247-119.1	193	272	1.45	57	9363	8.0E-5	35	0.11	73.6	0.417	1.6	2.2	1.5	0.1644	0.8	10.012	1.8	0.4443	1.5	0.870	0.1634	0.9	2370	30	2491	15	+6
11247-007.1	646	195	0.31	51	12068	8.4E-5	22	0.12	247.9	0.086	2.4	2.2	1.4	0.1655	0.6	10.136	1.5	0.4471	1.4	0.924	0.1644	0.6	2382	28	2502	10	+6
11247-089.1	138	188	1.41	50	8613	3.2E-4	26	0.46	53.0	0.401	2.5	2.2	1.8	0.1742	1.2	10.516	2.3	0.4480	1.8	0.792	0.1702	1.4	2386	36	2560	23	+8
11247-102.2	132	138	1.08	20	9570	8.4E-5	35	0.12	51.5	0.307	2.0	2.2	1.5	0.1672	0.9	10.430	1.8	0.4553	1.5	0.866	0.1661	0.9	2419	31	2519	15	+5
11247-105.1	179	260	1.50	55	9572	2.8E-4	20	0.39	71.1	0.433	1.8	2.2	1.6	0.1714	1.0	10.710	1.9	0.4625	1.6	0.826	0.1679	1.1	2451	32	2537	18	+4
11247-097.1	90	161	1.84	41	8261	8.9E-5	50	0.13	36.4	0.517	2.2	2.1	1.8	0.1637	1.2	10.516	2.2	0.4690	1.8	0.815	0.1626	1.3	2479	38	2483	22	+0
11247-095.1	202	192	0.98	84	8132	6.5E-5	38	0.09	83.9	0.286	1.9	2.1	1.5	0.1704	0.8	11.288	1.7	0.4829	1.5	0.882	0.1695	0.8	2540	32	2553	14	+1
11247-044.1	240	225	0.97	37	11016	9.4E-6	71	0.01	112.2	0.274	1.4	1.8	1.4	0.2110	0.5	15.812	1.5	0.5437	1.4	0.940	0.2109	0.5	2799	32	2913	8	+5
Sample BD1437, Quartzite (upper), Latitude: 28.15515, Longitude: 85.39807																											See footnote C
11246-034.1	1093	2	0.00	37	13995	4.6E-3	26	8.53	2.3	-0.141	38.9	378.6	1.4	0.0646	9.6	0.002	238.4	0.0024	2.8	0.012	0.0074	238.4	15.6	0.4	-	-	-
11246-049.1	1002	9	0.01	43	13685	2.3E-3	29	4.36	4.3	0.020	160.5	189.5	1.3	0.0866	3.6	0.036	20.8	0.0050	1.8	0.088	0.0524	20.7	32.5	0.6	301	473	+89
11246-042.3	594	17	0.03	37	13274	3.0E-3	21	5.59	5.4	0.079	38.2	89.2	1.3	0.0970	7.4	0.077	23.2	0.0106	1.8	0.076	0.0530	23.1	67.9	1.2	328	524	+80
11246-042.1	158	51	0.33	31	9830	4.9E-4	32	0.86	13.7	0.120	8.5	9.8	1.5	0.0737	5.1	0.927	6.8	0.1009	1.5	0.228	0.0667	6.6	619	9	827	137	+26
11246-006.1	1475	1117	0.78	71	12479	2.2E-4	18	0.39	146.3	0.312	1.7	8.6	1.7	0.0714	0.9	1.087	2.1	0.1155	1.7	0.804	0.0683	1.3	704	11	877	26	+21
11246-045.1	213	181	0.88	50	10933	5.4E-4	27	0.94	22.7	0.293	4.3	8.0	1.5	0.0709	1.8	1.079	4.2	0.1241	1.5	0.361	0.0631	3.9	754	11	710	83	-7
11246-073.1	167	209	1.29	34	10930	1.8E-3	33	3.21	18.5	0.477	12.3	7.5	2.1	0.1318	19.9	1.899	26.7	0.1291	2.4	0.089	0.1067	26.6	783	18	1743	488	+58
11246-033.1	656	314	0.49	64	10245	2.3E-4	25	0.41	72.8	0.139	3.8	7.7	1.4	0.0694	1.2	1.176	2.3	0.1292	1.4	0.600	0.0660	1.8	783	10	806	38	+3
11246-036.1	420	253	0.62	47	11429	5.4E-4	19	0.94	47.1	0.190	4.1	7.6	1.8	0.0733	2.7	1.178	4.2	0.1303	1.8	0.433	0.0656	3.8	790	14	792	80	+0
11246-001.1	856	541	0.65	47	10968	4.3E-5	45	0.08	95.8	0.197	2.2	7.7	1.3	0.0693	0.9	1.234	1.6	0.1303	1.3	0.801	0.0687	1.0	790	9	889	20	+12
11246-063.1	226	182	0.83	57	11341	1.7E-3	26	2.91	25.8	0.238	19.2	7.3	1.9	0.0962	14.7	1.324	22.1	0.1329	2.0	0.092	0.0723	22.0	804	15	993	447	+20
11246-079.1	54	43	0.82	73	9282	2.4E-3	24	4.22	6.1	0.295	10.7	7.2	2.2	0.1140	2.8	1.467	11.7	0.1335	2.4	0.206	0.0797	11.5	808	18	1189	227	+34
11246-010.1	25	24	0.98	80	7132	3.4E-3	32	5.97	2.9	0.301	19.0	7.0	3.3	0.1294	19.6	1.500	39.3	0.1344	3.9	0.098	0.0809	39.1	813	30	1219	769	+35
11246-042.2	118	50	0.44	34	9712	1.3E-3	19	2.24	13.7	0.120	10.2	7.3	1.5	0.0780	1.7	1.102	6.7	0.1347	1.6	0.234	0.0594	6.6	815	12	580	142	-43
11246-071.1	119	113	0.98	30	9937	2.3E-3	21	3.99	13.8	0.275	9.8	7.1	2.0	0.0868	11.3	0.992	23.8	0.1352	2.2	0.093	0.0532	23.7	817	17	337	537	-152
11246-006.3	194	191	1.02	91	9991	9.5E-4	20	1.65	23.1	0.296	4.6	7.1	1.5	0.0787	3.8	1.243	6.6	0.1386	1.6	0.240	0.0650	6.4	837	12	775	134	-8
11246-066.1	1240	284	0.24	64	14308	2.4E-4	20	0.42	149.9	0.071	4.9	7.1	1.3	0.0705	0.9	1.302	1.9	0.1407	1.3	0.674	0.0671	1.4	849	10	841	30	-1
11246-026.1	61	67	1.14	28	10130	4.3E-3	54	7.42	7.3	0.342	31.3	6.6	2.8	0.1314	26.7	1.361	74.8	0.1408	5.2	0.069	0.0701	74.6	849	41	931	1531	+9

Table 4.1: (continued)

												Ratios											Ages				
												Uncorrected				204 corrected							204 corrected				
Analyses	U (ppm)	Th (ppm)	$^{232}Th/^{238}U$	Yb (ppm)	Hf (ppm)	$^{204}Pb/^{206}Pb$	1σ (%)	f(206)[4] (%)	$^{206}Pb^*$ (ppm)	$^{208}Pb^*/^{206}Pb^*$	1σ (%)	$^{238}U/^{206}Pb$	1σ (%)	$^{207}Pb/^{206}Pb$	1σ (%)	$^{207}Pb^*/^{235}U$	1σ (%)	$^{206}Pb^*/^{238}U$	1σ (%)	error corr.	$^{207}Pb^*/^{206}Pb^*$	1σ (%)	$^{206}Pb^*/^{238}U$	1σ Ma	$^{207}Pb^*/^{206}Pb^*$	1σ Ma	Disc. (%)
11246-008.1	65	70	1.11	72	7476	1.3E-3	28	2.21	8.0	0.308	7.5	6.9	2.0	0.0771	3.0	1.147	10.1	0.1419	2.1	0.207	0.0586	9.9	856	17	553	215	-59
11246-032.1	81	71	0.91	85	7279	2.5E-3	22	4.37	9.9	0.204	13.8	6.7	2.1	0.0928	7.7	1.096	20.3	0.1421	2.4	0.116	0.0560	20.1	856	19	451	447	-96
11246-065.1	278	233	0.87	110	11501	4.6E-4	29	0.80	34.3	0.279	4.3	6.9	1.6	0.0753	4.0	1.359	5.5	0.1434	1.6	0.287	0.0687	5.3	864	13	891	109	+3
11246-018.1	618	900	1.51	112	9452	1.6E-4	29	0.28	76.3	0.466	1.8	6.9	1.3	0.0711	1.0	1.365	2.0	0.1439	1.3	0.676	0.0688	1.4	866	11	893	30	+3
11246-052.1	328	131	0.41	73	10262	2.6E-4	31	0.44	42.0	0.128	9.5	6.7	1.4	0.0730	1.4	1.424	2.6	0.1490	1.4	0.544	0.0693	2.2	895	12	908	45	+1
11246-007.1	202	339	1.73	60	8677	1.9E-3	18	3.26	26.4	0.501	4.6	6.4	1.8	0.0865	8.1	1.238	15.2	0.1522	1.9	0.124	0.0590	15.1	913	16	567	329	-66
11246-049.2	106	59	0.58	32	9832	3.4E-3	24	5.91	13.9	0.217	29.0	6.2	2.5	0.1334	20.5	1.788	37.2	0.1522	3.0	0.079	0.0852	37.1	914	25	1320	718	+33
11246-038.1	435	248	0.59	56	11210	2.9E-4	25	0.50	57.6	0.167	3.9	6.5	1.4	0.0749	1.2	1.503	2.4	0.1542	1.4	0.580	0.0707	2.0	925	12	948	40	+3
11246-012.1	928	99	0.11	90	13946	3.0E-4	19	0.51	123.6	0.030	15.6	6.4	1.3	0.0746	1.9	1.503	2.7	0.1550	1.3	0.495	0.0703	2.3	929	11	938	47	+1
11246-002.1	414	227	0.57	31	11475	4.1E-5	58	0.07	55.1	0.175	3.0	6.4	1.3	0.0726	1.0	1.540	1.8	0.1552	1.3	0.758	0.0720	1.1	930	12	985	23	+6
11246-015.1	748	99	0.14	45	13385	1.5E-4	26	0.27	100.9	0.044	6.4	6.4	1.3	0.0755	0.9	1.587	1.8	0.1570	1.3	0.737	0.0733	1.2	940	11	1023	24	+9
11246-025.1	318	116	0.38	57	9617	9.1E-4	18	1.56	43.1	0.077	11.0	6.2	1.5	0.0777	1.6	1.404	4.5	0.1576	1.5	0.343	0.0646	4.2	943	13	761	89	-26
11246-053.1	231	286	1.28	94	11113	9.2E-4	19	1.59	31.3	0.389	3.4	6.2	1.5	0.0776	3.6	1.398	6.1	0.1577	1.5	0.253	0.0643	5.9	944	14	751	125	-28
11246-068.1	205	103	0.52	28	12569	1.2E-3	26	2.09	27.8	0.166	16.9	6.2	2.0	0.0862	2.6	1.503	7.8	0.1584	2.1	0.270	0.0688	7.5	948	18	893	154	-7
11246-044.1	1032	319	0.32	118	13172	1.5E-4	24	0.26	142.9	0.096	3.5	6.2	1.3	0.0735	0.8	1.586	1.7	0.1613	1.3	0.755	0.0713	1.1	964	11	967	23	+0
11246-013.1	1107	769	0.72	82	12772	7.0E-5	32	0.12	154.3	0.225	1.9	6.2	1.3	0.0726	0.7	1.603	1.6	0.1624	1.3	0.824	0.0716	0.9	970	12	975	18	+0
11246-070.1	923	561	0.63	88	12569	1.0E-4	32	0.17	131.5	0.191	2.6	6.0	1.3	0.0732	1.6	1.641	2.2	0.1658	1.3	0.604	0.0718	1.7	989	12	980	36	-1
11246-076.1	2409	120	0.05	129	15309	5.3E-5	21	0.09	350.0	0.015	5.0	5.9	1.2	0.0729	0.4	1.683	1.3	0.1691	1.2	0.930	0.0722	0.5	1007	11	991	10	-2
11246-023.1	903	64	0.07	105	13678	1.8E-5	50	0.03	212.6	0.024	4.7	3.6	1.3	0.1008	0.5	3.799	1.4	0.2741	1.3	0.925	0.1005	0.5	1561	18	1634	10	+5
11246-041.1	364	37	0.11	13	13847	2.8E-4	20	0.44	92.4	0.030	10.2	3.4	1.5	0.1158	0.8	4.564	1.8	0.2956	1.5	0.815	0.1120	1.1	1669	22	1832	19	+10
11246-075.1	899	338	0.39	265	17465	1.9E-4	27	0.29	239.2	0.121	3.2	3.2	1.4	0.1122	2.6	4.682	3.1	0.3097	1.4	0.456	0.1096	2.7	1739	21	1793	50	+3
11246-074.1	274	237	0.89	43	10433	2.1E-4	24	0.31	105.0	0.248	2.4	2.2	1.5	0.1658	0.7	10.020	1.7	0.4456	1.5	0.889	0.1631	0.8	2376	30	2488	13	+5
11246-034.1	56	66	1.20	44	9105	8.8E-4	25	1.24	22.7	0.339	4.9	2.1	2.4	0.1676	1.6	10.092	3.5	0.4677	2.4	0.697	0.1565	2.5	2473	50	2418	43	-3
Sample BD1215, pelitic Kfs augen gneiss, Latitude: 28.23144, Longitude: 85.55761																											See footnote D
11119-68.2	4951	37	0.01	88	19100	1.8E-4	70	0.32	17.4	0.001	31.2	243.1	1.4	0.0516	2.9	0.028	5.1	0.0041	1.4	0.278	0.0490	4.9	26.4	0.4	150	114	+125
11119-68.1	3582	25	0.01	126	18294	3.6E-4	18	0.65	14.2	-0.010	19.4	215.8	1.6	0.0492	2.3	0.028	3.8	0.0046	1.6	0.409	0.0439	3.5	29.6	0.5	-118	86	+34
11119-158.2	7094	54	0.01	148	17973	1.1E-4	20	0.20	31.8	0.000	13.5	191.3	1.3	0.0486	1.8	0.034	2.3	0.0052	1.3	0.556	0.0470	1.9	33.5	0.4	51	46	+105
11119-110.1	2469	20	0.01	114	12028	1.2E-3	31	2.08	12.4	-0.030	23.4	167.8	1.5	0.0511	3.1	0.027	16.8	0.0058	1.6	0.097	0.0339	16.7	37.5	0.6	-802	474	+128
11119-4.1	2647	20	0.01	69	15167	4.6E-4	44	0.84	13.4	-0.004	12.7	168.0	1.2	0.0504	3.0	0.035	7.9	0.0059	1.3	0.161	0.0435	7.8	37.9	0.5	-136	192	+85
11119-67.1	4383	34	0.01	58	16432	1.0E-4	19	0.18	22.2	0.003	23.5	168.9	1.3	0.0528	2.0	0.042	2.5	0.0059	1.3	0.516	0.0514	2.1	38.0	0.5	257	49	+81
11119-38.1	2811	22	0.01	62	14890	1.6E-4	27	0.28	14.5	0.010	20.0	165.9	1.2	0.0525	2.8	0.042	3.4	0.0060	1.2	0.359	0.0502	3.2	38.6	0.5	206	73	+77
11119-22.1	4518	32	0.01	151	17484	-4.2E-6	1149	-0.01	23.4	0.010	22.1	166.0	1.2	0.0493	2.5	0.041	3.1	0.0060	1.2	0.385	0.0494	2.9	38.7	0.5	165	68	+48
11119-158.1	7603	56	0.01	144	17340	2.4E-5	207	0.04	39.9	0.003	15.5	163.8	1.5	0.0479	1.0	0.040	2.4	0.0061	1.5	0.620	0.0475	1.9	39.2	0.6	75	45	+73
11119-146.1	1313	15	0.01	157	13709	3.1E-4	38	0.57	14.1	-0.001	13.3	79.8	1.6	0.0566	1.5	0.089	4.0	0.0125	1.6	0.393	0.0520	3.7	79.8	1.3	287	85	+58
11119-100.1	1303	8	0.01	121	14413	4.9E-4	38	0.89	22.4	-0.008	19.6	49.6	1.6	0.0596	2.1	0.144	6.0	0.0200	1.6	0.273	0.0524	5.7	128	2	303	131	+57
11119-9.3	1708	15	0.01	142	15356	6.5E-5	72	0.12	43.4	0.004	12.4	33.8	3.1	0.0564	0.6	0.226	3.4	0.0296	3.1	0.914	0.0554	1.4	188	6	429	31	+186
11119-59.1	785	9	0.01	67	7635	1.2E-3	13	2.10	30.3	-0.038	11.2	21.7	1.6	0.0574	1.0	0.249	6.2	0.0450	1.7	0.269	0.0401	6.0	284	5	-348	154	+19
11119-116.1	1359	56	0.04	210	13738	1.6E-4	19	0.30	66.2	0.016	4.1	17.6	2.1	0.0580	0.7	0.435	2.3	0.0568	2.1	0.892	0.0556	1.1	356	7	435	24	+17
11119-90.1	1442	10	0.01	173	14522	4.1E-6	58	0.01	72.1	0.004	9.6	17.2	1.5	0.0557	0.6	0.447	1.6	0.0583	1.5	0.922	0.0557	0.6	365	5	439	14	+32
11119-3.1	1086	10	0.01	174	15048	1.1E-4	43	0.20	54.6	0.003	15.6	17.0	1.3	0.0598	1.3	0.469	2.2	0.0585	1.3	0.580	0.0581	1.8	367	5	535	40	+20

Table 4.1 (continued)

												Ratios										Ages				
												Uncorrected				204 corrected										
Analyses	U (ppm)	Th (ppm)	$^{232}Th/^{238}U$	Yb (ppm)	Hf (ppm)	$^{204}Pb/^{206}Pb$	1σ (%)	f(206)[4] (%)	$^{206}Pb^*$ (ppm)	$^{208}Pb^*/^{206}Pb^*$	1σ (%)	$^{238}U/^{206}Pb$	1σ (%)	$^{207}Pb/^{206}Pb$	1σ (%)	$^{207}Pb^*/^{235}U$	1σ (%)	$^{206}Pb^*/^{238}U$	1σ (%)	error corr.	$^{207}Pb^*/^{206}Pb^*$	1σ (%)	$^{206}Pb^*/^{238}U$	1σ Ma	$^{207}Pb^*/^{206}Pb^*$	1σ Ma	Disc. (%)
11119-50.1	1109	5	0.00	108	13703	1.3E-4	25	0.24	57.5	-0.002	13.5	16.5	1.5	0.0583	0.7	0.470	1.9	0.0604	1.5	0.798	0.0564	1.1	378	5	467	25	+10
11119-63.1	623	45	0.07	250	12652	5.8E-5	27	0.10	36.3	0.027	8.3	14.7	1.5	0.0572	0.9	0.528	1.8	0.0679	1.5	0.845	0.0564	1.0	424	6	468	22	+11
11119-142.1	1413	22	0.02	164	13715	1.3E-4	23	0.23	83.7	0.010	8.2	14.5	1.2	0.0586	1.1	0.540	1.8	0.0690	1.2	0.673	0.0568	1.3	430	5	483	29	+11
11119-11.1	1557	15	0.01	209	16021	7.2E-5	15	0.13	94.3	0.003	12.1	14.2	1.2	0.0580	1.0	0.554	1.6	0.0705	1.2	0.759	0.0570	1.0	439	5	490	23	+7
11119-49.1	1772	34	0.02	178	15287	6.5E-5	25	0.12	107.4	0.005	5.5	14.2	1.5	0.0574	0.5	0.549	1.6	0.0706	1.5	0.917	0.0564	0.6	440	6	469	14	+4
11119-154.1	648	483	0.77	159	12284	3.1E-5	41	0.06	40.2	0.266	1.8	13.8	1.9	0.0568	1.0	0.561	2.2	0.0722	1.9	0.876	0.0564	1.1	449	8	467	24	-7
11119-105.1	1765	12	0.01	213	16523	1.2E-4	21	0.23	110.4	0.000	13.3	13.7	1.3	0.0571	0.9	0.555	1.8	0.0728	1.3	0.729	0.0553	1.2	453	6	425	27	+5
11119-44.1	1949	43	0.02	182	15939	4.2E-5	32	0.08	125.4	0.007	5.2	13.3	1.5	0.0576	0.5	0.589	1.6	0.0749	1.5	0.922	0.0570	0.6	466	7	491	14	-1
11119-7.1	1351	10	0.01	235	16283	9.8E-5	26	0.18	87.0	0.002	7.7	13.3	1.5	0.0576	0.6	0.581	1.8	0.0750	1.5	0.857	0.0562	0.9	466	7	460	20	-16
11119-9.2	1170	32	0.03	218	13094	1.9E-4	18	0.34	75.5	0.004	5.3	13.3	1.5	0.0576	0.6	0.568	1.9	0.0751	1.5	0.811	0.0548	1.1	467	7	406	24	-14
11119-56.1	585	90	0.16	133	9678	1.4E-4	39	0.25	38.0	0.042	3.8	13.2	1.5	0.0571	0.9	0.574	2.3	0.0756	1.5	0.666	0.0551	1.7	470	7	416	38	+14
11119-95.1	718	406	0.58	173	13107	-6.5E-7	364	0.00	46.7	0.189	1.8	13.2	1.7	0.0583	0.8	0.608	1.9	0.0757	1.7	0.891	0.0583	0.8	470	7	542	18	+14
11119-37.1	1405	12	0.01	199	16919	6.1E-5	117	0.11	92.2	0.002	15.7	13.1	1.9	0.0577	1.0	0.598	2.8	0.0764	1.9	0.674	0.0568	2.1	474	9	485	46	+8
11119-33.1	1208	8	0.01	198	17602	-7.2E-6	146	-0.01	79.3	0.005	14.7	13.1	1.3	0.0575	1.0	0.607	1.7	0.0765	1.3	0.765	0.0576	1.1	475	6	515	24	-4
11119-115.1	672	247	0.38	121	11249	1.2E-5	397	0.02	44.3	0.119	2.3	13.0	1.6	0.0563	0.8	0.594	2.1	0.0767	1.6	0.731	0.0562	1.5	476	7	458	32	-2
11119-85.1	1305	14	0.01	226	16537	3.7E-5	45	0.07	87.0	0.003	8.6	12.9	1.5	0.0571	0.6	0.605	1.7	0.0776	1.5	0.900	0.0566	0.7	482	7	474	16	+28
11119-9.4	143	117	0.85	102	10257	2.2E-4	28	0.39	9.6	0.306	5.4	12.7	1.3	0.0651	3.0	0.672	3.7	0.0787	1.3	0.352	0.0619	3.5	488	6	672	75	+4
11119-128.1	682	29	0.04	217	13864	6.3E-6	354	0.01	47.0	0.014	6.5	12.5	1.8	0.0577	0.8	0.637	2.1	0.0802	1.8	0.877	0.0576	1.0	497	9	516	22	-0
11119-164.1	773	42	0.06	295	13308	8.8E-5	61	0.16	53.5	0.017	5.2	12.4	1.5	0.0584	0.8	0.635	2.2	0.0806	1.5	0.686	0.0572	1.6	500	7	498	35	-20
11119-84.1	467	193	0.43	52	10411	1.3E-4	27	0.23	42.1	0.127	2.1	9.5	3.2	0.0602	2.4	0.846	4.1	0.1051	3.2	0.780	0.0584	2.6	644	20	543	57	+10
11119-4.2	146	102	0.72	45	11301	3.6E-4	41	0.64	18.8	0.233	4.7	6.7	5.7	0.0773	2.1	1.487	6.8	0.1494	5.7	0.838	0.0722	3.7	898	48	992	76	+12
11119-89.1	1598	404	0.26	143	13352	5.8E-6	38	0.01	210.9	0.089	1.3	6.5	1.5	0.0741	0.4	1.567	1.5	0.1536	1.5	0.971	0.0740	0.4	921	13	1041	8	+1
11119-22.2	179	107	0.62	70	9939	1.3E-4	29	0.23	25.8	0.192	4.2	5.9	1.3	0.0746	1.8	1.687	2.4	0.1682	1.3	0.558	0.0728	2.0	1002	12	1007	40	+11
11119-38.2	399	57	0.15	44	12747	3.4E-5	28	0.06	61.7	0.051	5.1	5.5	1.4	0.0804	3.2	1.986	3.5	0.1803	1.4	0.412	0.0799	3.2	1069	14	1194	63	+11
Sample BD1435, Arkosic psammite (base of unit), Latitude: 28.23224, Longitude: 85.55896																										See footnote E
11245-005.2	570	41	0.07	123	12601	9.6E-4	24	1.75	18.6	0.043	34.4	25.9	1.7	0.0692	4.4	0.289	8.4	0.0379	1.8	0.212	0.0553	8.3	240	4	423	184	+44
11245-005.1	719	533	0.77	192	11420	2.0E-4	29	0.36	49.4	0.243	2.9	12.5	1.5	0.0606	1.3	0.635	2.5	0.0799	1.5	0.611	0.0577	2.0	496	7	517	44	+4
11245-006.1	543	43	0.08	51	12965	6.2E-5	41	0.11	51.7	0.057	4.8	9.0	2.0	0.0736	1.7	1.110	2.7	0.1107	2.0	0.739	0.0727	1.8	677	13	1007	37	+34
11245-009.1	359	150	0.43	35	12515	5.5E-5	58	0.09	47.3	0.144	3.8	6.5	1.4	0.0734	1.2	1.533	1.9	0.1531	1.4	0.711	0.0726	1.4	918	12	1003	28	+9
11245-004.1	425	170	0.41	159	10189	2.1E-4	26	0.37	56.3	0.117	4.1	6.5	1.3	0.0713	1.1	1.449	2.1	0.1541	1.3	0.640	0.0682	1.6	924	12	875	34	-6
11245-007.1	278	212	0.79	115	9638	1.8E-4	28	0.31	38.8	0.262	2.5	6.1	1.3	0.0750	1.0	1.627	2.0	0.1629	1.3	0.679	0.0724	1.5	973	12	998	29	+3
11245-001.1	496	1591	3.31	155	9243	2.0E-4	26	0.35	70.9	1.036	1.3	6.0	1.4	0.0740	1.0	1.629	2.1	0.1664	1.4	0.661	0.0710	1.5	992	12	958	31	-4
11245-002.1	245	130	0.55	49	9571	4.3E-4	24	0.73	37.9	0.174	4.7	5.5	2.5	0.0774	1.6	1.769	3.7	0.1802	2.5	0.683	0.0712	2.7	1068	25	963	56	-12
11245-003.1	595	328	0.57	176	10616	1.7E-4	24	0.28	98.2	0.181	2.5	5.2	1.3	0.0771	1.6	1.978	2.2	0.1921	1.3	0.596	0.0747	1.8	1133	14	1060	36	-8
11245-008.1	412	164	0.41	93	9763	7.1E-5	26	0.09	196.7	0.118	2.2	1.8	1.8	0.1921	0.4	14.664	1.9	0.5561	1.8	0.971	0.1913	0.5	2850	43	2753	7	-4

Notes: A) IP752; 23µm spot, 4nA primary beam; Primary standard Temora 2 (GSC lab number 10493); Calibration error 1.18% (included), external error 0.42% not included; Secondary standard 6266: measured 204 corr $^{206}Pb/^{238}U$ age 557.3±3.6 Ma (accepted age 559 Ma).

B) IP752; 23µm spot, 4nA primary beam; Primary standard Temora 2 (GSC lab number 10493); Calibration error 1.25% or 1.18% (included), external error 0.59% or 0.42% not included (Session 2 and 3 respectively); Secondary standard 6266: measured 204 corr $^{206}Pb/^{238}U$ age 558±14 Ma (accepted age 559 Ma) for session 2, see other footnotes for session 3.

C) IP752; 23µm spot, 4nA primary beam; Primary standard Temora 2 (GSC lab number 10493); Calibration error 1.18% (included), external error 0.42% not included (Session 3); Secondary standard 6266: measured 204 corr $^{206}Pb/^{238}U$ age 557.3±3.6 Ma (accepted age 559 Ma).

D) IP720; 16µm spot, 6nA primary beam or 12µm spot, 2.5nA primary beam; Primary standard Temora 2 (GSC lab number 10493); Calibration error is 1.49% (large spot) or 1.20% (small spot) and is included in all calculations, external error 0.43% (large spot) and 0.39% (small spot) is not included; Secondary standard 6266: measured 204 corr $^{206}Pb/^{238}U$ age 557.9±4.4 Ma (accepted age 559 Ma).

E) IP752; 23µm spot, 4nA primary beam; Primary standard Temora 2 (GSC lab number 10493); Calibration error 1.18% (included), external error 0.42% not included (Session 3); Secondary standard 6266: measured 204 corr $^{206}Pb/^{238}U$ age 557.3±3.6 Ma (accepted age 559 Ma).

Table 4.2 U-Th-Pb monazite geochronology data

Sample BD1435, Arkosic psammite, Latitude: 28.23224, Longitude: 85.55896

												Ratios									Ages			
												Uncorrected				204 corrected					204 corrected		207 corrected	
Analyses	Domain interp'n	U (ppm)	Th (ppm)	$^{232}Th/^{238}U$	$^{204}Pb/^{206}Pb$	1σ (%)	$f(206)^2_{04}$ (%)	$^{206}Pb^*$ (ppm)	$^{208}Pb^*/^{206}Pb^*$	1σ (%)	$^{238}U/^{206}Pb$	1σ (%)	$^{207}Pb/^{206}Pb$	1σ (%)	$^{207}Pb^*/^{235}U$	1σ (%)	$^{206}Pb^*/^{238}U$	1σ (%)	error corr.	$^{207}Pb^*/^{206}Pb^*$	1σ (%)	$^{206}Pb^*/^{238}U$	1σ (Ma)	$^{206}Pb^*/^{238}U$	1σ (Ma)
11245M-028.1	rim	7211	33653	4.82	2.0E-3	19	3.67	19.9	1.502	2.6	31.1	2.6	0.0880	1.7	0.025	11.1	0.0032	1.5	0.135	0.0560	11.0	21	0.3	20.5	0.3
11245M-026.2	rim	5774	21956	3.93	3.1E-3	20	5.74	16.2	1.250	3.2	25.5	1.0	0.0603	1.1	0.023	20.4	0.0033	2.1	0.102	0.0505	20.3	21	0.4	20.9	0.4
11245M-029.1	rim	6051	31609	5.40	3.8E-3	16	7.13	18.2	1.714	2.5	24.1	1.0	0.0685	1.1	0.009	59.7	0.0035	2.0	0.034	0.0188	59.7	23	0.5	23.3	0.4
11245M-061.1	rim	6975	34175	5.06	3.6E-3	16	6.69	21.9	1.600	2.4	22.4	1.1	0.0609	2.4	0.017	31.0	0.0037	1.6	0.051	0.0336	31.0	24	0.4	23.9	0.3
11245M-069.1	rim	6533	22255	3.52	4.4E-3	13	8.23	21.1	1.072	3.2	19.9	1.5	0.0743	2.0	0.013	39.0	0.0038	2.4	0.062	0.0256	38.9	24	0.6	24.8	0.5
11245M-067.2	rim	5537	26335	4.91	1.9E-3	20	3.50	18.0	1.519	2.6	18.8	1.1	0.0662	1.1	0.021	15.6	0.0038	2.1	0.136	0.0400	15.5	24	0.5	24.5	0.5
11245M-024.2	rim	5722	27132	4.90	4.0E-3	16	7.50	19.6	1.466	2.9	18.4	1.9	0.0615	1.0	0.008	75.6	0.0040	1.7	0.023	0.0146	75.6	26	0.4	26.7	0.3
11245M-049.2	rim	6349	41060	6.68	2.6E-3	21	4.89	23.9	1.485	3.8	15.0	1.6	0.0763	1.9	0.020	38.0	0.0044	2.7	0.072	0.0334	37.9	28	0.8	28.6	0.8
11245M-057.1	rim	5934	35719	6.22	2.7E-3	19	5.00	22.3	1.889	2.2	14.3	1.1	0.0656	1.2	0.024	20.8	0.0044	1.7	0.081	0.0402	20.7	28	0.5	28.4	0.4
11245M-052.2	rim	6139	30785	5.18	2.2E-3	20	4.09	23.9	5.629	1.4	14.2	1.3	0.0683	1.2	0.027	16.0	0.0045	1.7	0.109	0.0430	15.9	29	0.5	29.2	0.4
11245M-005.1	mixed	6689	44822	6.92	2.9E-3	14	5.34	32.8	2.070	1.8	13.9	1.3	0.0690	1.3	0.025	21.2	0.0057	1.5	0.072	0.0319	21.2	37	0.6	37.3	0.5
11245M-066.2	mixed	5735	41311	7.44	2.0E-3	20	3.74	38.7	3.463	1.5	14.0	1.3	0.0601	1.5	0.050	15.2	0.0079	1.9	0.122	0.0460	15.1	50	0.9	50.5	0.9
11245M-044.2	mixed	4998	30485	6.30	2.8E-3	15	5.19	40.9	2.419	1.7	13.9	1.2	0.0627	1.1	0.058	15.7	0.0095	1.5	0.097	0.0441	15.6	61	0.9	61.4	0.8
11245M-055.2	mixed	4339	16703	3.98	8.0E-4	19	1.49	47.8	1.766	2.5	13.7	1.3	0.0658	1.3	0.097	4.8	0.0128	1.0	0.209	0.0549	4.7	82	0.8	81.3	0.8
11245M-049.3	mixed	2757	22687	8.50	2.0E-3	15	3.61	56.1	5.745	1.7	13.5	1.6	0.0710	1.6	0.188	8.4	0.0237	2.3	0.274	0.0575	8.1	151	3	149	3
11245M-015.1	mixed	1233	22833	19.13	2.5E-3	15	4.62	32.4	11.988	1.1	13.4	1.2	0.0654	1.1	0.216	12.0	0.0306	2.7	0.228	0.0512	11.7	194	5	194	5
11245M-052.1	mixed	3066	30190	10.17	4.6E-4	21	0.84	102.6	4.161	0.8	13.3	1.3	0.0657	1.2	0.288	3.1	0.0390	1.0	0.330	0.0536	2.9	246	2	246	2
11245M-015.2	mixed	2763	54325	20.31	1.0E-3	14	1.83	96.9	9.818	1.2	13.4	1.0	0.0586	2.5	0.303	4.2	0.0408	1.0	0.250	0.0539	4.0	258	3	257	3
11245M-026.1	mixed	2489	21851	9.07	5.2E-4	23	0.95	94.5	3.272	1.3	13.1	1.2	0.0659	1.2	0.325	4.5	0.0442	1.1	0.249	0.0533	4.3	279	3	278	3
11245M-049.1	mixed	784	9240	12.17	1.2E-3	21	2.14	33.1	5.001	1.3	13.1	1.3	0.0709	1.3	0.387	7.1	0.0491	1.6	0.222	0.0572	7.0	309	5	307	5
11245M-069.2	mixed	1773	12212	7.12	6.3E-4	19	1.14	80.2	2.766	0.8	13.2	1.0	0.0606	0.9	0.414	3.5	0.0526	1.1	0.316	0.0571	3.3	331	4	329	4
11245M-044.1	mixed	2601	22595	8.98	5.6E-4	17	1.03	120.4	2.967	1.6	13.1	1.2	0.0641	1.2	0.396	3.4	0.0539	1.9	0.549	0.0533	2.8	338	6	338	6
11245M-018.2	mixed	633	16183	26.40	1.6E-3	20	2.98	35.1	8.304	1.1	13.2	1.0	0.0595	0.8	0.465	10.1	0.0646	1.7	0.171	0.0522	9.9	404	7	405	6
11245M-066.1	core	1536	26110	17.57	5.8E-4	18	1.04	91.4	5.493	0.7	13.1	1.0	0.0605	0.9	0.547	3.2	0.0693	1.2	0.365	0.0572	2.9	432	5	431	5
11245M-018.1	core	1419	24945	18.16	7.8E-4	18	1.41	84.5	5.753	0.7	13.0	1.2	0.0622	1.2	0.544	4.2	0.0693	1.3	0.307	0.0569	4.0	432	5	431	5
11245M-032.1	core	951	37930	41.20	1.5E-3	13	2.63	57.1	12.530	0.8	12.6	1.2	0.0650	1.2	0.458	6.7	0.0699	1.4	0.205	0.0475	6.5	436	6	440	6
11245M-026.3	core	1806	13888	7.95	4.4E-4	22	0.79	109.9	2.323	1.1	299.4	1.3	0.0846	2.3	0.524	3.4	0.0708	1.3	0.380	0.0537	3.2	441	6	442	6
11245M-033.1	core	1629	15261	9.68	5.6E-4	18	1.01	99.5	2.983	0.9	288.1	1.7	0.0957	3.7	0.534	3.3	0.0711	1.2	0.362	0.0545	3.1	443	5	443	5
11245M-005.2	core	1412	22262	16.29	7.1E-4	20	1.28	87.3	4.996	0.8	265.3	1.6	0.0772	6.0	0.550	4.3	0.0720	1.3	0.309	0.0555	4.1	448	6	448	6
11245M-024.1	core	708	33667	49.11	7.9E-4	20	1.43	44.4	15.179	0.8	254.8	1.1	0.0874	5.5	0.597	4.7	0.0729	1.6	0.338	0.0594	4.4	454	7	452	7
11245M-014.1	core	1952	57694	30.54	9.2E-4	14	1.66	123.1	9.700	1.0	244.2	2.1	0.0924	3.2	0.525	4.2	0.0734	1.2	0.282	0.0518	4.1	457	5	459	5
11245M-053.1	core	1253	52798	43.55	9.3E-4	16	1.68	79.4	13.340	0.6	255.1	2.0	0.0679	2.6	0.529	4.8	0.0738	1.3	0.270	0.0520	4.6	459	6	461	6
11245M-001.1	core	4410	34813	8.16	2.1E-4	20	0.38	281.6	2.504	0.6	232.2	1.1	0.0763	2.5	0.570	3.0	0.0743	1.0	0.326	0.0556	2.8	462	4	463	4
11245M-056.1	core	1334	64577	50.01	1.2E-3	13	2.20	85.6	15.624	0.6	217.4	2.5	0.0727	11.8	0.493	5.3	0.0747	1.3	0.237	0.0478	5.2	464	6	469	6
11245M-029.2	core	1255	47230	38.87	9.1E-4	18	1.63	80.8	12.090	0.7	217.2	1.3	0.0800	2.2	0.596	4.6	0.0749	1.3	0.287	0.0577	4.4	466	6	465	6
11245M-055.1	core	2445	36696	15.51	2.4E-4	19	0.43	158.6	4.862	1.0	212.0	1.5	0.0755	2.1	0.594	1.8	0.0755	1.0	0.576	0.0570	1.5	469	5	469	5
11245M-005.3	core	1727	63069	37.73	6.3E-4	19	1.13	112.1	11.735	0.6	166.0	1.3	0.0750	2.1	0.572	3.7	0.0756	1.2	0.333	0.0549	3.5	470	6	470	6
11245M-067.1	core	3372	32479	9.95	2.9E-4	18	0.52	218.9	3.095	0.6	122.6	1.7	0.0756	4.4	0.576	1.9	0.0756	1.0	0.525	0.0552	1.6	470	5	470	5
11245M-036.1	core	3203	58554	18.89	2.7E-4	20	0.48	208.8	5.753	0.5	99.5	1.3	0.0854	1.8	0.592	2.0	0.0759	1.0	0.517	0.0566	1.7	472	5	471	5
11245M-028.2	core	1674	64910	40.05	7.5E-4	17	1.35	109.5	12.195	1.6	76.9	1.0	0.0667	1.8	0.538	4.1	0.0762	1.2	0.298	0.0513	3.9	473	6	476	6
11245M-017.1	core	1551	66259	44.14	7.8E-4	17	1.41	104.0	13.530	1.0	40.7	2.2	0.0859	1.6	0.577	4.2	0.0781	1.2	0.298	0.0536	4.0	485	6	487	6

Analytical details: mount IP752; 26µm spot, 1nA primary beam (O2-); primary standard GSC lab number 8153; Calibration error 0.8% (included); No secondary standard measured.

4.6 PROTOLITH IDENTIFICATION

While there is considerable variation in mineral assemblages and rock textures during the prograde metamorphism of pelitic rocks, (e.g. Weller *et al.*, 2013, Dyck *et al.*, 2015) the bulk rock composition of un-metamorphosed and high-grade pelite differs significantly only in volatile content (Shaw, 1956). In the absence of large quantities of fluid, compositional mass transfer during regional metamorphism is restricted to the grain and microdomain scale (Walther & Orville, 1982). Consequently, sedimentary structures that are compositionally defined, such as cross-bedding, graded bedding, heavy-mineral laminations, and increasing mud content in a turbidite sequence often remain identifiable following regional metamorphism (e.g. Walker, 1988, Myers, 2001). Likewise, strata that are compositionally homogeneous, such as reworked wave or tidal units, are expected to remain homogeneous on the microdomain scale (e.g. McClelland *et al.*, 1992). Throughout metamorphism, the most substantive textural evolution and mass transfer occur during anatexis, with the introduction of mobile partial melts (e.g. Waters, 2001). The presence of partial melt increases the rate of intergranular-diffusion, which enables grain-size coarsening and mass transfer between compositional microdomains (Dell'Angelo & Tullis, 1988, Evans *et al.*, 2001). In cases where a partial melt may have migrated away from the metamorphic source rock, identifying peritectic minerals, such as sillimanite or cordierite, are useful to differentiate melting reactions and original compositions in rocks (e.g. Waters, 1988).

Another useful criterion for distinguishing primary sedimentary units is the differentiation of event bedding versus continuous deposition–reworking environments. Punctuated deposition events, such as storm deposits or turbidite flows, result in discrete strata (e.g. Immenhauser, 2009, Talling *et al.*, 2012), which can be identified through the

veil of overprinting deformation and metamorphism. Likewise, continuous deposition-reworking environments, such as contourite slopes or migrating fluvial-deltaic channels, produce transitionally layered structures, that can retain their (often fine) morphological bedding characteristics during subsequent overprinting (e.g. McClelland *et al.*, 1992). Thus, despite penetrative fabric development in medium to high-grade metasedimentary terrains, a protolith lithostratigraphy can still be extracted with careful observation of rock type and distribution, variation in composition, and preserved primary features.

4.7 GREATER HIMALAYAN SERIES PROTOLITH LITHOSTRATIGRAPHY

The amphibolite-grade sequence of Greater Himalayan Series metasedimentary units in the Langtang area is interpreted as a right-way-up (at the regional scale) late Neoproterozoic to early Ordovician cratonic margin lithostratigraphic sequence (figure 4.7) that accumulated on Paleoproterozoic Indian crystalline basement (BD1438; figure 4.6a). The basement-cover contact is exposed at two structural levels; in-sequence at the base of the Greater Himalayan Series, and as thick-skinned thrust imbricates within the MCT zone (e.g. figure 4.2 and figure 4.3). The maximum age of basal continental quartzite deposition (ca. 815 Ma; BD1411 and BD1437) indicates that rifting along the northern Indian margin and deposition of the Greater Himalayan Series began no earlier than the Tonian. The thinning of quartzite beds up-section and the gradual transition to a finely laminated and fine-grained sand and mud-dominated siliciclastic unit is interpreted to reflect an increase in water depth during gradual basin subsidence. The thin quartzite strata near the base of the overlying pelitic unit are interpreted as the distal portion of the prograding continental margin clastic-shoreline sequence (c.f. McKie, 1990). Overall the mud-dominated siliciclastic unit (BD1215) is devoid of repeating event beds and is interpreted as a sequence of margin-parallel contourites (c.f. Faugères & Stow, 2008) that accumulated in a

continental slope basinal setting of late Cambrian to early Ordovician age. The rare calc-silicate horizons reported from Langtang (Reddy *et al.*, 1993) and the presence of the thin unit of calcareous marl at the top of the mud-dominated siliciclastic unit also support a slope contourite depositional environment marked by intervals of deep-water carbonate precipitation within a deepening-upwards basinal setting. In contrast, overlying rhythmically bedded arkosic psammites (BD1435) are recognised as distinct sandy turbidites preserving repeating graded bedding compositional profiles (c.f. Mutti, 1985). The sharp contact at the base of the turbidites is interpreted as the maximum flooding surface (i.e. greatest basin depth; figure 4.7; c.f. Posamentier, 1988), after which infilling of the basin occurred during the middle Ordovician to Silurian with the source of the detritus markedly different from that of the basal quartzites (figure 4.6b). The thinning of the turbidite beds and the overall increase in mud content up-section marks a shallowing-upwards depositional sequence that culminated with accumulation of carbonate strata recognized elsewhere along the Greater Himalaya Series (Annapurna Yellow Formation and Everest Yellow Band Formation; Colchen *et al.*, 1986, Searle *et al.*, 2003, Searle & Godin, 2003, Searle *et al.*, 2006b, Myrow *et al.*, 2009, Myrow *et al.*, 2010). In contrast to the siliciclastic-dominated Greater Himalayan Series in the Langtang area, the Greater Himalayan Series in the Annapurna area is uncharacteristically thin and comprises a carbonate-dominated sequence (Colchen *et al.*, 1986, Hodges *et al.*, 1996, Searle & Godin, 2003, Gleeson & Godin, 2006). The simplified stratigraphy of the Greater Himalayan Series in this area is made up of five units: (1) finely interlayered pelitic and psammitic schist, (2) calcareous gneisses, marbles and psammitic schist, (3) interlayered greywackes, biotite schist, and K-feldspar augen gneiss, (4) micaceous marble, (5) interlayered biotite phyllite and biotite- garnet- schist (Searle & Godin, 2003, Gleeson & Godin, 2006). Gleeson and Godin (2006) suggest unit (5) formed in a back-lagoon or lower slope

depositional environment based on the presence of pelmatazoan echinoderm fossils. Figure 4.7 illustrates the interpreted relationship between the Greater Himalayan Series sequence in the Annapurna, Langtang, and Everest regions. The interlayered graywackes, biotite schist and K-feldspar augen gneiss (unit 3; Searle & Godin, 2003, Gleeson & Godin, 2006) are interpreted to represent the pelite and K-feldspar augen gneiss in Langtang (figure 4.2) whose protolith is suggested to be a basinal mudstone (figure 4.7). The maximum flooding surface in the Annapurna section is interpreted as the contact between the K-feldspar augen gneiss and micaceous marble (unit 3 and 4; Searle & Godin, 2003, Gleeson & Godin, 2006), above which the depositional environment shallows and the deposited strata are increasingly mud- and sand-dominated. Variation in the thickness of the Greater Himalayan Series across the length of the orogen (e.g. Yin, 2006, Prasad *et al.*, 2011) is interpreted as reflecting the location of thick siliciclastic Tonian to Ordovician depocenters situated in northern India and in central (Langtang) Nepal. The thinner and carbonate-dominated Greater Himalayan Series in the Annapurna area may have formed as a shelf promontory analogous to present day Bahamas Bank (e.g. Burke, 1988). A first order comparison of the Langtang section with Annapurna suggests a similar sequence of initial basin subsidence followed by accumulation of a shallowing upwards sequence. Based on the continuity of mapped units (figure 4.2 & 4.3) and the interpreted sequence of metasedimentary protoliths, I suggest that the Greater Himalayan Series represents a semi-coherent north-facing passive margin sequence without any repetition of major map-scale units.

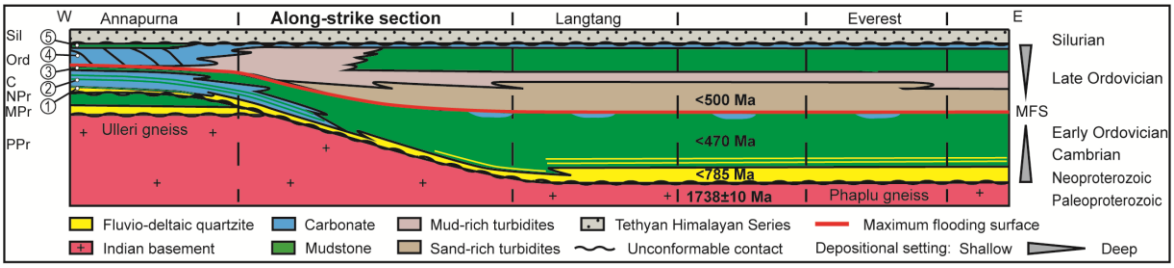


Figure 4.7 Schematic along-strike section from west to east across the central Himalaya as interpreted for the Silurian, showing lateral variation in protolith lithostratigraphy, detrital zircon ages from the Langtang transect (this study), and the local unit name for the base orthogneiss unit in Annapurna and Everest. Solid lines represent stratigraphic boundaries and wavy lines represent erosional unconformities. The maximum flooding surface (MFS) is denoted by a solid red line. The protolith lithostratigraphy of Langtang and Everest represents a siliciclastic depocenter, which preserves a late Neoproterozoic to Ordovician deepening-upwards basin-fill sequence followed by middle Ordovician to Silurian shallowing-upwards drift sequence. The thinner, carbonate-dominated stratigraphy in Annapurna represents a coeval carbonate shelf. The Annapurna and Everest stratigraphic successions are based on the lithological descriptions in Colchen *et al.* (1986), Searle and Godin (2003), Searle *et al.* (2003), Gleeson and Godin (2006), and Searle *et al.* (2006b).

4.8 IMPLICATIONS FOR HIMALAYAN STRUCTURE

Constraining the nature and contrasting origins of the lower 'Ulleri'/'Phaplu' augen gneiss and the upper pelitic K-feldspar augen gneiss ('Formation III augen gneiss' or 'Pumori K-feldspar augen gneiss') is important for unravelling the fundamental structure of the Himalaya. The composition and zircon age profile of the lower augen gneiss in Langtang clearly documents an igneous protolith, whereas the presence of peritectic sillimanite and the characteristic pelitic augen gneiss textures outlined in chapter 2 indicate the upper K-feldspar augen gneiss has a metasedimentary origin. Although late Cambrian to early Ordovician granites are documented in the Kathmandu Klippe (Schärer & Allègre, 1983, Gehrels *et al.*, 2003) and portions of the Greater Himalayan Series in northern India (Foster, 2000, Marquer *et al.*, 2000, Catlos *et al.*, 2002) and central Nepal (Stöcklin, 1980, Le Fort, 1986, Godin *et al.*, 2001), based on the observations and data presented here I suggest that not all of the K-feldspar augen gneiss unit that is commonly mapped as the Formation III augen gneiss is the deformed equivalent of these granites. This interpretation is contrary to previous interpretations of the K-feldspar augen gneiss layer having an

igneous origin (e.g. Le Fort, 1986, Inger & Harris, 1992, Reddy *et al.*, 1993, Fraser *et al.*, 2000, Searle *et al.*, 2003, Mottram *et al.*, 2014). This new interpretation simplifies the tectonic history of the Greater Himalayan Series because it does not require the emplacement of late Cambrian to early Ordovician granites along the entire length of the northern Indian margin.

The protolith lithostratigraphy documented for the Greater Himalayan Series in this paper provides additional support for viewing the stratigraphic evolution of the Himalaya as involving a single protracted, north-facing, Indian cratonic margin with the Lower, Greater and Tethyan Himalaya corresponding to different structural domains rather than different stratigraphic sequences (Myrow *et al.*, 2003, Searle *et al.*, 2003, Searle & Godin, 2003, Steck, 2003, Searle *et al.*, 2008, Myrow *et al.*, 2009, Myrow *et al.*, 2010). Furthermore, the stratigraphy of the northern Indian margin can be reconstructed without a need to include a suture or plate boundary (DeCelles *et al.*, 2000) along the MCT zone. The imbricate thrust slices of Indian crystalline basement at the base of the Greater Himalayan Series, and the exposed basement-cover contact, suggest that the MCT zone roots into the upper part of the Indian basement. Variations in the presence and thickness of Indian basement slices along the length of the orogen (e.g. Searle *et al.*, 1997a, Searle *et al.*, 2003, Searle & Godin, 2003) may be influenced by heterogeneities in the underplating Indian basement (i.e. basement highs or 'ridges'; Godin & Harris, 2014). Repetition of the basal quartzite and pelite in the MCT zone indicates that thrusting was in-sequence and climbed up-section, placing the undisrupted Greater Himalayan Series above a proximal equivalent of the basinal pelite. The transition from homogeneous, ductile, layer-parallel shortening to brittle thrusting as proposed by Godin *et al.* (2006a), is precisely dated by the *in-situ* monazite chronology of the MCT zone faults in Langtang (Kohn *et al.*, 2005), yielding a Miocene age (16±1 Ma) for thrust initiation. The timing of thrust initiation

corresponds to the youngest crystallisation ages of the Himalayan cordierite-bearing leucogranites (Searle *et al.*, 2010), suggesting that orogen-wide strengthening of the metamorphic core during high-grade metamorphism allowed the Greater Himalayan Series to act as coherent package, which was exhumed by thick-skinned thrusting along the MCT zone.

The preservation of a semi-coherent right-way-up cratonic margin lithostratigraphy in spite of subsequent Himalayan shortening and metamorphism necessitates that any model constructed to explain the exhumation of the Himalayan metamorphic core must maintain the overall protolith geometry of the Greater Himalayan Series at the regional scale. It follows that the extent of mid-crustal extrusion in any crustal model that invokes ductile flow of the Himalayan core must be commensurate with preserving the first-order foreshortened basin geometry. To preserve the passive margin stratigraphy, deformation across the Greater Himalayan Series must have been predominately layer-perpendicular pure shear. Any significant contribution of layer-parallel simple shear would have resulted in a reversal of the protolith stratigraphic order, something that is not documented.

The protolith lithostratigraphy presented here can be tested with further detailed stratigraphic studies of the Greater Himalayan Series in other regions along the length of the Himalaya. It is easy to overlook protolith lithostratigraphy in metamorphic terranes, but there is much to be gained by exploring the crossroads of basin stratigraphy and metamorphic petrology.

5 Synthesis and conclusions

5.1 FATE OF WATER RELEASED BY MUSCOVITE DEHYDRATION MELTING

The results and interpretations presented in the preceding chapters are focused on processes relating to the generation, transfer, and solidification of anatectic melt. On the scale of the Greater Himalayan Series, the transfer of melt from its source to sink has been viewed as a closed chemical system. However, as noted in chapter 3, there is an apparent imbalance between the quantity of water contained in the Himalayan leucogranites, and the water released during the dehydration melting of muscovite. This implies that anatexis acted as an open system, with respect to water, and there was a net transfer of metamorphic water out of the Greater Himalayan Series. In this section I integrate the results from Chapters 2–4 to construct a petrographically informed mass-balance calculation that traces the efficiency of water release during Himalayan anatexis. This leads into a broader discussion on the potential fate of water released during high-grade metamorphism, and the implications of crustal anatexis on the global water cycle.

In chapter 2, systematic analysis of K-feldspar microstructures revealed a set of textural criteria that can be used to distinguish K-feldspar of a peritectic origin from K-feldspar that formed during melt crystallisation. In theory, these textures provide a tool that can be used to differentiate vapour(water)-absent muscovite dehydration melting from vapour(water)-present muscovite melting in migmatite, because peritectic K-feldspar is only a product of the former reaction. Accordingly, the modal proportions of peritectic sillimanite and K-feldspar should reflect the relative contribution of either reaction, and may therefore be used to quantify the amount of external (free fluid phase) or internal (lattice-bound) water involved in the anatectic event. This approach presupposes that all K-feldspar and sillimanite are generated exclusively during muscovite dehydration melting,

and that both peritectic phases remain in the source throughout anatexis. As noted in chapter 2, sillimanite can form prior to the dehydration of muscovite, and is readily entrained by migrating melt. I therefore suggest caution in using the modal proportions of peritectic sillimanite and K-feldspar to resolve small differences between the contribution of vapour-absent and vapour-present melting. However, this method is expected to work as a first-order approach to determining the presence of external water during muscovite dehydration melting. To reiterate one of the findings presented in chapter 2, the high modal proportion of peritectic K-feldspar present in pelitic migmatite collected from Langtang and Everest indicate that the dominant melting reaction during peak metamorphism of the Greater Himalayan Series was vapour-absent muscovite dehydration, and there was no external source of water.

5.1.1 Motivation for calculation

The movement of Earth's tectonic plates governs the transport of water, bound in hydrous mineral phases, between surficial and deep reservoirs. This global water cycle consists of two parts: 1) the oceanic-mantle cycle – the exchange of water between subducting oceanic plates and degassing at mid-oceanic ridges and volcanic arcs; and 2) the continental cycle – the transport of water through the accumulation, metamorphism, and devolatilisation of sediments at continental margins (figure 5.1). The first part of the cycle has been a subject of intense study, ever since Armstrong (1968) recognised that subduction exerts a critical control on continental growth. It is now recognised that the subduction of hydrous minerals not only plays a critical role in crustal growth, but it also governs the styles of arc magmatism and the refertilisation of the mantle (e.g. Plank & Langmuir, 1998, Jarrard, 2003). Water is removed from surface reservoirs and carried down subduction zones as pore water, and lattice-bound water in sediments, altered oceanic crust, and serpentinised

lithospheric mantle (Parai & Mukhopadhyay, 2012). Numerous studies have explored the downward flux of water at destructive margins, and the upwards flux of water at arc volcanoes and mid-ocean ridges (e.g. Poli & Schmidt, 1995, Kerrick & Connolly, 1998, Plank & Langmuir, 1998, Hacker, 2008, Parai & Mukhopadhyay, 2012), and mass-balance calculations suggest there is a net flux of water into the mantle (Plank & Langmuir, 1998, Parai & Mukhopadhyay, 2012). Remarkably, despite this imbalance in the oceanic–mantle cycle, continental freeboard studies indicate that global sea level has fluctuated by <500 m over the past ca. 3000 Ma (Galer, 1991).

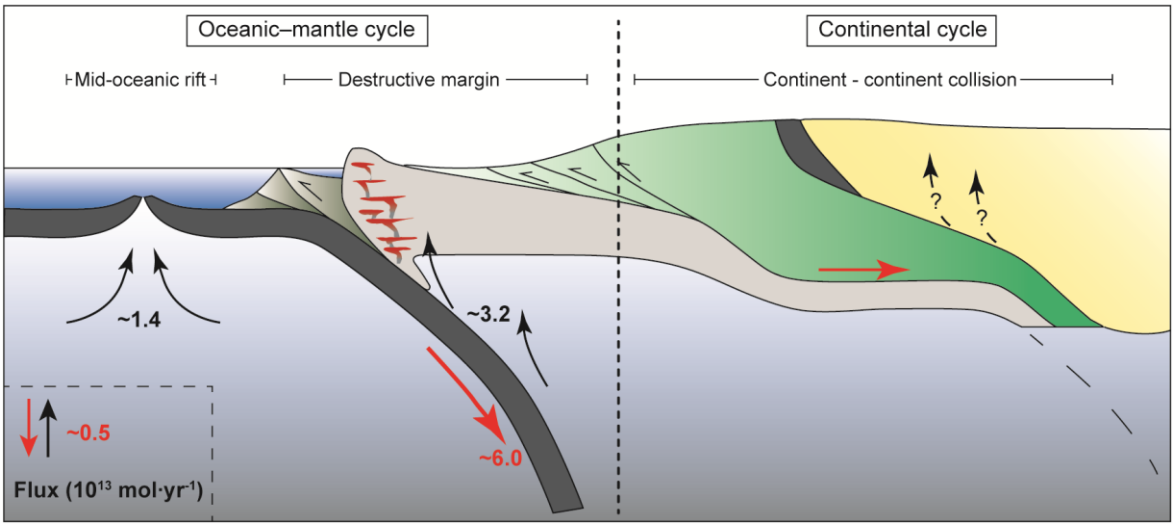


Figure 5.1 Schematic of the global water cycle, showing the downward (red) and upward (black) fluxes of water in different tectonic settings. The cycle is divided into two parts: the oceanic–mantle cycle and the continental cycle.The values shown are taken from Parai & Mukhopadhyay (2012), and represent the annual global water flux (mol·yr^{-1}) at mid oceanic rifts and destructive margins.

Surprisingly little is known concerning the second part of the cycle, the role continents play in the global water cycle over geological time. Specifically, whether or not continental crust acts as a source or sink of water to the surface reservoirs over geological time is uncertain. Unlike the exchange of water through oceanic crust and mantle, which sequesters water in deep reservoirs, in the continental cycle water is progressively released

from (meta)sedimentary margin strata. Hydrous minerals, formed during compaction, diagenesis, and prograde metamorphism of strata deposited along continental margins, are largely consumed during regional metamorphic events (i.e. continent-continent collision; figure 5.1). The breakdown of hydrous minerals during prograde metamorphism liberates lattice-bound water (i.e. hydroxide as a stoichiometric mineral component), which can form a free fluid phase, or combine with other components to form a silicate melt (Thompson & Algor, 1977). As a free fluid phase, water is less dense and viscous than the surrounding rock and will therefore migrate along grain boundaries and fractures towards lower-pressure regions (c.f. Ague, 2003). As water migrates through the crust it may react with the surrounding minerals, triggering retrograde reactions and the formation of hydrous minerals (Haack & Zimmermann, 1996). Nominally anhydrous minerals, such as the feldspars, can contain relatively small quantities of structural water (0-512 ppm), although measuring these values in natural samples is often complicated by the effect of low-temperature equilibration and deuteric alteration (Johnson & Rossman, 2004). As such, there is a balance (or imbalance) between the release of water during prograde metamorphism, and the consumption (or retention) of water during crustal retrogression. At temperatures above the (wet granite) solidus ~650 °C, the balance between the release and retention of water in the crust plays out in two stages: 1) during melt generation and solidification, and 2) following melt-devolatilisation, through the ascent of free aqueous fluid (c.f. London *et al.*, 1988).

The total amount of water cycled through continental crust is governed by the composition of the down-going and thickened margin. In a passive or rifted margin setting, the lithology with the greatest capacity to carry lattice-bound water to the middle and lower crust is mudstone (c.f. Thompson, 1996). Under Barrovian metamorphic conditions, the prevailing hydrous minerals that form in metamorphosed mudstone are chlorite, muscovite,

and biotite (figure 5.2). At the lithostatic pressures expected for the middle crust (0.3–0.7 GPa) chlorite fully dehydrates at ~550°C, which means that the majority of lattice-bound water supplied to the migmatitic core of a collisional mountain belt such as the Himalaya is retained in muscovite and biotite. Following muscovite dehydration melting at ~700°C, liberated water is expected to move through the crust in two stages. Firstly, as a component of hydrous silicate melt (i.e. leucogranitic melt), and secondly as a free aqueous fluid.

Using the textural tool provided in chapter 2, the melt–rock reaction developed in chapter 3, and the Greater Himalayan Series lithostratigraphy documented in chapter 4, I examine the release and transfer of water during anatexis, and the contribution of this process to the global water cycle.

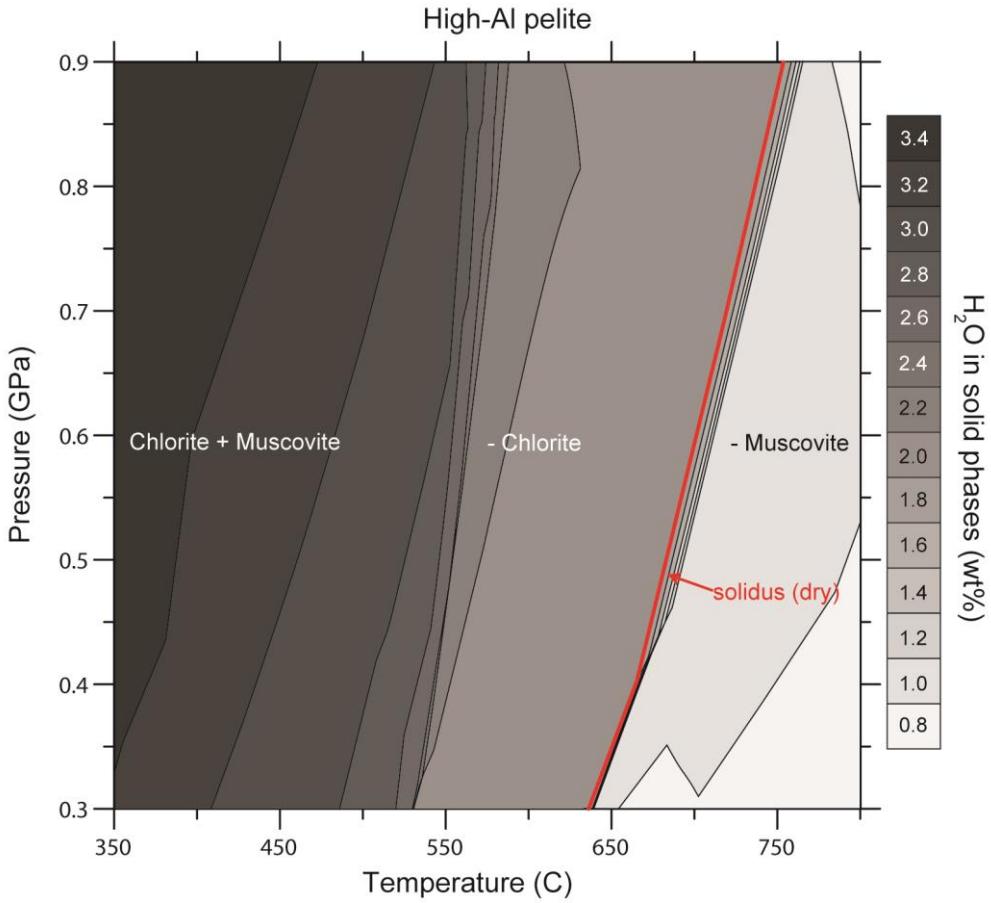


Figure 5.2 Equilibrium phase diagram shaded to depict the amount of lattice-bound water (weight %) in pressure and temperature space for sample BD1233. Field shading corresponds to 0.2 weight % increments. The red line marks the vapour-absent muscovite dehydration melting solidus.

5.1.2 Muscovite dehydration melting in the Himalaya

The Greater Himalayan Series exposes a sequence of metamorphosed sedimentary rocks that were initially deposited along the northern margin of the Indian Craton, and subsequently buried, thickened, and heated during the collision of India with Eurasia. The rocks exposed at the surface level preserve a record of vapour-absent muscovite dehydration melting across the 2400 km length of the Himalaya, which resulted in the formation of leucogranite sills and dykes over a 2–13 Myr time period between ca. 23–10 Ma (e.g. Schärer *et al.*, 1986, Wang *et al.*, 2016). The Greater Himalayan Series in Langtang is an ideal natural laboratory for considering the effect of anatexis on crustal fluid budgets because the ~20 km thick passive-margin sequence reached temperatures sufficient for muscovite but not biotite dehydration melting (see chapter 2). On the regional scale, the Greater Himalayan Series has been correlated with the location of ongoing high-temperature metamorphism occurring 20–40 km below the Tibetan Plateau, which is inferred from magnetotelluric and seismic surveys (Bai et al, 2010; figure 5.3). The Greater Himalayan Series is overlain by the relatively low- to unmetamorphosed Tethyan Himalayan Series, which forms the Himalayan upper crust. The presence of a crustal layer with low resistivity and reduced seismic velocity below Tibet today (Nelson *et al.*, 1996, Wei *et al.*, 2001), together with thermal modelling of the Himalayan Orogeny (Nábělek & Nábělek, 2014), suggest the temperatures required for vapour-absent muscovite dehydration melting have been sustained for the past 25–35 Ma (Yin & Harrison, 2000). With an estimated modern plate convergence rate of ~20 mm/yr (Bilham *et al.*, 1997), the area below Tibet that has reached the conditions of vapour-absent muscovite dehydration is estimated to be approximately 1.75×10^6 km^2 (Fielding, 1996, Unsworth *et al.*, 2005). The net flux of water from the dehydrating middle-crust to upper-crustal reservoirs depends on

the initial volume of muscovite in the reacting crustal layer, informed here by Greater Himalayan Sequence lithostratigraphy, and the efficiency of water release during melt crystallisation and mid-crustal hydration reactions.

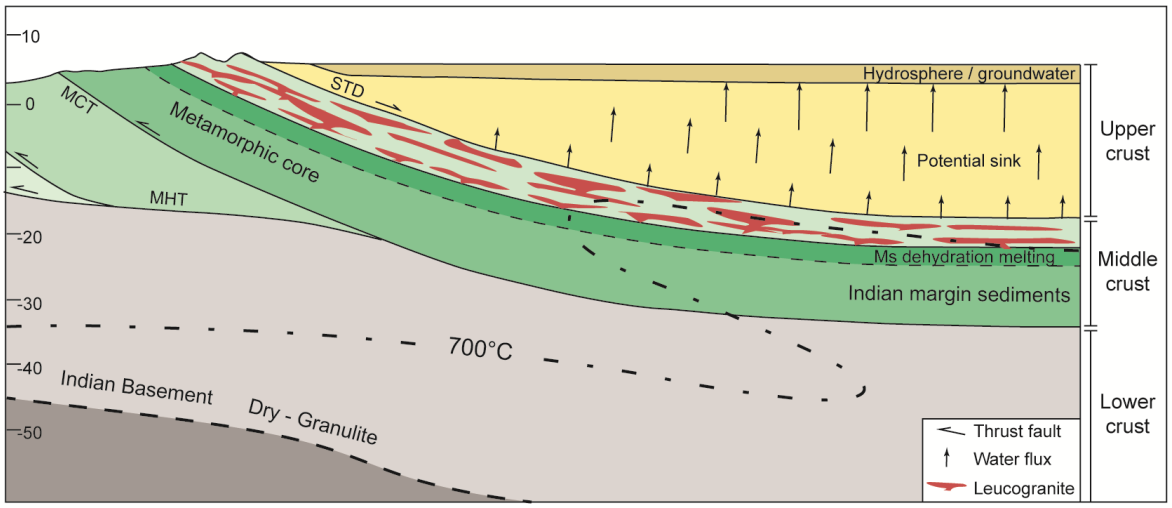


Figure 5.3 Schematic cross-section through the Himalaya and Tibetan Plateau, showing the source and potential sink of water released by muscovite dehydration melting. Relative positions of the Main Central Thrust (MCT), Main Himalaya Thrust (MHT), and Indian basement are modified after the results of the INDEPTH seismic profile (Li *et al.*, 2003). The depth of partial melting below the Tibetan Plateau is taken from the INDEPTH magnetotelluric profile (Unsworth *et al.*, 2005), and the 700°C isotherm is adapted after (Nábělek & Nábělek, 2014).

5.1.3 Methods and model assumptions

The phase equilibria calculations presented in figure 5.1 and figure 5.5 are modelled in the chemical system MnNCKFMASHTO ($MnO–Na_2O–CaO–K_2O–FeO–MgO–Al_2O_3–SiO_2–H_2O–TiO_2–O$). The phase diagrams were calculated using *Theriak–Domino* version 03.01.2012 (de Capitani & Brown, 1987, de Capitani & Petrakakis, 2010) using the thermodynamic database (dataset 5.5; Holland & Powell, 1998). Activity models used were: melt, biotite and ilmenite (White *et al.*, 2007), feldspar (Baldwin *et al.*, 2005), chlorite (Holland *et al.*, 1998), white mica (Coggon & Holland, 2002) and garnet (Kelsey *et al.*, 2004). The input composition used for figure 5.1 and figure 5.5b was a modified whole-rock XRF analysis of sample BD1233, a high-Al pelite from the Main Central

Thrust zone with ~30% muscovite at conditions immediately below the solidus. Accessory apatite and monazite in equal proportions was corrected for by removing P_2O_5 from the bulk with a proportional adjustment to CaO (Palin *et al.*, 2015). To generate the model presented in figure 5.1, sufficient H_2O was added to saturate the assemblage in the immediate sub-solidus at a pressure of 0.6 GPa, equivalent to 6.75 mol. %. The effective bulk composition of sample BD1233 in oxide mol. % was: H_2O – 6.75; SiO_2 – 71.03; Al_2O_3 – 10.52; CaO – 0.21; MgO – 2.86; FeO – 4.47; K_2O – 3.30; Na_2O – 0.27; TiO_2 – 0.45; MnO – 0.13; O – 0.02. The composition modelled in figure 5c was a modified whole-rock XRF analyses of sample BD1209, a muscovite-biotite leucogranite from the Langtang Greater Himalayan Series. Its effective bulk composition in oxide mol. % was: SiO_2 – 79.74; Al_2O_3 – 9.78; CaO – 0.83; MgO – 0.98; FeO – 1.45; K_2O – 4.20; Na_2O – 2.76; TiO_2 – 0.22; MnO – 0.02. The high value of SiO_2 in sample BD1209 should be noted, which may indicate that the leucogranite formed from an evolved melt. The calculations presented in figure 5.5 were performed by setting H_2O to saturate the assemblage immediately below respective mica dehydration conditions. The models were run along a crustal geotherm that was calculated following the procedure of (Smye & Stockli, 2014), with a base condition of 750°C at 18 km depth, and a surface temperature of 0°C. The thermal diffusivity was set to 25.3 $km^2 \cdot Ma^{-1}$, and a constant value of $3.0x10^3$ ($J \cdot Ma \cdot km^{-3}$) was used to model radiogenic heat production.

Two main assumptions are made in the following calculation:

1) All of the initial water is derived from vapour-absent muscovite dehydration melting (see chapter 2).

2) The dehydrated muscovite is stoichiometric and fully hydrated, taking the form of $K_2Al_4Si_6Al_2O_{20}(OH)_4$.

The calculation is set up as a crustal column with a dimension of 1 x 1 x *d*, where *d* represents crustal thickness in meters, and water quantities are expressed as $mol \cdot m^{-2}$. This was done so that extensive properties (i.e. mass, volume) could be considered and the results could be easily expressed in terms of the efficiency of water release. The term *water* used throughout this section refers broadly to molecular H_2O and its dissociated components OH^- and H^+ (e.g. in terms of mineral compositions). However, where the unit expressed is molar, I have treated *water* as molecular H_2O.

5.1.4 Initial contribution of water

The stratigraphic and mineral parameters used for the calculation are summarised in Table 5.1. Based on the observed Greater Himalayan Series lithostratigraphy in the Langtang area and initial modal amounts of muscovite in the melt source, as inferred by modal proportions of peritectic sillimanite and K-feldspar (see chapters 2 & 4), water was initially derived from two layers of K-feldspar augen gneiss. The two layers of K-feldspar augen gneiss are 1300 and 2200 m thick, and based on the proportion of peritectic K-feldspar are inferred to have formed from protoliths with 25 and 15 modal % muscovite, respectively. The total amount of melt generated by vapour-absent dehydration melting in both layers of K-feldpsar augen gneiss was 451.7 m (column thickness). Based on the observed ratio of muscovite-biotite leucogranite / metasedimentary host (0.13; table 5.1), the calculated column thickness of melt crystallised as muscovite-biotite leucogranite is 401.7 m. The 11.2 % difference between the volume of melt in the source, and volume of leucogranite in the sink is interpreted to primarily reflect the negative volume change of melt solidification, although a small degree of melt may have also remained in the source (see chapter 2). When combined, the dehydration of muscovite within these layers released a

total of 4.15 x10^6 mol·m^{-2} of water (figure 5.4). Upon dehydration, the released water was subsumed into the leucogranitic melt phase.

[1]Average crust density (g/cm^3)	2.81
[1]Ms density @ 650°C, 0.7 GPa (g/cm^3)	2.81
[1]Melt density @ 750°C, 0.7 GPa (g/cm3)	2.20
[1]Volume ratio melt/muscovite	0.69
Molecular weight of muscovite (g/mol)	398.71
[2]Molar volume of tourmaline (cm^3/mol)	318.83
[3]Weight fraction H_2O in muscovite	0.0407
[3]Weight fraction H_2O in leucogranite	0.005–0.009
H^+ consumed per mole of tourmaline produced by reaction 3.8 (mol)	0.08
Langtang stratigraphy (structural thickness)	
Pelite with 15% muscovite (m)	2200
Pelite with 25% muscovite (m)	1300
Arkosic psammite (m)	3090
Melt/Host ratio in sink	0.13
Tur leucogranite : Ms-Bt leucogranite	3
[1]Extracted from Theriak using BD1233; [2]Garofalo *et al.* (2000); [3]Scaillet *et al.* (1995)	

Table 5.1 Calculation input parameters. Note the structural thickness of pelite only include the layers that have reached solidus temperatures.

5.1.5 Two stages of water retention

The initial composition of silicate melt generated by vapour-absent muscovite dehydration melting is expected to have contained 5.0–7.5 weight % water (Scaillet *et al.*, 1995). In layers where the melt fraction exceeded the melt percolation threshold (Φ>0.07; chapter 2) melt migrated both laterally and upwards through the crust, crystallising as leucogranite with the mineral assemblage: muscovite–biotite–quartz–plagioclase–K-feldspar ± tourmaline. The first stage where water could be retained was during melt crystallisation, with the formation of hydrous muscovite, biotite, and tourmaline. The resulting leucogranite contains 0.50–0.90 weight % water (Scaillet *et al.*, 1995, Visonà & Lombardo, 2002), which is primarily held in lattices of muscovite, biotite, and tourmaline. Within the Greater Himalayan Series in the Langtang area, the formation of hydrous

minerals during leucogranite crystallisation is estimated to have consumed between 0.35–0.63 x10^6 mol·m^{-2}. This corresponds to ~8.4–15.1 % of the initial amount of water released by the dehydration of muscovite, and indicates that the efficiency of water released during leucogranite crystallisation was 84.9–91.6 % (figure 5.4).

In the late stages of leucogranite crystallisation, an immiscible volatile-rich melt phase is expected to have formed (see chapter 3), which would have been the primary host of the remaining water. The formation of the nebulitic tourmaline leucogranite by the melt–rock reaction presented in chapter 3 (see reaction 3.8 in section 3.10), consumed water and represents the second stage where water was retained. Based on a 3:1 ratio of nebulitic tourmaline leucogranite to muscovite-biotite leucogranite and 10 modal % tourmaline in the product assemblage (table 5.1), the formation of nebulitic tourmaline leucogranite in the Greater Himalayan Series in the Langtang area is predicted to have consumed ~0.17 x10^6 mol·m^{-2}. This corresponds to ~0.4 % of the initial amount of water released by the dehydration of muscovite (figure 5.4).

Based on the values reported above, the net amount of water released from the top of the anatectic zone of the Greater Himalayan Series in Langtang is between 3.51–3.79 x10^6 mol·m^{-2}. These results imply that in the Langtang area 84.5–91.6% of the initial amount of water released by the dehydration of muscovite migrated away from the melt source and sink regions (figure 5.4). Similarly low values are expected in other middle and lower crustal environments, since the efficiency of water release is primarily a function of the volume of hydrous minerals formed during melt crystallisation, and is independent of the leucogranite host lithology. Following the crystallisation of leucogranite and associated melt–rock interaction, the remaining water is expected to have separated from the residual melt and formed a free aqueous fluid phase, which ascended into the upper crust (figure 5.4).

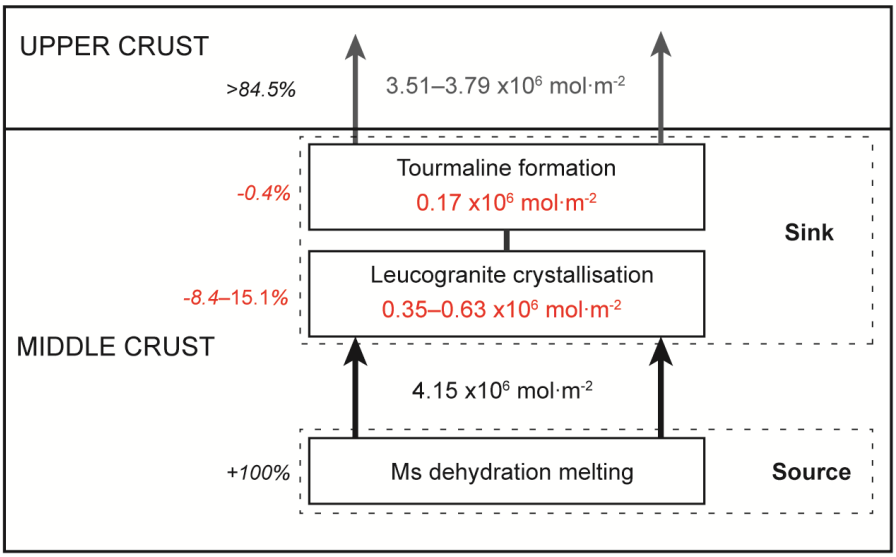


Figure 5.4 Schematic of the water fluxes considered in the middle and upper crust of the Himalaya and Tibetan Plateau. Water is released from muscovite dehydration melting in the pelitic source, and partially retained by leucogranite crystallisation and the formation of tourmaline in psammitic country rock. Arrows mark the direction of the calculated fluxes of water released from muscovite dehydration melting (black) and from the middle crust (grey). The amount of water retained during leucogranite crystallisation and tourmaline formation are marked in red.

5.1.6 Mechanism of fluid escape

In general, the retention of water in the middle crust requires both the formation of stable hydrous minerals and a high fluid–rock interaction. The two end-member regimes for the movement of fluid through the crust are pervasive and channelised flow (Walther & Orville, 1982). Pervasive fluid flow, along grain boundaries and finely spaced fractures (millimetre spacing), offers the largest surface area of reaction and maximises fluid–rock interaction. In contrast, channelised flow, on the scale of decimetres or metres, considerably limits the potential fluid–rock interaction (Walther & Orville, 1982). Analogue studies on porous fluid flow demonstrate that fluid–rock interaction is highest near the fluid source, and the reaction surface area decreases as fracture networks coalesce in a dendritic pattern (Walther & Orville, 1982, Brown, 2007a). In the psammitic strata near the top of the Greater Himalayan Series, the channelisation of fluid flow was manifest

in en-echelon arrays of quartz veins with meter-scale spacing (Law *et al.*, 2004). In the structurally higher Tethyan Himalayan Series, veined precipitates of quartz and tourmaline crosscut the foliation in low-medium grade marbles (Corthouts *et al.*, 2016). The spatial distribution of veins and lenses increases in higher crustal levels (Wu *et al.*, 1998), indicating fluid flow was more channelised within the structurally higher Tethyan Himalayan Series.

5.1.7 Retrograde reactions in the upper crust

Water-consuming retrograde reactions are predicted to occur when water comes in contact with a cooling rock that hosts a metastable mineral assemblage (Haack & Zimmermann, 1996). Accordingly, rock composition and the pre-existing mineral assemblage exert a primary control on the amount of water that can be retained in the upper crust. The upper crust of the Himalaya and Tibetan Plateau hosts a range of rock types. Volcano-sedimentary strata of the Tethyan Himalayan Series crops out along the Himalaya range (Searle *et al.*, 1987a), whereas, the upper crust of the Tibetan Plateau is composed of a complex mosaic of terranes dominated by granitoid and metasedimentary compositions (Dewey *et al.*, 1988, Weller *et al.*, 2013, Weller *et al.*, 2015). To evaluate the amount of water that could be consumed by retrograde reactions in the Tethyan Himalaya Series and Tibetan Plateau, I modelled the stability of chlorite, muscovite, biotite, and zeolite for a sample of high-Al pelite (BD1233) and muscovite-biotite leucogranite (BD1209), and calculated the amount of lattice-bound water in weight % as a function of depth (figure 5.5). The reported values are aggregated to represent the amount of water that would be retained in pelitic and granitic rocks, which have experienced progressive metamorphism and remained metastable upon cooling. For example, the chlorite lines (Chl) on figure 5b, c represent the amount of lattice-bound water that would be consumed if water were added

to a rock that underwent chlorite dehydration. Similarly, the chlorite + muscovite (Chl + Ms) line represents a rock that underwent chlorite and muscovite dehydration. At any given crustal depth, the amount of lattice-bound water in pelite is approximately three times greater than the amount of lattice-bound water in leucogranite. In both compositions, muscovite is the phase with the largest potential to consume water (figure 5.5). However, this requires an upper crust that has a history of high-grade metamorphism, with peak condition beyond that of muscovite dehydration (>700°C). For this reason, the retrograde formation of chlorite is considered to be the reaction with the largest potential to consume and retain water in the upper crust.

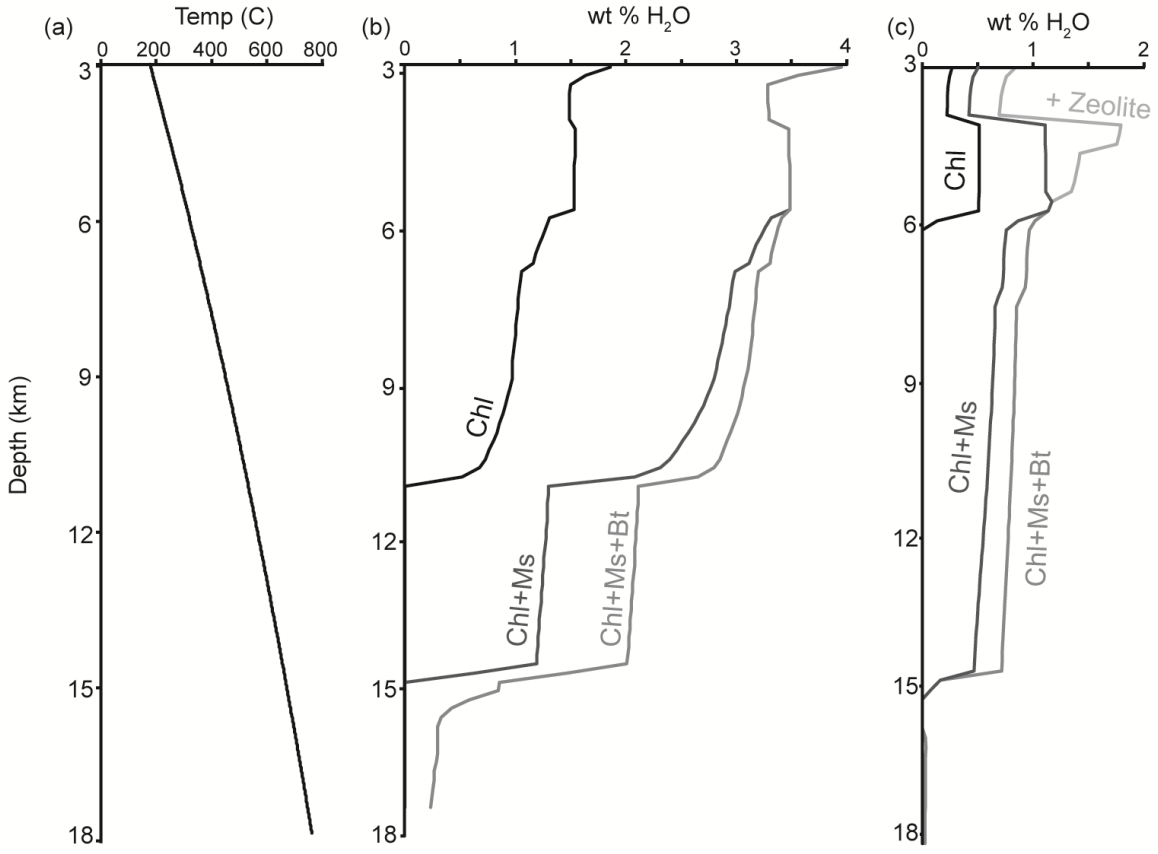


Figure 5.5 Phase equilibrium models showing the amount of lattice-bound water, in weight %, predicted for pelitic and granitic crust as a function of temperature and depth. (a) Thermal profile used in the phase equilibrium calculations. (b) Equilibrium weight % of water at depth in a high-Al pelitic composition (sample BD1233). The lines denote the cumulative amount of water held in chlorite (Chl), muscovite (Ms) and biotite (Bt). (c) Equilibrium weight % of water at depth in a peraluminous granitic composition (sample BD1209).

The lines denote the cumulative amount of water held in chlorite (Chl), muscovite (Ms), biotite (Bt), and zeolite.

5.1.8 Control on upper crustal strength

The influx of aqueous fluid is expected to develop hydrofractures that propagate both upwards and laterally along structural anisotropies (Sibson, 1994, Vry *et al.*, 2010). The presence of large volumes of aqueous fluids is predicted to weaken the rocks that it migrates through, by enhancing creep rates and concentrating shear deformation (Etheridge *et al.*, 1984, Connolly, 1997, Collettini *et al.*, 2009). As the fluid migrates across the brittle-ductile transition into the upper crust, two end-member scenarios are predicted. The aqueous fluid may react with minerals along fracture planes to form networks of hydrous phyllosilicates (i.e. chlorite, muscovite, talc) subject to pressure, temperature and composition of the fractured rock (Jefferies *et al.*, 2006, Moore & Rymer, 2007). The growth of phyllosilicates along fracture planes could lead to fault weakening by reducing the coefficient of friction along the mineralised fault plane (Jefferies *et al.*, 2006). The other scenario is that the passage of aqueous fluid through the base of the brittle crust, where initial permeability is low, could raise the pore pressure, initiating earthquake slip events (Beeler *et al.*, 2000). In either scenario, the high efficiency of water release in the middle crust would result in a large supply of metamorphic water at depths below the brittle-ductile transition, which may generate rheological instabilities above the zone of partial melting.

5.1.9 Upward flux of water beneath the Tibetan Plateau

If the crystallisation of melt below the portion of the Tibetan Plateau that is inferred to have experienced partial melting (approximately 1.75×10^6 km^2) (Fielding, 1996, Unsworth *et al.*, 2005) was continuous over the protracted 35 Myr period of partial

melting, the area integrated flux of water from the middle to upper crust is estimated to be between 0.17–0.19 $x10^{12}$ $mol \cdot yr^{-1}$.

5.1.10 Contribution to global water cycle

Mass-balance calculations for the recycling of water through subduction zones suggest there is a global net loss of water to the asthenosphere and lower lithosphere, equivalent to 14–20 $x10^{12}$ $mol \cdot yr^{-1}$ (Parai & Mukhopadhyay, 2012). This downward flux in water, averaged globally over an estimated 44,450 km (Jarrard, 2003) of destructive margin length, and scaled to 1000 km margin length is on the order of 0.32–0.45 $x10^{12}$ $mol \cdot yr^{-1}$. Expressed in the same terms, the positive flux of water released during vapour-absent muscovite dehydration melting along 1000 km length of the Himalaya is calculated here to be approximately 0.07–0.08 $x10^{12}$ $mol \cdot yr^{-1}$. The values reported in this section indicate that the up-welling flux of water in zones of continental protracted anatexis is not large enough to offset the downward flux of water at destructive margins. However, anatexis and dehydration reactions in the continents may buffer the global flux of water over long periods (40–100 Ma) of crustal growth and supercontinent assembly, when high-temperature metamorphism and anatexis is widespread (Brown, 2007b, Hawkesworth *et al.*, 2010).

In this section I have shown that the efficiency of water release from the Greater Himalayan Series in the Langtang area was >84.5% and that regional metamorphism and anatexis in the Himalaya could have release a large amounts of water from the metamorphic middle crust, sufficient enough to weaken the upper crust. In conclusion, I suggest that the continents have a limited potential to store water over geological time and that continental crust plays a passive role in the global water cycle.

5.2 THERMAL EVOLUTION OF THE GREATER HIMALAYAN SERIES

The widespread record of anatexis in the Greater Himalayan Series has stimulated a vibrant and ongoing discussion about the sources of crustal heat in orogenic belts (e.g. Molnar *et al.*, 1983, Searle & Rex, 1989, England *et al.*, 1992, Jamieson *et al.*, 1998, Foster *et al.*, 2002, Kumar *et al.*, 2009, Chakraborty *et al.*, 2016). In a mountain belt undergoing crustal thickening there are three clear sources of heat: heat conducted from the lower crust/mantle, radiogenic heat that is generated within the crust, and frictional heat generated along shear planes (ibid). Thermal models have demonstrated that it is possible to reach anatectic temperatures by considering a range of heat source combinations (e.g. Molnar *et al.*, 1983, England *et al.*, 1992). Moreover, external tectonic parameters, such as the rate of plate convergence and surface erosion can be varied to reproduce the metamorphic timescales observed in studies of natural samples (e.g. Jamieson *et al.*, 1998). However, these models do not take into account the thermal output of retrograde (volatilisation) reactions (e.g. Haack & Zimmermann, 1996).

Based on concepts developed in this thesis I propose the following three-stage model for the tectonothermal evolution of the Greater Himalayan Series, which takes into account the exothermic formation of the nebulitic tourmaline leucogranite:

1) Following the initial collision between India and Eurasia, the metasedimentary middle and upper crust of India was thickened by predominately layer-perpendicular pure shear. Crustal thickening in the Eocene led to the widespread kyanite-grade metamorphism (c.f. Godin *et al.*, 2001).

2) Subsequent thermal relaxation within the thickened middle crust coupled with surface erosion resulted in an open clockwise *P–T* loop. Initiation of (basement-included) thick-skin thrusts in the early Miocene (c.f. Kohn, 2008) resulted in the rapid exhumation of the

thickened middle crust. Decompression of muscovite-rich strata in the high-grade Greater Himalayan Series resulted in widespread vapour-absent muscovite dehydration melting and the emplacement of muscovite-biotite leucogranites. The transfer of melt advected heat upwards through the crust, towards less fertile lithostratigraphic units.

3) During crystallisation, the anatectic melt separated into two melt phases; one that was volatile-poor and one that was volatile-rich. The volatile-rich melt infiltrated the host metasedimentary rocks, which led to pervasive melt–rock interaction and the strongly exothermic formation of both tourmaline and apatite. Due to the large volume of crust affected by the formation of the nebultitic tourmaline leucogranite, it is estimated that the majority of the upper portion of the Greater Himalayan Series would have acted as a thermochemical heat engine. While it is beyond the scope of this thesis to model the temporal and thermomechanical implications of this process, I propose it as a topic for future research.

5.3 HIGH-GRADE REACTION TEXTURES

A common theme in the mineral reaction processes described in this thesis is the importance of nucleation preferences and interface processes associated with the textural evolution of high-grade metamorphism. As noted in all three studies, chemical ordering in a protolith establishes chemical potential gradients, which lead to self-organised chemical systems. One of the important consequences of self-organisation in metamorphic reactions is that the reaction textures observed in a set of samples from any one location will be representative of the textures associated with that same reaction elsewhere in the crust. Accordingly, the rock textures and mineral microstructures described for vapour-absent muscovite dehydration melting (chapter 2) and the formation of nebulitic tourmaline

leucogranite (chapter 3) should be taken as a general description of these reaction processes and are not necessarily restricted to the Himalaya.

In the following section I provide a brief summary of three reaction processes that play a fundamental role in the textural evolution of anatectic and melt-present reactions:

1) Nucleation preferences - Nucleation of product phases at energetically favoured sites exerts a primary control on the spatial distribution and domain-scale association of minerals. During vapour-absent muscovite dehydration melting the lowest energy site of peritectic K-feldspar nucleation is at the interface of isomorphic plagioclase in the quartzofeldspathic domain rather than in the aluminous domains where muscovite is dehydrating. Conversely, peritectic sillimanite nucleates in (muscovite-rich) aluminous domains, initially on [001] mica cleavage planes. Nucleation of silicate melt does not require nucleation energy; rather it is generated at the interface of the hydrous reactant (muscovite). The nucleation preferences exhibited by sillimanite and melt result in a close association between sillimanite and melt that is continued throughout the process of melting and melt transfer. Furthermore, the nucleation and growth of K-feldspar in the quartzofeldpsathic domain results in the retention of peritectic K-feldspar in the restite. A second example of this process is the preferred nucleation of tourmaline on protolith biotite [001] cleavage planes during the formation of the nebulitic tourmaline leucogranite, which results in crystallographic preferred orientation of tourmaline that mimics the layering of the protolith psammite.

2) Mass transfer - The transfer of chemical components between mineral domains is driven by gradients in chemical potential (c.f. Wood, 1976). In general, there are two forms of mass transfer in high-grade reactions, ionic diffusion and advection. Ionic diffusion operates on a range of scales within both crystalline and fluid mediums. Based on the

textures described in chapters 2 and 3, the relative diffusion rates of the major elements are ordered as follows: within minerals (i.e. intracrystalline) < along grain boundaries < within an aqueous solution < within a silicate melt. Accordingly, the supra-solidus textural evolution of a rock may involve a greater transfer of mass than a similar reaction at sub-solidus conditions. The observed increase in grain-size in rocks that have experienced >7 melt % (chapter 2) and rocks that were pervasively infiltrated by melt (chapter 3), indicates that the advection of components through melt plays a significant role in high-grade reaction textures.

3) Interface processes - The way in which mineral grain boundaries migrate controls the initial microstructures of product phases. For example, as noted in chapter 2 there is a topotactic relationship between peritectic K-feldspar and protolith plagioclase. The advance of the K-feldspar-plagioclase grain boundary by the selective replacement of plagioclase results in a poikiloblastic texture. Similarly, the selective replacement of plagioclase by quartz during the formation of the nebulitic tourmaline leucogranite produces a distinctive 'saw-tooth' grain boundary texture. If the replacement of plagioclase were continued, it is expected that quartz would mimic the shape of protolith plagioclase. Another example of an interface-controlled process is the growth of tourmaline at the expense of biotite folia (chapter 3); where the protolith Fe-Mg zoning in biotite is preserved in the newly grown tourmaline. Interface processes and the resulting (metamict) growth of a pseudomorph (c.f. section 7.8.5 in Passchier & Trouw, 1996), plays an important role in the preservation of protolith textures. With the exception of the generation of melt in aluminous domains, all of the interface processes described in this thesis are inferred to locally conserve volume. Moreover, as first noted by Carmichael (1969) the acting interfaces commonly conserve Al, so that there is a similar Al/Si ratio in

the parent and daughter phase(s) (e.g. plagioclase–K-feldspar, muscovite– intergrowths of sillimanite+quartz).

In theory, it may be possible to predict the textural evolution of other high-grade reactions if something is known of the nucleation preferences, mechanisms of mass transfer, and the interfaces where the reaction occurs.

5.4 FUTURE DIRECTIONS

The results from this work have highlighted several future research directions. On a more general note, continued investigation of the rheological behaviour of minerals and rocks during partial melting and melt transfer is required to constrain the structural significance of anatexis. The rheology of an individual mineral will evolve with changing pressure and temperature conditions, but the rheology of a rock will also be dependent on its grain-size and texture. While experimental studies have demonstrated that partial melting weakens a rock (e.g. Rosenberg & Handy, 2005), the strain rates that can be achieved by experimental apparatuses ~10^{-5} s^{-1} are more than 6 orders of magnitude higher than natural crustal rates of strain ~10^{-11}–10^{-14} s^{-1} (ibid). In light of the work presented here and the general observation that partial melting and melt infiltration result in significant bulk coarsening, which strengthens a rock at conditions where grain-boundary sliding dominates (c.f. section 3.9 in Passchier & Trouw, 1996), it is important to consider the rates of melt transfer and intergranular diffusion when extrapolating experimental results to natural conditions. If we consider the rates of fluid-assisted intergranular diffusion ~ 10^{-8} $m{\cdot}s^{-1}$ (Rubie, 1986) and silicate melt transfer ~10^{-9}–10^{-12} $m{\cdot}s^{-1}$ (Neogi *et al.*, 2014), it is evident that the coarsening of minerals in the presence of melt operates on a shorter timescale than the process of melting. To address this problem I suggest using a set of natural examples that have experienced variable degrees of partial melting while undergoing continued

deformation to identify the dominant deformation mechanisms and the effect of partial melting on rock rheology.

Additionally, the following chapter-specific recommendations for further work are made:

- Chapter 2 - Further analyses of the chemical and textural evolution of accessory minerals during muscovite dehydration melting is recommended. The initial work presented here indicates that it may be possible to link monazite and xenotime microstructures to different stages of partial melting. This could prove a useful avenue for constraining the timescales of anatexis and melt transfer.
- Chapter 3 - Activity model for tourmaline and apatite, and thermodynamic models that address the fluid speciation of boron and phosphorus are required to further assess the conditions of melt–rock interaction during late-stage melt crystallisation and in general, the evolution of granitic melt.
- Chapter 4 - The architecture of the northern Indian margin (prior to its collision with Eurasia) can be further constrained by analysing the stratigraphy of the Greater Himalayan Series in western Nepal and northern India, with a particular focus on the depositional setting of carbonate strata.
- Chapter 5 - To evaluate the amount of water that could be retained in the upper crust through the formation of hydrates, and constrain the net flux of water released during muscovite dehydration melting, a fluid flow model is required that links phase equilibrium (chemical) with the dynamics of fluid flow (thermomechanical).

Bibliography

Acosta-Vigil, A., Buick, I., Hermann, J., Cesare, B., Rubatto, D., London, D., Morgan, G. B. (2010). Mechanisms of crustal anatexis: a geochemical study of partially melted metapelitic enclaves and host dacite, SE Spain. *Journal of Petrology*, egp095.

Ague, J. J. (1998). Simple models of coupled fluid infiltration and redox reactions in the crust. *Contributions to Mineralogy and Petrology* **132**, 180-197.

Ague, J. J. (2003). Fluid infiltration and transport of major, minor, and trace elements during regional metamorphism of carbonate rocks, Wepawaug Schist, Connecticut, USA. *American Journal of Science* **303**, 753-816.

Aharon, P., Schidlowski, M., Singh, I. B. (1987). Chronostratigraphic markers in the end-Precambrian carbon isotope record of the Lesser Himalaya.

Almqvist, B. S., Misra, S., Klonowska, I., Mainprice, D., Majka, J. (2015). Ultrasonic velocity drops and anisotropy reduction in mica-schist analogues due to melting with implications for seismic imaging of continental crust. *Earth and Planetary Science Letters* **425**, 24-33.

Argand, E. (1924). La tectonique de l'Asie. Conférence faite á Bruxelles, le 10 août 1922. *Congrès géologique international (XIIIe session)-Belgique 1922*, 171-372.

Armstrong, R. L. (1968). A model for the evolution of strontium and lead isotopes in a dynamic earth. *Reviews of geophysics* **6**, 175-199.

Avigad, D., Kolodner, K., McWilliams, M., Persing, H., Weissbrod, T. (2003). Origin of northern Gondwana Cambrian sandstone revealed by detrital zircon SHRIMP dating. *Geology* **31**, 227-230.

Ayres, M. & Harris, N. (1997). REE fractionation and Nd-isotope disequilibrium during crustal anatexis: constraints from Himalayan leucogranites. *Chemical Geology* **139**, 249-269.

Bachmann, F., Hielscher, R., Schaeben, H. (2010). Texture analysis with MTEX–free and open source software toolbox. *Solid State Phenomena* **160**, 63-68.

Baldwin, J., Powell, R., Brown, M., Moraes, R., Fuck, R. (2005). Modelling of mineral equilibria in ultrahigh-temperature metamorphic rocks from the Anápolis–Itauçu Complex, central Brazil. *Journal of Metamorphic Geology* **23**, 511-531.

Barbey, P., Brouand, M., Le Fort, P., Pecher, A. (1996). Granite-migmatite genetic link: the example of the Manaslu granite and Tibetan Slab migmatites in central Nepal. *Lithos* **38**, 63-79.

Beaumont, C., Jamieson, R., Nguyen, M., Lee, B. (2001). Himalayan tectonics explained by extrusion of a low-viscosity crustal channel coupled to focused surface denudation. *Nature* **414**, 738-742.

Beeler, N., Simpson, R., Hickman, S., Lockner, D. (2000). Pore fluid pressure, apparent friction, and Coulomb failure. *Journal of Geophysical Research: Solid Earth* **105**, 25533-25542.

Bettinelli, P., Avouac, J.-P., Flouzat, M., Jouanne, F., Bollinger, L., Willis, P., Chitrakar, G. R. (2006). Plate motion of India and interseismic strain in the Nepal Himalaya from GPS and DORIS measurements. *Journal of Geodesy* **80**, 567-589.

Bhowmik, S. K., Wilde, S. A., Bhandari, A., Pal, T., Pant, N. C. (2012). Growth of the Greater Indian Landmass and its assembly in Rodinia: geochronological evidence from the Central Indian Tectonic Zone. *Gondwana Research* **22**, 54-72.

Bilham, R., Larson, K., Freymueller, J., Jouanne, F., LeFort, P., Leturmy, P., Mugnier, J., Gamond, J., Glot, J., Martinod, J. (1997). GPS measurements of present-day convergence across the Nepal Himalaya. *Nature* **386**, 61-64.

Bird, P. (1978). Initiation of intracontinental subduction in the Himalaya. *Journal of Geophysical Research: Solid Earth* **83**, 4975-4987.

Bollinger, L., Avouac, J., Beyssac, O., Catlos, E., Harrison, T., Grove, M., Goffé, B., Sapkota, S. (2004). Thermal structure and exhumation history of the Lesser Himalaya in central Nepal. *Tectonics* **23**.

Booth, A. L., Chamberlain, C. P., Kidd, W. S., Zeitler, P. K. (2009). Constraints on the metamorphic evolution of the eastern Himalayan syntaxis from geochronologic and petrologic studies of Namche Barwa. *Geological Society of America Bulletin* **121**, 385-407.

Booth, A. L., Zeitler, P. K., Kidd, W. S., Wooden, J., Liu, Y., Idleman, B., Hren, M., Chamberlain, C. P. (2004). U-Pb zircon constraints on the tectonic evolution of southeastern Tibet, Namche Barwa area. *American Journal of Science* **304**, 889-929.

Bowen, N. L. (1940). Progressive metamorphism of siliceous limestone and dolomite. *The Journal of Geology*, 225-274.

Brearley, A. & Rubie, D. (1990). Effects of H2O on the disequilibrium breakdown of muscovite+ quartz. *Journal of Petrology* **31**, 925-956.

Brokus, S. A., Silletti, D. K., Lunderberg, J. M., DeYoung, P. A., Peaslee, G. F., Carpenter, D. E., Buscaglia, J. (2015). Cathodoluminescence dependence on feldspar mineral structure and implications for forensic geology. *American Mineralogist* **100**, 451-458.

Brookfield, M. (1993). The Himalayan passive margin from Precambrian to Cretaceous times. *Sedimentary Geology* **84**, 1-35.

Brown, L., Zhao, W., Nelson, K., Hauck, M., Alsdorf, D., Ross, A., Cogan, M., Clark, M., Liu, X., Che, J. (1996). Bright spots, structure, and magmatism in southern Tibet from INDEPTH seismic reflection profiling. *Science* **274**, 1688-1690.

Brown, M. (1994). The generation, segregation, ascent and emplacement of granite magma: the migmatite-to-crustally-derived granite connection in thickened orogens. *Earth-Science Reviews* **36**, 83-130.

Brown, M. (2007a). Crustal melting and melt extraction, ascent and emplacement in orogens: mechanisms and consequences. *Journal of the Geological Society* **164**, 709-730.

Brown, M. (2007b). Metamorphic conditions in orogenic belts: a record of secular change. *International Geology Review* **49**, 193-234.

Brown, M. & Rushmer, T. (2006). *Evolution and differentiation of the continental crust*: Cambridge University Press.

Brown, M. & Solar, G. S. (1998). Granite ascent and emplacement during contractional deformation in convergent orogens. *Journal of Structural Geology* **20**, 1365-1393.

Bryon, D., Atherton, M., Hunter, R. (1995). The interpretation of granitic textures from serial thin sectioning, image analysis and three-dimensional reconstruction. *Mineralogical Magazine* **59**, 203-212.

Bryon, D. N., Atherton, M. P., Hunter, R. H., Parsons, I. (1994). The description of the primary textures of "Cordilleran" granitic rocks. *Contributions to Mineralogy and Petrology* **117**, 66-75.

Buick, I., Stevens, G., Gibson, R. (2004). The role of water retention in the anatexis of metapelites in the Bushveld Complex Aureole, South Africa: an experimental study. *Journal of Petrology* **45**, 1777-1797.

Bureau, H. & Keppler, H. (1999). Complete miscibility between silicate melts and hydrous fluids in the upper mantle: experimental evidence and geochemical implications. *Earth and Planetary Science Letters* **165**, 187-196.

Burg, J. P., Davy, P., Nievergelt, P., Oberli, F., Seward, D., Diao, Z., Meier, M. (1997). Exhumation during crustal folding in the Namche-Barwa syntaxis. *Terra Nova* **9**, 53-56.

Burke, K. (1988). Tectonic evolution of the Caribbean. *Annual Review of Earth and Planetary Sciences* **16**, 201-230.

Cabane, H., Laporte, D., Provost, A. (2001). Experimental investigation of the kinetics of Ostwald ripening of quartz in silicic melts. *Contributions to Mineralogy and Petrology* **142**, 361-373.

Capitani, C. d. & Petrakakis, K. (2010). The computation of equilibrium assemblage diagrams with Theriak/Domino software. *American Mineralogist* **95**, 1006-1016.

Carmichael, D. M. (1969). On the mechanism of prograde metamorphic reactions in quartz-bearing pelitic rocks. *Contributions to Mineralogy and Petrology* **20**, 244-267.

Cashman, K. (1990). Textural constraints on the kinetics of crystallization of igneous rocks. *Reviews in Mineralogy and Geochemistry* **24**, 259-314.

Catlos, E., Harrison, T. M., Kohn, M. J., Grove, M., Ryerson, F., Manning, C. E., Upreti, B. (2001). Geochronologic and thermobarometric constraints on the evolution of the Main Central Thrust, central Nepal Himalaya. *Journal of Geophysical Research: Solid Earth* **106**, 16177-16204.

Catlos, E., Harrison, T. M., Manning, C. E., Grove, M., Rai, S. M., Hubbard, M. S., Upreti, B. (2002). Records of the evolution of the Himalayan orogen from in situ Th–Pb ion microprobe dating of monazite: Eastern Nepal and western Garhwal. *Journal of Asian Earth Sciences* **20**, 459-479.

Cesare, B. (2000). Incongruent melting of biotite to spinel in a quartz-free restite at El Joyazo (SE Spain): Textures and reaction characterization. *Contributions to Mineralogy and Petrology* **139**, 273-284.

Chakraborty, S., Anczkiewicz, R., Gaidies, F., Rubatto, D., Sorcar, N., Faak, K., Mukhopadhyay, D., Dasgupta, S. (2016). A review of thermal history and timescales of tectonometamorphic processes in Sikkim Himalaya (NE India) and implications for rates of metamorphic processes. *Journal of Metamorphic Geology*.

Chatterjee, S., Goswami, A., Scotese, C. R. (2013). The longest voyage: tectonic, magmatic, and paleoclimatic evolution of the Indian plate during its northward flight from Gondwana to Asia. *Gondwana Research* **23**, 238-267.

Clemens, J. D. (2006). *Melting of the continental crust: fluid regimes, melting reactions, and source-rock fertility*: Cambridge University Press.

Coggon, R. & Holland, T. (2002). Mixing properties of phengitic micas and revised garnet-phengite thermobarometers. *Journal of Metamorphic Geology* **20**, 683-696.

Colchen, M., Le Fort, P., Pêcher, A. (1986). Annapurna–Manaslu–Ganesh Himal. *Centre National de la Recherche Scientifique, Paris*, 75-136.

Collettini, C., Niemeijer, A., Viti, C., Marone, C. (2009). Fault zone fabric and fault weakness. *Nature* **462**, 907-910.

Connolly, J. (1997). Devolatilization-generated fluid pressure and deformation-propagated fluid flow during prograde regional metamorphism. *Journal of Geophysical Research: Solid Earth* **102**, 18149-18173.

Connolly, J. A. & Trommsdorff, V. (1991). Petrogenetic grids for metacarbonate rocks: pressure-temperature phase-diagram projection for mixed-volatile systems. *Contributions to Mineralogy and Petrology* **108**, 93-105.

Corthouts, T. L., Lageson, D. R., Shaw, C. A. (2016). Polyphase deformation, dynamic metamorphism, and metasomatism of Mount Everest's summit limestone, east central Himalaya, Nepal/Tibet. *Lithosphere* **8**, 38-57.

Cottle, J. M., Searle, M. P., Horstwood, M. S., Waters, D. J. (2009). Timing of midcrustal metamorphism, melting, and deformation in the Mount Everest region of southern Tibet revealed by U (-Th)-Pb geochronology. *The Journal of Geology* **117**, 643-664.

Cottle, J. M., Searle, M. P., Jessup, M. J., Crowley, J. L., Law, R. D. (2015). Rongbuk re-visited: Geochronology of leucogranites in the footwall of the South Tibetan Detachment System, Everest Region, Southern Tibet. *Lithos* **227**, 94-106.

Cox, K. G. (2013). *The interpretation of igneous rocks*: Springer Science & Business Media.

Crowley, J. L., Waters, D., Searle, M., Bowring, S. (2009). Pleistocene melting and rapid exhumation of the Nanga Parbat massif, Pakistan: Age and P–T conditions of accessory mineral growth in migmatite and leucogranite. *Earth and Planetary Science Letters* **288**, 408-420.

Dahlen, F. (1990). Critical taper model of fold-and-thrust belts and accretionary wedges. *Annual Review of Earth and Planetary Sciences* **18**, 55.

de Capitani, C. & Brown, T. H. (1987). The computation of chemical equilibrium in complex systems containing non-ideal solutions. *Geochimica et Cosmochimica Acta* **51**, 2639-2652.

de Capitani, C. & Petrakakis, K. (2010). The computation of equilibrium assemblage diagrams with Theriak/Domino software. *American Mineralogist* **95**, 1006-1016.

DeCelles, P., Gehrels, G., Najman, Y., Martin, A., Carter, A., Garzanti, E. (2004). Detrital geochronology and geochemistry of Cretaceous–Early Miocene strata of Nepal: implications for timing and diachroneity of initial Himalayan orogenesis. *Earth and Planetary Science Letters* **227**, 313-330.

DeCelles, P., Gehrels, G., Quade, J., LaReau, B., Spurlin, M. (2000). Tectonic implications of U-Pb zircon ages of the Himalayan orogenic belt in Nepal. *Science* **288**, 497-499.

DeCelles, P. G., Robinson, D. M., Zandt, G. (2002). Implications of shortening in the Himalayan fold-thrust belt for uplift of the Tibetan Plateau. *Tectonics* **21**.

Dell'Angelo, L. & Tullis, J. (1988). Experimental deformation of partially melted granitic aggregates. *Journal of Metamorphic Geology* **6**, 495-515.

Dewey, J., Cande, S., Pitman, W. C. (1989). Tectonic evolution of the India/Eurasia collision zone. *Eclogae Geologicae Helvetiae* **82**, 717-734.

Dewey, J. F., Shackleton, R. M., Chengfa, C., Yiyin, S. (1988). The tectonic evolution of the Tibetan Plateau. *Philosophical Transactions of the Royal Society of London A: Mathematical, Physical and Engineering Sciences* **327**, 379-413.

Ding, L. & Zhong, D. (1999). Metamorphic characteristics and geotectonic implications of the high-pressure granulites from Namjagbarwa, eastern Tibet. *Science in China Series D: Earth Sciences* **42**, 491-505.

Douce, A. E. P. & Harris, N. (1998). Experimental constraints on Himalayan anatexis. *Journal of Petrology* **39**, 689-710.

Dyck, B., Reno, B. L., Kokfelt, T. F. (2015). The Majorqaq Belt: A record of Neoarchaean orogenesis during final assembly of the North Atlantic Craton, southern West Greenland. *Lithos* **220**, 253-271.

Dyck, B. & St-Onge, M. (2013). Dehydration-melting reactions, leucogranite emplacement and the Paleoproterozoic structural evolution of Hall Peninsula, Baffin Island, Nunavut. *Summary of Activities*, 73-84.

Eggleton, R. A. & Buseck, P. R. (1980). The orthoclase-microcline inversion: A high-resolution transmission electron microscope study and strain analysis. *Contributions to Mineralogy and Petrology* **74**, 123-133.

Elliott, D. (1976). The motion of thrust sheets. *Journal of Geophysical Research* **81**, 949-963.

England, P., Le Fort, P., Molnar, P., Pêcher, A. (1992). Heat sources for Tertiary metamorphism and anatexis in the Annapurna-Manaslu region central Nepal. *Journal of Geophysical Research: Solid Earth* **97**, 2107-2128.

Etheridge, M. A., Wall, V., Cox, S., Vernon, R. (1984). High fluid pressures during regional metamorphism and deformation: implications for mass transport and deformation mechanisms. *Journal of Geophysical Research: Solid Earth* **89**, 4344-4358.

Evans, B., Renner, J., Hirth, G. (2001). A few remarks on the kinetics of static grain growth in rocks. *International Journal of Earth Sciences* **90**, 88-103.

Evans, B. W. & Guidotti, C. V. (1966). The sillimanite-potash feldspar isograd in western Maine, USA. *Contributions to Mineralogy and Petrology* **12**, 25-62.

Farr, T. G., Rosen, P. A., Caro, E., Crippen, R., Duren, R., Hensley, S., Kobrick, M., Paller, M., Rodriguez, E., Roth, L. (2007). The shuttle radar topography mission. *Reviews of geophysics* **45**.

Faugères, J.-C. & Stow, D. (2008). Contourite drifts: nature, evolution and controls. *Developments in sedimentology* **60**, 257-288.

Fielding, E. J. (1996). Tibet uplift and erosion. *Tectonophysics* **260**, 55-84.

Flora, N. J., Yoder, C. H., Jenkins, H. D. B. (2004). Lattice Energies of Apatites and the Estimation of Δ H f°(PO43-, g). *Inorganic chemistry* **43**, 2340-2345.

Foster, G., Vance, D., Argles, T., Harris, N. (2002). The Tertiary collision-related thermal history of the NW Himalaya. *Journal of Metamorphic Geology* **20**, 827-843.

Foster, G. L. (2000). The pre-Neogene thermal history of the Nanga Parbat Haramosh Massif and the NW Himalaya. Open University.

Fraser, G., Worley, B., Sandiford, M. (2000). High-precision geothermobarometry across the High Himalayan metamorphic sequence, Langtang Valley, Nepal. *Journal of Metamorphic Geology* **18**, 665-681.

Frey, M., Capitani, C. d., Liou, J. (1991). A new petrogenetic grid for low-grade metabasites. *Journal of Metamorphic Geology* **9**, 497-509.

Funakawa, S. (2001). Lower Paleozoic Tethys sediments from the Kathmandu nappe. *Phulchauki area, central Nepal: Journal of Nepal Geological Society* **25**, 123-134.

Galer, S. (1991). Interrelationships between continental freeboard, tectonics and mantle temperature. *Earth and Planetary Science Letters* **105**, 214-228.

Gansser, A. (1983). *Geology of the Bhutan Himalaya*: Birkh@: auser Basel etc.

Gardien, V., Thompson, A. B., Grujic, D., Ulmer, P. (1995). Experimental melting of biotite+ plagioclase+ quartz±muscovite assemblages and implications for crustal melting. *Journal of Geophysical Research: Solid Earth (1978–2012)* **100**, 15581-15591.

Garofalo, P., Audétat, A., Günther, D., Heinrich, C., Ridley, J. (2000). Estimation and testing of standard molar thermodynamic properties of tourmaline end-members using data of natural samples. *American Mineralogist* **85**, 78-88.

Garzanti, E. (1999). Stratigraphy and sedimentary history of the Nepal Tethys Himalaya passive margin. *Journal of Asian Earth Sciences* **17**, 805-827.

Garzanti, E., Baud, A., Mascle, G. (1987). Sedimentary record of the northward flight of India and its collision with Eurasia (Ladakh Himalaya, India). *Geodinamica Acta* **1**, 297-312.

Garzanti, E., Casnedi, R., Jadoul, F. (1986). Sedimentary evidence of a Cambro-Ordovician orogenic event in the northwestern Himalaya. *Sedimentary Geology* **48**, 237-265.

Gehrels, G., DeCelles, P., Martin, A., Ojha, T., Pinhassi, G., Upreti, B. (2003). Initiation of the Himalayan orogen as an early Paleozoic thin-skinned thrust belt. *GSA today* **13**, 4-9.

Gehrels, G., Kapp, P., DeCelles, P., Pullen, A., Blakey, R., Weislogel, A., Ding, L., Guynn, J., Martin, A., McQuarrie, N. (2011). Detrital zircon geochronology of pre-Tertiary strata in the Tibetan-Himalayan orogen. *Tectonics* **30**.

Gleeson, T. P. & Godin, L. (2006). The Chako antiform: a folded segment of the Greater Himalayan sequence, Nar valley, Central Nepal Himalaya. *Journal of Asian Earth Sciences* **27**, 717-734.

Godin, L., Gleeson, T., Searle, M., Ullrich, T., Parrish, R. R. (2006a). Locking of southward extrusion in favour of rapid crustal-scale buckling of the Greater Himalayan

sequence, Nar valley, central Nepal. *Geological Society, London, Special Publications* **268**, 269-292.

Godin, L., Grujic, D., Law, R., Searle, M. (2006b). Channel flow, ductile extrusion and exhumation in continental collision zones: an introduction. *Geological Society, London, Special Publications* **268**, 1-23.

Godin, L. & Harris, L. B. (2014). Tracking basement cross-strike discontinuities in the Indian crust beneath the Himalayan orogen using gravity data–relationship to upper crustal faults. *Geophysical Journal International* **198**, 198-215.

Godin, L., Parrish, R. R., Brown, R. L., Hodges, K. V. (2001). Crustal thickening leading to exhumation of the Himalayan metamorphic core of central Nepal: Insight from U-Pb geochronology and 40Ar/39Ar thermochronology. *Tectonics* **20**, 729-747.

Goscombe, B., Gray, D., Hand, M. (2006). Crustal architecture of the Himalayan metamorphic front in eastern Nepal. *Gondwana Research* **10**, 232-255.

Götze, J., Plötze, M., Habermann, D. (2001). Origin, spectral characteristics and practical applications of the cathodoluminescence (CL) of quartz–a review. *Mineralogy and Petrology* **71**, 225-250.

Green, O. R., Searle, M. P., Corfield, R. I., Corfield, R. M. (2008). Cretaceous-Tertiary carbonate platform evolution and the age of the India-Asia collision along the Ladakh Himalaya (Northwest India). *The Journal of Geology* **116**, 331-353.

Groppo, C., Rolfo, F., Mosca, P. (2013). The cordierite-bearing anatectic rocks of the higher Himalayan crystallines (eastern Nepal): low-pressure anatexis, melt productivity, melt loss and the preservation of cordierite. *Journal of Metamorphic Geology* **31**, 187-204.

Groppo, C., Rubatto, D., Rolfo, F., Lombardo, B. (2010). Early oligocene partial melting in the main central thrust zone (Arun valley, eastern Nepal Himalaya). *Lithos* **118**, 287-301.

Grujic, D., Casey, M., Davidson, C., Hollister, L. S., Kündig, R., Pavlis, T., Schmid, S. (1996). Ductile extrusion of the Higher Himalayan Crystalline in Bhutan: evidence from quartz microfabrics. *Tectonophysics* **260**, 21-43.

Guillot, S. & Le Fort, P. (1995). Geochemical constraints on the bimodal origin of High Himalayan leucogranites. *Lithos* **35**, 221-234.

Guilmette, C., Indares, A., Hébert, R. (2011). High-pressure anatectic paragneisses from the Namche Barwa, Eastern Himalayan Syntaxis: Textural evidence for partial melting, phase equilibria modeling and tectonic implications. *Lithos* **124**, 66-81.

Haack, U. & Zimmermann, H. (1996). Retrograde mineral reactions: a heat source in the continental crust? *Geologische Rundschau* **85**, 130-137.

Hacker, B. R. (2008). H_2O subduction beyond arcs. *Geochemistry, Geophysics, Geosystems* **9**.

Harley, S. L. (1998). On the occurrence and characterization of ultrahigh-temperature crustal metamorphism. *Geological Society, London, Special Publications* **138**, 81-107.

Harlov, D. E., Wirth, R., Hetherington, C. J. (2011). Fluid-mediated partial alteration in monazite: the role of coupled dissolution–reprecipitation in element redistribution and mass transfer. *Contributions to Mineralogy and Petrology* **162**, 329-348.

Harris, N., Ayres, M., Massey, J. (1995). Geochemistry of granitic melts produced during the incongruent melting of muscovite: implications for the extraction of Himalayan leucogranite magmas. *Journal of Geophysical Research: Solid Earth (1978–2012)* **100**, 15767-15777.

Harris, N. & Inger, S. (1992). Trace element modelling of pelite-derived granites. *Contributions to Mineralogy and Petrology* **110**, 46-56.

Harris, N. & Massey, J. (1994). Decompression and anatexis of Himalayan metapelites. *Tectonics* **13**, 1537-1546.

Harrison, M. T., Grove, M., Mckeegan, K. D., Coath, C., Lovera, O. M., Le Fort, P. (1999). Origin and episodic emplacement of the Manaslu intrusive complex, central Himalaya. *Journal of Petrology* **40**, 3-19.

Harrison, T. M., Grove, M., Lovera, O. M., Catlos, E. (1998). A model for the origin of Himalayan anatexis and inverted metamorphism. *Journal of Geophysical Research: Solid Earth* **103**, 27017-27032.

Harrison, T. M., Ryerson, F., Le Fort, P., Yin, A., Lovera, O. M., Catlos, E. (1997). A late Miocene-Pliocene origin for the central Himalayan inverted metamorphism. *Earth and Planetary Science Letters* **146**, E1-E7.

Harrison, T. M. & Watson, E. B. (1984). The behavior of apatite during crustal anatexis: equilibrium and kinetic considerations. *Geochimica et Cosmochimica Acta* **48**, 1467-1477.

Hawkesworth, C., Dhuime, B., Pietranik, A., Cawood, P., Kemp, A., Storey, C. (2010). The generation and evolution of the continental crust. *Journal of the Geological Society* **167**, 229-248.

Higgins, M. D. (2000). Measurement of crystal size distributions. *American Mineralogist* **85**, 1105-1116.

Hillert, M. (1988). Inhibition of grain growth by second-phase particles. *Acta Metallurgica* **36**, 3177-3181.

Hodges, K. (2006). A synthesis of the channel flow-extrusion hypothesis as developed for the Himalayan-Tibetan orogenic system. *Geological Society, London, Special Publications* **268**, 71-90.

Hodges, K., Parrish, R., Searle, M. (1996). Tectonic evolution of the central Annapurna range, Nepalese Himalayas. *Tectonics* **15**, 1264-1291.

Hodges, K. V. (2000). Tectonics of the Himalaya and southern Tibet from two perspectives. *Geological Society of America Bulletin* **112**, 324-350.

Holland, T., Baker, J., Powell, R. (1998). Mixing properties and activity-composition relationships of chlorites in the system MgO-FeO-Al_2O_3-SiO_2-H_2O. *European Journal of Mineralogy*, 395-406.

Holland, T. & Powell, R. (1998). An internally consistent thermodynamic data set for phases of petrological interest. *Journal of Metamorphic Geology* **16**, 309-343.

Holland, T. & Powell, R. (2001). Calculation of phase relations involving haplogranitic melts using an internally consistent thermodynamic dataset. *Journal of Petrology* **42**, 673-683.

Holness, M. (2006). Melt–solid dihedral angles of common minerals in natural rocks. *Journal of Petrology* **47**, 791-800.

Holness, M. & Siklos, S. (2000). The rates and extent of textural equilibration in high-temperature fluid-bearing systems. *Chemical Geology* **162**, 137-153.

Holness, M. B. (1997). *Deformation-enhanced fluid transport in the earth's crust and mantle*: Springer Science & Business Media.

Holness, M. B., Cesare, B., Sawyer, E. W. (2011). Melted rocks under the microscope: microstructures and their interpretation. *Elements* **7**, 247-252.

Holness, M. B., Cheadle, M. J., McKenzie, D. (2005). On the use of changes in dihedral angle to decode late-stage textural evolution in cumulates. *Journal of Petrology* **46**, 1565-1583.

Holness, M. B. & Sawyer, E. W. (2008). On the pseudomorphing of melt-filled pores during the crystallization of migmatites. *Journal of Petrology* **49**, 1343-1363.

Hubbard, M. (1996). Ductile shear as a cause of inverted metamorphism: example from the Nepal Himalaya. *The Journal of Geology*, 493-499.

Hunter, R. (1996). Texture development in cumulate rocks. *Developments in Petrology* **15**, 77-101.

Immenhauser, A. (2009). Estimating palaeo-water depth from the physical rock record. *Earth-Science Reviews* **96**, 107-139.

Inger, S. & Harris, N. (1992). Tectonothermal evolution of the High Himalayan crystalline sequence, Langtang Valley, northern Nepal. *Journal of Metamorphic Geology* **10**, 439-452.

Inger, S. & Harris, N. (1993). Geochemical constraints on leucogranite magmatism in the Langtang Valley, Nepal Himalaya. *Journal of Petrology* **34**, 345-368.

Jamieson, R., Beaumont, C., Fullsack, P., Lee, B. (1998). Barrovian regional metamorphism: Where's the heat? *Geological Society, London, Special Publications* **138**, 23-51.

Jan, M. Q. & Howie, R. (1981). The mineralogy and geochemistry of the metamorphosed basic and ultrabasic rocks of the Jijal complex, Kohistan, NW Pakistan. *Journal of Petrology* **22**, 85-126.

Jarrard, R. D. (2003). Subduction fluxes of water, carbon dioxide, chlorine, and potassium. *Geochemistry, Geophysics, Geosystems* **4**.

Jefferies, S., Holdsworth, R., Wibberley, C., Shimamoto, T., Spiers, C., Niemeijer, A., Lloyd, G. (2006). The nature and importance of phyllonite development in crustal-scale fault cores: an example from the Median Tectonic Line, Japan. *Journal of Structural Geology* **28**, 220-235.

Jiang, G., Christie-Blick, N., Kaufman, A. J., Banerjee, D. M., Rai, V. (2002). Sequence stratigraphy of the Neoproterozoic Infra Krol Formation and Krol Group, Lesser Himalaya, India. *Journal of Sedimentary Research* **72**, 524-542.

Johnson, E. A. & Rossman, G. R. (2004). A survey of hydrous species and concentrations in igneous feldspars. *American Mineralogist* **89**, 586-600.

Kelemen, P., Hirth, G., Shimizu, N., Spiegelman, M., Dick, H. (1997). A review of melt migration processes in the adiabatically upwelling mantle beneath oceanic spreading ridges. *Philosophical Transactions of the Royal Society of London A: Mathematical, Physical and Engineering Sciences* **355**, 283-318.

Kelemen, P. B., Whitehead, J., Aharonov, E., Jordahl, K. A. (1995). Experiments on flow focusing in soluble porous media, with applications to melt extraction from the mantle. *Journal of Geophysical Research: Solid Earth* **100**, 475-496.

Kellett, D., Grujic, D., Warren, C., Cottle, J., Jamieson, R., Tenzin, T. (2010). Metamorphic history of a syn-convergent orogen-parallel detachment: The South Tibetan detachment system, Bhutan Himalaya. *Journal of Metamorphic Geology* **28**, 785-808.

Kellett, D. A., Grujic, D., Erdmann, S. (2009). Miocene structural reorganization of the South Tibetan detachment, eastern Himalaya: Implications for continental collision. *Lithosphere* **1**, 259-281.

Kelsey, D., White, R., Holland, T., Powell, R. (2004). Calculated phase equilibria in K_2O-FeO-MgO-Al_2O_3-SiO_2-H_2O for sapphirine-quartz-bearing mineral assemblages. *Journal of Metamorphic Geology* **22**, 559-578.

Kerrick, D. & Connolly, J. (1998). Subduction of ophicarbonates and recycling of CO_2 and H_2O. *Geology* **26**, 375-378.

Kohn, M., Wieland, M., Parkinson, C., Upreti, B. (2005). Five generations of monazite in Langtang gneisses: implications for chronology of the Himalayan metamorphic core. *Journal of Metamorphic Geology* **23**, 399-406.

Kohn, M. J. (2008). PTt data from central Nepal support critical taper and repudiate large-scale channel flow of the Greater Himalayan Sequence. *Geological Society of America Bulletin* **120**, 259-273.

Kohn, M. J., Wieland, M. S., Parkinson, C. D., Upreti, B. N. (2004). Miocene faulting at plate tectonic velocity in the Himalaya of central Nepal. *Earth and Planetary Science Letters* **228**, 299-310.

Kumar, P. S., Menon, R., Reddy, G. (2009). Heat production heterogeneity of the Indian crust beneath the Himalaya: Insights from the northern Indian Shield. *Earth and Planetary Science Letters* **283**, 190-196.

Larson, K. M., Bürgmann, R., Bilham, R., Freymueller, J. T. (1999). Kinematics of the India-Eurasia collision zone from GPS measurements. *Journal of Geophysical Research: Solid Earth* **104**, 1077-1093.

Law, R., Searle, M., Simpson, R. (2004). Strain, deformation temperatures and vorticity of flow at the top of the Greater Himalayan Slab, Everest Massif, Tibet. *Journal of the Geological Society* **161**, 305-320.

Le Breton, N. & Thompson, A. B. (1988). Fluid-absent (dehydration) melting of biotite in metapelites in the early stages of crustal anatexis. *Contributions to Mineralogy and Petrology* **99**, 226-237.

Le Fort, P. (1975). Himalayas: the collided range. Present knowledge of the continental arc. *American Journal of Science* **275**, 44.

Le Fort, P. (1986). Metamorphism and magmatism during the Himalayan collision. *Geological Society, London, Special Publications* **19**, 159-172.

Le Fort, P., Cuney, M., Deniel, C., France-Lanord, C., Sheppard, S., Upreti, B., Vidal, P. (1987). Crustal generation of the Himalayan leucogranites. *Tectonophysics* **134**, 39-57.

Lejeune, A. M. & Richet, P. (1995). Rheology of crystal-bearing silicate melts: An experimental study at high viscosities. *Journal of Geophysical Research: Solid Earth* **100**, 4215-4229.

Leloup, P. H., Liu, X., Mahéo, G., Paquette, J.-L., Arnaud, N., Aubray, A., Liu, X. (2015). New constraints on the timing of partial melting and deformation along the Nyalam section (central Himalaya): implications for extrusion models. *Geological Society, London, Special Publications* **412**, 131-175.

Li, S., Unsworth, M. J., Booker, J. R., Wei, W., Tan, H., Jones, A. G. (2003). Partial melt or aqueous fluid in the mid-crust of Southern Tibet? Constraints from INDEPTH magnetotelluric data. *Geophysical Journal International* **153**, 289-304.

London, D. (1999). Stability of tourmaline in pei aluminous granite systems: the boron cycle from anatexis to hydrothermal aureoles. *European Journal of Mineralogy*, 253-262.

London, D., Hervig, R. L., VI, G. B. M. (1988). Melt-vapor solubilities and elemental partitioning in peraluminous granite-pegmatite systems: experimental results with Macusani glass at 200 MPa. *Contributions to Mineralogy and Petrology* **99**, 360-373.

London, D. & Manning, D. A. (1995). Chemical variation and significance of tourmaline from Southwest England. *Economic geology* **90**, 495-519.

Ludwig, K. (2003). *User's manual for Isoplot 3.00: a geochronological toolkit for Microsoft Excel*: Kenneth R. Ludwig.

Macfarlane, A. (1993). Chronology of tectonic events in the crystalline core of the Himalaya, Langtang National Park, central Nepal. *Tectonics* **12**, 1004-1025.

Macfarlane, A. (1995). An evaluation of the inverted metamorphic gradient at Langtang National Park, central Nepal Himalaya. *Journal of Metamorphic Geology* **13**, 595-612.

Macfarlane, A. M. (1992). The tectonic evolution of the core of the Himalaya, Langtang National Park, central Nepal. Massachusetts Institute of Technology.

Macfarlane, A. M. (1999). The metamorphic history of the crystalline rocks in the high Himalaya, Nepal: insights from thermobarometric data. *Journal of Asian Earth Sciences* **17**, 741-753.

Marquer, D., Chawla, H., Challandes, N. (2000). Pre-alpine high-grade metamorphism in High Himalaya crystalline sequences: Evidence from Lower palaeozoic Kinnauer Kailas granite and surrounding rocks in the Sutlej Valley (Himachal Pradesch, India). *Eclogae Geologicae Helvetiae* **93**, 207-220.

Martin, A. J., Burgy, K. D., Kaufman, A. J., Gehrels, G. E. (2011). Stratigraphic and tectonic implications of field and isotopic constraints on depositional ages of Proterozoic Lesser Himalayan rocks in central Nepal. *Precambrian Research* **185**, 1-17.

Maruo, Y. & Kizaki, K. (1981). Structure and metamorphism in eastern Nepal. *Metamorphic Tectonites of the Himalaya*, 175-230.

McClelland, W. C., Gehrels, G. E., Samson, S. D., Patchett, P. J. (1992). Protolith relations of the Gravina belt and Yukon-Tanana terrane in central southeastern Alaska. *The Journal of Geology*, 107-123.

McKie, T. (1990). A model for marine shelf storm deposition in the Lower Cambrian Fucoid Beds of northwest Scotland. *Geological Magazine* **127**, 45-53.

McQuarrie, N., Robinson, D., Long, S., Tobgay, T., Grujic, D., Gehrels, G., Ducea, M. (2008). Preliminary stratigraphic and structural architecture of Bhutan: Implications for the along strike architecture of the Himalayan system. *Earth and Planetary Science Letters* **272**, 105-117.

Molnar, P. (1988). A review of geophysical constraints on the deep structure of the Tibetan Plateau, the Himalaya and the Karakoram, and their tectonic implications. *Philosophical Transactions of the Royal Society of London A: Mathematical, Physical and Engineering Sciences* **326**, 33-88.

Molnar, P., Chen, W. P., Padovani, E. (1983). Calculated temperatures in overthrust terrains and possible combinations of heat sources responsible for the Tertiary granites in the Greater Himalaya. *Journal of Geophysical Research: Solid Earth* **88**, 6415-6429.

Molnar, P. & Stock, J. M. (2009). Slowing of India's convergence with Eurasia since 20 Ma and its implications for Tibetan mantle dynamics. *Tectonics* **28**.

Molnar, P. & Tapponnier, P. (1975). Cenozoic tectonics of Asia: effects of a continental collision. *Science* **189**, 419-426.

Moore, D. E. & Rymer, M. J. (2007). Talc-bearing serpentinite and the creeping section of the San Andreas fault. *Nature* **448**, 795-797.

Mottram, C. M., Argles, T., Harris, N., Parrish, R., Horstwood, M., Warren, C., Gupta, S. (2014). Tectonic interleaving along the Main Central Thrust, Sikkim Himalaya. *Journal of the Geological Society* **171**, 255-268.

Müller, A., Seltmann, R., Behr, H.-J. (2000). Application of cathodoluminescence to magmatic quartz in a tin granite–case study from the Schellerhau Granite Complex, Eastern Erzgebirge, Germany. *Mineralium Deposita* **35**, 169-189.

Mutti, E. (1985). Turbidite systems and their relations to depositional sequences. *Provenance of arenites*: Springer, 65-93.

Myers, J. S. (2001). Protoliths of the 3.8–3.7 Ga Isua greenstone belt, west Greenland. *Precambrian Research* **105**, 129-141.

Myrow, P. M., Hughes, N. C., Goodge, J. W., Fanning, C. M., Williams, I. S., Peng, S., Bhargava, O. N., Parcha, S. K., Pogue, K. R. (2010). Extraordinary transport and mixing of sediment across Himalayan central Gondwana during the Cambrian–Ordovician. *Geological Society of America Bulletin* **122**, 1660-1670.

Myrow, P. M., Hughes, N. C., Paulsen, T., Williams, I., Parcha, S. K., Thompson, K., Bowring, S. A., Peng, S.-C., Ahluwalia, A. (2003). Integrated tectonostratigraphic analysis of the Himalaya and implications for its tectonic reconstruction. *Earth and Planetary Science Letters* **212**, 433-441.

Myrow, P. M., Hughes, N. C., Searle, M. P., Fanning, C., Peng, S.-C., Parcha, S. K. (2009). Stratigraphic correlation of Cambrian–Ordovician deposits along the Himalaya: Implications for the age and nature of rocks in the Mount Everest region. *Geological Society of America Bulletin* **121**, 323-332.

Nábělek, P. I. & Nábělek, J. L. (2014). Thermal characteristics of the Main Himalaya Thrust and the Indian lower crust with implications for crustal rheology and partial melting in the Himalaya orogen. *Earth and Planetary Science Letters* **395**, 116-123.

Nelson, K. D., Zhao, W., Brown, L., Kuo, J., Che, J., Liu, X., Klemperer, S., Makovsky, Y., Meissner, R., Mechie, J. (1996). Partially molten middle crust beneath southern Tibet: synthesis of project INDEPTH results. *Science* **274**, 1684-1688.

Neogi, S., Bolton, E. W., Chakraborty, S. (2014). Timescales of disequilibrium melting in the crust: constraints from modelling the distribution of multiple trace elements and a case study from the Lesser Himalayan rocks of Sikkim. *Contributions to Mineralogy and Petrology* **168**, 1-22.

Noble, S. & Searle, M. (1995). Age of crustal melting and leucogranite formation from U-Pb zircon and monazite dating in the western Himalaya, Zanskar, India. *Geology* **23**, 1135-1138.

O'Brien, P., Zotov, N., Law, R., Khan, M. A., Jan, M. Q. (2001). Coesite in Himalayan eclogite and implications for models of India-Asia collision. *Geology* **29**, 435-438.

Palin, R., St-Onge, M., Waters, D., Searle, M., Dyck, B. (2014). Phase equilibria modelling of retrograde amphibole and clinozoisite in mafic eclogite from the Tso Morari massif, northwest India: constraining the P–T–M (H_2O) conditions of exhumation. *Journal of Metamorphic Geology* **32**, 675-693.

Palin, R. M., Weller, O. M., Waters, D. J., Dyck, B. (2015). Quantifying geological uncertainty in metamorphic phase equilibria modelling; a Monte Carlo assessment and implications for tectonic interpretations. *Geoscience Frontiers*.

Parai, R. & Mukhopadhyay, S. (2012). How large is the subducted water flux? New constraints on mantle regassing rates. *Earth and Planetary Science Letters* **317**, 396-406.

Parrish, R. R. & Hodges, V. (1996). Isotopic constraints on the age and provenance of the Lesser and Greater Himalayan sequences, Nepalese Himalaya. *Geological Society of America Bulletin* **108**, 904-911.

Passchier, C. W. & Trouw, R. A. (1996). *Microtectonics*: Springer.

Patiño-Douce, A. E. & Harris, N. (1998). Experimental constraints on Himalayan anatexis. *Journal of Petrology* **39**, 689-710.

Patiño-Douce, A. E. & Johnston, A. D. (1991). Phase equilibria and melt productivity in the pelitic system: implications for the origin of peraluminous granitoids and aluminous granulites. *Contributions to Mineralogy and Petrology* **107**, 202-218.

Pattison, D. R. & Tracy, R. J. (1991). Phase equilibria and thermobarometry of metapelites. *Reviews in Mineralogy and Geochemistry* **26**, 105-206.

Pearce, M. & Wheeler, J. (2010). Modelling grain-recycling zoning during metamorphism. *Journal of Metamorphic Geology* **28**, 423-437.

Pearson, O. (2002). Structural evolution of the central Nepal fold-thrust belt and regional tectonic and structural significance of the Ramgarh thrust.

Pearson, O. N. & DeCelles, P. G. (2005). Structural geology and regional tectonic significance of the Ramgarh thrust, Himalayan fold-thrust belt of Nepal. *Tectonics* **24**.

Pecher, A. & Le Fort, P. (1977). Origin and significance of the Lesser Himalayan augen gneisses. *Colloque International CNRS*, 319-329.

Petö, P. (1976). An experimental investigation of melting relations involving muscovite and paragonite in the silica-saturated portion of the system K2O-Na2OAl2O3-SiO2-H2O to 15 kbar total pressure. *Progress in Experimental Petrology* **3**, 41-45.

Plank, T. & Langmuir, C. H. (1998). The chemical composition of subducting sediment and its consequences for the crust and mantle. *Chemical Geology* **145**, 325-394.

Pognante, U., Castelli, D., Benna, P., Genovese, G., Oberli, F., Meier, M., Tonarini, S. (1990). The crystalline units of the High Himalayas in the Lahul-Zanskar region (northwest India): metamorphictectonic history and geochronology of the collided and imbricated Indian plate. *Geological Magazine* **127**, 101-116.

Poli, S. & Schmidt, M. W. (1995). H_2O transport and release in subduction zones: experimental constraints on basaltic and andesitic systems. *Journal of Geophysical Research: Solid Earth* **100**, 22299-22314.

Posamentier, H. (1988). Eustatic controls on clastic deposition I—conceptual framework.

Powell, R., Holland, T., Worley, B. (1998). Calculating phase diagrams involving solid solutions via non-linear equations, with examples using THERMOCALC. *Journal of Metamorphic Geology* **16**, 577-588.

Prasad, B. R., Klemperer, S. L., Rao, V. V., Tewari, H., Khare, P. (2011). Crustal structure beneath the Sub-Himalayan fold–thrust belt, Kangra recess, northwest India, from seismic reflection profiling: Implications for Late Paleoproterozoic orogenesis and modern earthquake hazard. *Earth and Planetary Science Letters* **308**, 218-228.

Prior, D. (1999). Problems in determining the misorientation axes, for small angular misorientations, using electron backscatter diffraction in the SEM. *Journal of Microscopy* **195**, 217-225.

Putnis, A. (2002). Mineral replacement reactions: from macroscopic observations to microscopic mechanisms. *Mineralogical Magazine* **66**, 689-708.

Putnis, A. & Austrheim, H. (2013). Mechanisms of metasomatism and metamorphism on the local mineral scale: the role of dissolution-reprecipitation during mineral re-equilibration. *Metasomatism and the Chemical Transformation of Rock*: Springer, 141-170.

Putnis, A. & Putnis, C. V. (2007). The mechanism of reequilibration of solids in the presence of a fluid phase. *Journal of Solid State Chemistry* **180**, 1783-1786.

Raith, M. M., Sengupta, P., Kooijman, E., Upadhyay, D., Srikantappa, C. (2010). Corundum–leucosome-bearing aluminous gneiss from Ayyarmalai, Southern Granulite Terrain, India: A textbook example of vapor phase-absent muscovite-melting in silica-undersaturated aluminous rocks. *American Mineralogist* **95**, 897-907.

Rampone, E., Romairone, A., Hofmann, A. (2004). Contrasting bulk and mineral chemistry in depleted mantle peridotites: evidence for reactive porous flow. *Earth and Planetary Science Letters* **218**, 491-506.

Rapp, R. P. & Watson, E. B. (1986). Monazite solubility and dissolution kinetics: implications for the thorium and light rare earth chemistry of felsic magmas. *Contributions to Mineralogy and Petrology* **94**, 304-316.

Reddy, S. M., Searle, M. P., Massey, J. A. (1993). Structural evolution of the High Himalayan gneiss sequence, Langtang valley, Nepal. *Geological Society, London, Special Publications* **74**, 375-389.

Renner, J., Evans, B., Hirth, G. (2000). On the rheologically critical melt fraction. *Earth and Planetary Science Letters* **181**, 585-594.

Richards, A., Argles, T., Harris, N., Parrish, R., Ahmad, T., Darbyshire, F., Draganits, E. (2005). Himalayan architecture constrained by isotopic tracers from clastic sediments. *Earth and Planetary Science Letters* **236**, 773-796.

Roduit, N. (2008). JMicroVision: Image analysis toolbox for measuring and quantifying components of high-definition images. Version 1.2. 7. *Software available for free download at http://www. jmicrovision. com.*

Rolfo, F., Lombardo, B., Compagnoni, R., Le Fort, P., Lemennicier, Y., Pêcher, A. (1997). Geology and metamorphism of the Ladakh terrane and Shyok suture zone in the Chogo Lungma–Turmik area (northern Pakistan). *Geodinamica Acta* **10**, 251-270.

Roscoe, R. (1952). The viscosity of suspensions of rigid spheres. *British Journal of Applied Physics* **3**, 267.

Rosenberg, C. & Handy, M. (2005). Experimental deformation of partially melted granite revisited: implications for the continental crust. *Journal of Metamorphic Geology* **23**, 19-28.

Royden, L. H., Burchfiel, B. C., King, R. W., Wang, E., Chen, Z., Shen, F., Liu, Y. (1997). Surface deformation and lower crustal flow in eastern Tibet. *Science* **276**, 788-790.

Rubatto, D., Müntener, O., Barnhoorn, A., Gregory, C. (2008). Dissolution-reprecipitation of zircon at low-temperature, high-pressure conditions (Lanzo Massif, Italy). *American Mineralogist* **93**, 1519-1529.

Rubie, D. C. (1986). The catalysis of mineral reactions by water and restrictions on the presence of aqueous fluid during metamorphism. *Mineralogical Magazine* **50**, 399-415.

Ruggles, T., Rampton, T., Khosravani, A., Fullwood, D. (2016). The effect of length scale on the determination of geometrically necessary dislocations via EBSD continuum dislocation microscopy. *Ultramicroscopy* **164**, 1-10.

Saxena, M. (1971). The crystalline axis of the Himalaya: the Indian shield and continental drift. *Tectonophysics* **12**, 433-447.

Scaillet, B., France-Lanord, C., Le Fort, P. (1990). Badrinath-Gangotri plutons (Garhwal, India): petrological and geochemical evidence for fractionation processes in a high Himalayan leucogranite. *Journal of Volcanology and Geothermal Research* **44**, 163-188.

Scaillet, B., Pichavant, M., Roux, J. (1995). Experimental crystallization of leucogranite magmas. *Journal of Petrology* **36**, 663-705.

Scaillet, B. & Searle, M. P. (2006). Mechanisms and timescales of felsic magma segregation, ascent and emplacement in the Himalaya. *Geological Society, London, Special Publications* **268**, 293-308.

Schärer, U. & Allègre, C. J. (1983). The Palung granite (Himalaya); high-resolution UPb systematics in zircon and monazite. *Earth and Planetary Science Letters* **63**, 423-432.

Schärer, U., Xu, R.-H., Allègre, C. J. (1986). U (Th) Pb systematics and ages of Himalayan leucogranites, South Tibet. *Earth and Planetary Science Letters* **77**, 35-48.

Schön, J. (1983). *Petrophysik: Physikalische Eigenschaften von Gesteinen und Mineralen*: F. Enke.

Searle, M. (1999). Emplacement of Himalayan leucogranites by magma injection along giant sill complexes: examples from the Cho Oyu, Gyachung Kang and Everest leucogranites (Nepal Himalaya). *Journal of Asian Earth Sciences* **17**, 773-783.

Searle, M., Cornfield, R. I., Stephenson, B., McCarron, J. (1997a). Structure of the North Indian continental margin in the Ladakh–Zanskar Himalayas: implications for the timing of obduction of the Spontang ophiolite, India–Asia collision and deformation events in the Himalaya. *Geological Magazine* **134**, 297-316.

Searle, M., Cottle, J., Streule, M., Waters, D. (2010). Crustal melt granites and migmatites along the Himalaya: melt source, segregation, transport and granite emplacement mechanisms. *Geological Society of America Special Papers* **472**, 219-233.

Searle, M., Khan, M. A., Fraser, J., Gough, S., Jan, M. Q. (1999). The tectonic evolution of the Kohistan-Karakoram collision belt along the Karakoram Highway transect, north Pakistan. *Tectonics* **18**, 929-949.

Searle, M., Law, R., Jessup, M. (2006b). Crustal structure, restoration and evolution of the Greater Himalaya in Nepal-South Tibet: implications for channel flow and ductile extrusion of the middle crust. *Geological Society, London, Special Publications* **268**, 355-378.

Searle, M., Parrish, R., Hodges, K., Hurford, A., Ayres, M., Whitehouse, M. (1997b). Shisha Pangma leucogranite, south Tibetan Himalaya: field relations, geochemistry, age, origin, and emplacement. *The Journal of Geology* **105**, 295-318.

Searle, M., Simpson, R., Law, R., Parrish, R., Waters, D. (2003). The structural geometry, metamorphic and magmatic evolution of the Everest massif, High Himalaya of Nepal–South Tibet. *Journal of the Geological Society* **160**, 345-366.

Searle, M., Windley, B., Coward, M., Cooper, D., Rex, A., Rex, D., Tingdong, L., Xuchang, X., Jan, M., Thakur, V. (1987a). The closing of Tethys and the tectonics of the Himalaya. *Geological Society of America Bulletin* **98**, 678-701.

Searle, M. P. (1991). *Geology and tectonics of the Karakoram Mountains*: John Wiley & Sons Inc.

Searle, M. P. & Godin, L. (2003). The south Tibetan detachment and the Manaslu Leucogranite: A structural reinterpretation and restoration of the Annapurna-Manaslu Himalaya, Nepal. *The Journal of Geology* **111**, 505-523.

Searle, M. P., Law, R. D., Godin, L., Larson, K. P., Streule, M. J., Cottle, J. M., Jessup, M. J. (2008). Defining the Himalayan main central thrust in Nepal. *Journal of the Geological Society* **165**, 523-534.

Searle, M. P. & Rex, A. (1989). Thermal model for the Zanskar Himalaya. *Journal of Metamorphic Geology* **7**, 127-134.

Searle, M. P., Windley, B. F., Coward, M. P., Cooper, D. J. W., Rex, A. J., Rex, D., Li, T. D., Xiao, X. C., Jan, M. Q., Thakur, V. C., Kumar, S. (1987b). The Closing of Tethys and the Tectonics of the Himalaya. *Geological Society of America Bulletin* **98**, 678-701.

Seyedolali, A., Krinsley, D. H., Boggs, S., O'Hara, P. F., Dypvik, H., Goles, G. G. (1997). Provenance interpretation of quartz by scanning electron microscope–cathodoluminescence fabric analysis. *Geology* **25**, 787-790.

Shaw, D. M. (1956). Geochemistry of pelitic rocks. Part III: Major elements and general geochemistry. *Geological Society of America Bulletin* **67**, 919-934.

Sibson, R. H. (1994). Crustal stress, faulting and fluid flow. *Geological Society, London, Special Publications* **78**, 69-84.

Simpson, R. (2002). Metamorphism, melting and extension at the top of the High Himalayan slab, Mount Everest region, Nepal and Tibet. *Department of Earth Sciences*: University of Oxford.

Simpson, R. L., Parrish, R. R., Searle, M. P., Waters, D. J. (2000). Two episodes of monazite crystallization during metamorphism and crustal melting in the Everest region of the Nepalese Himalaya. *Geology* **28**, 403-406.

Sirbescu, M.-L. C. & Nabelek, P. I. (2003). Crystallization conditions and evolution of magmatic fluids in the Harney Peak Granite and associated pegmatites, Black Hills, South Dakota—Evidence from fluid inclusions. *Geochimica et Cosmochimica Acta* **67**, 2443-2465.

Smith, J. & Stenstrom, R. (1965). Electron-excited luminescence as a petrologic tool. *The Journal of Geology*, 627-635.

Smye, A. J. & Stockli, D. F. (2014). Rutile U–Pb age depth profiling: A continuous record of lithospheric thermal evolution. *Earth and Planetary Science Letters* **408**, 171-182.

Spear, F. S. & Cheney, J. T. (1989). A petrogenetic grid for pelitic schists in the system SiO2-Al2O3-FeO-MgO-K2O-H2O. *Contributions to Mineralogy and Petrology* **101**, 149-164.

Spencer, C., Harris, R., Dorais, M. (2012). Depositional provenance of the Himalayan metamorphic core of Garhwal region, India: Constrained by U–Pb and Hf isotopes in zircons. *Gondwana Research* **22**, 26-35.

Spencer, C. J., Hawkesworth, C., Cawood, P. A., Dhuime, B. (2013). Not all supercontinents are created equal: Gondwana-Rodinia case study. *Geology* **41**, 795-798.

Spiegelman, M. & Kelemen, P. B. (2003). Extreme chemical variability as a consequence of channelized melt transport. *Geochemistry, Geophysics, Geosystems* **4**.

Spiegelman, M., Kelemen, P. B., Aharonov, E. (2001). Causes and consequences of flow organization during melt transport: The reaction infiltration instability in compactible media. *Journal of Geophysical Research: Solid Earth* **106**, 2061-2077.

St-Onge, M. (1981). "Normal" and "inverted" metamorphic isograds and their relation to syntectonic Proterozoic batholiths in the Wopmay orogen, Northwest Territories, Canada. *Tectonophysics* **76**, 295-316.

St-Onge, M., Rayner, N., Palin, R., Searle, M., Waters, D. (2013). Integrated pressure–temperature–time constraints for the Tso Morari dome (Northwest India): implications for the burial and exhumation path of UHP units in the western Himalaya. *Journal of Metamorphic Geology* **31**, 469-504.

St-Onge, M. R. (1984). The muscovite-melt bathograd and low-P isograd suites in north-central Wopmay Orogen, Northwest Territories, Canada. *Journal of Metamorphic Geology* **2**, 315-326.

Stampfli, G., Marcoux, J., Baud, A. (1991). Tethyan margins in space and time. *Palaeogeography, Palaeoclimatology, Palaeoecology* **87**, 373-409.

Steck, A. (2003). Geology of the NW Indian Himalaya. *Eclogae Geologicae Helvetiae* **96**, 147-196.

Stephenson, B., Searle, M., Waters, D., Rex, D. (2001). Structure of the Main Central Thrust zone and extrusion of the High Himalayan deep crustal wedge, Kishtwar–Zanskar Himalaya. *Journal of the Geological Society* **158**, 637-652.

Stephenson, B., Waters, D., Searle, M. (2000). Inverted metamorphism and the Main Central Thrust: field relations and thermobarometric constraints from the Kishtwar Window, NW Indian Himalaya. *Journal of Metamorphic Geology* **18**, 571-590.

Stern, R. (1997). The GSC Sensitive High Resolution Ion Microprobe (SHRIMP): analytical techniques of zircon U-Th-Pb age determinations and performance evaluation. *Radiogenic age and isotopic studies: Report* **10**, 1-31.

Stern, R. A. & Berman, R. G. (2001). Monazite U–Pb and Th–Pb geochronology by ion microprobe, with an application to in situ dating of an Archean metasedimentary rock. *Chemical Geology* **172**, 113-130.

Stöcklin, J. (1980). Geology of Nepal and its regional frame Thirty-third William Smith Lecture. *Journal of the Geological Society* **137**, 1-34.

Streule, M., Searle, M., Waters, D., Matthew, S., Horstwood, M. (2010a). Metamorphism, melting and channel flow in the Greater Himalaya Sequence and Makalu leucogranite: constraints from thermobarometry, metamorphic modelling and U–Pb geochronology. Tectonics 29, TC5011.

Streule, M. J., Searle, M. P., Waters, D. J., Horstwood, M. S. (2010b). Metamorphism, melting, and channel flow in the Greater Himalayan Sequence and Makalu leucogranite:

Constraints from thermobarometry, metamorphic modeling, and U-Pb geochronology. *Tectonics* **29**.

Suda, H., Yashima, M., Kakihana, M., Yoshimura, M. (1995). Monoclinic. tautm. Hexagonal Phase Transition in Hydroxyapatite Studied by X-ray Powder Diffraction and Differential Scanning Calorimeter Techniques. *The Journal of Physical Chemistry* **99**, 6752-6754.

Suhr, G. (1999). Melt migration under oceanic ridges: inferences from reactive transport modelling of upper mantle hosted dunites. *Journal of Petrology* **40**, 575-599.

Suhr, G., Seck, H., Shimizu, N., Gunther, D., Jenner, G. (1998). Circulation of refractory melts in the lowermost oceanic crust: evidence from a trace element study of dunite-hosted clinopyroxenes in the Bay of Islands Ophiolite. *Contrib Mineral Petrol* **122**, 387-405.

Takagi, H., Arita, K., Danhara, T., Iwano, H. (2007). Timing of the Tsergo Ri landslide, Langtang Himal, determined by fission-track dating of pseudotachylyte. *Journal of Asian Earth Sciences* **29**, 466-472.

Takagi, H., Arita, K., Sawaguchi, T., Kobayashi, K., Awaji, D. (2003). Kinematic history of the Main Central Thrust zone in the Langtang area, Nepal. *Tectonophysics* **366**, 151-163.

Talling, P. J., Masson, D. G., Sumner, E. J., Malgesini, G. (2012). Subaqueous sediment density flows: depositional processes and deposit types. *Sedimentology* **59**, 1937-2003.

Taylor, M. & Yin, A. (2009). Active structures of the Himalayan-Tibetan orogen and their relationships to earthquake distribution, contemporary strain field, and Cenozoic volcanism. *Geosphere* **5**, 199-214.

Thomas, R., Förster, H.-J., Heinrich, W. (2003). The behaviour of boron in a peraluminous granite-pegmatite system and associated hydrothermal solutions: a melt and fluid-inclusion study. *Contributions to Mineralogy and Petrology* **144**, 457-472.

Thomas, R., Webster, J., Heinrich, W. (2000). Melt inclusions in pegmatite quartz: complete miscibility between silicate melts and hydrous fluids at low pressure. *Contributions to Mineralogy and Petrology* **139**, 394-401.

Thompson, A. B. (1982). Dehydration melting of pelitic rocks and the generation of H 2 O-undersaturated granitic liquids. *American Journal of Science* **282**, 1567-1595.

Thompson, A. B. (1996). Fertility of crustal rocks during anatexis. *Geological Society of America Special Papers* **315**, 1-10.

Thompson, A. B. & Algor, J. R. (1977). Model systems for anatexis of pelitic rocks. *Contributions to Mineralogy and Petrology* **63**, 247-269.

Unsworth, M., Jones, A. G., Wei, W., Marquis, G., Gokarn, S., Spratt, J., Bedrosian, P., Booker, J., Leshou, C., Clarke, G. (2005). Crustal rheology of the Himalaya and Southern Tibet inferred from magnetotelluric data. *Nature* **438**, 78-81.

Van Hinsbergen, D. J., Lippert, P. C., Dupont-Nivet, G., McQuarrie, N., Doubrovine, P. V., Spakman, W., Torsvik, T. H. (2012). Greater India Basin hypothesis and a two-stage Cenozoic collision between India and Asia. *Proceedings of the National Academy of Sciences* **109**, 7659-7664.

Vance, D. & Harris, N. (1999). Timing of prograde metamorphism in the Zanskar Himalaya. *Geology* **27**, 395-398.

Vannay, J. C. & Hodges, K. (1996). Tectonometamorphic evolution of the Himalayan metamorphic core between the Annapurna and Dhaulagiri, central Nepal. *Journal of Metamorphic Geology* **14**, 635-656.

Vernon, R. (1979). Formation of late sillimanite by hydrogen metasomatism (base-leaching) in some high-grade gneisses. *Lithos* **12**, 143-152.

Vernon, R. (1987). Growth and concentration of fibrous sillimanite related to heterogeneous deformation in K-feldspar-sillimanite metapelites. *Journal of Metamorphic Geology* **5**, 51-68.

Vernon, R. (1990). K-feldspar augen in felsic gneisses and mylonites—deformed phenocrysts or porphyroblasts? *GFF* **112**, 157-167.

Vernon, R. H. (1986). K-feldspar megacrysts in granites—phenocrysts, not porphyroblasts. *Earth-Science Reviews* **23**, 1-63.

Vidal, P., Cocherie, A., Le Fort, P. (1982). Geochemical investigations of the origin of the Manaslu leucogranite (Himalaya, Nepal). *Geochimica et Cosmochimica Acta* **46**, 2279-2292.

Vielzeuf, D. & Holloway, J. R. (1988). Experimental determination of the fluid-absent melting relations in the pelitic system. *Contributions to Mineralogy and Petrology* **98**, 257-276.

Vigneresse, J. l., Barbey, P., Cuney, M. (1996). Rheological transitions during partial melting and crystallization with application to felsic magma segregation and transfer. *Journal of Petrology* **37**, 1579-1600.

Visonà, D. & Lombardo, B. (2002). Two-mica and tourmaline leucogranites from the Everest–Makalu region (Nepal–Tibet). Himalayan leucogranite genesis by isobaric heating? *Lithos* **62**, 125-150.

Voorhees, P. W. (1985). The theory of Ostwald ripening. *Journal of Statistical Physics* **38**, 231-252.

Vry, J., Powell, R., Golden, K. M., Petersen, K. (2010). The role of exhumation in metamorphic dehydration and fluid production. *Nature Geoscience* **3**, 31-35.

Walker, C., Searle, M., Waters, D. (2001). An integrated tectonothermal model for the evolution of the High Himalaya in western Zanskar with constraints from thermobarometry and metamorphic modeling. *Tectonics* **20**, 810-833.

Walker, J. D. (1988). Paleogeography and tectonic evolution interpreted from deformed sequences: principles, limitations, and examples from the southwestern united States. *New Perspectives in Basin Analysis*: Springer, 281-294.

Walther, J. V. & Orville, P. M. (1982). Volatile production and transport in regional metamorphism. *Contributions to Mineralogy and Petrology* **79**, 252-257.

Wang, J.-M., Zhang, J.-J., Liu, K., Zhang, B., Wang, X.-X., Rai, S., Scheltens, M. (2016). Spatial and temporal evolution of tectonometamorphic discontinuities in the central Himalaya: Constraints from P–T paths and geochronology. *Tectonophysics* **679**, 41-60.

Waters, D. (1988). Partial melting and the formation of granulite facies assemblages in Namaqualand, South Africa. *Journal of Metamorphic Geology* **6**, 387-404.

Waters, D. J. (2001). The significance of prograde and retrograde quartz-bearing intergrowth microstructures in partially melted granulite-facies rocks. *Lithos* **56**, 97-110.

Webb, A. A. G., Yin, A., Harrison, T. M., Célérier, J., Burgess, W. P. (2007). The leading edge of the Greater Himalayan Crystalline complex revealed in the NW Indian Himalaya: Implications for the evolution of the Himalayan orogen. *Geology* **35**, 955-958.

Webster, J., Goldoff, B., Sintoni, M., Shimizu, N., De Vivo, B. (2014). C–O–H–Cl–S–F Volatile Solubilities, Partitioning, and Mixing in Phonolitic–Trachytic Melts and Aqueous–Carbonic Vapor±Saline Liquid at 200 MPa. *Journal of Petrology*, egu055.

Wei, W., Unsworth, M., Jones, A., Booker, J., Tan, H., Nelson, D., Chen, L., Li, S., Solon, K., Bedrosian, P. (2001). Detection of widespread fluids in the Tibetan crust by magnetotelluric studies. *Science* **292**, 716-719.

Weller, O., St-Onge, M., Searle, M., Waters, D., Rayner, N., Chen, S., Chung, S. L., Palin, R. (2015). Quantifying the P–T–t conditions of north–south Lhasa terrane accretion: new insight into the pre-Himalayan architecture of the Tibetan plateau. *Journal of Metamorphic Geology* **33**, 91-113.

Weller, O., St-Onge, M., Waters, D., Rayner, N., Searle, M., Chung, S. L., Palin, R., Lee, Y. H., Xu, X. (2013). Quantifying Barrovian metamorphism in the Danba structural culmination of eastern Tibet. *Journal of Metamorphic Geology* **31**, 909-935.

White, R., Powell, R., Holland, T. (2001). Calculation of partial melting equilibria in the system Na_2O–CaO–K_2O–FeO–MgO–Al_2O_3–SiO_2–H_2O (NCKFMASH). *Journal of Metamorphic Geology* **19**, 139-153.

White, R., Powell, R., Holland, T. (2007). Progress relating to calculation of partial melting equilibria for metapelites. *Journal of Metamorphic Geology* **25**, 511-527.

Whitney, D. L. & Evans, B. W. (2010). Abbreviations for names of rock-forming minerals. *American Mineralogist* **95**, 185.

Whittington, A., Harris, N., Baker, J. (2000). Low-pressure crustal anatexis: the significance of spinel and cordierite from metapelitic assemblages at Nanga Parbat, northern Pakistan. *Geological Society of London Special Publications* **138**, 183-198.

Wolf, M. B. & London, D. (1997). Boron in granitic magmas: stability of tourmaline in equilibrium with biotite and cordierite. *Contributions to Mineralogy and Petrology* **130**, 12-30.

Wood, B. J. (1976). *Elementary thermodynamics for geologists*: Oxford University Press, USA.

Wu, C., Nelson, K., Wortman, G., Samson, S. D., Yue, Y., Li, J., Kidd, W., Edwards, M. (1998). Yadong cross structure and South Tibetan Detachment in the east central Himalaya (89 -90). *Tectonics* **17**, 28-45.

Xu, Y.-G., Menzies, M. A., Thirlwall, M. F., Huang, X.-L., Liu, Y., Chen, X.-M. (2003). "Reactive" harzburgites from Huinan, NE China: products of the lithosphere-asthenosphere interaction during lithospheric thinning? *Geochimica et Cosmochimica Acta* **67**, 487-505.

Yin, A. (2006). Cenozoic tectonic evolution of the Himalayan orogen as constrained by along-strike variation of structural geometry, exhumation history, and foreland sedimentation. *Earth-Science Reviews* **76**, 1-131.

Yin, A. & Harrison, T. M. (2000). Geologic evolution of the Himalayan-Tibetan orogen. *Annual Review of Earth and Planetary Sciences* **28**, 211-280.

Zeitler, P. K., Koons, P. O., Bishop, M. P., Chamberlain, C. P., Craw, D., Edwards, M. A., Hamidullah, S., Jan, M. Q., Khan, M. A., Khattak, M. (2001). Crustal reworking at Nanga Parbat, Pakistan: Metamorphic consequences of thermal-mechanical coupling facilitated by erosion. *Tectonics* **20**, 712-728.

Zhang, H., Harris, N., Parrish, R., Kelley, S., Zhang, L., Rogers, N., Argles, T., King, J. (2004). Causes and consequences of protracted melting of the mid-crust exposed in the North Himalayan antiform. *Earth and Planetary Science Letters* **228**, 195-212.

Zhang, Z., Dong, X., Santosh, M., Liu, F., Wang, W., Yiu, F., He, Z., Shen, K. (2012). Petrology and geochronology of the Namche Barwa Complex in the eastern Himalayan syntaxis, Tibet: constraints on the origin and evolution of the north-eastern margin of the Indian Craton. *Gondwana Research* **21**, 123-137.

Zhu, B., Kidd, W. S., Rowley, D. B., Currie, B. S., Shafique, N. (2005). Age of initiation of the India-Asia collision in the east-central Himalaya. *The Journal of Geology* **113**, 265-285.

Zieg, M. & Marsh, B. (2002). Crystal size distributions and scaling laws in the quantification of igneous textures. *Journal of Petrology* **43**, 85-101.

Appendices

A1 Description of external contributions

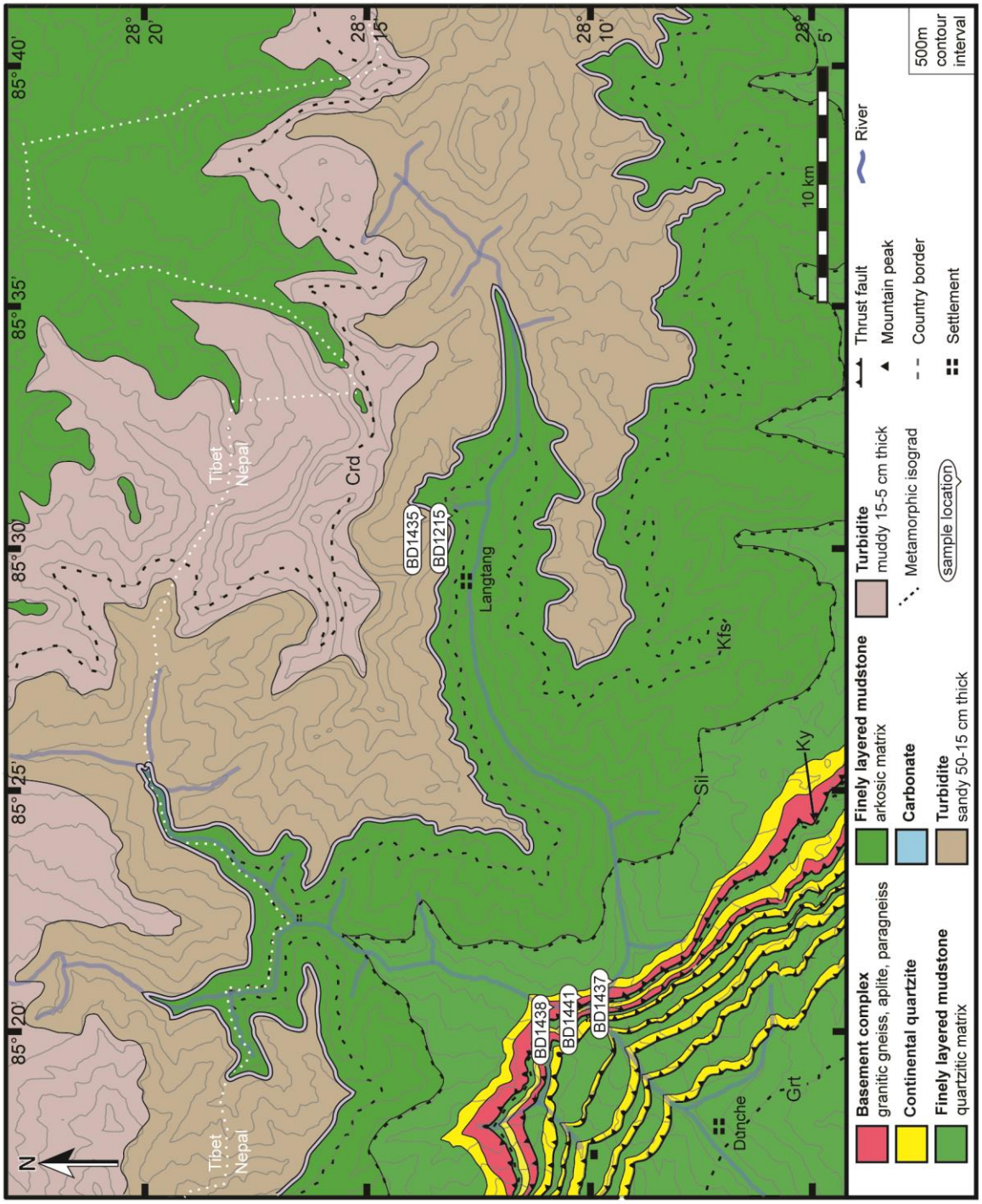
Chapter 2 – This chapter was written by B.J. Dyck. Fieldwork and sample collection was conducted by B.J. Dyck with assistance from M.R. St-Onge (GSC) and M.P. Searle (Oxford). Co-author manuscript reviews were given by D.J. Waters (Oxford), M.R. St-Onge (GSC), and M.P. Searle (Oxford). SEM and EBSD support was provided by N. Charnley (Oxford), L. Hansen (Oxford) and D. Wallis (Oxford).

Chapter 3 – This chapter was written by B.J. Dyck. Fieldwork and sample collection was conducted by B.J. Dyck with assistance from M.R. St-Onge (GSC). Co-author manuscript reviews were given by D.J. Waters (Oxford), M.R. St-Onge (GSC), and M.P. Searle (Oxford). D. Wallis (Oxford) provided EBSD support.

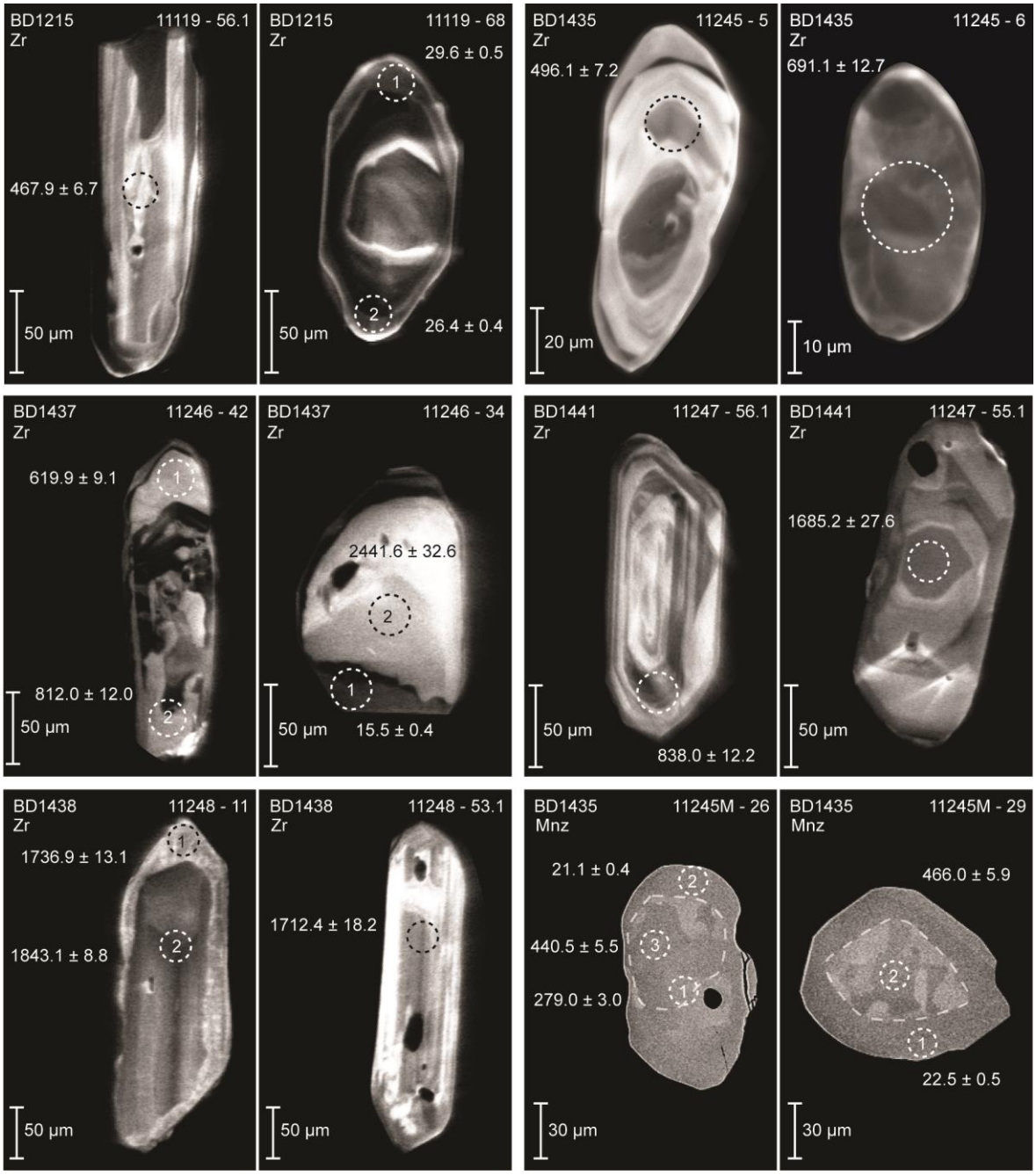
Chapter 4 – This chapter was written by B.J. Dyck. Fieldwork and sample collection was conducted by B.J. Dyck with assistance from M.R. St-Onge (GSC). Co-author manuscript reviews were given by M.R. St-Onge (GSC), M.P. Searle (Oxford), N. Rayner (GSC), D.J. Waters (Oxford), and O. Weller (Oxford). U–Pb geochronology was conducted at the GSC with invaluable support from N. Rayner in data collection, reduction and analysis. SEM support was provided by P. Hunt (GSC).

Chapter 5 – The research presented in this chapter was conceived, carried out, and written by B.J.Dyck. The thermal profile used to calculate figure 5.5a was calculated by A.J. Smye (Penn State).

A1 Protolith map of the Langtang area



A3 Representative zircon (Zr) CL and monazite (Mnz) BSE images from samples: BD1215, BD1435, BD1437, BD1438, and BD1441



A4 Sample GPS coordinates

Sample ID	Rock type	Latitude (N)	Longitude (E)	Elevation (m)
BD1201	Grt-schist	28.14650	85.34699	2304
BD1202	Ky-schist	28.14581	85.35226	2288
BD1203	Ky-schist	28.15321	85.37598	1797
BD1204	Sil-migmatite	28.19628	85.44826	2823
BD1205	Sil-migmatite	28.20287	85.58466	3825
BD1206	Bt-psammite	28.21582	85.66725	4173
BD1207	Bt-psammite	28.21582	85.66725	4173
BD1208	Tur-leucogranite	28.21582	85.66725	4173
BD1209	Crd-leucogranite	28.23714	85.68827	4461
BD1210	Sil-migmatite	28.23714	85.68827	4461
BD1211	Sil-migmatite	28.22245	85.57284	4436
BD1212	Sil-migmatite	28.22848	85.56671	4023
BD1213	Ms-Bt-leucogranite	28.22942	85.56957	4080
BD1214	Bt-Mag-psammite	28.21829	85.56361	3831
BD1215	Sil-migmatite	28.23144	85.55761	4094
BD1216	Ms-Bt-leucogranite	28.23144	85.55761	4094
BD1217	Sil-migmatite	28.21707	85.52550	3565
BD1218	Bt-psammite	28.21942	85.49627	3483
BD1219	Psammitic migmatite leucosome	28.21942	85.49627	3483
BD1222	Sil-migmatite	28.20044	85.45514	3065
BD1223	Sil-migmatite	28.18628	85.44190	2841
BD1224	Sil-migmatite leucosome	28.17225	85.43621	2711
BD1225	Sil-migmatite	28.16094	85.41996	2380
BD1226	Ky-Sil-migmatite	28.16094	85.41996	2380
BD1227	Ky-schist	28.15697	85.39710	1978
BD1228	Ky-schist	28.15312	85.36946	1834
BD1229	Ky-migmatite	28.15312	85.36946	1834
BD1230	Grt-schist	28.15359	85.35962	1718
BD1231	Grt-schist	28.15876	85.35053	1632
BD1232	Grt-schist	28.16053	85.33308	1362
BD1233	Grt-schist	28.16014	85.33006	1385
BD1234	Grt-schist	28.14410	85.31939	1639
BD1235	Grt-schist	28.14065	85.31507	1770
BD1236	Grt-schist	28.13254	85.31497	1872
BD1401	Ky-schist	28.15901	85.42369	2414
BD1402	Ky-schist	28.15901	85.42369	2414
BD1403	Kfs augen gneiss	28.23144	85.55761	4094
BD1404	Bt-aplite	28.21829	85.56361	3831
BD1405	Ms-Bt-leucogranite	28.21829	85.56361	3831
BD1406	Ms-Bt-leucogranite	28.21829	85.56361	3831
BD1407	Contact: Ms-Bt-Leucogranite & Bt-aplite	28.21829	85.56361	3831

BD1408	Contact: Ms-Bt-Leucogranite & Bt-aplite	28.21829	85.56361	3831
BD1409	Contact: Ms-Bt-Leucogranite & Bt-aplite	28.21829	85.56361	3831
BD1410	Kfs augen gneiss	28.20261	85.58324	3827
BD1411	Kfs augen gneiss	28.20261	85.58324	3827
BD1412	Tur-leucogranite	28.21794	85.67606	4067
BD1413	Bt-psammite	28.21582	85.66725	4173
BD1414	Tur-leucogranite	28.21582	85.66725	4173
BD1415	Tur-leucogranite	28.21582	85.66725	4173
BD1416	Sil-Kfs-semipelite	28.22851	85.68480	4336
BD1417	Tur-leucogranite (pegmatitic)	28.22851	85.68480	4336
BD1419	Bt-Sil-psammite	28.21701	85.66377	4205
BD1420	Ms-Bt-leucogranite	28.21701	85.66377	4205
BD1421	Tur-leucogranite (with Bt-selvage)	28.21868	85.66301	4287
BD1422	Crd-leucogranite	28.21966	85.66216	4367
BD1423	Bt-psammite	28.21966	85.66216	4367
BD1424	Tur-leucogranite	28.22001	85.66130	4356
BD1425	Tur-Grt-leucogranite (pegmatitic)	28.22001	85.66130	4356
BD1426	Bt-Sil-psammite	28.22001	85.66130	4356
BD1427	Bt-Sil-psammite	28.24401	85.69747	4523
BD1428	Bt-psammite	28.24401	85.69747	4523
BD1429	Kfs augen gneiss (glacial float)	28.24401	85.69747	4523
BD1430	Bt-psammite	28.21582	85.66725	4173
BD1431	Tur-leucogranite (pegmatitic)	28.21582	85.66725	4173
BD1432	Contact: Tur-leucogranite & Bt-psammite	28.21582	85.66725	4173
BD1433	Calcareous gneiss	28.20413	85.64366	3872
BD1434	Kfs augen gneiss	28.20413	85.64366	3872
BD1435	Bt-psammite (base of unit)	28.23328	85.55847	4199
BD1436	Grt-schist	28.15072	85.37090	1707
BD1437	Quartzite	28.15665	85.35201	1519
BD1438	Granodioritic augen gneiss	28.16919	85.34208	1456
BD1439	Granitic aplite	28.16919	85.34208	1456
BD1440	Quartzite	28.19011	85.34813	1524
BD1441	Quartzite	28.19011	85.34813	1524
BD1442	Bt-paragneiss	28.18856	85.34673	1541
BD1443	Psammite with Tur-leucogranite veins	28.21582	85.66725	4173

WGS84 grid reference